Javier Del Pino Gutiérrez

Vibrational and electronic strong light-matter coupling with molecular excitations

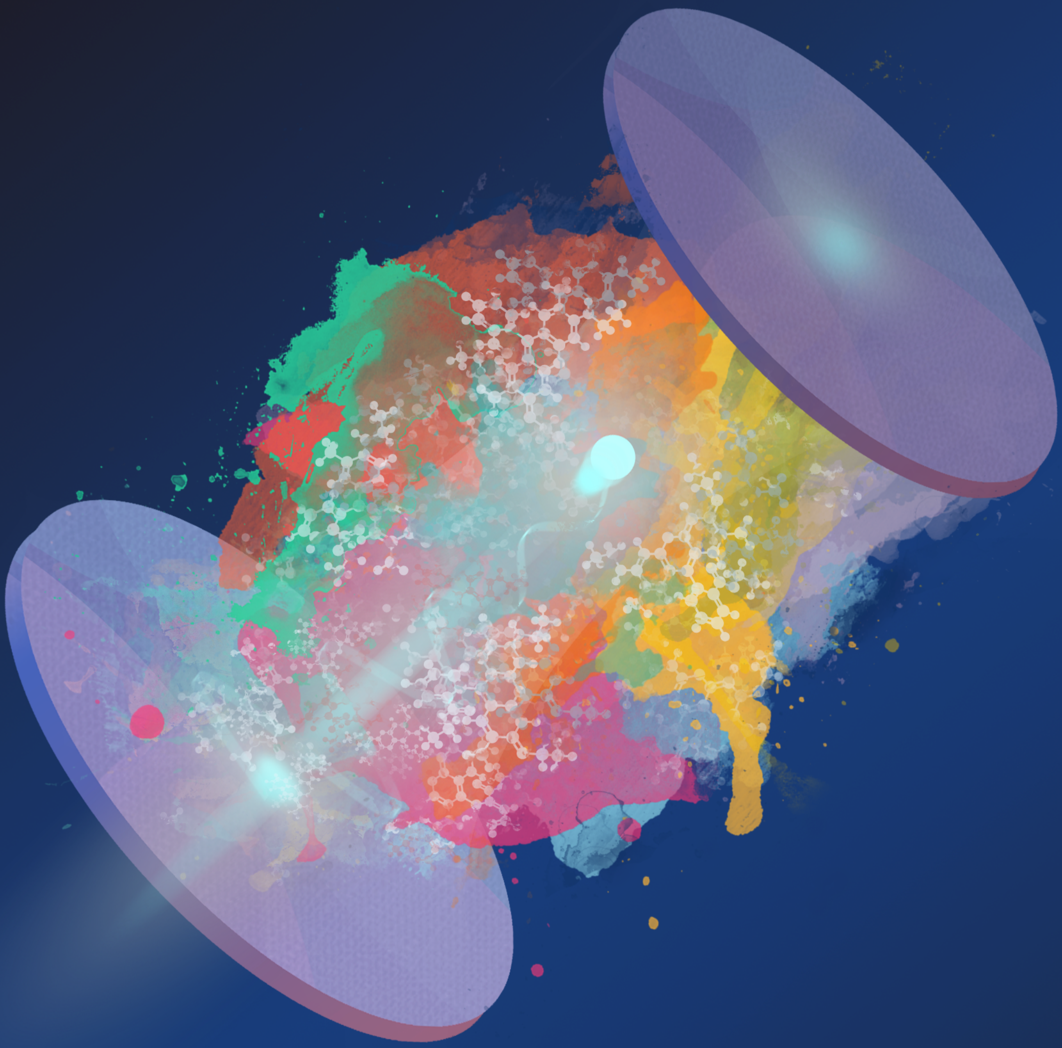

Universidad Autónoma de Madrid

Memoria presentada para optar al grado de Doctor en Ciencias Físicas

Universidad Autónoma de Madrid

Departamento de Física Teórica de la Materia Condensada

Condensed Matter Physics Center (IFIMAC)

Directores:
Dr. Francisco José García Vidal
Dr. Johannes Feist

Tribunal:
Dra. Susana Huelga
Dra. Francesca M. Marchetti
Dra. Elisabet Romero
Dr. Daniele Sanvitto
Dra. Elena del Valle (reserva)
Dr. Juan José García Ripoll (reserva)

Madrid, Junio de 2018

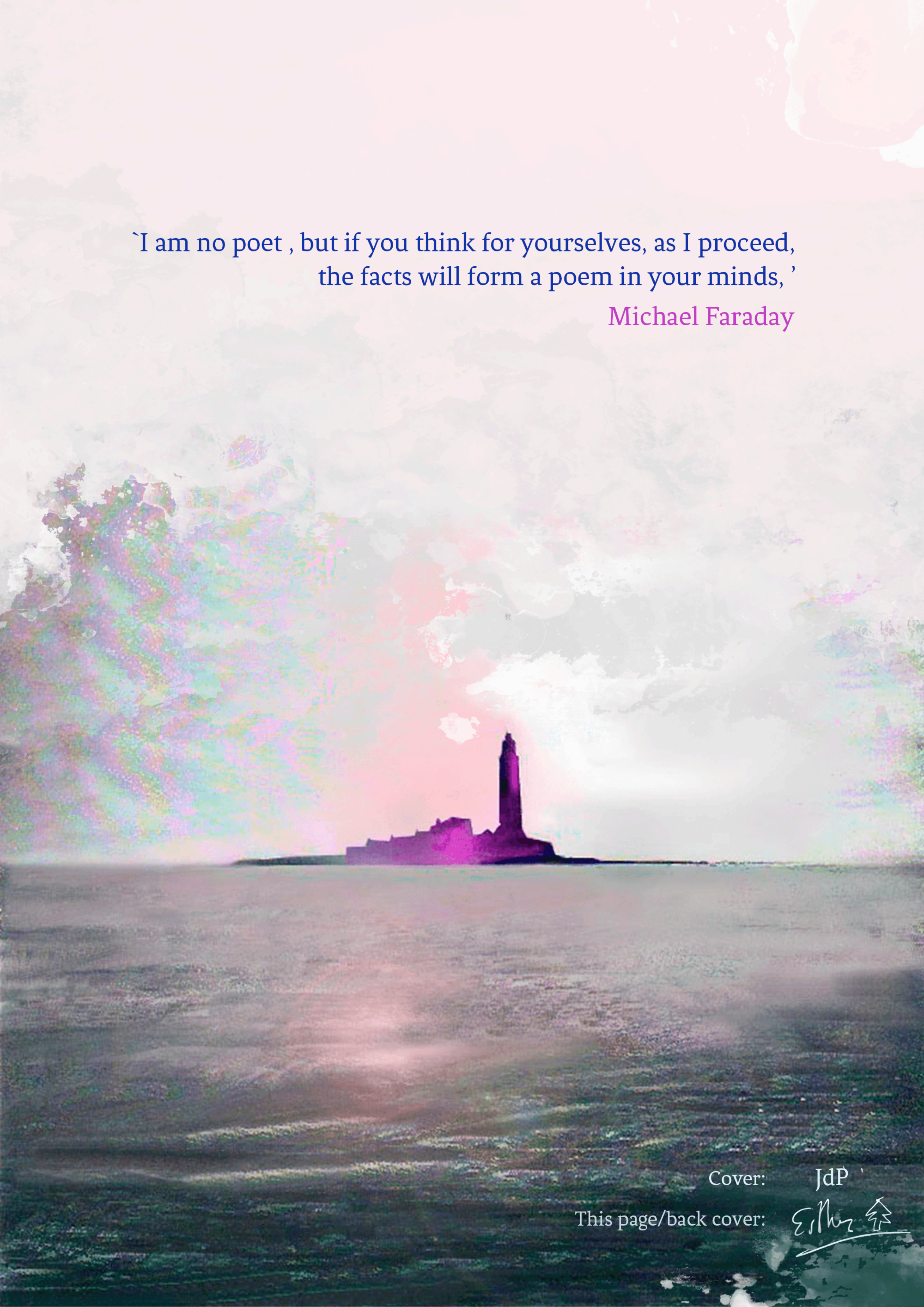

`I am no poet , but if you think for yourselves, as I proceed,
the facts will form a poem in your minds, ’

Michael Faraday

Cover: JdP

This page/back cover:

Agradecimientos

La elaboración de la tesis se ha encontrado plagado de momentos cruciales. Ella no es sino el producto final de mucho esfuerzo, aprendizaje y vivencias, no solo mías, sino paralelamente, de personas esenciales a las que les dedico estas líneas.

Comienzo agradeciendo a mis directores FJ y Johannes, por su inefable paciencia. Del primero tuve la suerte de ser alumno previamente al doctorado, donde sin duda sentí la motivación de seguir adelante y buscar aprender más, entre otras cosas en base a numerosas *pausas dramáticas* durante las explicaciones, justo donde acaban las ecuaciones y empieza la física. También le debo, a enseñarme (espero que con éxito) a dirigir mi atención a las preguntas interesantes, en la dimensión humana de la ciencia en donde es necesario pensar hacia quien se dirigen resultados y a resolver problemas que busquen generar avances realizables. En segundo lugar, y no por ello menos importantes, le debo a mi codirector Johannes Feist, por ejemplo haber entendido lo lejos que puede llegarse en el manejo de técnicas, sobre todo computacionales, en física teórica, asi cómo haber desarollado gusto e interés por ellas dentro y fuera de la ciencia. A ellos les debo la oportunidad de poder accedido a un grupo con experiencia y proyección en el cual ha sido un privilegio completar mi proceso formativo como doctor.

A la experiencia de estos años también es necesario añadir el período enriquecedor de mi trabajo de final de máster realizado bajo la supervisión de Juanjo García Ripoll. Fue aquí donde pude comenzar a desarrollar un interés práctico por la fascinante óptica cuántica. Le agradezco rambién su disposición como miembro suplente del tribunal.

I would like to dedicate this paragraph to the still not-mentioned members of the jury of my doctoral thesis, Drs Susana Huelga, Francesca M. Marchetti, Elisabet Romero, Daniele Sanvitto, Jonathan Keeling and Elena del Valle, for your time to read this memory, and your willingness to attend from various locations to form part in the defense.

I have good memories of my months in Cambridge, where I had the opportunity to work with Drs Alex Chin and Florian Schröder, to whom I owe their vision, input, and availability to start collaborations together.

Dentro del departamento no solo he podido tener compañeros, sino que he podido hacer amigos duraderos, con la fortuna de ser testigo de la evolución y paso adelante de muchos de ellos. La variedad de estilos y pensamientos han hecho de muchas discusiones interesantes, barriendo el espectro desde la física hasta la biología, y de historia o política hasta lo *pasmoso y maravilloso* de la telebasura. El valor personal de todos ellos ha hecho mi experiencia enriquecedora y apasionante. Difícil de empezar con alguien, agradezco los numerosos buenos recuerdos a mis ex-compañeros de despacho, Sergio, quien lo mismo *te afaita* como se mete a bucear en una fosa marina o emplea flamenco fusión para concentrarse; Dieguito, para quien el doctorado ha sido una *excusa* para formar una familia y contarnos sus historias; especial mención a Víctor y sus *hamburguesas de 2 pavos*; a Rubén que me ha acompañado tanto en momentos buenos (de cañas) como en malos, (e.g. en alguna que otra *agónica* clase de HIIT, también llamado *pánico muscular*). Aquí, no debo olvidar tampoco a los más tardíos María y a Raúl. Todos ellos se han esforzado siempre por mantener un clima de trabajo inmejorable con su *viernes fusión* y sus cafetadas.

I would like to dedicate a very special hug to my friend, now also doctor, Raj, who has visited our department in several occasions during his PhD in Marseille, and has accompanied us sharing many moments inside the walls of the office (also, teaching us a lot of stuff about India!). Também gostaria de fazer uma *pequena dedicatoria* ao meu amigo Gilherme pelo seus conselhos e o seu jeito *bacana* e acolhedor de ser.

Un piso más abajo, en el fondo de un pasillo algo oscuro rodeado de laboratorios de biología, tras una entrada que en realidad era una *salida de emergencia* encontré un lugar perfecto para continuar mi doctorado durante los últimos 3 años. Es allí donde tuve el placer de conocer mejor a los señores Carlos González Ballestero y sus frases de impacto (*yolooo losers!, dress for success*), Javier Galego y sus peligrosas *salidas al campo*, Álvaro Cuartero y su *preocupante* conocimiento en geopolítica, y por último el reciente fichaje Miguel Alvarado y su *inquietante cartera de hombro siempre pegada a él.* Situados en distintos pasos en la escala como *obviamente* futuros investigadores, brillantes es la palabra que los define, dentro y fuera de la ciencia, ambos escenarios en los cuales he podido conocerles y aprender de ellos.

Me gustaría también agradecer a otros miembros un más senior en el departamento con quienes mis interacciones siempre han sido positivas, como Antonio Fernández, Stefan Bilan, Juan Antonio Porto, Laura y Almudena. A todos ellos debo añadir a otros ex-miembros del departamento, actualmente dentro y fuera de la UAM: Carlos Romero, Carlos Sánchez, además de ex miembros de nuestro grupo, Paloma, Diego M.C. y Javier Cuerda. Agradezco también a miembros con los que he podido compartir sus períodos en la UAM como Yuri, Jose, Javi el Vasco, así cómo a los más recientemente llegadas, unidas y luchadoras Mónica Sánchez, Rocío y Clàudia. También a Rui, de quien estoy seguro avanzará en la dirección seguida en segunda parte de esta tesis. Me gustaría hacer una mención especial a Pili, en la cafetería, por siempre recibirme con una sonrisa de oreja a oreja al comprar un ticket para un café.

Deben estar mencionados en igual medida los *colosales* biológos moleculares Hernán con sus *miguelitos* ACGT, Filip y Silvia, además de Predes, quien espero pueda leer eventualmente estos agradecimientos. A ellos les debo también el poder tener muchos momentos divertidos sobre temas absurdos y no tanto. De ellos he podido entender cómo muchas de las idiosincrasias que imaginaba particulares de la física se extienden a la biología y por supuesto he aprendido día a día. Ha sido un privilegio compartir con ellos comidas durante años.

Menciono el apoyo de mi familia, principalmente de mi madre y mi padre, qué bastante me han tenido que aguantar ya, a mi hermanas Esther (gracias por tus ilustraciones) y Vane, a Filippo, y también de otros que se quedaron por el camino aunque siguen conmigo. Especial mención a mi sobrino Dani Pro., que con sus 8 años hace *la coca cola* con un balón de fútbol mucho mejor que yo y me gana en todos los juegos de memoria. Una frase de la serie Rick & Morty para cuando seas mayor: *break the cycle Morty, stay above, focus on science!*. Além disso, não poderia terminar sem fazer um agradecimento especial para minha familia do hemisferio oposto, em particular para os Drs. Rosana e João, pelo apoio deles ao longo do tempo mesmo com a distância.

Finalizando me gustaría agradecer profundamente a mi ya antigua y mejor amiga y brillante doctora, Mónica, de quien no puedo estar más contento de ver crecer profesional y persolmente. También a mi más *ancestral* amigo hoy y siempre, Charlie, con quien sin duda no he parado de vivir el resto de la vida, básicamente. No me olvido de los enormes Julio y Juancho.

As últimas linhas destes agradecimentos só poderiam estar dedicadas ao verdadeiro motivo pelo qual cualquer esforço vale a pena, a pessoa responsável pelos *momentos cruciais* das primeiras linhas. Bruna, o que mais feliz me faz de terminar esta memória é voltar a me reunir com você para continuar caminhando juntos.

Madrid 2018

Contents

Abstract

English

This thesis is devoted to the theoretical study of the organic polaritons that arise in the strong interaction of electromagnetic modes and molecular excitations. The description of material and light entities is done in the few quantum limit, where the number of molecular excitations and photons in the system is scarce. To this end, light is considered typically a single quantised electromagnetic mode, corresponding to a microcavity resonance. In contrast, molecular systems present an intricate geometry, which results in a hierarchical structure of energy levels due to internal motion. Such complications require models refining the crudest representation of matter in optics, namely, the two-level system, which would be unable to account for the complex interplay of energy scales of molecules. Our work explores phenomena arising for organic polaritons by applying models and methods, described in chapter 2, that increase in complexity along the exposition but are still tractable in the framework of quantum optics, open quantum systems and quasi-exact numerical methods in many-body physics.

Polaritons supported by organic systems offer a broad set of advantages compared to their inorganic counterparts realised mainly in semiconductor platforms. Among them, organic exciton-polaritons formed in optical microcavities exhibit substantial binding energies, which enable their potential use for applications such as room temperature Bose–Einstein condensation and lasing. Moreover, the formation of exciton-polaritons involves modification in the internal conformation of molecules and also, in the way different molecules in a material exchange energy. This represents a pathway towards the tuning of chemical reactions and material properties via strong coupling, as demonstrated in experiments conducted in the last decades. Thanks also to the support offered by theoretical work, more insight on the microscopic mechanisms behind such modifications has been gained in the very last few years. In addition to exciton-polaritons, organic molecules also enable an alternative class of strongly coupled states, with the recently coined name of vibro-polaritons. These form upon the mixture of molecular bond vibrations with confined mid-infrared photonic modes. In this thesis, we address fundamental questions for organic polaritons, such as their intrinsic properties or how they evolve in time after they are formed. Furthermore, we discuss some novel applications that exploit the use of polaritons.

The first part of this thesis is devoted to strongly-coupled organic polaritons at mid-infrared frequencies. Along with the lines of recent experiments, we first analyse the formation and evolution of vibro-polaritons. To this end, we develop a theory in chapter 3 which includes not only the hybrid light-matter quasiparticles in the system, but the many uncoupled dark states, and their mutual incoherent dynamics with polaritons resulting from dephasing. Our results highlight the non-trivial role played by the vibrational dark states in the steady-state infrared absorption and time evolution features. We next provide a fundamental study of the Raman spectrum of vibro-polaritons in chapter 4, which arises when the vibrational transitions involved are both infrared and Raman active. Remarkably, we show how the material component of vibro-polaritons mediates Raman scattering. This observation permits to widen the capabilities of Raman laser devices, based on the process of stimulated Raman scattering. In particular, we propose in chapter 5 a device where strong coupling can be used to devise a low-threshold optical parametric oscillator, with outputs in visible and mid-infrared frequencies.

In the second part of this thesis, we switch to the topic of exciton-polaritons formed upon hybridisation of molecular Frenkel excitons with optical microcavity modes. We illustrate first in chapter 6 how the complex vibrational spectrum that results from nuclear motion affects and is affected by strong coupling of many molecular excitons to a single photon. Our results are grounded on the exact numerical exploration of the lower polariton of an organic microcavity, obtained via variational minimisation over a tensor network trial wavefunction, which is appropriate for systems with a very large set of degrees of freedom. In this manner, we unveil how the complex interplay of excitonic, photonic and vibrational degrees of freedom leads to reduction of vibronic effects for exciton-polaritons as compared to bare molecules. Finally, in chapter 7 we exploit an extension of the previous numerical approach to calculate the exact time propagation for organic exciton-polaritons at arbitrary short timescales. Our findings reveal the crossover, as the light-matter coupling is varied, from incoherent to coherent dynamics between polariton and excitonic dark states, driven by ultrafast nuclei motion. We observe strong memory effects and the significant modification of lifetimes, which emerges from trapping of polariton population into the non-emissive dark states. The internal dynamics of the system is linked to distinctive fingerprints in the far-field emission spectrum.

Castellano

Esta tesis está dedicada al estudio teórico de los polaritones orgánicos que surgen en la interacción fuerte de modos electromagnéticos y excitaciones moleculares. La descripción de las entidades materiales y luz participantes en en este fenómeno tiene lugar en el límite cuántico, definido por el bajo número de excitaciones y fotones en el sistema. En estos términos, la luz se considera en el modelo considerado más sencillo como un solo modo electromagnético cuantizado, correspondiente a una resonancia de microcavidad.Por otro lado, los sistemas moleculares presentan una geometría intrincada que da lugar a una estructura jerárquica de niveles energéticos, entendida en términos de movimiento interno. Esta organización interna de la materia requiere de modelos que refinen la representación más simplista de la materia en óptica, el sistema de dos niveles, incapaz de reflejar la complejidad de la interacción entre las escalas de energía moleculares. Nuestro trabajo explora fenómenos que surgen en polaritones orgánicos mediante la aplicación de métodos descritos en el capítulo 2, que aumentan en complejidad a lo largo de la exposición pero aún manejables en el marco de la óptica cuántica y los métodos numéricos cuasi-exactos aplicables al problema cuántico de muchos cuerpos.

Los polaritones soportados por sistemas orgánicos ofrecen un amplio conjunto de ventajas en comparación con sus contrapartidas inorgánicas, realizadas principalmente en plataformas de semiconductores. Entre ellos, los excitones-polaritones formados en microcavidades ópticas exhiben una energía de unión significativa, lo que permite su uso potencial para aplicaciones tales como condensación de Bose–Einstein a temperatura ambiente y láseres. Además, la formación de excitones-polaritones implica modificaciones en el conformación interna de moléculas y también, en la forma en que diferentes moléculas en un material intercambian energía. Esto representa un camino prometedor hacia la modificación de reacciones químicas y propiedades materiales a través del acoplamiento fuerte, tal y como han demostrado experimentos llevados a cabo en las últimas décadas. Gracias también al apoyo ofrecido por el trabajo teórico, se ha logrado un mayor entendimiento sobre los mecanismos microscópicos detrás de tales modificaciones. Además de los excitones-polaritones, las moléculas orgánicas permiten la formación de una clase alternativa de estados fuertemente acoplados. Estos estados, recientemente nombrados como vibropolaritones, se constituyen a partir de la mezcla de modos de vibración en enlaces moleculares y modos fotónicos confinados en el infrarrojo medio. En esta tesis, abordamos preguntas fundamentales en el área de polaritones orgánicos, tales como sus propiedades intrínsecas o cómo evolucionan en el tiempo tras su formación. Además, discutimos algunas aplicaciones novedosas que explotan el uso de polaritones.

La primera parte de esta tesis está dedicada a polaritones orgánicos fuertemente acoplados en frecuencias del infrarrojo medio. Paralelos a líneas experimentales recientes, analizamos en primer lugar la formación y evolución de vibropolaritones. Para tal fin desarrollamos una teoría en el capítulo 3 que incluye no solo las cuasipartículas híbridas materia-luz en el sistema, sino los muy abundantes estados oscuros desacoplados, y su dinámica incoherente mutua con polaritones, resultante de procesos de decoherencia. Nuestros resultados resaltan el papel no trivial desempeñado por los estados oscuros vibracionales en la absorción infraroja y evolución temporal de vibro-polaritones. A continuación proporcionamos un estudio fundamental del espectro Raman de vibro-polaritones en el capítulo 4, posible cuando las transiciones vibracionales involucradas sonactivas infrarrojas y Raman simultáneamente. Nuestros resultados muestran cómo el componente material de los vibropolaritones media la dispersión Raman. Esta observación permite ampliar las capacidades de los denominados láseres Raman, basados en el dispersión Raman estimulada. En particular, proponemos en el capítulo 5 la idea de un dispositivo donde el acoplamiento fuerte es empleado para diseñar un oscilador paramétrico óptico de baja potencia umbral, con salidas en la región visible e infrarroja media.

En la segunda parte de esta tesis se dedica a los excitones-polaritones formados a partir de la hibridización de excitones moleculares de Frenkel con modos ópticos de microcavidad. En primer lugar, ilustramos en el capítulo 6 cómo el complejo espectro fonónico en las moléculas, resultante del movimiento nuclear afecta y se ve afectado por el fuerte acoplamiento de muchos excitones a un único fotón. Nuestros resultados se basan en la exploración numérica exacta del polaritón inferior en una microcavidad orgánica mediante minimización variacional de una red tensorial como *ansätz* para dicha función de onda, apropiado para sistemas con un gran número de grados de libertad. De esta manera, revelamos cómo la interacción compleja de grados de libertad excitónicos, fotónicos y vibracionales conducen a la reducción de los efectos vibrónicos para excitones-polaritones en comparación con las moléculas desacopladas. Finalmente, en el capítulo 7 hacemos uso de una extensión del método numérico anterior con el fin de calcular la propagación temporal exacta para polaritones orgánicos en tiempos arbitrariamente cortos. Nuestros hallazgos revelan el *crossover*, a medida que el acoplamiento luz-materia es modificado, desde dinámica incoherente a coherente entre estados polaritónicos y excitónicos oscuros, determinada por movimiento nuclear ultrarápido. Observamos fuertes efectos de memoria y la modificación significativa de las vidas medias aparentes, la cual emerge del atrapamiento de la población polaritónica en estados oscuros no emisivos. Además revelamos cómo la dinámica interna del sistema está relacionada con distintas señales distintivas en la emisión de campo lejano.

List of acronyms

This is a list of the acronyms used in the text (in alphabetical order).

BRW	Bloch–Redfield–Wangsness
D	Debye (unit)
DMRG	Density Matrix renormalisation group
EM	Electromagnetic
ESC	Electronic strong coupling
HOMO	Highest-occupied molecular orbital
HTC	Holstein-Tavis-Cummings
LUMO	Lowest-unoccupied molecular orbital
LSP	Localised surface plasmons
MPS	Matrix product state
PES	Potential energy surface
QE	Quantum emitter
QED	Quantum electrodynamics
RS	Raman scattering
RVD	Reduced vibrational dressing
RWA	Rotating-wave approximation
SBM	Spin boson model
SRS	Stimulated Raman scattering
TC	Tavis–Cummings
TDVMPS	Time-dependent variational matrix product states
TN	Tensor network
USC	Ultrastrong coupling
VSC	Vibrational strong coupling
VMPS	Variational matrix product state
WC	Weak coupling
WGM	Whispering gallery mode

1 | Introduction and State-of-the-Art

1.1. Light-matter interactions for new technologies

The tailoring of interaction between electromagnetic fields (EM) and matter plays a central role in modern physics. Underlying many phenomena that form part of our daily experience, for a long time, technological and scientific development has gone completely unrelated to the existence of the innumerable quantised excitations of the EM field. Precisely, the controlled interaction of such *photons* has been attained with great success in the XX century resulting in profound technological advances that are nowadays indispensable. Examples include the invention of holograms [1, 2], solar cells [3–5], the laser [6–10], optical fibers [11, 12] or CCD cameras [13, 14], to cite a few.

While charged particles interact strongly and straightforwardly respond to electrical fields, photons need to be interfaced with material degrees of freedom to be manipulated. The route to attain it is, and has always been, intricately encoded in Maxwell's equations. A beautiful summary of the long storyline that follows from this milestone is presented in [15]. The eagerness to answer questions about the fundamental nature of light has culminated in Planck's theory of black-body radiation, special relativity [16], quantum electrodynamics [17] and quantum optics [18], parents of many branches of modern physics. Light is a long-standing subject of development of far-reaching fundamental and technological impact. Specifically, in the last decades, we have witnessed the emergence of novel areas such as quantum information [19–21], attosecond science [22–24], cavity optomechanics [25–28], photonic crystals [29–31] and plasmonics [32–35].

One of the indelible ingredients in photonics is the realisation of strong interactions between light and quantum emitters. It is noteworthy that the effective light-matter coupling is enhanced by the emitter density, and the global light-matter interaction will be measured by the *Rabi frequency* Ω_R. Typical setups pursue this *collective strong coupling* by employing many emitters, as indeed exploited in pioneering demonstrations carried out for atomic ensembles in microwave cavities and plasmonic systems [36, 37]. Strong coupling is nowadays a hot topic in nanophotonics [38]. Research in this area is concerned with the interaction between visible light and material systems with comparable lengths (i.e., below few hundred nanometers). In loose terms, one of the leading ingredients to enable strong light-matter interactions consists on 'shrinking' sufficiently the EM field to small volumes. Very often the way to achieve this is employing micro-cavities with sizes comparable to EM wavelength [39], filled with active materials to reach collective strong coupling. On the other side, cutting-edge plasmonic cavities permit concentration of visible light in deeply sub-wavelength volumes [40, 41], where only a tiny portion of matter is involved. This extreme conditions can even lead to strong coupling of a *single emitter*.

Within the strong coupling regime, light and matter become profoundly mixed, indistinguishable from one another. The emerging quasiparticles, known as *exciton-polaritons*, constitute a promising avenue for tailoring effective photon-photon interactions, giving rise to unusual phenomena such as Bose–Einstein condensates [42, 43] or polariton superfluidity [44], with technological applications that include coherent light sources and quantum simulators [45]. Within the last decade, the strong coupling regime has also been highlighted due to its potential to shape material and chemical properties [46]. Among many candidates, including natural and engineered materials, organic molecules enable very robust polaritons at room temperature. In addition, nuclear degrees of freedom in molecules can strongly couple to infrared cavity photons, leading to a different type of organic polaritons known as *vibro-polaritons*.

The fact that light and organic materials can be interfaced in strong coupling has established the multidisciplinary framework of *organic polaritons* [47], with many synergies between fields so diverse as nanophotonics, quantum optics and molecular physics. The work developed in this thesis focuses on several open problems in the area of organic polariton physics. In this introductory chapter, we will briefly summarise the fundamental concepts of light-matter interaction regimes at the nanoscale. Right after, we will overview different experimental platforms to attain strong light-matter interactions in the visible and mid-infrared frequencies. Here, we give an exhaustive comparison of advantages and disadvantages of different photonic structures and material components for collective and individual strong coupling. As a particular and central case in this thesis, we show the capabilities of organic molecules for strong coupling and provide an overview of the state-of-the-art research in organic exciton- and vibro-polaritons.

1.2. From weak to strong light-matter interactions

At the microscopic level, where energy scales of light and matter become comparable, their mutual interaction will be accurately described by quantum mechanics. In this limit, classical light scattering is replaced by resonant interactions in which photons provide the energy difference of (discrete) internal energy levels. Each of the material entities participating in this interaction is denoted as *quantum emitter* (QE). For electronic transitions, present in atoms, molecules and artificial 'quantum confined' systems (which we shall describe in section 1.3), such resonances are found at optical frequencies. Typically QEs posses complex internal structures, associated with a 'finer' ladder (IR or microwave) internal motion levels on top of the optical transitions.

As will be detailed in chapter 2, one of the leading ingredients in a formalism describing the interaction of light with materials is the quantisation of the EM field [17]. For low-energy (non-relativistic) interactions, matter is treated in a first quantisation scheme as a sum of point charges that are coupled to the second-quantised elementary excitations of the EM field, the photons. In this manner, matter and light phenomena are accounted for in the same framework, commonly referred to as quantum optics [18, 48]. Conversely to classical electrodynamics, where field strengths can have arbitrary values, electric fields cannot be identically zero even in the absence of sources. The presence of counter-intuitive effects such as these vacuum fluctuations have supposed a breakthrough in atomic physics [49–51], and motivated modern fields such as cavity quantum electrodynamics (QED) [52–55]. Remarkably, the phenomenon of vacuum Rabi splitting [56], observed in early cavity QED experiments with few atoms [57] emerges when the vacuum state of the EM field is tailored by a cavity, in such a way it 'mixes' with QE states leading to finite energy splittings.

In the following, we outline different regimes that arise in the interaction of QEs with EM modes. Firstly, when the coupling scale between both constituents is slower than individual decay (excitation loss) and dephasing (loss of quantum coherence) rates, the system is said to be in the so-called *weak coupling* regime. In this scenario, the most common in nature, matter and photonic excitations decay into the continuum of photonic or non-radiative modes, which itself becomes essentially unaffected by this dynamics. For instance, in the interaction of QE with free space modes, the coupling amplitude g is much smaller than the QE transition frequency ω_0. As a result, the excited state of the QE (located at $\mathbf{r}_0$) depopulates exponentially with a rate γ_0 that involves the *transition dipole moment* of the emitter, $\boldsymbol{\mu}$, (more details in the original reference of

Wigner-Weisskopf theory [49]),

$$\gamma_0 = \frac{\pi\omega}{3\hbar\epsilon_0}|\boldsymbol{\mu}|^2\rho_\mu(\mathbf{r}_0,\omega_0). \tag{1.1}$$

This exponential decay law indeed results from destructive interference of the probability amplitudes for events where the QE returns to the excited state (as would occur in the interaction with a single mode). In Equation 1.1 the density of EM modes in free space reads $\rho_\mu(\mathbf{r}_0,\omega) = \omega^2/(\pi^2c^3)$, where $\hbar$ and c are the reduced Planck constant and the speed of light. In this manner, the spontaneous emission is controlled by the fluctuations of the vacuum field, which stimulate the transition. Remarkably, the structure of Equation 1.1 is irrespective of the environment felt by the emitter. The density ρ_μ has to be replaced by the local density of states of the medium in each case, introducing corrections related to the EM distribution in the vicinities of the emitter [58, 59]. An interesting consequence that follows is that the emission rate can be controlled by modifying the boundary conditions of the surrounding vacuum field, the so-called Purcell effect [60].

To measure the intensity of such effect, a key figure of merit in nanophotonics is the ratio between the modified rate γ_r with respect to the value of free space or Purcell factor $\mathcal{F}_P = \gamma_r/\gamma_0$. Emission is enhanced with respect to free space if transition energies in the QE are close to resonances in the EM density of states caused by oscillating dipoles in the nanostructure. Away from the EM mode, the density of states and hence the radiative decay rate is suppressed. The lineshape of such resonant modes is a Lorentzian [61] with frequency ω_0 and width κ (accounting for the intrinsic losses), and so the resonant Purcell factor becomes proportional to the ratio of the 'target' excitation *quality factor* and *mode volume*, i.e. $\mathcal{F}_P \propto Q/V$. For the electric field, denoted as $\mathbf{E}(\mathbf{r})$, stored in a region with permittivity $\epsilon(\mathbf{r})$, this quantity arises in the canonical quantisation of the EM energy [62] and reads ($\mu = 1$)

$$Q = \frac{\omega_0}{\kappa}, \qquad V = \frac{\int \epsilon(\mathbf{r})|\mathbf{E}(\mathbf{r})|^2\,\mathrm{d}\mathbf{r}}{\max(\epsilon(\mathbf{r})|\mathbf{E}(\mathbf{r})|^2)}. \tag{1.2}$$

Experimentally, the Q-factor can be easily estimated by measuring the transmission spectrum of the nanophotonic system in the absence of QEs. Turning back our attention to materials, in general, the QE radiative decay (measured by a rate γ_r) adds up to other non-radiative pathways (global rate γ_{nr}). Typically, if the QE encompasses a larger number of degrees of freedom, the bigger the quantity γ_{nr} will be.

Purcell effect, described above, is a characteristic signature of perturbative light-matter coupling. As this interaction increases, the QE depopulation deviates slightly from exponential behaviour, within what some authors define as *intermediate* coupling regime (see for instance [63], in the context of solid state cavities). As expected, the perturbative treatment ultimately breaks down if g exceeds the individual losses. Photons cannot then be regarded as uncorrelated, passive entities in this *strong coupling* regime. This can occur for example in good cavities with high-quality mirrors (large Q), or in lossy plasmonic nanostructures where the field can be confined in sub-wavelength scales (small V). Especially if resonant conditions between QE excitations and the EM field hold, matter and radiation modes will exchange energy coherently. From the perspective of the emitter and the photon, an initial excitation residing in one of the subsystems will undergo damped oscillations, populating and depopulating with opposite phases. This oscillatory behaviour will occur at the natural *Rabi frequency*, $\Omega_R = 2g$, with damping rates $\gamma_r + \gamma_{nr}$ (QE) and κ (photon).

Like any population exchange between two energy levels, oscillations are a clear indication that light and matter excitations are no longer proper eigenstates [64]. Instead, within this limit, two new branches of eigen-excitations show up, announcing the formation of composite EM-matter particles or *dressed-states*[1], which inherit properties from their basic constituents. Those are conventionally referred as the *upper* and *lower polaritons* (denoted as UP and LP respectively)[2]. The strong coupling regime is achieved in practice by exploiting the *collective* interaction of many emitters. In this case, Ω_R scales with the square root of the number of emitters, $\sqrt{N}$, as initially tested in experiments [57]. Indeed, first experimental demonstrations of the phenomenon of strong coupling were attained in excitonic materials coupled to surface plasmons [37] and many-atom systems [36]. Ensembles employed in strong coupling include very often about $N = 10^{12}$ QEs within the mode volume. This collective nature is central for strong coupling applications, as not only induces an enhanced transition dipole moment at the microscopic level $\Omega_R \mapsto \Omega_R\sqrt{N}$ but also implies long-range interactions between different QEs, since EM modes are more delocalised. In this manner, distant emitters with no direct communication are bypassed via the cavity mode, which mediates an effective ‘cross-talk’. Most of the current realisations of polaritons phenomenon do exploit this enhancement. Only very recently plasmonic cavities that exhibit very strong EM fields in sub-wavelength volumes (more details will be presented in a forthcoming section) have demonstrated

---

[1] As an additional remark, the existence of polaritons is not inherent to the fully quantum picture of the light-matter interaction. Polaritons appeared first in the context of classical optics as ‘collective oscillation of polarisation charges in the matter’ sustained by interfaces that separate media with permittivities of opposite signs [65, 66].

[2] Polaritons are similar to the mixture of molecular states into bonding/antibonding orbitals in covalent chemical bonds, and so terminology *hybridisation* is very often imported.

polaritons with a dramatically reduced number of emitters (tens or even few), paving the way towards *single emitter* strong coupling.

Different families of polaritons are distinguished by their origin (see for example the recent review in [67]). Especially relevant are the modes resulting from hybridisation of electron-hole excitations in semiconductors (*excitons*) with optical fields or *exciton-polaritons*. These quasiparticles were first observed in 1992 through reflectivity measurements on an inorganic semiconductor micro-cavity [68]. Only six years later, Lidzey and co-workers demonstrated the formation of organic polaritons employing porphyrin molecules [69]. Both experiments explored two extreme scenarios in the nature of the underlying excitons [45]. The former is characteristic of inorganic semiconductors, where electronic excitations are delocalised over spatial extensions comparable to the size of the unit cell, resulting in the so-called Wannier-Mott excitons [70]. These display binding energies of $\sim 1-10$ meV, comparable to thermal energy at room temperature, ($T_0 = 300K$, $k_B T_0 \simeq 25.6$ meV) and Rabi frequencies up to $\Omega_R \sim 100$ meV. Therefore, inorganic polaritons will generally disassociate if not held at cryogenic temperatures. The latter scenario is the one found in ensembles of organic molecules, where electronic excitations are very localised over molecular sizes. Such Frenkel excitons [71] exhibit considerably larger binding energies than their inorganic counterparts reaching $\sim 0.1-1$ eV and large dipole moments enabling $\Omega_R \sim 1$ eV at room T[3]. Organic molecules also exhibit rovibrational states resulting from molecule internal motion. Many of these bond modes exhibit transition dipole moments and therefore can absorb IR radiation. Intriguingly, this implies the potential for a different type of polaritons, known as *vibro-polaritons*, produced after rovibrational states enter in the strong coupling regime with mid-IR photons.

Finally, as the light-matter interaction keeps growing beyond the strong coupling regime, further counter-intuitive effects start to show. For instance, ground states display finite photonic occupation and intrinsic quantum properties such as squeezing and entanglement [72], and saturation of decay rates for spontaneous emission is predicted [73]. In this case, some of the theoretical approximations that are customary in 'conventional' strong coupling (for instance, the so-called rotating-wave approximation that will be introduced after) become inadequate. Such limit is conventionally referred to as the ultra-strong coupling (USC) regime, and it was first observed in intersubband polaritons in semiconductors [74–76][4]. Remarkably, single-emitter USC has been reported in

---

[3] As we shall describe below this could imply effects beyond the 'conventional' strong coupling regime.

[4] As the Rabi frequency becomes of a similar order or even surpasses the QE frequency $\Omega_R/\omega_0 \geq 1$, the so-called *Deep Strong Coupling* limit [77], leads to exotic effects such as light-matter decoupling and the breakdown of Purcell effect [78].

a wide range of experimental setups, ranging from superconducting circuits [79] to two-dimensional electron gases [80, 81]. In a different direction, collective strong coupling in organic exciton-polaritons [82, 83] (the current record is $\Omega_R/\omega_0 = 0.6$) and vibro-polaritons [84] ($\Omega_R/\omega_0 = 0.24$) has been demonstrated.

In this thesis, we focus on polaritons formed in organic micro-cavities, namely exciton-polaritons and vibro-polaritons, addressing their features in section 1.4. Our interest is mainly devoted to the conventional collective strong coupling regime. The reason for this choice is twofold. On the one hand, the weak coupling regime has been subject to intense study during the last decades, while experiments nowadays recreate the conditions for strong coupling routinely. On the other hand, while fingerprints of USC effects have been detected in molecular polaritons, the vast majority of current research in the field explores the less restrictive strong coupling regime. Devising photonic and material systems that satisfy the required conditions requires very precise engineering. Also, selection and integration of the adequate QEs for the desired goal is crucial. In the following section 1.3 we review the accomplishments of several experimental architectures for strong coupling. Our analysis is split into the discussion of EM structures, followed by an outline on QEs.

1.3. Experimental platforms for strong EM-matter interactions

As commented above, polaritons are known to exist in a large variety of solid-state and organic systems with various dimensionality and energy scales that range from microwave to ultraviolet wavelengths. The ‘choice’ of the platform not only depends on the operating frequency that is desired for the output, but it is also determined by the technological purpose intended for polaritons. For example, some applications require a significant degree of quantum coherence, such as single photon emitters and quantum memories [45]. Others pursue to efficiently retrieve energy in the output or change material properties without requiring robust quantum properties of the states involved [46]. In this manner, conditions for both QEs and the EM modes can be relaxed, as long as sufficient ‘photonic character’ of polaritons (e.g. radiative emission and delocalisation) is present. Here we will describe in further detail some of the results of the experimental effort in enabling strong EM-matter interactions, with focus on proposals at visible and mid-IR frequencies.

In the following, it is instrumental to recall the light-matter coupling strength g. Formally, its expression depends on the the EM field gauge. For interaction between light and QEs, a generally adequate choice is the *length gauge* and the *dipole approximation* [85], where g is simply given by (more details in chapter 2)

$$g(\mathbf{r}_0) = -\boldsymbol{\mu} \cdot \mathbf{E}(\mathbf{r}_0). \tag{1.3}$$

Equation 1.3, suggests the following factors will determine the success in forming polaritons at a given frequency:

- The electric field amplitude $|\mathbf{E}|$ scales with the quantisation volume Equation 1.2, as $1/\sqrt{V}$. The coupling is therefore enhanced for confined EM fields at reduced volumes. Noting that EM losses will scale as $\kappa \sim 1/Q$, the determinant ratio to maximise in a given photonic nano-structure is indeed $Q/\sqrt{V}$. To exploit this effect, in the case of collective strong coupling, experiments allow for a relative dense 'packing' of QEs in the volume of the EM mode.

- QEs with a large transition dipole moment $|\boldsymbol{\mu}|$, or equivalently, large absorption cross-section are favourable. Besides, the large 'binding' energies of molecular excitations implies robustness of hybrid states against thermal fluctuations, with longer excitonic lifetimes. Therefore, determination or engineering of a material component meeting these conditions is essential.

Besides, the light-matter coupling is a resonant phenomenon, implying that, to maximise coupling, photonic and material frequencies need to be adjusted to minimise detuning. As a consequence, reaching polaritons is typically a two-way process: nanophotonic structures are engineered and finely tuned for resonance conditions to hold, and sometimes emitters are prepared artificially. Despite the challenges posed by these conditions, the number of experimental realisations where strong coupling has been attained is vast. The next two subsections are aimed to overview some of the relevant platforms for single-emitter and collective strong coupling.

1.3.1. Tailoring the electromagnetic field

The confinement of the EM in microscopic scales is a formidable experimental challenge. Numerous efforts over the last decades have opened the door to tailoring fields in the nanoscale via an exquisite control in the materials and fabrication of nanostructures. The goal of this section is to facilitate the reader's contact with the extensive literature covering this topic, partially developed in textbooks [39] and reviews [86].

To begin with, we overview the platforms reaching the collective strong coupling regime. The structure of greater conceptual simplicity is undoubtedly the Fabry–Pérot

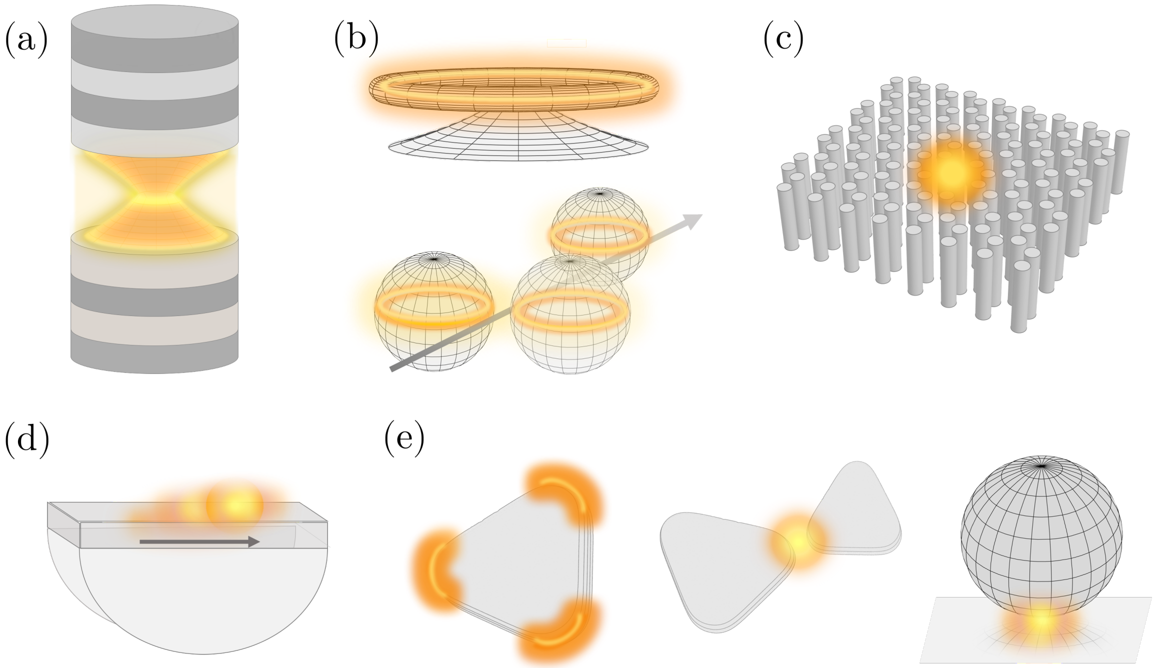

Figure 1.1: Typical devices and structures employed to confine the EM field.

micro-cavity formed by planar reflectors. Mode volumes, in this case, are above the diffraction limit ($V \sim \lambda_{\mathrm{EM}}^3$, where λ_{EM} is the mode wavelength) and determined by mirror-mirror separation (typically hundreds of nm). Common choices for materials include noble metals due to their ease of deposition, and dielectrics arranged in layers of alternating thickness and refractive indexes. While metal mirrors can introduce absorption losses resulting in low Q at visible frequencies, distributed Bragg reflector (DBR) micro-cavities (cf. Figure 1.1a) enable large quality factors $Q \sim 10^3$ [87]. By changing the dielectric properties and the layer thickness in the mirrors, it also possible to devise similar structures supporting mid-IR resonances [88]. These systems offer advantages regarding integration and scalability for inorganic polaritons systems, such as the possibility to grow built-in semiconductor quantum dots inside the cavity setups. Moreover, while micro-cavities offer confinement in one direction, modes are relatively extended in the other two. Therefore photons along the cavity axis can be collected along the longitudinal direction to probe the system, making them ideal for studying polariton propagation [39] and condensation [89]. Lateral confinement can be introduced by etching DBRs to form micropillars that exploit total internal reflection.

Microcavities can also exploit more complex geometries to achieve ultra-high Q-factors such as whispering gallery mode (WGM) resonators (see Figure 1.1b). In this case, values reaching $Q \sim 10^8$ for microdisks and microtoroids and $Q \sim 10^{10}$ for dielectric spheres [90, 91] result from the trade-off between total internal reflection (beneficial) and increased evanescent losses for small curvatures (detrimental). Mid-IR resonators in silicon-based platforms have also been demonstrated [92, 93]. Tuning the wavelength of WGM resonances and getting access to the EM stored inside is generally an issue, and thus they are not as widespread as micro-cavities for strong coupling experiments. Nevertheless, because of their small size and their direct integrability into photonic circuitry WGM resonators constitute a common platform for efficient on-chip coherent light sources such as quantum cascade lasers [94] and optical parametric oscillators [95].

In addition to ‘closed ’structures above, alternative candidates for strong coupling are cavities formed in photonic crystals [29], periodic arrays of alternating dielectric species that generalise the DBRs mentioned earlier to higher dimensions [96]. The lattice periodicity opens a bandgap in which no photons can propagate, while, the presence of a defect in the array creates an edge state inside the gap. Photons resonate inside the defect, forming cavity modes that reach $Q \sim 10^5$ [97]. Moreover, photonic crystals can be built to confine mid-IR photons with $Q \sim 10^6$ [98, 99].

Finally, one of the most prominent examples of structures employed in collective strong coupling experiments is extended material interfaces supporting EM modes called surface plasmon polaritons (SPPs). Due to SPPs having a momentum larger than light in free space, they cannot be excited directly by shining light onto a metal surface. Methods to overcome this include the so-called Kretschmann configuration, where the SPP is excited via a higher-index prism on the bottom (see Figure 1.1d). As the evanescent mode is excited on the other surface of the metal layer, any active material deposited on the metal will be in close contact. This geometry was employed for electronic [100] and recently also for vibrational strong coupling [101]. Finally, for patterned surfaces (e.g.. two-dimensional arrays of metallic nanoparticles or holes), localised plasmons and diffracted orders of the lattice (Rayleigh anomalies), hybridise forming relatively narrow lattice resonances ($Q \sim 10^1 - 10^2$) [102–104] enabling exciton-polaritons [105].

Although plasmonic systems are intrinsically lossy, they are capable of sub-wavelength EM field profiles in plasmonic cavities. Experimental advances along this road currently grasp the limit of strong coupling of localised surface plasmons (LSPs) with a single QE. This results from the large enhancement of the single QE coupling by typically three orders of magnitude compared to Fabry–Pérot micro-cavity setups. In this case, an abundance of different variants of plasmonic nanocavities (with $Q \sim 10 - 100$) have been described in the literature (see examples in Figure 1.1c). The strategy to increase the coupling efficiency consists therefore on shrinking the mode volume V instead of achieving better Q-factors. Simple examples, shown in (see Figure 1.1e) are plasmonic nanorods and nano-prisms [106], bow-tie nano-antennas [107] ($V \sim 10^{-7}\lambda_{\mathrm{EM}}^3$) and the very recent proposal of nanoparticle-on-mirror geometry, where optical fields are located even below the cubic nanometer and form 'pico-cavities' [40, 108]. At mid-IR frequencies, the role of LSPs is played by phonon-polariton resonances, supported e.g. by silicon carbide micropillars [109, 110] and boron nitride (hBN) nanoantennas [111]. Q-factors of $Q \sim 100$, in many cases unparalleled in plasmonic resonances, and sub-wavelength confinements $V \sim 10^{-2}\lambda_{\mathrm{EM}}^3 - 10^{-4}\lambda_{\mathrm{EM}}^3$ have been reported, enabling a very promising route for strong coupling with vibrations of few molecules [112].

1.3.2. Determining the optimal matter component

Choosing an appropriate QE is a determinant factor in the operation frequency for the structures described above. In the following, we present an overview of different experimental platforms with a focus on optical and mid-IR frequencies, the regions of the EM spectrum investigated in this thesis.

In the optical regime, the experimental effort carried out during last decades has revealed a multitude of QE variants adapted for each purpose. The origins of strong coupling are found in experiments carried out in the 1980s with large ensembles of rubidium (Rydberg) atoms in microwave cavities [53], and years later, for caesium atoms passed through optical cavities [57]. Atoms show favourable properties for strong coupling, such as sizeable dipole moments (e.g. Rb and Cs dipole moments are of ~ 1 Debye (D) and low decoherence rates. This makes them particularly attractive as single-photon sources since the emission of a single isolated atom is characterised by a high purity. Atom decay cascades can also be used for entangled photon generation [113]. Unfortunately, the inherent experimental complexity of trapping atoms, requiring vacuum and low temperatures, severely restricts the performance of more complex experiments.

Physical theories initially established in these systems are nowadays tested in a mesoscopic length scale within an extended range of parameters, thanks to the development of quantum systems with discrete energy levels known as *artificial atoms*. Paradigmatic examples are the quantum dots [114], point-like semiconductor systems formed by colloidal or micro-crystalline semiconductors, and vacancy defects in insulating inorganic crystals known as colour centres, with diamond being by far the most popular platform [115]. Below visible frequencies, in the mid-IR spectral region, a number of candidates in artificial atoms is reported [116–118]. These advances have prompted an extensive investigation of a photonic platform for a possible future quantum computer [119–121].

In a different direction, molecular systems have attracted considerable interest for the engineering of strong light-matter interactions at room T. As mentioned in section 1.2, the prototypic optical transitions employed in organic molecules are the Frenkel excitons. In this case, dipole moments, typically in the range of 0.5 and 5 D for individual molecules (e.g. a *dye molecule* such rhodamine-6G [122]), are enhanced by one order of magnitude upon aggregation of molecules in solution [123, 124]. Such aggregates keep bound by non-covalent intermolecular interactions such as van der Waals-like attractive forces. Interactions can also lead to the extremely regular organisation of constituent molecules, forming crystals such as naphthalene and anthracene, with intermolecular distances of ~ 1 nm [125]. Organic micro-cavities filled with anthracene have been featured strong coupling at the visible region [126] and room temperature polariton lasing with a single molecular crystal [127]. Less regular, disordered arrangement such as J-aggregates [128], show inter-molecular separations in the range 0.4–2 nm, and intense dipole moments of typically 10-20 D. Compared to the monomer emission, spectra is much narrower and red-shifted, as a result of electronic excitations extended over the whole aggregate [129]. J-aggregates have been recognised as a useful framework for describing, and imitating, natural photosynthetic light-harvesting complexes [130–132], and also remarkable, in the exciton-polariton physics context [133–137]. Nowadays, strong coupling of few J-aggregates and methylene blue molecules packed in extremely confined EM mode volumes has been reported [40, 135].

Due to the substantial mass difference between electrons an nuclei, molecular systems present a hierarchy of motional states. Namely, the ratio of electronic and nuclear energies lies in the range $10^{-1} - 10^{-2}$ [138]. Internal motion in molecules includes vibrational and rotational contributions. Rotational states give fine structure to the vibrational spectrum and are sometimes jointly referred to as *rovibrational states*. The energy scales of both differ by orders of magnitude, with rotational and vibrational transitions having splittings at microwave and IR frequencies respectively. Rotational states are therefore not typically resolved in the optical or IR spectra of molecules. A major effect in optical processes in organic molecules is the interaction between electronic and vibrational motion in the nuclei or *vibronic coupling*. This is crucial to explain the interesting optical properties in molecules, such as the energy shift between emission and absorption spectra (the so-called Stokes shift) which can be comparable with other energy scales in the system even for polaritons (more details are presented in chapter 2).

Below the visible region, the mid-IR spectral region is dominated by fundamental absorption bands attributable to molecular vibrations, particularly prominent in some families of molecular QEs. This implies favourable properties for reaching very large couplings to mid-IR fields [139] and vibro-polariton formation, such as sizeable dipole moments of few D. Therefore, these organic molecules are good candidates as infrared QEs, as first demonstrated in 2015 [140] (more details in section 1.5). Molecular bond vibrations can display larger splittings than thermal energies and have longer lifetimes than electronic states as they present a more 'elementary' internal structure and hence fewer channels to decay into.

For further deepening in organic molecules, in section 1.4 we detail some of their advantages and the intricate energy transfer processes that occur in after they interact with light fields. This is the basis to understand the formation of excitonic and vibrational polaritons.

1.4. Organic polaritons

Typical dye molecules employed in strong coupling encompass between tens to hundreds of atoms. The additional fact that molecules form crystals or are surrounded by an involved host environment implies that interaction with light involves numerous energy transfer pathways among internal molecular states [141]. The trade-off between time-scales associated to such processes and the interaction with EM fields is central in understanding polariton formation in molecules. Many examples of them are summarised in the 'timeline' of Figure 1.2. In the following section, we discuss first the most relevant mechanisms a molecule undergoes after absorbing optical or infrared photons, disregarding rotational states in the molecules.

Optical transitions typically occur within the lowest energy electronic states, located between the *highest occupied molecular orbital* (HOMO or S_0 in this context, denoting the state by the total electronic spin) and the *lowest unoccupied molecular orbital* (LUMO or S_1). Already mentioned, at room temperature, the thermal energy is often small compared to the separation between vibrational states. Thus photo-excitation of a molecule usually starts from the electronic ground state with no vibrational quanta excited, as sketched in the Jablonski diagram at Figure 1.3. The frequency of excitation can be resonant into the vibrational ground state of the LUMO, or it can be non-resonant into higher vibrational modes of the LUMO.

Nuclear dynamics and solvent relaxation time (e.g. some tens of ps for water or methanol at room T [142]), is much slower than electronic motion. Thus, the electronic transition is virtually instantaneous ($\sim$ 1 fs) as seen from the molecular environment. After photo-excitation, molecules are thus very far from equilibrium and many vibrational states become excited. Following immediately, vibrations relax in $\sim 0.1 - 100$ ps timescales. This is due to two separate channels, namely redistribution of molecular en-

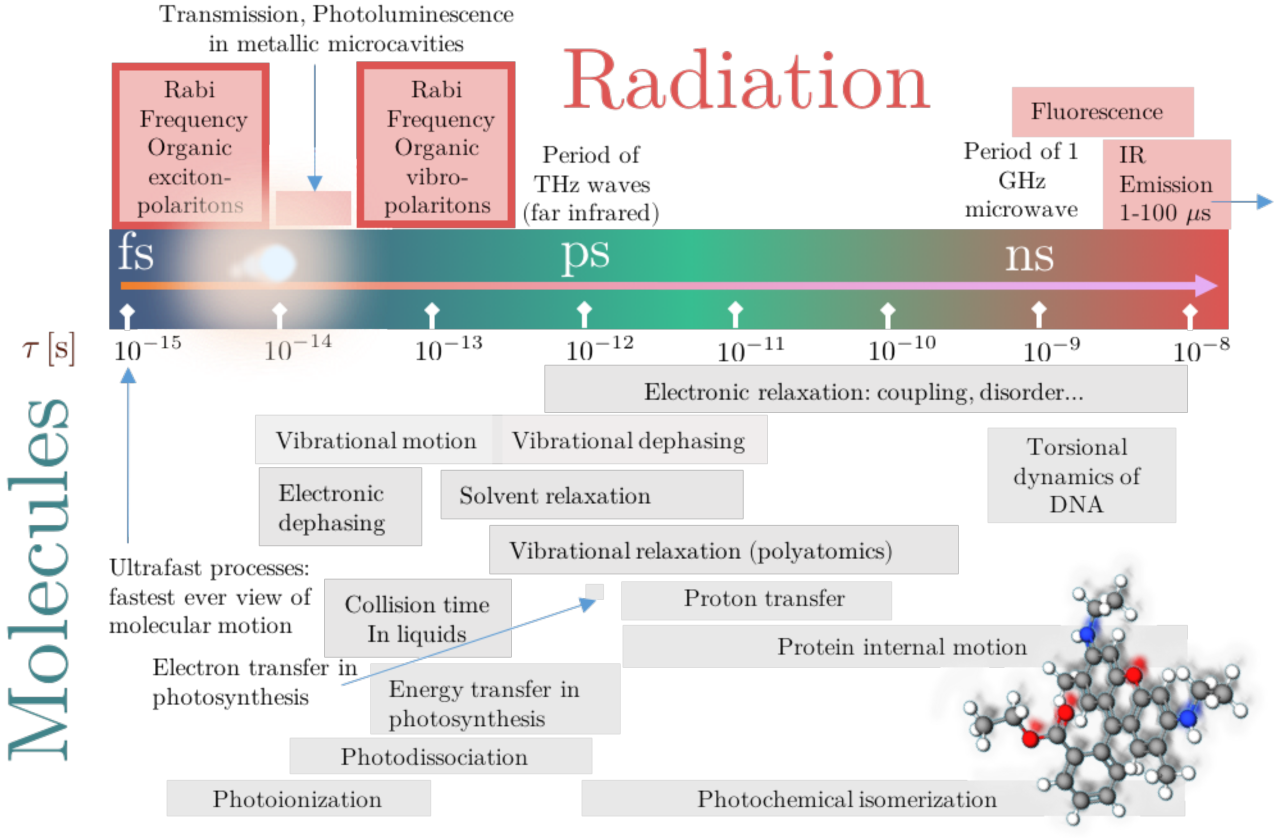

Figure 1.2: Relevant timescales in organic molecules and confined EM modes.

ergy in the molecular environment or *intermolecular energy transfer* (essentially in the form of heat) and *intra-molecular vibrational energy transfer* within molecular phonons. Vibrational relaxation facilitates a fast decay cascade towards the ground state of the LUMO. Also, it is also possible that two degenerate vibrational states associated to different electronically-excited states are slightly coupled, inducing a radiation-less process $S_2 \rightarrow S_1$, in timescales $\sim$ 10 fs−10 ps, named internal conversion [143]. Regardless, the radiative lifetime of the LUMO groundstate is much longer for a fluorescent molecule, of the order of $1-10$ ns. Therefore emission occurs from this lowest excited state (the so-called Kasha rule in photochemistry). Even if a molecule is excited resonantly into the ground state of the LUMO, non-resonant relaxation can also occur to vibrationally excited sidebands of the HOMO (red-shifted fluorescence).

Radiative decay occurs only for a particular class of molecules that exhibit a low density of vibronic states of the HOMO at the LUMO energy. Particularly efficient fluorescence occurs for small and rigid aromatic or conjugated molecules, the previously

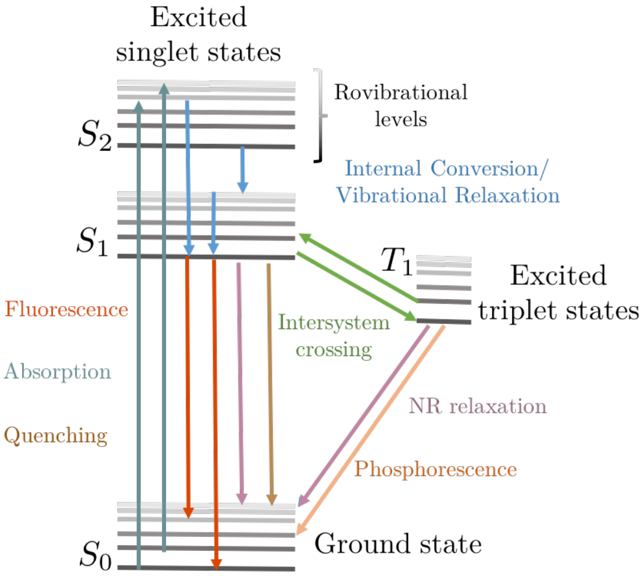

Figure 1.3: Jablonski diagram displaying transition processes that occur triggered by external excitation. The colours for the arrows and labels for each process are matched. Electronic states are denoted by their total spin. Only a portion of the rovibrational states is represented due to their massive number of typical molecules.

mentioned *dye molecules* [123][5]. In a similar way to the Purcell enhancement of spontaneous emission by nano-photonic structures, molecular lifetimes are affected by the local density of non-radiative solvent modes surrounding the molecules. Therefore, vibrational lifetimes can be enhanced by embedding molecules in rigid crystalline matrices at cryogenic temperatures or employing molecular crystals.

From the experimental point of view, there are several spectroscopic methods to access to information about optical or vibrational processes in molecules [145]. The most widespread techniques are the stationary absorption and photoluminescence spectra, where an optical beam is passed through the molecular sample and recorded in a detector. The combination of steady-state measurements and theoretical modelling enables to infer many aspects of the time dynamics in molecules. Nevertheless, time-resolved spectroscopy is necessary to discern the energy redistribution at short times. Typically, dynamics is dominated by photon leakage, which for organic micro-cavities many times

---

[5] Due to non-negligible spin-orbit coupling in the molecule, there is a finite probability for $S_1 \rightarrow T_1$, (intersystem crossing) [144]. This typically occurs at a rate much smaller than the excited state decay (in ~ 10 ns -1 ms timescales), and involves the reduction of energy because of the stronger exchange interaction in T_1. The radiative decay $T_1 \rightarrow S_0$ in a spin-forbidden transition process known as phosphorescence, that occurs in extremely slow timescales (ms) leading to photoblinking.

is $\sim 10 - 100$ fs. Access to such short scales is challenging. One possibility is to employ ultrafast pump-probe (also denoted transient absorption) spectroscopy, where a short, intense pump pulse impinges into the system, and a weak (and broad) laser pulse measures the ground state absorption. The first step promotes the system into the excited state. The comparison of the transmission before and after the pulse by sweeping the time delay for the arrival of pump and probe pulses enables to trace the excited state dynamics with resolution down to tenths or even few fs. After its first use in organic polaritons in [146], pump-probe has been widely used in time-tracing exciton-polariton dynamics [147–149]. The role of quantum coherence and delocalisation in energy transfer is shown by techniques such as two-dimensional electronic spectroscopy, which uses three laser pulses to generate the required response in the sample. This is one of the pillars in the study of photosynthetic complexes [150, 151].

An arbitrary molecule with N_{at} atoms contains, excluding overall rotations and translations, $3N_{\text{at}} - 6$ internal motional degrees of freedom. Close to the mechanical equilibrium, this motion can be considered harmonic, as will be detailed in chapter 2. Polyatomic molecules undergo complex vibrations that can be resolved into normal modes of vibration [152]. Interestingly, vibrational modes in different molecules are found to have similar frequencies, due to the short range of the Coulomb interactions. Owing to this fact, Raman and IR spectroscopies are widely used to identify and characterise organic systems. In a typical IR spectroscopy setup, the spectrum is recorded, similarly to visible spectroscopy, by passing a beam of IR light through the sample. When the incoming photon frequency matches the vibrational frequency of a bond or collection of bonds, absorption occurs. For this, nuclei vibrations must present a transition dipole moment, an intrinsic feature related to the mode symmetry. In this manner, only specific 'functional' groups are expected in linear spectroscopy. A prominent example of IR-active nuclei vibration is the stretching mode in the carbonlyl ($\mathrm{C} = \mathrm{O}$) bond, with a large absorption band associated to a transition dipole moment of the order of 1 D, which has been investigated in depth in the results compiled in part I of this thesis. Vibrational spectra do not display separate absorption signals for each of the dipole-active bonds, but instead, such number may be modified as a consequence of combination tones and overtones of the fundamental vibrations.

Another relevant measurement is Raman spectroscopy, resulting from the interaction of molecular vibrations with far-off resonant optical photons or Raman scattering (RS). The selection rules, in this case, require a change in the vibrational bond polarisability during the transition. RS is one of the principal methods used to obtain information about material properties and chemical structure [153]. In particular, it probes the rovibrational structure of matter and can thus be used to provide a 'fingerprint', making it useful for a wide range of applications in research and industry. In further detail, its operating principle relies on the inelastic scattering of optical photons (frequency ω_L), which leads to the emission of photons at shifted frequencies $\omega_L - \delta\omega$. The observed frequency shifts $\delta\omega$ correspond to Raman-allowed excitations in the system under study and thus provide detailed information about its (rovibrational) states. Since vibrational excitations are often well-approximated by harmonic oscillators, RS leads to a series of equidistant *Stokes* lines $\delta\omega = n\omega_v$ for each mode, corresponding to excitation of n vibrational quanta.

1.5. State-of-the-art review

Polariton physics and in particular the strong coupling regime with organic systems is today an active research topic, which has roots in great efforts made over decades in inorganic polariton systems and molecular photo-physics. The aim of this final section is to revisit the experimental and theoretical advances reported in the two main subtopics of interest in the thesis, namely, the organic polaritons formed in the electronic strong coupling (ESC) and vibrational strong coupling (VSC) regimes. Besides, we contextualise the work carried out in each case, highlighting our approach for pre-existing open problems in the field as well as our proposals made on the basis of experiments.

The exciton- (vibro-) polaritons obtained by ESC (VSC) are formed by superpositions of a cavity photon and excitons (excited molecular bond vibrations) that are collectively distributed over a large number of molecules. Moreover, since molecular QEs display a complex geometry, the theoretical modelling of these systems involves a subtle level of detail in the microscopic description of molecules, which requires going beyond the widespread two- or three- level limit of quantum optics. Finally, dissipation is omnipresent in these systems, either for photons or molecules. One of the goals of this thesis is to model these features, supplementing more straightforward pictures with further insight and, importantly, exploring features of organic exciton polaritons inaccessible any other way.

1.5.1. Exciton-polaritons

In the following, we describe how experiments have shown that strong light-matter coupling results in modified nuclear effects in molecules, eventually leading to tailored material and chemical properties. In particular, we overview the impact of nuclear effects in polariton formation and time evolution. The outcome of our work forms the part II of this thesis.

Polariton formation and modification of molecular properties

Strong coupling of optical modes with organic molecules was first demonstrated in a dielectric micro-cavity by Lidzey et al. 20 years ago in [69]. In the years that followed, strong coupling gained interest gradually in the nanophotonics community, with arising experimental platforms such as sub-wavelength hole and nanoparticle arrays [105, 134], strong coupling to single organic crystals [126] and surface plasmons [122, 154]. Moreover, first indications of signatures beyond 'conventional' strong coupling, with experiments achieving reversible switching of USC were provided in [155].

Experimental progress during the following years [135] has yielded the generation of robust organic polaritons at room temperature with only tens of molecules participating in the collective coupling [106]. Intriguingly, strong coupling with photosynthetic molecules has been demonstrated both ex vivo [156] and for living bacteria [157]. Very recently, results suggesting the coupling of a single molecule to a plasmonic nanocavity has been presented [40]. Further advances in experimental techniques even enable the positioning of emitters with an unprecedented precision thanks to DNA-origami constructs [158].

In parallel to developments in nanophotonic platforms pushing the experimental boundaries in polariton formation, promising applications of strong coupling with organic molecules have been vital in attracting interest in this field of research. Crucially, the experiments conducted during the second half of the 2010's marked a historical turning point, with first demonstrations of the potential of ESC in modifying molecular and material properties. Namely, early studies by Ebbesen and co-workers showed the suppression of a photochemical reaction [159]. To prove these effects, the authors considered the 'ring cleavage' photoisomerisation reaction in the spiropyran molecule to give merocyanine, which usually is triggered after excitation by visible/ultraviolet light. Recent experiments in a similar direction have reported the suppression of photo-bleaching of J-aggregates by ESC to a plasmonic cavity [160].

A multitude of theoretical frameworks to address these phenomena have flourished over the last few years, pursuing to describe EM-induced microscopic mechanisms in molecules responsible for chemical changes. The first theory to address nuclear modifications driven by strong coupling from a 'quantum chemistry perspective' dates from 2015 [161]. This model, which introduces the molecular energy landscape was further explored by other authors [162–164]. In particular, hybridisation of electronic and photonic states results, within this approach, in the nuclear-coordinate-resolved analogue of polariton states, namely, *polaritonic potential energy surfaces*. Thanks to this approach, the theoretical demonstration of suppression and triggering of many molecule photoisomerisation reactions by a single micro-cavity photon were given [165, 166]. These findings are attributed to the novel mechanism of *collective protection*[6].

Works in a similar direction have predicted tuning of the intra-molecular electron transfer reactions within individual molecules in the ensemble as a result of suppression of nuclear dynamics due to the exciton-cavity coupling [167]. To illustrate these particular results, the authors considered molecular models one step further to those employed in quantum optics, by including a single collective vibrational coordinate in molecules [168], yielding the so-called Holstein-Tavis-Cummings (HTC) model [167, 169, 170]. A severe limitation of this approach is that it assumes molecules are close to the mechanical equilibrium. Therefore, they wash out the complex electronic landscape that is explored in far from equilibrium situations, such as, indeed, in the photochemical reactions of experiments outlined above. Nevertheless, they enable exact numerical treatment of the problem employing the quantum optics toolbox, with direct access to the quantum wave function of the nuclear (vibrational) states of the system. Theoretical calculations therefore have demonstrated the extreme richness of the lower polariton of the system, which is formed by a complex threefold mixture of photons, excitons and bond vibrational excitations [169]. In this state, suppression of the mechanical displacement of molecular vibrations is observed for large ensembles, a phenomenon dubbed as *polaron decoupling*, which in some sense is a particular realisation of the collective protection effect mentioned above. These results constitute a dramatic change in the perception of polaritons as simple hybrid states between just two quantum systems, the exciton in the QE and the photon.

A common denominator in the approaches predicting either collective protection or polaron decoupling is that the molecular description involves a single nuclear degree of freedom. Such assumptions are not straightforward for typical scenarios, in which tens or even hundreds of intra-molecular vibrations play a role in the electronic dynamics. Along with this complication, it must be noted that the interaction with the molecular environment (e.g. molecules are embedded in a host matrix) is responsible for many of the complex effects relevant in experimental systems. Previous theoretical studies

---

[6] In particular, the polariton is a coherent superposition of the electronic excitation over all molecules, and therefore in such state, the probability of exciting a single molecule scales down with the density. Any molecule is, therefore, most likely to be at its ground state, which either has a higher energy barrier than the excited surface, suppressing the reaction, or a lower, opening a reaction pathway.

emphasise the influence of strong light-matter coupling in large molecular ensembles, in which the photon mediates a long-range cross-talk between different molecules. However, the question of whether such cavity-mediated interaction can influence different intramolecular modes or the molecular environment, even the single-molecule level, was still open at that time. In this manner, to recreate in a more detailed way a micro-cavity setup, we introduce an extended model for molecules close to equilibrium, where the full vibrational spectrum is incorporated in chapter 6.

To solve the problem, we determine the lower exciton-polariton of an organic microcavity numerically by applying the Density Matrix Renormalisation Group (DMRG) algorithm [171]. This enables to describe the excitonic, photonic and vibrational parts of the quasi-exact polariton wavefunction in the same footing, by exploiting 'redundancies' in the description of the state. This method was introduced for strongly-correlated many-body closed systems and more recently extended to the context of open quantum systems [172, 173]. Our results unveil excitonic and photonic properties of the lower exciton-polariton in the system, where we found a universal behaviour that is quite independent of the molecular species. Instead, we observe the lower polariton depends on two collective parameters in the molecules, namely, the energy shift between emission and absorption spectra or *Stokes shift*, and the frequency of a collective reaction coordinate encompassing intra- and extra- molecular vibrations. We also found unambiguous signatures of reduced nuclear effects in the molecules, caused by strong coupling (a precursor to polaron decoupling). Finally, beyond the capabilities of simpler single-mode models, we unveil how different vibrational modes in the molecules are affected by the EM mode.

Polariton evolution and ultra-fast molecular processes

Following very closely in time experiments have been reporting changes in the work function of organic materials (i.e. the energy necessary to remove an electron from the Fermi level into vacuum), via strong light-matter coupling [174]. Only one year after the enhancement of the conductivity of organic semiconductors, attained by injecting carriers into polariton states was announced [175]. These pieces of evidence laid the foundations of *polaritonic material-science*, the field of research concerned with the modification of material properties in organic systems via hybrid light-matter states. In a related direction the enhancement in the *excitonic energy transfer* of spatially separated molecules has been reported in recent years [176]. Current theories attribute the enhanced transport to the delocalised character of the polariton, which makes molecules 'immune' to local disorder [177, 178].

Many conceptual similarities between organic and inorganic exciton-polaritons have been explored in parallel [45]. For instance, an example of their potential use as coherent light sources is in the experiments showing room temperature polariton lasing [127] and condensation [179]. Similar studies in plasmonic systems, have suggested thermalisation and cooling of exciton-polaritons [180] and very recently, this direction has culminated in the demonstration of a reduced threshold for lasing [181]. Besides, theoretical approaches underline the relevance of the *exciton reservoir* (formed by non-photonic superpositions of electronic states) in the relaxation towards the bottom of the lower polariton branch [182, 183].

In a different direction, experiments capable of tracing the temporal dynamics (e.g. pump-probe mentioned before) allow revealing a substantial richness in the processes of energy transfer in ultra-fast timescales (∼fs) that takes place in strongly coupled organic micro-cavities [82, 149]. In particular, a number of the organic dyes employed in experiments display comparable vibronic and exciton-photon couplings [184]. This signifies, in particular, that molecular phonons influence very profoundly the excitonic-photonic dynamics (Rabi oscillations).

The impact of vibronic coupling in the stationary optical spectra of these systems have been analysed using the aforementioned HTC model [185, 186], in which the complex spectral density of the vibronic modes in organic molecules is modelled by a single phonon mode, in the same fashion to the polaron decoupling studies. A detailed understanding of the microscopic processes lying behind the observed phenomena is difficult from modelling of measurements in the steady state. Standard techniques of open quantum systems, which assume that vibrational modes form a static bath (and therefore do not see its equilibrium state altered by the polariton dynamics) [187], are thus insufficient to address the observed physics fully.

Intriguingly, from the formal point of view, organic micro-cavities share many ingredients to biomolecular networks in light-harvesting complexes [188]. Namely, polaritonic systems display similarly intense vibronic coupling scales and interactions with cavity modes, while in the latter, intermolecular (dipole-dipole) and intense intra-molecular (vibronic) interactions could coexist. Indeed, these theories reveal that local vibronic coherences play a central role in the efficiency of exciton transport [189, 190], supporting experimental observations [191–193]. Due to the massive amount of relevant states in the system, the number of methods capable of obtaining precise numerical solutions in both families of systems is very scarce.

By exploiting an extension of the previous quasi-exact method [172, 173], denominated Time-Dependent Variational Matrix Product States algorithm [194, 195], we calculate in chapter 7 the exact many-body time dynamics of the organic polaritons supported by an optical cavity. Optical, vibrational and radiative processes are treated on an equal footing. We demonstrate clear signatures of 'memory' (non-Markovian) effects caused by vibronic dynamics and its fingerprints in the far-field photon emission spectrum at arbitrary light-matter interaction scales, ranging from the weak to the strong coupling regimes. We analyse both the single and many-molecule cases, showing the crucial role played by the collective motion of molecular nuclei and dark states in determining the polariton dynamics and the subsequent photon emission.

1.5.2. Vibro-polaritons

In contrast to the long history lagging behind the extensively studied ESC, the field of VSC is still extremely young. In this case, the seminal contribution to the field is given by the experiments reported by Shalabney et al. in [140] and Long et al. in [196], on C=O bonds in a polymer (PVAc). The roots of this area of research are in the community of electronic strong coupling [38], a phenomenon VSC shares many ingredients with.

For instance, in VSC the hybrid light-matter quasiparticles or vibro-polaritons combine elements from molecular bond vibrational resonances sitting in many different molecules and photonic states. In an analogue way to most platforms for exciton-polaritons, the vibro-polaritons obtained under VSC are formed by superpositions of a cavity photon and excited molecular bond vibrations that are collectively distributed over an extremely large number of molecules.

The subsequent experimental effort has demonstrated further fundamental features of vibro-polaritons, such as the $\sqrt{n}$ characteristic scaling of the Rabi frequency with the density n [197] and the relation with the spatial distribution of molecular samples [198]. Intriguingly, very recent experiments evidence a route to modify chemical reactions in the ground state via suppression of a deprotection reaction in an organic compound under VSC [199]. In particular, our work on vibro-polaritons is compiled in part I of this thesis.

Polariton formation and application to resonant optomechanics

Vibrational strong coupling is probably one of the most recent examples of how universal polariton formation is. Within a window smaller than five years, many experiments have demonstrated VSC in a broad range of molecules and micro-cavity setups, including polymers glasses [140, 196, 197, 200], dilute aqueous solutions of polymers, organometallic complexes and proteins [82, 201, 202]. Recently, sub-wavelength vibro-polaritons formed via SPPs have also been demonstrated [101]. Most of the experiments to date exploit the coupling to a single EM resonance with a specific bond oscillation mode, although the multimode micro-cavity scenario has also been examined [82], showing spectral signatures of USC in vibro-polaritons for the first time. Photonic pumping is the primary approach employed in experiments to populate polaritons, although very recently emission retrieved after thermal pumping of polaritons [203] has shown vibro-polariton-induced modifications in the black-body spectrum of a polymer. Typical vibrational transition dipole moments have values comparable to the ones found in organic excitons. However, while the limit of ESC is currently reaching the few-molecule limit in plasmonic systems, sub-wavelength confinement of mid-IR photons is a less developed area, with efforts currently being made in this direction [112].

Right after the first experimental evidence of VSC, one of the open questions was, provided the apparent similarities with ESC, whether vibro-polaritons display a complex internal structure resulting in energy transfer processes, in analogy to exciton-polaritons. This question is, for example, relevant in possible applications of VSC to resonant cavity optomechanics, a field that explores the interaction between EM radiation and the quantised mechanical motion of nano- or micro-oscillators [25–27]. For instance, recent developments promise a rich variety of applications such as precision mechanical measurements and coherent control of quantum states (see [28] for a recent review). This application of vibro-polaritons would exploit the sizeable vibrational spacing of molecular vibrations, enabling ground state manipulation at room temperature, without requiring any cooling.

In the strong coupling with an ensemble of vibrational modes, the cavity resonance couples to a collective superposition of the molecular vibrations, the so-called bright state, forming the vibro-polaritons. In principle, all other superpositions of vibrational excitations (the so-called dark states) remain uncoupled. In principle, it could be expected that vibro-polaritons are well approximated as harmonic oscillators or two-level systems in the low excitation regime, and therefore more standard open quantum systems techniques can be used. Nevertheless, for IR-active strongly coupled bond vibrations, vibrational-light coupling timescales competes with vibrational decoherence times, caused by interaction with a thermal bath of low-frequency rovibrational modes in the molecular environment and within the molecules [204, 205]. This influences the system dynamics and, moreover, results in fingerprints in the stationary spectrum. It is an open question how decoherence mechanisms affect the dynamics and what role the dark states play. In particular, it was not known whether the bright mode in such system effectively behaves like a single isolated oscillator, which would enable the direct application of protocols developed in cavity optomechanics.

To address this problem, we found the most straightforward and widespread theory for open quantum systems, the Lindblad master equation [206], was needed to be refined by obtaining a phenomenological reduced time evolution for the vibro-polaritons. In chapter 3 we employ the Bloch-Redfield-Wangness (BRW) formalism, well known in the context of nuclear magnetic resonance [207, 208] and light-harvesting complexes [209, 210]. Sharing some ingredients with the problem of exciton-polariton dynamics [182, 183, 211], we find in chapter 3 that a *vibrational reservoir*, formed by uncoupled molecular phonons and collective lattice motions, in full analogy with the exciton reservoir mentioned previously, plays a fundamental role in the lifetimes of vibro-polaritons. Moreover, we show the conditions under which the bright state behaves as a single isolated oscillator.

Vibrational spectroscopy and coherent light sources

Shortly after the first evidence on the vibro-polariton formation, a pioneering demonstration of spontaneous Raman scattering under collective strong coupling of $\mathrm{C}=\mathrm{O}$ (IR- and Raman-active) bonds was attained [212]. Showing a substantial enhancement of the Raman cross section of vibro-polariton compared to the original bare vibrational modes, with emission at energy shifts $\delta\omega$ approximately corresponding to the upper and lower polaritons, this was the first indication of the modification of the material properties under VSC.

This intriguing result motivated the study in chapter 4, where we theoretically model the signatures of vibro-polaritons in the Raman spectrum with increasingly complex approaches. In this phenomenon, the vibrational excitation is modified by interaction with the cavity. In contrast to the well-known technique of surface-enhanced Raman scattering [213–215], in which plasmonic modes enhance the *optical transitions* directly, the thin metallic mirrors used in the experimental setup in [212] do not efficiently confine light at optical wavelengths, and the optical transitions are almost unmodified [212]. As opposed to surface-enhanced Raman scattering (SERS), no known simple picture explains a possible enhancement of the Raman cross section under VSC. Additionally, vibrational pumping effects such as recently found for SERS within a quantised model [216] do not play a role here, either. It is also noteworthy that very recent experiments have studied in further detail anharmonicities intrinsic to vibro-polaritons, which show up in pump-probe spectroscopy [217, 218].

In particular, our calculations show that the Raman effect actually occurs in the vibro-polaritons, mediated by their material component. In the first place, this fact results in

Stokes lines displaced in the Raman spectrum and, what is more important, it provides a photonic component to the final states of the scattering. If then this system is place inside an resonator tuned to the Stokes frequency, photons at this energy can be accumulated very efficiently leading to stimulated Raman scattering (SRS), what can be exploited to manufacture a very tunable Raman laser. Raman lasers have been realised using a variety of nonlinear media and configurations, such as under pulsed operation in optical fibers [219], nonlinear crystals [220], gases [221], or Si [222], as well as under continuous-wave operation in Si [223, 224], silica [225] and molecular hydrogen [226]. Since the threshold powers for these systems are typically large, they suffer from detrimental effects such as Kerr non-linearities, four-wave mixing, and heat deposition [220].

The modification of the Raman cross section is precisely the idea that paves the way to a theoretical proposal in chapter 5 for a device that exploits VSC. We theoretically demonstrate that the hybrid light-matter nature of vibro-polaritons can be utilised to obtain photon emission from the vibrationally excited final states of a Raman laser. A single-output Raman laser device then becomes analogous to a non-degenerate optical parametric oscillator (OPO), which converts an input pump beam into two coherent output beams [227] at different frequencies. In the present case, the ‘signal’ beam in the visible corresponds to the conventional Raman laser output, while the ‘idler’ beam is emitted by the vibro-polaritons in the mid-IR. Importantly, the signal and idler beams emitted by OPOs are coherent and have a stable phase relation, as well as providing possibly entangled pairs of photons with non-classical correlations [228–233].

A compact solid-state OPO as proposed here could thus have applications in quantum information transmission and storage [234, 235]. In addition to the OPO properties, our approach has the advantage over Raman lasers of effectively getting rid of the energy deposited into material vibrations; instead of being dissipated as heat, this energy is emitted in the form of photons. Finally, we show that the coexistence of the upper and lower polariton modes with very similar properties can be exploited to produce an all-optical switch [236, 237]. Here, one (gate) pump beam can be used to switch Raman lasing of a second (signal) pump beam.

2 | Models and Methods

In this chapter, we aim to present a self-contained description of the formal methods used throughout the thesis. The discussion has been divided into two main blocks. First, we introduce in section 2.1 the model Hamiltonian for a collection of molecules strongly coupled to an EM mode as the fundamental pillar of the description. In this case, we highlight the formal differences between the two cases of interest analysed, namely the exciton-polaritons and vibro-polaritons. Finally, we describe the simplifying assumptions from which we obtain analytically and computationally tractable models.

Environmental degrees of freedom are omnipresent in organic micro-cavities. These include not only the inter-molecular or radiative modes but in many cases intra-molecular phonons. When these are weakly coupled to the quantum states of interest (for instance the molecular vibrations forming vibro-polaritons coupled to background phonons), they act as noise, causing losses and decoherence. In section 2.2 we start by revisiting the standard theory of open quantum systems, in which the environment is treated as an inert *thermal bath*. For molecules with sizeable vibronic couplings, nuclear states can be largely affected by the strong coupling to optical fields. For this, we describe in the second part of this section a sophisticated formalism, formulated in terms of a *tensor network* representation of the global wavefunction that allows treating quasi-exactly all parts of the system. Finally, we briefly connect these approaches to the content of the following chapters in section 2.3.

2.1. Quantum Hamiltonian for organic polaritons

When the mutual coupling of the rovibrational or electronic states in organic molecules and confined EM field is sufficiently strong, hybrid excitations are formed, as outlined in chapter 1, leading to strong correlations between material and EM modes. In the following, we introduce the microscopic theory, including the impact of EM field quantisation, which applies to both vibro- and exciton-polaritons. We offer the reader the minimal steps that are instrumental in understanding our results, omitting many details in the derivation that is extensively covered in the literature [85, 238–240].

The basic building block is the following *length gauge* Hamiltonian for a collection of N molecules interacting with the EM field given by $\hat{H} = \sum_{i=1}^{N} \hat{H}^{(i)} + \hat{H}_{\text{EM}} + \hat{H}_{\text{int}}$, where $i = \big(1, 2, \cdots, N\big)$ indexes the QEs. Molecular, EM, and light-matter interaction contributions are given by (here and in the following, we set $\hbar = 1$)[1]

$$\begin{aligned}
\hat{H}^{(i)} =& \sum_{\alpha} \frac{1}{2m_\alpha} \hat{\mathbf{p}}_{\alpha,i}^2 + V(\hat{\mathbf{R}}_i), && \text{(2.1a)}\\
\hat{H}_{\text{EM}} =& \frac{\epsilon_0}{2} \int [\hat{\mathbf{E}}_\perp^2(\mathbf{r}) + c^2 \hat{\mathbf{B}}^2(\mathbf{r})]\, \mathrm{d}\mathbf{r}, && \text{(2.1b)}\\
\hat{H}_{\text{int}} =& \sum_{i=1}^{N} \hat{\boldsymbol{\mu}}_i \cdot \hat{\mathbf{D}}_\perp(\mathbf{R}_i) + \frac{1}{2\epsilon_0} \int (\hat{\mathbf{P}}_\perp(\mathbf{r}))^2\, \mathrm{d}\mathbf{r} + \sum_{i,j} V(\hat{\mathbf{R}}_i, \hat{\mathbf{R}}_j). && \text{(2.1c)}
\end{aligned}$$

In previous equation Eq. (2.1a) is the free Hamiltonian for a single molecule at the center of mass position $\mathbf{R}_i$, where all charges, indexed by α, are bound by the overall Coulomb potential $V(\mathbf{R}_i)$. Moreover, the second line Eq. (2.1b) stands for the total energy of the EM field, $\{\hat{\mathbf{E}}, \hat{\mathbf{B}}\}$[2]. The light-matter interaction Hamiltonian Eq. (2.1c) couples the net dipole operator including all point-charges in the matter,

$$\hat{\boldsymbol{\mu}}_i = e \sum_{\alpha} (\hat{\mathbf{r}}_\alpha^i - \mathbf{R}_i) = \hat{\mu}_i \mathbf{e}_i, \tag{2.2}$$

oriented along the unitary direction $\mathbf{e}_i$ with the displacement field $\hat{\mathbf{D}}(\mathbf{r}) = \hat{\mathbf{E}}(\mathbf{r}) + \frac{1}{\epsilon_0}\hat{\mathbf{P}}(\mathbf{r})$, which includes contributions from the *bare* micro-cavity electric field $\hat{\mathbf{E}}(\mathbf{r})$ and matter electric polarisation, $\hat{\mathbf{P}}(\mathbf{r}) = \sum_i \sum_\alpha e_\alpha \delta(\mathbf{r} - \hat{\mathbf{r}}_\alpha^i)$. In this model, EM fields are evaluated at the charge positions, within the so-called *dipole-approximation.* Thus, just outside the charges region, $\hat{\mathbf{D}} = \hat{\mathbf{E}}$, given by the mode expansion

$$\hat{\mathbf{E}}_\perp(\mathbf{r}) = i \sum_{\mathbf{k},\lambda} \sqrt{\frac{\omega_k}{2\epsilon_0}} \big[\mathbf{f}_{\mathbf{k},\lambda}(\mathbf{r}) \hat{a}_{\mathbf{k},\lambda}^\dagger - \mathbf{f}_{\mathbf{k},\lambda}^*(\mathbf{r}) \hat{a}_{\mathbf{k},\lambda}\big]. \tag{2.3}$$

where $\hat{a}_{\mathbf{k},\lambda}$ stands for the annihilation operator for a photon with wavevector $\mathbf{k}$, energy ω_k and polarisation λ. The spatial mode functions $\mathbf{f}_{\mathbf{k},\lambda}(\mathbf{r})$ are obtained by solving the classical EM problem [240]. The dipole approximation is intimately related to the so-called

---

[1] In typical micro-cavity setups, molecules are deposited in a surface [26, 100], dissolved in a liquid [82, 201], embedded into a solid matrix [134] or forming a crystal [241]. Translational motion and overall rotations can, therefore, be excluded. Also, in the cases studied in this thesis, materials are neutral, preventing net currents induced by the EM field.

[2] The extension to include the effects from the dielectric host medium is discussed in [240].

long-wavelength limit, in which the spatial modulation of the coupled EM field is assumed to be much bigger than system length-scales. Just beyond the dipole-approximation the contribution of the molecular quadrupolar tensor $\bar{\mathbf{Q}}_i$ coupled to the *gradient* of the electric field is non-negligible [3]. Such corrections are irrelevant in micro-cavities, where spatial changes in the EM field are roughly $\sim \lambda_c$ and modes can be very efficiently isolated in frequency and space. Hence, we consider for simplicity the case of 1D Fabry-Pérot micro-cavities, described in chapter 1, where mirrors are planar. The profile for the mode with polarisation parallel to the mirrors, or *transverse electric* mode is

$$\mathbf{f}_{\mathbf{k},\mathrm{T.E.}}(\mathbf{r}) = \sqrt{\frac{2}{V}}(\mathbf{e}_{\mathbf{k}_\parallel} \times \mathbf{e}_z)\sin(k_z z)e^{-i\mathbf{k}_\parallel\cdot\mathbf{r}}, \qquad k_z = \frac{\pi j}{L_z}, \tag{2.4}$$

where $\mathbf{k}_\parallel$ is the wavevector parallel to the mirrors and j is a non-negative integer. We will assume the absence of any polarisation mixing with the transverse magnetic mode [245] mediated by the molecular ensemble, since organic materials are largely isotropic.

In many experiments, the mirror-mirror distance L_z is tuned such that transition frequencies in QEs are resonant with the mode $j = 1$. Perpendicular photonic modes form a continuum, with a dispersion relation depending on the in-plane momentum $\mathbf{k}_\parallel$. However, it can be safely assumed all molecules are collectively coupled to a single EM mode. This is justified when comparing the density of EM modes with the molecule density in the experiment. The 2D density of EM modes with wavevector $k \equiv |\mathbf{k}_\parallel| < k_{\max}$ is $N_{\mathrm{ph}} = \frac{1}{4\pi^2}\int_0^{k_{\max}} 2\pi k \, \mathrm{d}k = k_{\max}^2/(4\pi)$. For the jth transversal mode in a cavity of length L_z with background refractive index n, the dispersion relation is $\omega_k = \frac{c}{n}\sqrt{k^2 + (\frac{j\pi}{L_z})^2}$, so that the density of states with energy $\omega < \omega_{\max}$ is [246]

$$N_{\mathrm{ph}}^{(j)} = \frac{n^2}{4\pi c^2}(\omega_{\max}^2 - \omega_j^2)\,, \qquad \omega_j = \frac{c}{n}\frac{j\pi}{L_z}. \tag{2.5}$$

We assume that modes with $j = 1$ and $\omega < \omega_{\max} \approx \omega_1 + \Omega_R$ participate in the dynamics. Taking parameters for a typical experiment [140] ($n \simeq 1.41$, $\omega_1 = 215$ meV, $\Omega_R = 20.7$ meV, $L_z \simeq 2$ μm), this leads to an EM mode density of $N_{\mathrm{ph}} \simeq 4 \cdot 10^6$ cm^{-2}. In contrast, a typical molecular density is $n \simeq 8 \cdot 10^{21}$ cm^{-3}, giving a 2D molecular density of $L_z n \simeq 2 \cdot 10^{18}$ cm^{-2}. There are thus on the order of 10^{12} molecular vibrational modes coupled to each photonic mode, so we just include the $k = 0$ T.E. mode along $\mathbf{e}_{\mathbf{E}}$, with

---

[3] The break-down of the dipole-approximation has attracted interest in the in the context of ultra confined plasmonic resonances [242, 243], and atomic systems [244] where the electric field is concentrated in scales of few nm^3, a value comparable to sizes of typical dye molecules (few nm), J-aggregates (1-10 nm) and inter-molecular separations ($\sim 1 - 10$ nm). Moreover, in nano-photonic structures EM quantisation must be refined to account for absorbing media, as detailed in [58].

canonical operator $\hat{a}$, such that

$$\hat{\boldsymbol{\mu}}_i \cdot \hat{\mathbf{E}} \simeq \sqrt{\frac{\omega_k}{\epsilon_0 V}} (\mathbf{e}_i \cdot \mathbf{e}_{\mathbf{E}}) \hat{\mu}_i (\hat{a} + \hat{a}^\dagger). \tag{2.6}$$

It is noteworthy that the single-mode approximation may be inadequate for less-confined systems, such as propagating plasmons [100, 101], requiring the inclusion of the continuum of EM modes.

Finally, $V(\hat{\mathbf{R}}_i, \hat{\mathbf{R}}_j)$ in Eq. (2.1c) accounts for the intermolecular Coulomb interaction. In the picture described here, it is common to employ a point-dipole approximation for the Coulomb interaction. The coupling between molecules is therefore modelled by the *dipole-dipole* interaction,

$$V(\hat{\mathbf{R}}_i, \hat{\mathbf{R}}_j) \simeq \frac{\hat{\boldsymbol{\mu}}_i \cdot \hat{\boldsymbol{\mu}}_j - 3(\hat{\boldsymbol{\mu}}_i \cdot \mathbf{e}_{i,j})(\hat{\boldsymbol{\mu}}_j \cdot \mathbf{e}_{i,j})}{4\pi\epsilon_0 |\mathbf{R}_i - \mathbf{R}_j|^3}, \qquad \mathbf{e}_{i,j} = \frac{\mathbf{R}_i - \mathbf{R}_j}{|\mathbf{R}_i - \mathbf{R}_j|}. \tag{2.7}$$

The scaling with the inverse cube of the QE distance, in addition to the fact that molecules are placed in a dielectric host or solvent (permitivity $\epsilon_d > 1$), renormalises $\hat{V} \to \hat{V}/\epsilon_d$, and therefore we will assume this is negligible in the following.

2.1.1. Molecular Hamiltonian

In the following, we present the simplifications of the molecular Hamiltonian Eq. (2.1a) that are pertinent for organic molecules. As commented above, molecules present a large number of internal degrees of freedom, associated with nuclear motion (see Fig. 2.1a). Namely, the large mass difference between electrons and nuclei implies the factorisation the molecular wavefunction $\psi(\mathbf{r}_i)$ into nuclear $\chi(\mathbf{R}_i)$ and electronic parts $\psi_e(\mathbf{r}_i; \mathbf{R}_i)$ within the *Born-Oppenheimer Approximation* (BOA) [247, 248] (here ';' denotes parametric dependence on the variable at right). This is equivalent to replace the position operator $\hat{\mathbf{R}}_i$ for the nuclei by the parameter $\mathbf{R}_i = (\mathbf{R}_1^{(i)}, \cdots, \mathbf{R}_{M_v}^{(i)})$ in the electron-nuclei Coulomb pair interaction, denoted as $\hat{V}_{e-n}$, where M_v stands for the number of nuclear degrees of freedom in the molecule. Purely nuclear terms become constant functions and the 'clamped' electronic Hamiltonian reads

$$\hat{H}_e^{(i)}(\mathbf{R}_i) = \hat{T}_e(\mathbf{r}_i) + \hat{V}_{e-n}(\hat{\mathbf{r}}_i; \mathbf{R}_i) + \hat{V}_{e-e}(\mathbf{r}_i). \tag{2.8}$$

In this equation, the kinetic energy for electrons reads $\hat{T}_e$ while the electron-electron interactions are given by $\hat{V}_{e-e}$. Within this framework nuclei feel an adiabatic potential energy surface (PES), created instantaneously by the electron cloud. The calculation of the PES is one of the central pillars in molecular theory [138]. It could be done in

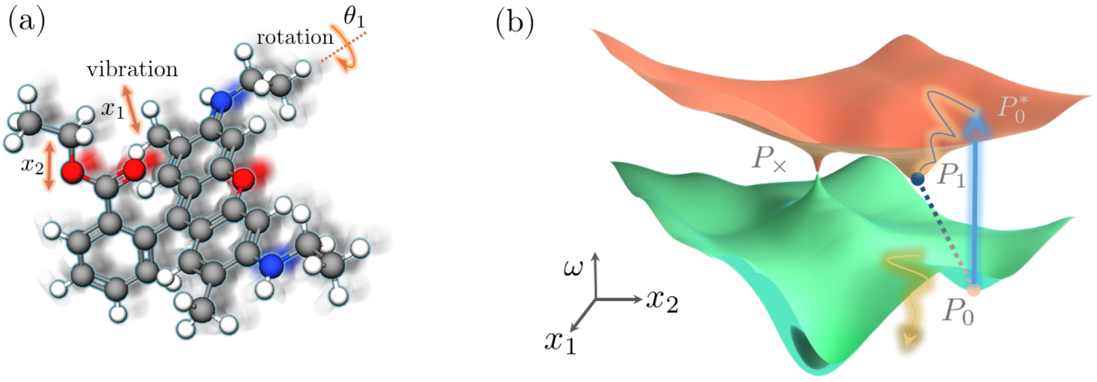

Figure 2.1: (a) Sketch of typical nuclear motion, which takes place, under the BOA, within the adiabatic potential created by the electrons (b) Example of a PES for a simple molecule with two motional degrees of freedom.

principle by solving the stationary Schrödinger equation $\hat{H}_e^{(i)}(\mathbf{R}_i)\psi_e = \omega_e^{(i,p)}(\mathbf{R}_i)\psi_e$ to give each of the $p \in (0, 1, 2, \cdots)$ surfaces, but this is often a daunting challenge.

Internal motion in molecules includes vibrational and (typically not resolved) rotational contributions (see Fig. 2.1a), which originate a rich hierarchy of energy scales. Therefore, molecular processes triggered by optical photons are very complex, as shown by the Jablonski diagram in section 1.4. A complementary picture is given by the two electronic PES at Fig. 2.1b, where we include only the two electronic transitions whose energy is closest to resonance to an optical (incoming of confined) photon and neglect intersystem crossing to the triplet electronic state. These correspond to electrons near or at the HOMO S_0 and the LUMO S_1. The vibrational spacing is much larger than the thermal occupation energy at room temperature, implying that the molecule will be in the equilibrium configuration P_0. If a resonant optical photon is absorbed, electrons will be promoted $S_0 \rightarrow S_1$, originating nuclear motion in S_1, that will be dissipated until the new stable conformation at P_1 is reached. This will occur even if there are no induced nuclear dynamics during the action of the pulse, which is the most favourable case (*Franck-Condon Approximation* or FCA) [249]. Eventually, a photon will be re-emitted, and the system will return to the ground PES.

In the example shown in Fig. 2.1b the S_0 PES includes two minima associated to two isomers, separated by a single transition state. Excitations can also experience non-radiative (gap-less) transitions $S_1 \rightarrow S_0$, reaching a different local minimum as the starting configuration (photo-isomerisation). Such effect takes place at the conical intersection $P_\times$ a region where the breakdown of the BO approximation occurs. We will assume that the system keeps far away from these regions. Thus, dynamics is well described by considering an *adiabatic basis* for the electronic wavefunctions, and coupling between PES only occurs via optical photons.

Focusing on the vibrational motion, it will be reasonable to assume that optical or infrared excitation will no excite the molecule far-away from nuclear equilibria. In this way, nuclear motions are well approximated with harmonic vibrations around $\mathbf{X}_0, \mathbf{X}_1$ (that correspond to the stable conformations of the molecule P_0, P_1, and will in general include the host medium coordinates), with amplitudes $\Delta\mathbf{R}^{(i,p)}$ in the PES indicated by $p \in (0,1)$. The potential energy operator can be diagonalised into normal modes $\mathbf{Q}^{(i,p)}, \mathbf{P}^{(i,p)}$, where frequencies $\boldsymbol{\omega}_v^{(i,p)}$ are determined by the local curvature of the PES. These modes admit a straightforward 'second quantisation' via canonical annihilation/creation operators for each PES $\{\hat{\mathbf{b}}^{(i,p)}, \hat{\mathbf{b}}^{(i,p)\dagger}\} = \sqrt{\frac{\boldsymbol{\omega}_v^{(i,p)}}{2}}\hat{\mathbf{Q}}^{(i,p)} \pm \frac{i}{\sqrt{2\boldsymbol{\omega}_v^{(i,p)}}}\hat{\mathbf{P}}^{(i,p)}$, yielding

$$\hat{H}^{(i)} = \sum_{p\in\{0,1\}} \sum_{i=1}^{N} \left[\omega_e^{(i,p)}(\mathbf{X}_p) + V_{n-n}(\mathbf{X}_p) + \boldsymbol{\omega}_v^{(i,p)} \hat{\mathbf{b}}^{(i,p)\dagger} \hat{\mathbf{b}}^{(i,p)}\right] \hat{\sigma}_{pp}. \tag{2.9}$$

where $\hat{\sigma}_{pp}$ denotes a projector over each of the two PES. Importantly, the BOA implies that the total dipole operator Eq. (2.2) is factorisable, i.e., setting the reference coordinate at the ground state coordinate ($\hat{\mathbf{Q}}^{(i,0)} \equiv \hat{\mathbf{Q}}^{(i)}$), $\hat{\mu}_i = \sum_{p,p'=\{0,1\}} \mu(\hat{\mathbf{Q}}^{(i)})\hat{\sigma}_{p',p}$, where the electronic matrix elements read

$$\mu(\hat{\mathbf{Q}}^{(i,p)}) \equiv \langle \psi_p(\mathbf{r}_i; \mathbf{Q}^{(i)}) | \hat{\mu}_i | \psi_{p'}(\mathbf{r}_i; \mathbf{Q}^{(i)}) \rangle. \tag{2.10}$$

In the following, we describe in more detail the two limiting cases of this expression addressed in this thesis, namely electronic and vibrational strong coupling.

Electronic strong coupling

The transformation diagonalising the potential energy close to equilibrium will be different for ground and excited electronic states. For simplicity, we assume in the following the normal modes in the PES for S_0 and S_1 close to the mechanical equilibrium have the same frequencies, therefore dropping the index p, while more general cases are treated in [138, 250]. Employing this assumption, normal modes in both parabolas are simply displaced by a factor of $\Delta\mathbf{Q}^{(i)}$. Setting the origin at P_0, Eq. (2.9) is readily expressed in terms of harmonic oscillators for S_0. Defining the Pauli matrices $\hat{\sigma}_- = \hat{\sigma}_{01}$, the molecular Hamiltonian reads

$$\hat{H}^{(i)} \simeq \hat{\sigma}_+^{(i)}\hat{\sigma}_-^{(i)}[\omega_e^{(i)} + \boldsymbol{\lambda}^{(i)}(\hat{\mathbf{b}}^{(i)} + \hat{\mathbf{b}}^{(i)\dagger})] + \boldsymbol{\omega}_v^{(i)}\hat{\mathbf{b}}^{(i)\dagger}\hat{\mathbf{b}}^{(i)}, \tag{2.11}$$

where we neglected anharmonic terms $\mathcal{O}(\left\langle \hat{\sigma}_+^{(i)}\hat{\sigma}_-^{(i)}(\hat{\mathbf{b}}^{(i)} + \hat{\mathbf{b}}^{(i)\dagger})^2 \right\rangle)$, $\omega_e^{(i)} = \omega_e^{(i,1)}(\mathbf{X}_1) - \omega_e^{(i,0)}(\mathbf{X}_0)$ is the energy splitting between PES minima and displacement is parametrised by the energy scale $\boldsymbol{\lambda}^{(i)} = \boldsymbol{\omega}_v^{(i)}\sqrt{\frac{\boldsymbol{\omega}_v^{(i)}}{2}}\Delta\mathbf{Q}^{(i)}$, which can be interpreted as a *vibronic coupling* amplitude between molecular excitons and phonons. Equation 2.11 is denoted as the *Independent Boson Model* in condensed matter physics, diagonalisable via polaron transformation $\hat{U} = e^{-\hat{\sigma}_{11}\sum_k(\lambda_k/\omega_k)(\hat{b}_k - \hat{b}_k^\dagger)}$ [251], to give

$$\hat{H}^{(i)} \mapsto \hat{H}^{(i)\prime} = \hat{U}\hat{H}^{(i)}\hat{U}^\dagger = (\omega_e^{(i)} - \Delta)\hat{\sigma}_+^{(i)}\hat{\sigma}_-^{(i)} + \boldsymbol{\omega}_v^{(i)}\hat{\mathbf{b}}^{(i)\dagger}\hat{\mathbf{b}}^{(i)}, \tag{2.12}$$

where $\Delta = \sum_k \lambda_k^2/\omega_k$ is the so-called *reorganisation energy.* To give a physical interpretation to this, we revisit the process of light absorption and emission by molecules. For ease of visualisation, we choose, the *reaction coordinate* that parametrises the path $P_0 - P_1$, displayed in Figure 2.2. This is given by the coherent superposition of all vibrational modes in each of the molecules

$$\hat{b}_{\mathrm{RC}}^{(i)} + \hat{b}_{\mathrm{RC}}^{(i)\dagger} = \frac{1}{\sqrt{\sum_{k=1}^{M_v}\lambda_k^2}}\sum_{k=1}^{M_v}\lambda_k(\hat{b}_k^{(i)} + \hat{b}_k^{(i)\dagger}). \tag{2.13}$$

After photo-absorption, the dipole moment will change in the electronic transition $S_0 \rightarrow S_1$. Owing to the FCA, there will not induced nuclear motion, and

$$\mu(\hat{\mathbf{Q}}^{(i)}) \simeq \mu_{0,1}^{\mathrm{eq}}\mathbf{1}_v, \qquad\qquad \text{if } p \neq p', \tag{2.14}$$

where $\mu_{0,1}^{\mathrm{eq}}$ is the transition dipole matrix element Equation 2.10 evaluated in the equilibrium configuration in S_0, and $\mathbf{1}_v$ is the identity operator over the vibrational manifold[4]. After the electronic transition (blue arrow in Figure 2.2), the molecules which end up in higher vibrational states immediately begin to relax to the lowest vibrational state. In this process, the vibrational modes $\hat{b}_k^{(i)}$ will ‘reorganise’, minimising the interaction energy, the excited state reorganisation energy Δ_e. Similarly a vertical transition will lead to photon emission and reorganisation in S_0 ($\Delta_g = \Delta_e = \Delta$ in the present model). Emission and absorption spectra are thus shifted by the *Stokes shift* $\delta\omega = 2\Delta_S$. Finally,

---

[4] Including the nuclear wavefunctions, the transition dipole matrix elements thus result from

$$\langle\psi_0(\mathbf{r}_i;\mathbf{Q}^{(i)}), \chi_v^0(\mathbf{Q}^{(i)})|\hat{\mu}_i|\psi_1(\mathbf{r}_i;\mathbf{Q}^{(i)}), \chi_{v'}^1(\mathbf{Q}^{(i)})\rangle \simeq \mu_{0,1}^{\mathrm{eq}}\mathcal{J}_{vv'}^{0,1}, \tag{2.15}$$

with the Franck-Condon overlap $\mathcal{J}_{vv'}^{p,p'} = \langle\chi_v^p(\mathbf{Q}^{(i)})|\chi_{v'}^{p'}(\mathbf{Q}^{(i)})\rangle$, which is maximum for the vertical transition $p = p'$.

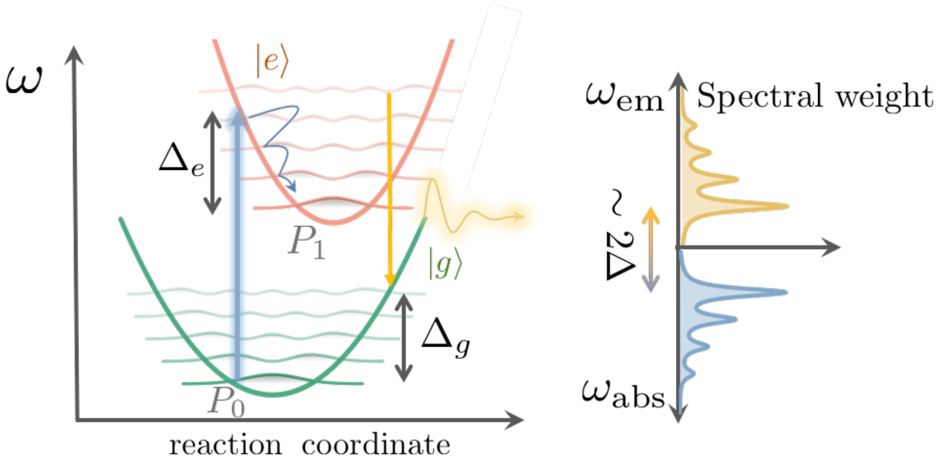

Figure 2.2: (a) Sketch of optical absorption and emission processes in the Franck-Condon limit (b) Typical steady-state absorption and emission spectra associated to this dynamics.

the Hamiltonian of the system takes the form

$$\hat{H} = \omega_{\text{EM}} \hat{a}^\dagger \hat{a} + \sum_i \left[\hat{H}^{(i)} + g_i (\hat{\sigma}_-^{(i)} + \hat{\sigma}_+^{(i)})(\hat{a} + \hat{a}^\dagger) + \frac{1}{2\epsilon_0 V} (\hat{\boldsymbol{\mu}}_i \cdot \mathbf{e_E})^2 \right], \tag{2.16}$$

where $g_i = \mu_{0,1}^{\text{eq}} |\mathbf{E}| (\mathbf{e}_i \cdot \mathbf{e_E})$ is the light-exciton coupling strength shown in chapter 1. In this treatment, permanent dipoles in molecules, typically resulting in overall shifts of ground and excited PES without affecting the transition mechanism, are disregarded. The Hamiltonian Equation 2.16 is the building block of the theory to be applied in part II of this thesis.

It is noteworthy that, even if any non-adiabatic coupling between PES is present in the bare molecules, cavity-induced couplings between different PES could emerge in ESC [161], questioning the accuracy of the BOA to estimate certain observables (e.g. absorption). Nevertheless, addressing this in detail implies to deal with the full PES, hindering the quantisation of nuclear vibrations, which as we will see is particularly insightful. Non-radiative transitions resulting from crossings of electronic surfaces will be partially accounted for by introducing non-Hermitian quantum dissipation in section 2.2.

Vibrational strong coupling

Strikingly different to the interaction with optical fields, where induced electronic transitions occur in a much shorter timescale than nuclear dynamics, bond oscillating frequencies can be resonant with IR photons. Therefore, only transitions within the ground PES are induced and the molecular Hamiltonian reads (omitting the electronic operators)

$$\hat{H}^{(i)} = \sum_{i=1}^{N} \boldsymbol{\omega}_v^{(i)} \hat{\mathbf{b}}^{(i)\dagger} \hat{\mathbf{b}}^{(i)}. \tag{2.17}$$

In the weak-intensity (even single-photon) limit, the response of nuclear vibrations is unveiled by considering the linearisation of the dipole operator in the vicinities of $\mathbf{X}_0$

$$\mu(\hat{\mathbf{Q}}^{(i)}) \simeq \mu_{0,0}^{\mathrm{eq}} \mathbf{1}_v + \left[\partial_{\mathbf{Q}^{(i)}} \mu(\mathbf{Q}^{(i)})\right] |^{\mathrm{eq}} \hat{\mathbf{Q}}^{(i)}, \tag{2.18}$$

Equation 2.18 implies that under external IR fields different bonds contributing to the normal mode $\hat{\mathbf{Q}}^{(i)}$ oscillate with different frequencies, inducing a transition dipole moment (the second term at the right), which can be strongly coupled to the EM field. In practice, this is a peaked function at specific vibrational modes and therefore we can approximate $(\hat{\mathbf{b}}^{(i)} + \hat{\mathbf{b}}^{(i)\dagger})\hat{\mathbf{E}} \mapsto (\hat{b}^{(i)} + \hat{b}^{(i)\dagger})\hat{\mathbf{E}}$. Extensions to many coupled cavity modes and molecular vibrations has also been recently addressed experimentally [82]. The permanent dipole moment term is disregarded, since it does not contribute to the transition, or is identically zero by symmetry arguments [82]. As a result

$$\hat{H} = \sum_{i=1}^{N} \left[\omega_v^{(i)} \hat{b}^{(i)\dagger} \hat{b}^{(i)} + \omega_{\mathrm{EM}} \hat{a}^\dagger \hat{a} + g_i (\hat{b}^{(i)} + \hat{b}^{(i)\dagger})(\hat{a} + \hat{a}^\dagger) + \frac{1}{2\epsilon_0 V} (\hat{\boldsymbol{\mu}}_i \cdot \mathbf{e}_{\mathbf{E}})^2\right], \tag{2.19}$$

where $g_i = \left[\partial_{\mathbf{Q}^{(i)}} \mu(\mathbf{Q}^{(i)})\right] |^{\mathrm{eq}} |\mathbf{E}| (\mathbf{e}_i \cdot \mathbf{e}_{\mathbf{E}})$ in this case. Compared to ESC, the ratios Rabi frequency/transition energy are typically smaller [252]. This is due to reduced values of the induced dipole moment in molecules and the fact that the vast majority of current experiments in VSC employ lossy cavities with mode volumes above the diffraction limit, reducing the single-molecule coupling strength.

2.1.2. Rotating-wave Approximation

The fully-quantised Hamiltonians Equation 2.16 and Equation 2.19 provide a direct link with models employed in quantum optics. To illustrate the formal similitudes between ESC and VSC, we denote the transition frequency generically as $\omega_E^{(i)} = \{\omega_e^{(i)}, \omega_v^{(i)}\}$. Equation 2.1c includes *i)* the so-called *counter-rotating* terms, which create or destroy two-photon/matter excitations. Moreover, it also includes *ii)* a quadratic term representing the molecular self-energy resulting from the coupling of the matter polarisation to its own field [85] (this is essential e.g. to prevent spurious ground-state transitions near the boundary $\Omega_R = \omega_E^{(i)}$ [253]). Close to resonance, i.e. if $|\omega_E^{(i)} - \omega_{\mathrm{EM}}| \ll \Omega_R$, and if the collective Rabi frequency Ω_R stays well below the transition frequencies, *i)* and *ii)* can be 'averaged-out' within the so-called *rotating-wave approximation* (RWA)[5]. Equation 2.16 thus reduces to

$$\hat{H} \simeq \omega_{\mathrm{EM}} \hat{a}^\dagger \hat{a} + \sum_{i=1}^{N} \hat{\sigma}_+^{(i)} \hat{\sigma}_-^{(i)} [\omega_e^{(i)} + \boldsymbol{\lambda}_i (\hat{\mathbf{b}}^{(i)} + \hat{\mathbf{b}}^{(i)\dagger})] + \boldsymbol{\omega}_v^{(i)} \hat{\mathbf{b}}^{(i)\dagger} \hat{\mathbf{b}}^{(i)} + g_i (\hat{a}^\dagger \hat{\sigma}_-^{(i)} + \hat{\sigma}_+^{(i)} \hat{a}), \tag{2.20a}$$

for optical micro-cavities, while Equation 2.19 for an IR micro-cavity simplifies as

$$\hat{H} \simeq \omega_{\mathrm{EM}} \hat{a}^\dagger \hat{a} + \sum_{i=1}^{N} \left[\omega_v^{(i)} \hat{b}^{(i)\dagger} \hat{b}^{(i)} + g_i (\hat{a}^\dagger \hat{b}^{(i)} + \hat{b}^{(i)\dagger} \hat{a}) \right]. \tag{2.20b}$$

The single excitation subspace

The power of the RWA resides in the conservation, by the light-matter interaction, of the number of excitations. Hence $[\hat{H}, \hat{N}] = 0$, where $\hat{N} = \hat{a}^\dagger \hat{a} + \sum_i \hat{\sigma}_+^{(i)} \hat{\sigma}_-^{(i)}$ (ESC) and $\hat{N} = \hat{a}^\dagger \hat{a} + \sum_i \hat{b}^{(i)\dagger} \hat{b}^{(i)}$ (VSC). Typical organic polariton experiments employ coherent drivings with very low intensity. In this manner, only the low-lying electronic or vibrational states become mixed with photons. Formally, this signifies the Hamiltonian can be projected on the single excitation subspace[6],

$$\mathcal{S}_1 = \{\hat{a}^\dagger \left|G\right\rangle, \left|E^{(1)}\right\rangle, \left|E^{(2)}\right\rangle, \cdots, \left|E^{(N)}\right\rangle\}, \tag{2.21}$$

where the states $\left|E^{(i)}\right\rangle \equiv \left|g^{(1)}, \cdots, g^{(i-1)}, E^{(i)}, \cdots, g^{(N)}\right\rangle = \{\left|e\right\rangle^{(i)}, \left|v\right\rangle^{(i)}\}$ denote generically singly-excited electronic or vibrational states with frequencies $\omega_E^{(i)}$. Intriguingly, the Hamiltonian acquires a similar form in ESC and VSC if vibronic coupling is disregarded ($\boldsymbol{\lambda}_i \to 0$). This is the often referred as Tavis-Cummings Hamiltonian [255, 256], whose eigenergies follow from [257],

$$\omega_{\mathrm{EM}} - \omega - \sum_{i=1}^{N} \frac{|g_i|^2}{\omega_E^{(i)} - \omega} = 0. \tag{2.22}$$

For zero disorder ($\omega_E^{(i)} = \omega_E$) and detuning ($\omega_{\mathrm{EM}} = \omega_E$) the *collective Rabi frequency* reads $\Omega_R = 2\sqrt{\sum_{i=1}^{N} |g_i|^2}$ or $\Omega_R = 2g\sqrt{N}$ if the couplings are assumed identical ($g_i = g$), reproducing the $\sim \sqrt{N}$ scaling mentioned in chapter 1.

---

[5] Since RWA and 2-level system limit implies approximations over the full-interaction Hamiltonian, predictions become gauge-dependent [240, 254]. The length gauge, where the position is well-defined, is a widespread choice for bound states in molecular and atomic physics.

[6] We note that since the system Hamiltonian Equation 2.20b is quadratic in the bosonic modes $\{\hat{a}, \hat{b}^{(i)}\}$, it can in principle be diagonalised without restriction to any excitation subspace.

Collective strong coupling emerges when Ω_R is larger than the losses of the system. Assuming this is the case, the $N+1$ singly excited eigenstates of this Hamiltonian are formed by: *i)* two *polaritons*, $|\pm\rangle$, symmetric and antisymmetric linear combinations of the cavity mode $a^\dagger|0\rangle$, with the collective *bright state* of the molecular excitation, $|B\rangle = \frac{1}{\sqrt{N}}\sum_i |E^{(i)}\rangle$; $|\pm\rangle = \frac{1}{\sqrt{2}}(\hat{a}^\dagger|0\rangle \pm |B\rangle)$ and *ii)* the so-called *dark states*, $N-1$ combinations of molecular excitations orthogonal to $|B\rangle$, which have eigenfrequencies ω_E and no mixing with the photonic mode. The eigenfrequencies of the two polariton modes are $\omega_\pm = \omega_E \pm \Omega_R/2$.

2.2. System-reservoir coupling

Any realistic quantum system couples unavoidably to the 'rest of the universe'. This *environment* is typically understood as a broad set of (many) 'uncontrollable' degrees of freedom, denoted by $\mathcal{E}$. The subspace of interest is the so-called *system*, $\mathcal{S}$[7]. This experiences, as a result of this interaction, dynamics ranging from irreversible loss of energy or coherence into $\mathcal{E}$ (*Markovian limit*), to reversible (*non-Markovian*) evolution.

In the following, we overview the approach to introduce such effects. The topic of open quantum systems (OQS) is covered extensively by many textbooks [187, 258–260]. Formally $\mathcal{S}$ is said to be open if it can be regarded as a subsystem of some larger closed system $\mathcal{S}+\mathcal{E}$, governed by

$$\hat{H}_{\mathcal{S}+\mathcal{E}} = \hat{H}_{\mathcal{S}} \otimes \mathbf{1}_{\mathcal{E}} + \mathbf{1}_{\mathcal{S}} \otimes \hat{H}_{\mathcal{E}} + \hat{H}_{\mathcal{I}}, \tag{2.23}$$

where $\hat{H}_{\mathcal{S}}$ and $\hat{H}_{\mathcal{E}}$ implement the free evolution of system and environment, respectively, and $\hat{H}_{\mathcal{I}}$ is the interaction Hamiltonian between $\mathcal{S}$ and $\mathcal{E}$[8]. Since the most common environments will be the EM field and phonons, $\mathcal{E}$ can be assumed to be formed by an assembly of harmonic oscillators. Similarly, $\mathcal{E}$ is only slightly perturbed away from its equilibrium configuration, and thus $\hat{H}_{\mathcal{I}}$ is linear in the bath coordinates[9]. Additionally, the spectrum of oscillator frequencies and the coupling constants for each frequency will be assumed dense functions. The brute-force diagonalisation of the combined $\mathcal{S}+\mathcal{E}$ is very common numerically unfeasible. The approaches to attack such problems in this thesis are divided into two.

---

[7] The separation of the physical system in $\mathcal{S}$ and $\mathcal{E}$ is arbitrary and particularly non-trivial in molecules, which present a substantial number of internal degrees of freedom.

[8] This does not exclude the presence of weak optical driving fields, which can be represented in terms of the dipole transition operator $\hat{\mu}_+$ as $\hat{H}_d(t) \sim \hat{\mu}_+ e^{-i\omega_d t} + \text{H.c.}$, and the time-dependence removed by a rotation at the laser frequency $\hat{H} \mapsto e^{i\omega_d \hat{\mu}_+ \hat{\mu}_- t} \hat{H} e^{-i\hat{\mu}_+ \hat{\mu}_- t} - \omega_d \hat{\mu}_+ \hat{\mu}_-$.

[9] Deviations from this limit appear, e.g. in the coupling of acoustic phonons in cavity QED [261, 262].

1. Simulation of the subsystem $\mathcal{S}$ by a *master equation* including the influence of $\mathcal{E}$. The problem is generally tractable if the interaction $\hat{H}_{\mathcal{I}}$ is weak, leading to a simpler Markovian master equation where $\mathcal{E}$ is static (see subsection 2.2.1).
2. Quasi-exact numerical solution of the energy minimisation or the time evolution of the complete system governed by $\hat{H}_{\mathcal{S}+\mathcal{E}}$, where $\mathcal{S}$ and $\mathcal{E}$ are treated indistinctly employing the so-called *tensor network* representation of the quantum states (see subsection 2.2.2).

2.2.1. Reduced system master equation: losses and decoherence

The first approach involves a reduced density operator, $\hat{\rho}_{\mathcal{S}} = \mathrm{Tr}_{\mathcal{E}}\{\hat{\rho}_{\mathcal{S}+\mathcal{E}}\}$, over the global density matrix $\hat{\rho} = |\psi_{\mathcal{S}+\mathcal{E}}\rangle\langle\psi_{\mathcal{S}+\mathcal{E}}|$. The goal is to obtain a master equation for $\hat{\rho}_{\mathcal{S}}$, introducing perturbatively the interaction $\hat{H}_{\mathcal{I}}$. For it, we switch operators to the interaction picture defined as $\tilde{O}(t) = e^{i(\hat{H}_{\mathcal{S}+\mathcal{E}}-\hat{H}_{\mathcal{I}})t}\hat{O}e^{-i(\hat{H}_{\mathcal{S}+\mathcal{E}}-\hat{H}_{\mathcal{I}})t}$[10], and we introduce a perturbative expansion to second-order by means of the *projection operator*. Right-after, we describe the *Markovian* limit and the BRW master equation.

General master equation

A very elegant approach to obtain the time evolution of the reduced density matrix $\hat{\rho}_{\mathcal{S}}$ is described in terms of the Nakajima-Zwanzig projector operators technique in [187]. This exploits the Von-Neumann master equation $i\tilde{\rho}_{\mathcal{S}+\mathcal{E}} = [\tilde{H}_{\mathcal{I}}, \tilde{\rho}_{\mathcal{S}+\mathcal{E}}] = \mathcal{L}_{\mathcal{I}}\tilde{\rho}_{\mathcal{S}+\mathcal{E}}$ assumes the total density operator can be written in terms of the orthogonal projectors $\mathcal{P}, \mathcal{Q}$, which enable to split the density matrix into a system-bath-separable contribution or *relevant part*, $\mathcal{P}\tilde{\rho}_{\mathcal{S}+\mathcal{E}}$ and a part $\mathcal{Q}\tilde{\rho}_{\mathcal{S}+\mathcal{E}}$ that contains all system-bath correlations and the environment dynamics. This results is a a lengthy integro-differential master equation, simplified by assuming that, at $t = 0$, $\mathcal{E}$ is in a thermal state with temperature $T = (k_B\beta)^{-1}$, (k_B is the Boltzmann constant), i.e. $\hat{\rho}_{\mathcal{E}} = e^{-\beta\hat{H}_{\mathcal{E}}}/\mathrm{Tr}\{e^{-\beta\hat{H}_{\mathcal{E}}}\}$, and the state is separable $\tilde{\rho}_{\mathcal{S}+\mathcal{E}}(0) = \tilde{\rho}_{\mathcal{S}}(0) \otimes \tilde{\rho}_{\mathcal{E}}(0)$, yielding

$$\partial_t\mathcal{P}\tilde{\rho}(t) = \mathcal{P}\mathcal{L}_{\mathcal{I}}\tilde{\rho}_{\mathcal{S}}(t) + \int_0^t \mathcal{K}(t,t')\mathcal{P}\tilde{\rho}(t-t')\,\mathrm{d}t', \tag{2.24a}$$

$$\mathcal{K}(t,t') = \mathcal{P}\mathcal{L}_{\mathcal{I}}(t)\mathcal{G}(t,t')\mathcal{Q}\mathcal{L}_{\mathcal{I}}(t')\mathcal{P}, \tag{2.24b}$$

where $\mathcal{K}$ is the memory kernel including all non Markovian effects in $\hat{\rho}_{\mathcal{S}}$ induced by the system-bath interaction, and $\mathcal{G}(t,s) = \mathcal{T}e^{\int_s^t \mathcal{Q}\mathcal{L}_{\mathcal{I}}(\tau)\,d\tau}$ is the propagator for the subspace

---

[10] Some additional care must be taken in this choice for strongly interacting systems, as pointed out by Carmichael et al [263].

projected by $\mathcal{Q}$[11]. Nevertheless, the practical calculation of the memory kernel is cumbersome, and typically the expansion $\mathcal{K}$ to second order in $\hat{H}_{\mathcal{I}}$ is considered, setting $\mathcal{G} \simeq \mathbf{1}$ (*Born approximation*). This implies that the bath will be static, i.e., it neglects any tweak of the equilibrium distribution in $\mathcal{E}$ induced by $\mathcal{S}$. The state at all times then becomes factorisable ($\tilde{\rho}_{\mathcal{S}+\mathcal{E}}(t) \simeq \tilde{\rho}_{\mathcal{S}}(t) \otimes \tilde{\rho}_{\mathcal{E}}(t)$) and the time evolution follows from

$$\partial_t \hat{\rho}_{\mathcal{S}}(t) = -\int_0^t \mathrm{Tr}_{\mathcal{E}}\big[\tilde{H}_{\mathcal{I}}(t), \big[\tilde{H}_{\mathcal{I}}(t'), \tilde{\rho}_{\mathcal{S}}(t') \otimes \tilde{\rho}_{\mathcal{E}}\big]\big]\, \mathrm{d}t'. \tag{2.25}$$

Despite its apparent simplicity, Equation 2.25 includes a time convolution, accounting for all the past history of $\hat{\rho}_{\mathcal{S}}$. To obtain a more tractable form, we *i)* rewrite $\tilde{H}_{\mathcal{I}} \rightarrow \alpha \tilde{V}_{\mathcal{I}}$, in terms of a dimensionless constant α that accounts for the strength of the interaction and *ii)* we impose the linear coupling condition $\tilde{V}_{\mathcal{I}} = \sum_k \tilde{A}_k \otimes \tilde{B}_k$, where $\{\tilde{A}_k, \tilde{B}_k\}$ are Hermitian system and environment operators respectively. Finally, *iii)*, we use the spectral decomposition of $\hat{H}_{\mathcal{S}}$ into eigenstates $|\psi_\epsilon\rangle$ with eigenvalue ϵ, $\tilde{A}_k(\omega) = \sum_{\epsilon'-\epsilon=\omega} \left\langle \psi_\epsilon | \tilde{A}_k | \psi_{\epsilon'} \right\rangle |\psi_\epsilon\rangle \langle \psi_{\epsilon'}|$. Equation 2.25 can thus be integrated to give

$$\begin{aligned}\tilde{\rho}_{\mathcal{S}}(t) = &\tilde{\rho}_{\mathcal{S}}(0) - \alpha^2 \int_0^t \mathrm{d}s \sum_{\omega,\omega'} \sum_{k,l} e^{i(\omega'-\omega)s} \Gamma^s_{kl}(\omega) \big[\tilde{A}_l(\omega) \tilde{\rho}_{\mathcal{S}}(s), \tilde{A}^\dagger_k(\omega')\big] \\ &+ e^{i(\omega-\omega')s} \Gamma^{s*}_{lk}(\omega) \big[\tilde{A}_l(\omega'), \tilde{\rho}_{\mathcal{S}}(s) \tilde{A}^\dagger_k(\omega)\big] + \mathcal{O}(\alpha^3).\end{aligned} \tag{2.26}$$

For the system part, examples include the transition operator $\hat{A}_k = \left|E^{(k)}\right\rangle \langle G| + \mathrm{H.c.}$ for *decay* or $\hat{A}_k = \left|E^{(k)}\right\rangle \left\langle E^{(k)}\right|$ for *pure dephasing*. Since the coupling to the bath is linear, the $\hat{B}_k$ can be expanded in terms of bosons $\{\hat{\mathbf{c}}_k, \hat{\mathbf{c}}^\dagger_k\}$ as $\hat{B}_k = \sum_l \lambda^{(l)}_k (\hat{c}^{(l)}_k + \hat{c}^{(l)\dagger}_k)$, where the information about the system-bath couplings $\boldsymbol{\lambda}^{(l)}$, and frequencies $\boldsymbol{\omega}^{(l)}$ is encoded in the *spectral density*

$$J^{(l)}(\omega) = \pi \sum_k \lambda^{(l)2}_k \delta(\omega - \omega^{(l)}_k), \tag{2.27}$$

defined over positive frequencies[12]. In Equation 2.26, the frequency integrals $\Gamma^s_{kl}(\omega) = \int_0^s e^{i\omega u} \phi_{kl}(u)\, \mathrm{d}u$, involve the *bath correlation functions* (time invariance in the bath dynamics is assumed)

$$\phi_{ij}(\tau) = \mathrm{Tr}_{\mathcal{E}}\{\tilde{B}_i(\tau) \tilde{B}_j(0) \hat{\rho}_{\mathcal{E}}\} = \sum_k \lambda^{(i)}_k \lambda^{(j)}_k \mathrm{Tr}_{\mathcal{E}}[(\tilde{c}^{(i)}_k(\tau) + \tilde{c}^{(i)\dagger}_k(\tau))(\tilde{c}^{(j)}_k(0) + \tilde{c}^{(j)\dagger}_k(0))\hat{\rho}_{\mathcal{E}}]. \tag{2.28}$$

---

[11] At this level, the evolution can be estimated employing techniques such as the Transfer Tensor Method [264], the path-integral formulation from Feynman and Vernon [265, 266], and the Hierarchical Equations of Motion approach [267].

[12] The π factor is included here to be reabsorbed in the calculation of some integrals in the Markovian limit.

These represent the time-non-local influence of the bath in the system, i.e., set the timescale for the memory effects. The indexes k, l here will account for correlations between oscillators from different baths (e.g. vibrational modes in different molecules)[13]. For a thermal bath the autocorrelation function can be expressed through the spectral density in Equation 2.27 [251]

$$\phi_{ll}(\tau) = \int_0^\infty J^{(l)}(\omega)\left\{[n(\omega)+1]e^{-i\omega\tau} + n(\omega)e^{i\omega\tau}\right\}\mathrm{d}\omega, \tag{2.29}$$

where $n(\omega) = (e^{\beta\omega}-1)^{-1}$ is the Bose occupation factor.

Weak environment coupling limit and Markovian approximation

At this point, another important timescale is the one set by the $\mathcal{S}$ evolution, represented by the phases in ω, ω'. If these phases evolve rapidly as compared with the characteristic timescale of $\phi(s)$, i.e. bath correlations decay quickly enough, those contributions can be averaged to zero (*secular approximation*)[14]. The resulting master equation does not depend on the past history of the reduced density matrix (thus, is time-local or Markovian) and preserves the positivity of $\hat{\rho}_{\mathcal{S}}$ during the evolution, preventing issues such as unbounded growth of populations. Separating the functions $\Gamma^{\infty}_{kl}(\omega)$ into Hermitian and anti-Hermitian parts $\Gamma^{\infty}_{kl}(\omega) = S_{kl}(\omega) + i\zeta_{kl}(\omega)$, the *secular master equation* reads

$$\partial_t\tilde{\rho}_{\mathcal{S}}(t) = \sum_{\omega}\sum_{k,l}\{-i[\zeta_{kl}(\omega)\tilde{A}_k^{\dagger}\tilde{A}_l, \tilde{\rho}_{\mathcal{S}}(t)] + S_{kl}(\omega)\mathcal{L}_{\tilde{A}_k,\tilde{A}_l}[\tilde{\rho}_{\mathcal{S}}(t)]\}, \tag{2.31}$$

where $\mathcal{L}_{\hat{X},\hat{Y}}[\cdot] = \hat{Y}\cdot\hat{X}^{\dagger} - \frac{1}{2}\{\hat{X}^{\dagger}\hat{Y}, \cdot\}$ is a crossed superoperator, which might be diagonalised in the k, l indexes to give the so-called *Lindblad* superoperator [270]

$$\mathcal{L}_{\hat{X}}[\,\cdot\,] = \hat{X}\cdot\hat{X}^{\dagger} - \frac{1}{2}\{\hat{X}^{\dagger}\hat{X}, \,\cdot\,\}. \tag{2.32}$$

The terms $\propto \zeta_{kl}(\omega)$, therefore, account for a bath-induced *fluctuations*, which can be reabsorbed in the coherent dynamics in the system (diagonal terms are precisely Lamb

---

[13] In chapter 3 we consider two possible scenarios, *i)* the *localised* bath, where only the terms with $k = l$ are non-zero, and the *ii) delocalised* bath, where there is no dependence on k, l at all (the system couples collectively to a common environment). For a discussion on the intermediate case, see [268].

[14] Mathematically, this is ensured by the so-called Riemann-Lebesgue lemma [269]. If $\tau = \alpha^2 t$ and $\sigma = \alpha^2 s$, then (See [259] for further details)

$$\lim_{\alpha\to 0}\int_0^{\tau} e^{i(\omega-\omega')\sigma/\alpha^2}\Gamma^{\sigma/\alpha^2}_{lk}(\omega) = \delta_{\omega,\omega'}\int_0^{\tau}\Gamma^{\infty}_{kl}(\omega). \tag{2.30}$$

shifts), and are thus disregarded in the treatment. Moreover, the contributions $\propto \gamma_{kl}(\omega)$ are amplitudes for the *incoherent* processes at frequency ω. The rapid decay of time correlations yielding Equation 2.31 is linked to the frequency bandwidth of the functions $\Gamma^{s}_{kl}(\omega)$, which needs to be large enough compared to system frequencies[15]. The Markov approximation, therefore, may fail for structured baths, where these functions are resonant with system eigenstates [271]. Very often, Lindblad terms are introduced phenomenologically in quantum optics, without explicit derivation from microscopic models. Nevertheless, care must be taken for systems with strongly coupled internal states (f.eg. phonons in organic molecules)[16].

Although Equation 2.31 enables for analytical results in many cases, the secular approximation is not strictly necessary for purely numerical simulations, since it leaves the overall size of the superoperators unchanged. Therefore, sometimes the less restrictive condition limit $s \to \infty$ is taken in the functions $\Gamma^{s}_{kl}(\omega)$ in Equation 2.26 to impose the Markovian limit, before secularisation. Such approach leads to the so-called BRW master equation [207, 208], (back to Schrödinger picture)

$$\partial_t \hat{\rho}_{\mathcal{S}} = -\, i[\hat{H}_{\mathcal{S}}, \hat{\rho}_{S}] + \mathcal{R}[\hat{\rho}_{\mathcal{S}}(t)], \tag{2.33}$$

where the bath-induced coherent terms are assumed to be negligible and the incoherent evolution follows from the *Bloch-Redfield* superoperator

$$\mathcal{R}[\,\cdot\,] = \sum_{\omega,\omega'} \sum_{k,l} S^{\infty}_{kl}(\omega-\omega') \left[\hat{A}_l(\omega), [\,\cdot\,, \hat{A}^{\dagger}_k(\omega')\right] + \text{H.c.}. \tag{2.34}$$

The particular case of dephasing interactions has been analysed in chapter 3. Moreover, by projecting Equation 2.33 in the eigenbasis of $\hat{H}_{\mathcal{S}}$, we get

$$\partial_t \rho_{\epsilon,\epsilon'} = -i(\epsilon-\epsilon')\rho_{\epsilon,\epsilon'} + \sum_{\zeta,\zeta'} \mathcal{R}_{\epsilon,\epsilon',\zeta,\zeta'}\rho_{\zeta,\zeta'}. \tag{2.35}$$

It must be noted that Equation 2.33 does not guarantee positivity in the density matrix a priori. In this case, the secular approximation implies neglecting coupling between diagonal and off-diagonal elements in $\mathcal{R}$ if the *energy differences* between states *differ* between them significantly. This condition needs detailed inspection of the matrix elements (see [274] for further details) and it is found to be numerically implemented for instance in QuTiP open-source libraries [275].

---

[15] The secular approximation is also sometimes called the *rotating wave approximation*, but should not be confused with the rotating wave approximation performed in the system Hamiltonian in Equation 2.20.

[16] In some scenarios is even legitimate to introduce the dissipative interaction by a non-Hermitian contribution of the system Hamiltonian, avoiding the use of the density matrix [272, 273]

Dephasing interactions

In this thesis, the case of *dephasing-type* interactions of the form $\hat{A}_l \sim \hat{b}^{(l)\dagger}\hat{b}^{(l)}$ or $\hat{A}_l \sim \hat{\sigma}_+^{(l)\dagger}\hat{\sigma}_-^{(l)}$ that shows up in electronic and nuclear transitions in molecules, is particularly relevant. A common origin of this loss of coherence is the presence of comparatively low frequency modes in the system, which interact elastically with the $\mathcal{S}$ states. In the single-excitation subspace described in subsection 2.1.2, the BRW master equation can be expanded as

$$\partial_t \tilde{\rho}_{\mathcal{S}} = \sum_{i,j=1}^{N} \sum_{p,q,r,s} \int_0^\infty \phi_{ij}(\tau) u_p^{(i)} u_q^{(i)} u_r^{(j)} u_s^{(j)} e^{i(\omega_{pq}-\omega_{sr})t + i\omega_{sr}\tau} \left[\hat{\sigma}_{rs}\tilde{\rho}_{\mathcal{S}}(t), \hat{\sigma}_{pq}\right] \mathrm{d}\tau + \text{H.c.}, \quad (2.36)$$

where i, j are molecular indexes, $\hat{\sigma}_{ab} = |a\rangle\langle b|$, $\hat{H}_{\mathcal{S}}|a\rangle = \omega_a|a\rangle$, $\omega_{ab} = \omega_a - \omega_b$, and the sums over p, q, r and s include all system eigenstates. Furthermore, $u_a^{(i)}$ give the overlaps between system eigenstates and vibrational mode excitations and can be chosen real. Inserting the correlation functions$\phi(\tau)$ from Equation 2.29 leads to integrals of the type

$$\int_0^\infty e^{\pm i\Delta\omega\,\tau}\mathrm{d}\tau = \pi\delta(\Delta\omega) \pm i\,\text{P.V.}(\Delta\omega^{-1}), \quad (2.37)$$

where P.V. denotes the Cauchy principal value (we neglect these imaginary parts as stated above, since they only induce small energy shifts that can be reabsorbed in the coherent dynamics), and arrive to

$$\partial_t \tilde{\rho}_{\mathcal{S}} = \sum_{i,j=1}^{N} \sum_{p,q,r,s} S_{ij}(\omega_{sr}) u_p^{(i)} u_q^{(i)} u_r^{(j)} u_s^{(j)} \left\{ e^{i(\omega_{pq}-\omega_{sr})t} \left[\hat{\sigma}_{rs}\tilde{\rho}_{\mathcal{S}}(t), \hat{\sigma}_{pq}\right] + \text{H.c.} \right\}, \quad (2.38)$$

with the bath noise-power spectrum

$$S(\omega) = \begin{cases} J(\omega)[n(\omega)+1] & \omega \geq 0 \\ J(-\omega)n(-\omega) & \omega < 0 \end{cases}. \quad (2.39)$$

2.2.2. Quasi-exact numerical approach and tensor networks

The reduced evolution approach described above is by far the most common method to treat open quantum systems since only the knowledge of a reduced part of the Hilbert space of the system $\mathcal{S}$ is typically required. Nevertheless, the most considerable part of the system, $\mathcal{E}$, can be profoundly affected beyond the weak $\hat{H}_{\mathcal{I}}$ limit. As we will see below, this is the case of molecular phonons in strongly coupled optical micro-cavities. Treating the full system is a formidable endeavour, but this is feasible by introducing a tensor network representation of the wavefunction $|\psi_{\mathcal{S}+\mathcal{E}}\rangle$. In the following, we explain the basics of this approach. We particularise our discussion to the case of ESC, analysed in part II.

Tensor network representation of full-coherent $\mathcal{S}-\mathcal{E}$ wavefunction

Tensor networks (TN) arise as a generalisation of the so-called *Matrix Product States* (MPS) [276]. These represent a very efficient way of 'compressing' the wavefunction by keeping only a fundamental set of parameters. In this section we assume a single environment $\mathcal{E}$, outlining right after the multi-environment extension that will be subsequently employed. The fundamental idea behind this approach is simple. We consider a many-body quantum system with $\mathcal{M}_v+1$ parts, i.e., the system $\mathcal{S}$ and $\mathcal{M}_v$ environment oscillators $\mathcal{H}=\mathcal{H}_{\mathcal{S}}\otimes\mathcal{H}_1\cdots\otimes\mathcal{H}_{\mathcal{M}_v}$, where each local Hilbert space is provided with $d_{\mathcal{S}},d_1,\cdots,d_{\mathcal{M}_v}$ states. Indexing such *local Hilbert space* states by $n_{\mathcal{S}},n_k\in(1,2,\cdots,d_k)$, a general wavefunction of the system reads

$$|\psi_{\mathcal{S}+\mathcal{E}}\rangle=\sum_{\{n_k\}}\psi_{n_{\mathcal{S}},n_1,\cdots,n_{\mathcal{M}_v}}\,|n_{\mathcal{S}},n_1,\cdots,n_{\mathcal{M}_v}\rangle \tag{2.40}$$

where $\{n_k\}$ indicate all possible $(d_{\mathcal{S}}\prod_{k=1}^{\mathcal{M}_v}d_k)$ configurations of many body states in the system. There are as many configurations as the number of components in the $(\mathcal{M}_v+1)^{\text{th}}$ order *tensor* $\bar{\boldsymbol{\psi}}$ (a multi-dimensional array in practice), which contains the same information as $|\psi\rangle$. This tensor can be displayed schematically as a rectangle with as many open legs as indexes (see Figure 2.3a). We assume for simplicity that the quantum system of interest is a 1D-lattice with open boundary conditions. Now, by combining *permutations* (exchange of indices that generalise matrix transpositions), *reshapes* (where indexes are joined to form collective indexes) and matrix *singular-value-decompositions* (SVD)[17], it is possible to rewrite each of the components of $\bar{\boldsymbol{\psi}}$ as a matrix product [171]

$$\psi_{n_{\mathcal{S}},n_1,\cdots,n_{\mathcal{M}_v}}=\sum_{\zeta_{\mathcal{S}},\zeta_1,\cdots\zeta_{\mathcal{M}v}}A^{n_{\mathcal{S}}}_{1,\zeta_{\mathcal{S}}}A^{n_1}_{\zeta_{\mathcal{S}},\zeta_1}\cdots A^{n_{\mathcal{M}_v}}_{\zeta_{\mathcal{M}_v},1}. \tag{2.42}$$

In this decomposition, the l^{th} part of the Hilbert space is associated to d_l rectangular matrices with dimensions (ζ_{l-1},ζ_l). Such matrices (or formally three-order tensors) are

---

[17] The SVD of a matrix is equivalent to the *Schmidt decomposition* of a bipartite state living in $\mathcal{H}_{\mathcal{A}}\otimes\mathcal{H}_{\mathcal{B}}$, that permits an expression into a combinations of states belonging to orthonormal basis in $\mathcal{A},\mathcal{B}$

$$|\psi_{\mathcal{A}+\mathcal{B}}\rangle=\sum_{k}^{r-1}\sigma_k\,|\xi_k\rangle^{\mathcal{A}}\otimes|\xi_k\rangle^{\mathcal{B}}, \tag{2.41}$$

and σ_k are the singular values. The number of non-zero terms (rank) is $r\leq\min\{\dim\mathcal{H}_{\mathcal{A}},\dim\mathcal{H}_{\mathcal{B}}\}$.

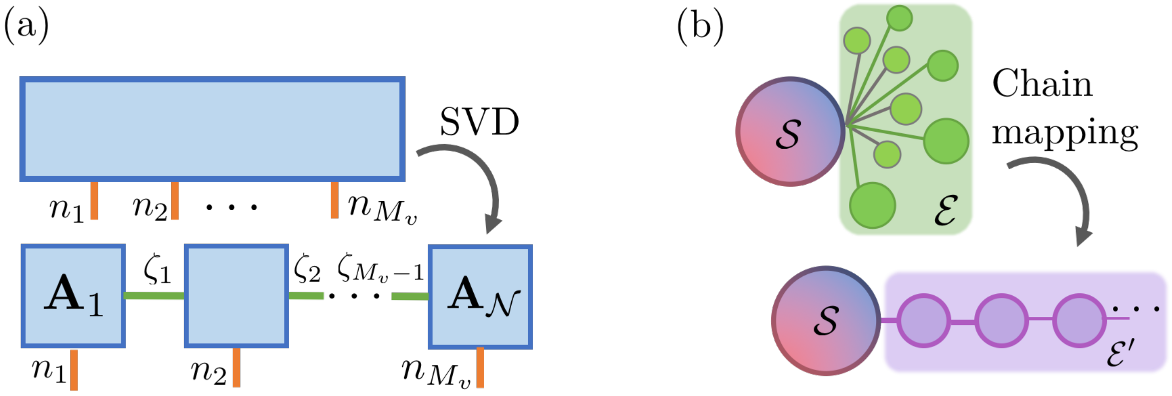

Figure 2.3: (a) Sketch of the 'breaking' by repeated SVDs of the system wavefunction into tensors connected by virtual bonds. The representation of the bath in a optimal boson basis is also displayed. (b) Mapping of the system-environment Hamiltonian into a 1D lattice or chain, where operators act on local Hilbert spaces where each $\mathbf{A}_k$ is defined.

connected via the auxiliary indexes $\zeta_k \in (1, 2, \cdots D_k)$, labelling the so-called *bond dimensions*, where D_k stands for the maximum allowed bond dimension. Intriguingly, the corresponding *bond states* embody the entanglement content of the state: higher bond dimensions signify more entanglement. Indeed, for arbitrary large D_k the MPS representation is numerically exact. The important observation here is related with the so-called *entanglement area law* [277], which this ensures that the quantum entanglement in the low-lying states of a *many body system with local interactions* grows with the size of the boundary area of the region and not as the volume. MPS are an optimal parametrisation to describe states fulfilling this condition, implying that we can exploit representations with relatively small D_k for states lying at the bottom of the eigenspectrum of $\hat{H}_{\mathcal{S}+\mathcal{E}}$ if adequately represented. A larger portion of the Hilbert space can be included, if necessary, by augmenting the internal dimensions of the MPS, to 'induce' more correlations.

The primary power of MPS-based approaches, therefore, relies on the efficient computer representation of the site tensors $\mathbf{A}^{n_k}$. In practice, this 'compression' is achieved by successive iterations of singular value decompositions (SVDs) and truncation of the states with small singular values (the so-called low-rank approximation [18]). This protocol reduces the maximum bond dimensions, enabling to restrict the possible states to a submanifold $\mathcal{M}_{\text{TN}} \subset \mathcal{H}_{\mathcal{S}+\mathcal{E}}$ that comprises the low-lying states of interest in minimisation or time evolution. In particular, a MPS with matrix (bond) dimensions equal to 1 mimics the case of a product state (e.g. the typical ansatz in mean field theory), while larger

---

[18] That is also equivalent to a low-entanglement approximation, since the Von-Neumann entropy reduced over $\mathcal{A}$ or $\mathcal{B}$ measuring it is $S = -|\sigma_k|^2 \log |\sigma_k|^2$.

dimensions open many possible entanglement channels between local Hilbert spaces.

The decomposition of the wavefunction into Equation 2.42 is not unique. The multidimensional array can be reshaped into multiple ways, ending in many possible structures bound by index multiplications or *contractions*; this is represented by joining tensor legs and labelling both legs with the same name (see [276] for further details). In practice, permutations and reshapes are central to prepare tensors for numerically efficient contractions. In particular, to reduce the size of local bosonic tensors, additional matrices are introduced, 'plugged' into the physical legs to map the local Hilbert spaces of the environment oscillators to a *smaller* set of bosonic states that actually contribute (see the bottom of Figure 2.3a). This leads to the so-called optimal boson basis (OBB) that will be determined on the fly of the algorithm to reduce the memory storage of boson tensors [195, 278].

The set of contracted tensors form the structure generally known as TN [276, 279]. These ideas can be applied to treat efficiently ground state minimisation and time dynamics of open quantum systems, even if the system is coupled to many large environments. In the following, we show how the $\mathcal{S}-\mathcal{E}$ Hamiltonian must be prepared for efficient application of TN-based methods.

Preparing the Hamiltonian for interface with tensor networks

We consider for simplicity the case of $\mathcal{S}$ coupled to a single environment $\mathcal{E}$, therefore

$$\hat{H}_{\mathcal{I}} = \hat{A}\sum_{k=1}^{M_v}\lambda_k(\hat{b}_k + \hat{b}_k^\dagger), \qquad\qquad \hat{H}_{\mathcal{E}} = \sum_{k=1}^{M_v}\omega_k\hat{b}_k^\dagger\hat{b}_k \tag{2.43}$$

where $\hat{A} = \hat{A}^\dagger$ is Hermitian. The properties of each of the M_v modes, $\{\omega_k, \lambda_k\}$, are encoded in the spectral density $J_v(\omega) = \pi\sum_{k=1}^{M_v}\lambda_k^2\delta(\omega-\omega_k)$ (see Equation 2.27), which in general (e.g. for molecular phonons) will display many resonances. We assume in the following $J(\omega)$ has a hard cutoff at $\omega = \omega_c$. MPSs are intrinsically one-dimensional structures. For ground-state optimisation and time-evolution algorithms it is crucial to enable efficient tensor contractions between MPS and system Hamiltonian. In order to adapt the Hamiltonian to 'accommodate' a TN representation, the first step is to consider the *chain-mapping* of the bath operators $\hat{c}_l = \int_0^1 U_l(x)\,\hat{b}_x\,\mathrm{d}x$, $x = \omega/\omega_c$ [173]. This mapping can be implemented via tridiagonalisation of the coupling matrix $\mathcal{C}$, where

$\hat{H}_{\mathcal{I}} = \frac{1}{2}\hat{\boldsymbol{\xi}}^\dagger \mathcal{C} \hat{\boldsymbol{\xi}}$ with $\hat{\boldsymbol{\xi}}^T = \left(\hat{A}, \hat{b}_1, \hat{b}_2, \cdots \hat{b}_{M_v}\right)$ and

$$\mathcal{C} = \begin{pmatrix} 0 & \lambda_1 & \lambda_2 & \cdots & \lambda_{M_v} \\ \lambda_1 & \omega_1 & & & \\ \lambda_2 & & \omega_2 & & \\ \vdots & & & \ddots & \\ \lambda_{M_v} & & & & \omega_{M_v} \end{pmatrix} \mapsto \begin{pmatrix} 0 & \eta & 0 & & \\ \eta & \Omega_v & t_1 & & \\ & t_1 & \tilde{\omega}_1 & \ddots & \\ & & \ddots & \ddots & t_{M_v-1} \\ & & & t_{M_v-1} & \tilde{\omega}_{M_v-1} \end{pmatrix}. \tag{2.44}$$

The coefficients $\{\Omega_v, \omega_l, \eta, t_l\}$ can be obtained by employing the Lanczos or the Stieltjes algorithm (more efficient but more inaccurate). After this transformation, the $\mathcal{S} - \mathcal{E}$ interaction Hamiltonian is thus given by a *chain Hamiltonian*

$$\hat{H}'_{\mathcal{I}} = \eta \hat{A}\left(\hat{c}_0 + \hat{c}_0^\dagger\right) + \sum_{l=0}^{M_v-1} t_l\left(\hat{c}_l^\dagger \hat{c}_{l+1} + \hat{c}_{l+1}^\dagger \hat{c}_l\right), \qquad \hat{H}'_{\mathcal{E}} = \Omega_v \hat{c}_0^\dagger \hat{c}_0 + \sum_{l=1}^{M_v-1} \omega_l \hat{c}_l^\dagger \hat{c}_l \tag{2.45}$$

Equation 2.45 accounts for the coupling of $\hat{A}$ to a collective environment mode $\hat{c}_0 = \sum_k \lambda_k \hat{b}_k / \sqrt{\sum_k \lambda_k^2}$, exactly equivalent to the reaction coordinate introduced in Equation 2.13 [280, 281], having a frequency Ω_v and average coupling amplitude η, given by

$$\Omega_v = \frac{\int_0^\infty \omega J_v(\omega)\,\mathrm{d}\omega}{\int_0^\infty J_v(\omega)\,\mathrm{d}\omega}, \qquad \eta = \sqrt{\int_0^{\omega_c} \frac{J_v(\omega)\,\mathrm{d}\omega}{\pi}}, \tag{2.46}$$

In addition, the second line contains the remaining orthogonal modes $\hat{c}_l$ with frequencies ω_l ($l \in (0, \cdots, M_v - 1)$), that form a chain, connected via nearest-neighbor couplings t_l. Thus, the previous mapping reveals that $\hat{c}_0$ channels the interaction between $\mathcal{S}$ with the remaining set of orthogonal modes that are not directly coupled [282, 283][19].

Besides, the mapping described above is invertible, a characteristic where resides the primary power of this approach. In this way, physical environment observables (f.ex. vibrational populations and correlations) in the original Hamiltonian can be obtained by an efficient TN-based computation in the chain basis (see [171] for details) followed by the inverse transformation of U applied to the chain observables. Finally, it is noteworthy that, for power law (the so-called Leggett-type) spectral densities, $J_v(\omega) \propto \omega^s$, $s > 0$ the problem can be reformulated into an orthogonal polynomial mapping enabling analytical solution [172, 173]. Besides, extensions to include finite bath temperatures, by duplicating the number of effective chains are reported [284].

---

[19] The procedure described above is general and might be similarly applied for fermionic systems.

Multi-environment Hamiltonian, star and tree tensor network states

One reason for the efficiency of TN-based algorithms is inherited from the fact that MPS and the Hamiltonian $\hat{H}_{\mathcal{S}+\mathcal{E}}$ share the same 1D structure. Nevertheless, the problem to solve will often consist of a 'small' system coupled to many environments. It is therefore desirable, after an adequate representation of $\hat{H}_{\mathcal{S}+\mathcal{E}}$, to employ a wavefunction representation that mimics it.

In the following we show how the problem of an organic micro-cavity (Equation 2.20a) can be reformulated into a quasi-one dimensional problem in the same spirit as above. This includes a collection of N identical molecules, containing a single exciton with frequency ω_e and ladder operators $\hat{\sigma}_{\pm}^{(i)}$ $(i = (1, \cdots, N))$, placed within the volume of a resonant EM mode (frequency ω_O), and annihilation operator $\hat{a}$. The total Hamiltonian contains three different parts, as schematically depicted in Figure 2.4a. First, the bare system $\mathcal{S}$ accounts for the excitons within the molecules, the cavity EM mode, and their coupling measured by the collective Rabi frequency Ω_R and treated within the RWA,

$$\hat{H}_{\mathcal{S}} = \omega_O \hat{a}^\dagger \hat{a} + \sum_{i=1}^{N} \omega_e \hat{\sigma}_+^{(i)} \hat{\sigma}_-^{(i)} + \frac{\Omega_R}{2\sqrt{N}} \sum_{i=1}^{N} (\hat{a}^\dagger \hat{\sigma}_-^{(i)} + \hat{\sigma}_+^{(i)} \hat{a}). \tag{2.47}$$

In the single-excitation subspace ($\dim \mathcal{H}_{\mathcal{S}} = N + 1$), $\hat{H}_{\mathcal{S}}$ is exactly solvable, as shown in section 2.1. The second part of the Hamiltonian describes the vibrational subspace $\mathcal{E}_v^{(i)}$ containing M_v vibrational modes for each molecule, and their elastic coupling to the excitons. The k^{th} vibrational mode is approximated by a harmonic oscillator of frequency ω_k (valid close to the equilibrium position) with annihilation operator $\hat{b}_k^{(i)}$ and exciton-phonon coupling strength $\lambda_k^{(i)}$,

$$\hat{H}_v = \sum_{i=1}^{N} \sum_{k=1}^{M_v} \omega_k \hat{b}_k^{\dagger(i)} \hat{b}_k^{(i)} + \sum_{i=1}^{N} \sum_{k=1}^{M_v} \lambda_k^{(i)} (\hat{b}_k^{(i)} + \hat{b}_k^{\dagger(i)}) \hat{\sigma}_+^{(i)} \hat{\sigma}_-^{(i)}. \tag{2.48}$$

The weak-coupling assumptions generally assumed in the OQS in subsection 2.2.1 are not expected to hold and so the exact solution must be pursued. In particular, for typical molecules, a large number of vibrational modes, $M_v \sim 10^2$, makes direct diagonalisation of the total Hamiltonian unfeasible, even for $N = 1$. This enforces the use of the following TN-based approach. Finally, the third part of the Hamiltonian describes radiative far-field photon modes $\hat{f}_l$ and their coupling to the cavity EM mode (RWA),

$$\hat{H}_r = \sum_{l} \omega_l \hat{f}_l^\dagger \hat{f}_l + \upsilon_l (\hat{a}^\dagger \hat{f}_l + \hat{f}_l^\dagger \hat{a}). \tag{2.49}$$

In a way similar to vibrational modes, we introduce here the spectral density for the photonic subspace, $\mathcal{E}_r$, as $J_r(\omega) = \pi \sum_l \upsilon_l^2 \delta(\omega - \omega_l) = \kappa\omega^3/(2\omega_O^3)$. This term accounts

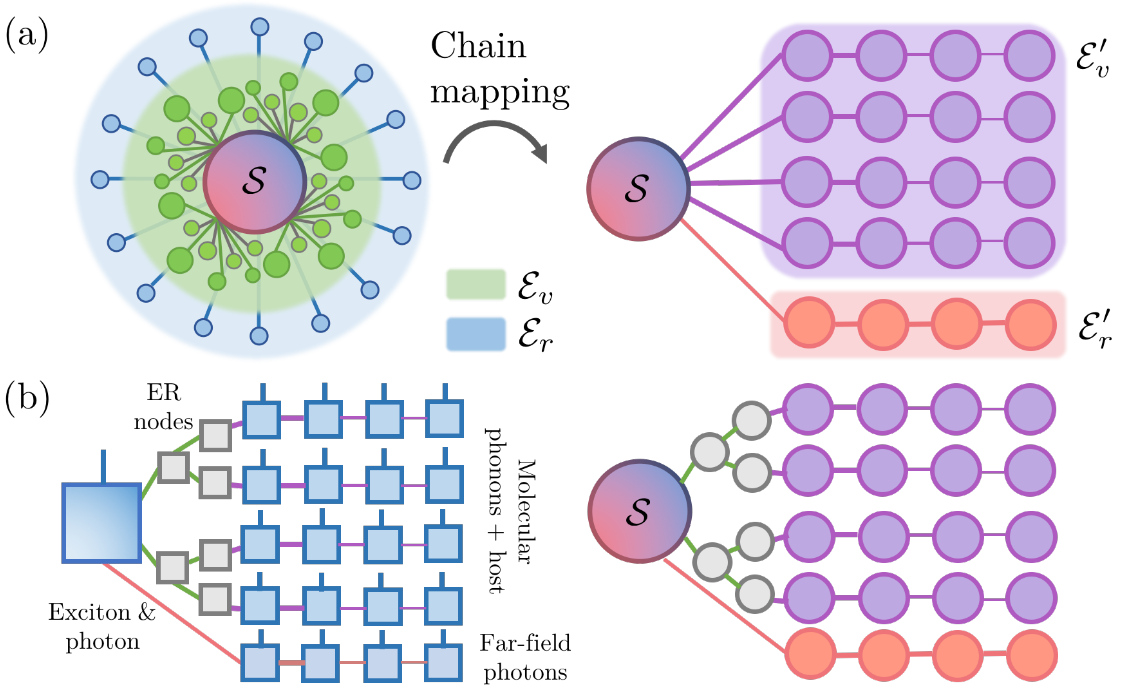

Figure 2.4: (a) Chain mapping of the multi-environment Hamiltonian in text to a star-structure that includes excitonic and photonic degrees of freedom in the root operator. (b) Efficient representation as a TN by further SVDs of the root node in the star-TN to form a tree-like structure introducing auxiliary non-physical sites (left) and corresponding coupling structure in the Hamiltonian.

for free-space decay of the bare cavity EM mode with rate $\kappa = 2J_r(\omega_O)$ in the Markovian limit of subsection 2.2.1. The system above is precisely equivalent to system-environment Hamiltonian discussed in this section, by relabelling $\hat{H}_v + \hat{H}_r \rightarrow \hat{H}_{\mathcal{E}} + \hat{H}_{\mathcal{I}}$ and $\hat{A} \in \{\hat{\sigma}_+^{(i)}\hat{\sigma}_-^{(i)}, \hat{a} + \hat{a}^\dagger\}$.

By applying the same chain-mapping idea for a single environment to this general case, we obtain the *star* Hamiltonian shown in Figure 2.4a. A TN that mimics this structure constitutes a pathway to simulate the system efficiently. This is indeed the approach followed to study the *full* LP of the system chapter 6, where a *star-TN* encompasses the photon/exciton degrees of freedom of the global wavefunction in the root node, while the chains account for the environment oscillators. Nevertheless, for large molecule ensembles, a severe memory bottleneck occurs if the system $\mathcal{S}$ is stored in a single root tensor leading to exponential scaling with N, $\mathcal{O}(D^{N+1})$. To restore the efficiency of the numerical method while maintaining precision, we decompose the system into a *tree tensor network state*, determined by entanglement analysis [285, 286], where each final branch represents an exciton or the cavity photon and is coupled to a single chain (see

Figure 2.4b). This introduces an additional set of auxiliary tensors with no physical indexes denoted as *entanglement renormalisation tensors* [287], determined (optimised) during runtime in a similar fashion to OBB matrices mentioned before. These enable to harness entanglement between physical nodes, by mixing bond states that reproduce a minimal effective basis set, thus reducing the required bond dimensions.

In this model, we have assumed that permutation symmetry in the molecular index i holds (no disorder in the on-site energies or interactions). Therefore every leg in the root node should account for the *same* bond states between $\mathcal{S}$ and different environments/chains. Motivated by this we infer that a very efficient TN is given by a structure with no privileged distribution of the tensors regarding different molecular environments. This is precisely a *perfect binary tree*. To show this structure is indeed optimal, we ran a star-TN simulation and therefore calculate the *relative entropy compression* of SVDs over bond legs. This enables to find pairings of subsystems that yield a network with lower entropy, which is highly non-trivial for environments with different interaction strengths, as detailed in [288].

Once the global Hamiltonian $\hat{H}_{\mathcal{S}+\mathcal{E}}$ is transformed into the quasi-one-dimensional topology, TN algorithms can be implemented based on MPS approaches. This extension, which we employ in this thesis, has been built upon the numerical approach primarily implemented by Florian Schröder (github repository) and Chen Guo (github repository). To close this section, we outline two key algorithms based on TN, first for a single chain, and finally outlining the multi-chain scheme.

Variational Matrix Product States: finding ground states

In the following, we outline the basics of ground state minimisation, achieved via the so-called Density Matrix Renormalisation Group (DMRG), introduced in 1992 [289]. We sketch here only the basics of the approach, referring the reader to a complete review on the subject [171]. DMRG is understood nowadays as the approach resulting from an application of the variational principle

$$\omega_G = \min_{|\psi_G\rangle} \frac{\langle\psi_G|\hat{H}_{\mathcal{S}+\mathcal{E}}|\psi_G\rangle}{\langle\psi_G|\psi_G\rangle}, \tag{2.50}$$

to MPS, hence assuming $|\psi_G\rangle \in \mathcal{M}_{\mathrm{TN}}$. Thus, we will employ the name Variational matrix product states (VMPS) when referring to this method, indistinctly. A numerical routine starting from a guess state (typically a random MPS), can permit the decomposition of the problem into a sequence of linear problems. One possibility to enable this is representing $\hat{H}_{\mathcal{S}+\mathcal{E}}$ as the operator-analogue of a MPS, known as matrix product operator.

Here we discuss an alternative, based on the so-called gauge invariance of the MPS, i.e. the fact that the physical state $\bar{\psi}$ is unchanged by the transformation for a given site $\mathbf{A}_l^{n_k} \mapsto \mathbf{G}_{l-1}^{-1}\mathbf{A}_l^{n_k}\mathbf{G}_l$. This gauge freedom enables to impose certain canonical formats that are convenient for the practical implementation. In particular, by applying SVDs (or less 'expensive' orthogonal decompositions such as QR), it is possible to bring the state into the *mixed canonical form* displayed in Figure 2.5a, where all matrices at the left of site l, $\mathbf{L}^{n_k}$ are normalised such that $\sum_{n_k} \mathbf{L}^{n_k\dagger}\mathbf{L}^{n_k} = \mathbf{1}$ $(k < l)$ (left-orthonormal), whereas matrices at the right $\mathbf{R}^{n_k}$ fulfil $\sum_{n_k} \mathbf{R}^{n_k}\mathbf{R}^{n_k\dagger} = \mathbf{1}$ $\boldsymbol{(}k > l\boldsymbol{)}$ $\boldsymbol{(}$they are right-orthonormal). This brings the state into a 'focused' form where the tensor at site l is denoted as $\mathbf{A}_l^C$. Defining a one-site effective Hamiltonian $\mathbf{H}_l$ as the tensor network in Figure 2.5b, the minimisation problem can be solved by the following steps:

- $\mathbf{H}_l$ is applied to the tensor $\mathbf{A}_l^C$ and the standard eigenvalue problem is solved, which can be formulated as a matrix-vector eigenvalue problem by reshaping tensors. $\mathbf{A}_l^C$ is updated as the lowest eigenvector of $\mathbf{H}_l$.

- An orthogonal factorisation (e.g. QR decomposition) is performed into $\mathbf{A}_l^C$ to shift the focused site (multiplying the left or right matrices of the factorisation) to the left or right so that the next tensor can be optimised.

- Reaching the end of the chain (a 'sweep'), one can then sweep back, so that every orthogonalisation step is immediately followed by an optimisation step.

In this algorithm, the maximum bond dimensions set by the original MPS ansatz determine the entanglement content allowed for the 'target' ground state[20].

The DMRG works exceptionally well targeting ground states in the 1D system, since the variational principle Equation 2.50 is reduced to a single optimisation step. Based on sequential 1D DRMG [171] sweeps along the chain, it is possible to devise a straightforward extension to the star-TN, sketched in Figure 2.5c. Finally, to ensure convergence of the DMRG for a finite chain-length (M_v can be formally infinite if the continuum approximation of the spectral density is used), it must be noted that for gap-less finite-bandwidth $J_v(\omega)$ the chain becomes asymptotically homogeneous for $L \gg 1$, saturating to $\omega_{l\gg1} \rightarrow \omega_c/2$ and $t_{l\gg1} \rightarrow \omega_c/4$, and giving rise to a cosine energy dispersion band $\sim \omega_c(1-\cos\pi q)$ [290].

---

[20] The OBB matrices depicted in Figure 2.3 must be similarly optimised for each site, employing the Hamiltonians $\hat{H}_V$ in Figure 2.5b

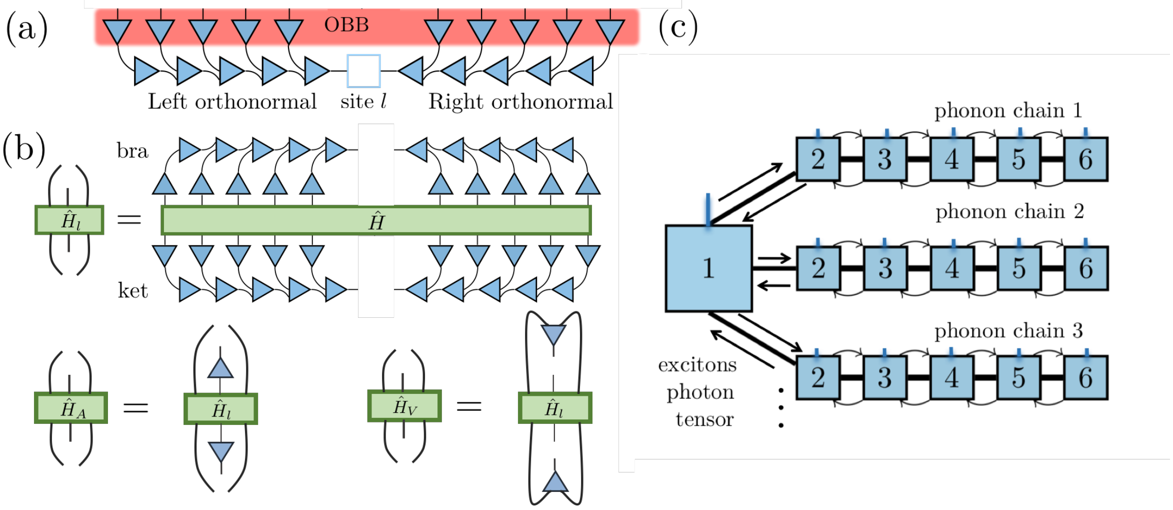

Figure 2.5: (a) Mixed canonical representation of a one-dimensional MPS, focused on site l, where the triangle orientation indicate the normalisation conditions, with the notation employed in [194, 195] and (b) effective one-site Hamiltonians that are instrumental to perform efficiently the variational optimisation of the all different types of tensors in the TN.(c) Sketch of the DRMG sweep procedure for the star-TN TN for the case $N = 3, M_v = 5$ that is used to represent the variational wavefunction in Equation 2.50.

Variational Matrix Product States: time evolution

TN-based methods can handle the problem of time evolution as well. The intricate details about how this is done are in [195]. Time evolution is implemented by the solution of the Schrödinger equation $i\partial_t|\psi_{\mathcal{S}+\mathcal{E}}(t)\rangle = \hat{H}_{\mathcal{S}+\mathcal{E}}|\psi_{\mathcal{S}+\mathcal{E}}(t)\rangle$. For a state at $t = 0$ represented as a TN, the time evolution will generally leave the manifold $\mathcal{M}_{\text{TN}}$, signifying the breakdown of the approach. The solution to this problem found in [194] consists of applying an orthogonal projection of the evolution vector onto the tangent space of the MPS manifold at the current state. After a very involved derivation, the result is the so-called Time-Dependent Variational Matrix Product States (TDVMPS) algorithm. A major insight into the practical implementation was given by Haegeman et al. in [291] where it was proved that time-evolution could be implemented by generalising the DMRG procedure outlined above[21]. A technical difference compared to the ground state optimisation is that TDVMPS equations can be shown to have an additional contribution standing

---

[21] Indeed, the DMRG itself emerges as the solution of the imaginary time evolution implemented through the variational principle, as shown for instance in [291].

for the evolution of zero-site centres $\mathbf{C}_l$, where all sites left at left including l are left-orthonormal and the sites are right are right orthonormal. An effective Hamiltonian $\mathbf{K}_l$ for these tensors can be defined (see [195]), and the algorithm, starting from a MPS in mixed-canonical form, proceeds in the following way:

- The time evolution operator by a timestep Δt is applied to the focused site, employing the effective Hamiltonian outlined above: $\mathbf{A}_l^C(t+\Delta t/2) = e^{-i\mathbf{H}_l \Delta t/2}\mathbf{A}_l^C(t)$.
- $\mathbf{A}_l^C(t+\Delta t/2)$ is written via orthogonal decomposition as $\mathbf{L}_l\mathbf{C}_l$.
- Due to the different complex phase of this term in the TDVMPS equations, evolution must be carried out backwards in time for zero-site matrices $\mathbf{C}_l(t+\Delta t/2) = e^{i\mathbf{K}_l\Delta t/2}\mathbf{C}_l(t)$. The time evolved tensor $\mathbf{C}_l$ is reabsorbed in the next site, such that $\mathbf{A}_{l+1}^C = \mathbf{C}_l\mathbf{R}_{l+1}$.
- Steps are repeated until the end of the chain is reached (completed a right sweep). A single left-to-right sweep evolves the MPS $t \mapsto t+\Delta t/2$.Then a right-to-left sweep occurs similarly, evolving the tensors with a quantity of $\Delta t/2$[22].

In the tree TN, different components appear, namely, entanglement renormalisation tensors, physical 'MPS-like' tensors and OBB matrices. This structure can be identified as parent nodes having multiple chain tensors. Since the quasi-1D structure of the tree ensures correct tree-TN state normalisation, we can use the insights from the previous update scheme to generalise it to nodes with more than one child. In practice, optimisation is carried out recursively to all children of a given node. The tree sweeps occur such that each tensor is updated twice by a factor $\Delta t/2$, yielding an algorithm with an error $\mathcal{O}(\Delta t^3)$ (see [288] for more details).

2.3. Summary of methods applied in this thesis

Reduced master equations and TN-based algorithms are applied to yield most of the results in following chapters. The next final section is devoted to briefly establish the link between models and methods described throughout the chapter and the results compiled in the following chapters of this thesis. The first part is devoted to studying the VSC regime in organic IR micro-cavities. Therefore, the fundamental pillar of the theory is

---

[22] Similiarly to the DMRG, OBB matrices must be appropriately time-evolved in the boson sites.

the Hamiltonian for an ensemble of molecular vibrations coupled to an IR micro-cavity mode described in Equation 2.20b, and repeated here for the sake of completeness:

$$\hat{H}_{\mathrm{VSC}} = \omega_{\mathrm{EM}} \hat{a}^{\dagger}\hat{a} + \sum_{i=1}^{N} \left[\omega_v^{(i)} \hat{b}^{(i)\dagger}\hat{b}^{(i)} + g_i(\hat{a}^{\dagger}\hat{b}^{(i)} + \hat{b}^{(i)\dagger}\hat{a})\right]. \tag{2.51}$$

On the one hand, in chapter 3 we consider the linear response to IR fields, where this Hamiltonian must be supplemented by a weak infrared coherent driving term modelled by $\hat{H}_d \sim \hat{a}e^{i\omega_d t} + \mathrm{H.c.}$. On the other, effects resulting from off-resonant interaction with optical fields, such as the Raman effect analysed in chapter 4 can be included by adding the excited electronic PES, similarly to Equation 2.20a, as

$$\hat{H}_{\mathrm{R}} = \hat{H}_{\mathrm{VSC}} + \sum_{i=1}^{N} \hat{\sigma}_+^{(i)}\hat{\sigma}_-^{(i)}[\omega_e^{(i)} + \lambda^{(i)}(\hat{b}^{(i)} + \hat{b}^{(i)\dagger})], \tag{2.52}$$

and correspondingly an coherent optical driving of the form $\hat{H}_d \sim \hat{\sigma}_-^{(i)} e^{i\omega_d t} + \mathrm{H.c.}$. In this analysis, we consider the additional effect of the counter-rotating terms (see Equation 2.19) in the Raman cross section, by adding $\hat{H}_{\mathrm{R}} \mapsto \hat{H}_{\mathrm{R}} + \sum_{i=1}^{N} g_i(\hat{a}^{\dagger}\hat{b}^{(i)\dagger} + \hat{b}^{(i)}\hat{a})$. To describe the incoherent dynamics in these systems, and in particular, the role played by the vibrational dephasing in strong light-matter coupling, we will generally use the BRW (Markovian) formalism in the secular approximation. Since we will typically restrict our calculations to the single excitation subspace, Equation 2.38 is our starting point,

$$\partial_t \tilde{\rho}_{\mathcal{S}} = \sum_{i,j=1}^{N} \sum_{p,q,r,s} S_{ij}(\omega_{sr}) u_p^{(i)} u_q^{(i)} u_r^{(j)} u_s^{(j)} \left\{ e^{i(\omega_{pq}-\omega_{sr})t} \left[\hat{\sigma}_{rs}\tilde{\rho}_{\mathcal{S}}(t), \hat{\sigma}_{pq}\right] + \mathrm{H.c.} \right\}, \tag{2.53}$$

with the bath noise-power spectrum Equation 2.39. The secular approximation will involve the exhaustive comparison of different terms frequencies, as detailed in chapter 3.

Moreover in the particular case of chapter 5, we devote our effort to characterise a device similar to a Raman laser which exploits vibro-polaritons. Laser operation as takes place in the semiclassical limit of many excitations in the system, and therefore the quantum treatment is replaced by mean field theory where losses are mostly introduced in a phenomenological way through the Lindblad equation shown in Equation 2.32, namely

$$\partial_t \hat{\rho}_{\mathcal{S}} = -i[\hat{\rho}_{\mathcal{S}}, \hat{H}_{\mathcal{S}}] + \sum_k \gamma_k \mathcal{L}_{\hat{A}_k}[\hat{\rho}_{\mathcal{S}}], \qquad \mathcal{L}_{\hat{X}}[\cdot] = \hat{X}\cdot\hat{X}^{\dagger} - \frac{1}{2}\{\hat{X}^{\dagger}\hat{X}, \cdot\}. \tag{2.54}$$

The second part of this thesis compiles our work for organic molecules in the ESC regime. The basic ingredient, in this case, is the Hamiltonian for molecules coupled to optical micro-cavity modes Equation 2.20a, which reads

$$\hat{H}_{\mathrm{ESC}} \simeq \omega_{\mathrm{EM}}\hat{a}^{\dagger}\hat{a} + \sum_{i=1}^{N} \hat{\sigma}_+^{(i)}\hat{\sigma}_-^{(i)}[\omega_e^{(i)} + \boldsymbol{\lambda}_i(\hat{\mathbf{b}}^{(i)} + \hat{\mathbf{b}}^{(i)\dagger})] + \boldsymbol{\omega}_v^{(i)}\hat{\mathbf{b}}^{(i)\dagger}\hat{\mathbf{b}}^{(i)} + g_i(\hat{a}^{\dagger}\hat{\sigma}_-^{(i)} + \hat{\sigma}_+^{(i)}\hat{a}). \tag{2.55}$$

Due to the intrinsic difficulties related to the non-perturbative nature of this problem, here we will treat the previous Hamiltonian in a quasi-exact manner, using the TN formalism detailed in subsection 2.2.2. In particular, in chapter 6 our aim is to study the exact LP of the system, which will involve the variational minimisation of the previous Hamiltonian (see Equation 2.50),

$$\omega_G = \min_{|\psi_G\rangle \in \mathcal{M}_{\mathrm{TN}}} \frac{\langle \psi_G | \hat{H}_{\mathrm{ESC}} | \psi_G \rangle}{\langle \psi_G | \psi_G \rangle}. \tag{2.56}$$

This is carried out using the DMRG/VMPS algorithm described in subsection 2.2.2. Finally, in the last chapter of results of the thesis, chapter 7, we will use the same model to describe the temporal dynamics of the polaritons supported by an organic microcavity. Since in typical experiments the lifetime of these states is critically determined by photonic losses, we will include the far-field modes explicitly, as described indeed in subsection 2.2.2, and treat the whole system quasi-exactly. To this end, we will employ the TDVMPS numerical algorithm.

Part I | Vibrational Strong Coupling

The following block of this thesis denoted as part I, is devoted to addressing several problems in the field of strong coupling of molecular bond vibrations with infrared modes. In the first place, we develop in chapter 3 a quantum mechanical formalism to treat the phenomenon of vibro-polariton formation and time evolution, arising in the strong coupling between an EM mode and vibrational excitations of an ensemble of organic molecules. Our model enables to relate the experimental outcomes of the linear absorption spectrum of the system with the microscopic vibrational dynamics. By employing a BRW approach, we show that the influence of dephasing-type interactions, i.e., elastic collisions with a background bath of phonons, depends critically on the nature of the bath modes. In particular, for long-range phonons corresponding to a common bath, the dynamics of the 'bright state' (the collective superposition of molecular vibrations coupling to the cavity mode) is effectively decoupled from other system eigenstates. For the case of independent baths (or short-range phonons), incoherent energy transfer occurs between the bright state and the uncoupled dark states. However, these processes are suppressed when the Rabi splitting is larger than the frequency range of the bath modes, as achieved in the experiment [140].

The fundamental study on the nature of vibro-polaritons serves as a motivation to analyse changes in other spectroscopic measurements caused by strong coupling. In particular, we investigate in chapter 4 how the emergence of VSC affects Raman scattering. This work is motivated by a recent experiment [212], which reported enhancements of up to three orders of magnitude in the Raman signal. By using different models within linear response theory, which extends the previous formalisms, we show that the total Raman cross section is maintained constant when the system evolves from the weak-coupling limit to the strong-coupling regime. A redistribution of the Raman signal between the two polaritons is the crucial fingerprint of VSC in the Raman spectrum, demonstrating that the final states of the scattering acquire a photonic component. Our next step in chapter 5 consists on exploiting this as a tool to widen the capabilities of Raman laser devices and even turn them into a more 'productive' device known as optical parametric oscillator with visible and mid-IR outputs. In this case, we study the stimulated Raman scattering for vibro-polaritons, exploring the conditions under which the threshold for the 'original' laser without VSC diminishes and this device can be transformed. Finally, we show how the dramatic reduction of the many final molecular states into two collective excitations can be used to create an all-optical switch with output in the mid-IR.

3 | Vibro-polariton Formation and Time Evolution

3.1. Motivation

In this chapter, we present a fully quantum theory of the phenomenon of collective strong coupling of molecular vibrations with a cavity mode. In contrast to standard transfer matrix calculations, which can be used to fit the experimental spectra [140, 196] but only provide very limited information about the incoherent dynamics in the system, our approach naturally incorporates the relevant incoherent processes, in particular, those induced by dephasing-type interactions. We describe the system using a quantum-mechanical model of a single photon mode coupled to an ensemble of harmonic oscillators representing molecular vibrations (the C=O bond stretching mode of polyvinyl acetate at an energy of 215 meV in the experiment [140]). To incorporate the coupling of the molecular vibrations to low-frequency rovibrational modes, we assume, in the way sketched in section 2.2 that the oscillators are connected to either a *common* or *independent* phononic baths (see Figure 3.1). We employ the BRW theory [207, 208] (see subsubsection 2.2.1) to obtain master equations describing the system dynamics under strong coupling. The final master equations only contain a few Lindblad terms, with rates determined by the product of *i)* the bath spectral density at the corresponding transition frequency and *ii)* algebraic prefactors obtained from transforming the system into its eigenstate basis. Using the specific properties of the system under study, we can evaluate all these prefactors *analytically*, and are thus able to directly read off the population transfer rates between the system eigenstates. This allows a detailed insight into the system dynamics and, specifically, the role of the dark states. Our results demonstrate that for large enough Rabi splitting, the bright state indeed behaves like a *single* isolated oscillator and the dark states play an almost negligible role. For the case of a

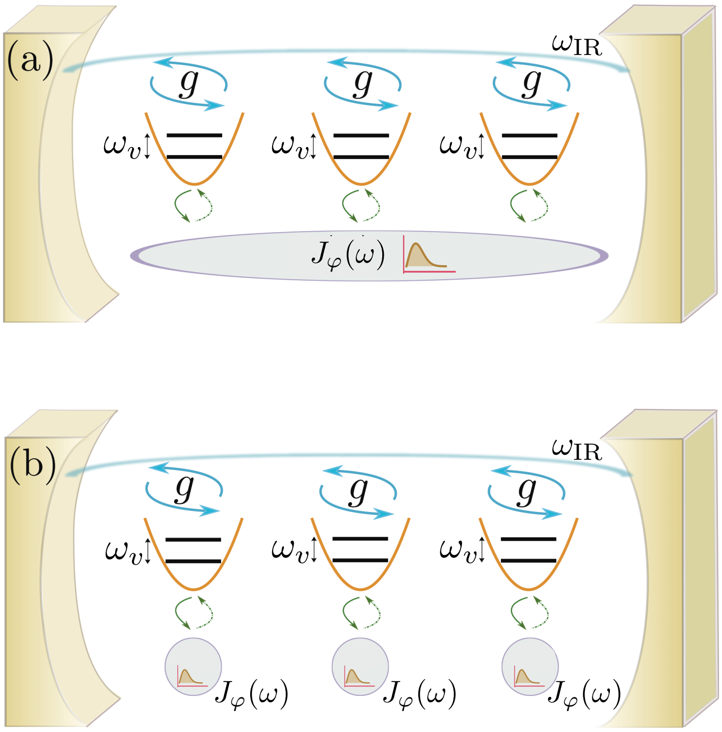

Figure 3.1: Sketch of the model system. An ensemble of N molecules interacts collectively with a cavity mode of frequency ω_{IR}. The cavity is tuned to a molecular vibrational mode. The remaining rovibrational modes are introduced by either connecting all molecules to a common bath (panel a) or by coupling each molecule with an independent bath (panel b). In both cases, the harmonic bath is characterised by a spectral density $J_\varphi(\omega)$.

common bath, corresponding to long-range bath phonons, this is even true regardless of the Rabi splitting.

This chapter is organised as follows: in section 3.2 we present the basic ingredients of the theory for an ensemble of molecules strongly coupled to a mid-IR micro-cavity mode, detailing which contributions need to be considered for vibrational dephasing in the secular approximation, and the resulting transitions induced between vibro-polaritons and dark states. Finally, we present in section 3.3 the steady-state absorption spectrum and time-resolved features (polariton dynamics) featured by two limiting cases (individual and collective) of dephasing-like couplings.

3.2. Theory for time-dynamics of vibro-polaritons

The basic aspects of linear response can be accounted for by simulating the cavity using classical transfer matrix simulations (see [140] for further details). In this case, a Drude

l	0	1	2	3	4	5
f_l [eV^2]	0.76	0.02	0.01	0.07	0.6	4.38
ω_l [eV]	9.03	0.41	0.83	2.96	4.3	13.32
γ_l [eV]	0.05	0.24	0.34	0.87	2.49	2.21

Table 3.1: Molecular parameters for the dielectric function employed in transfer matrix simulations.

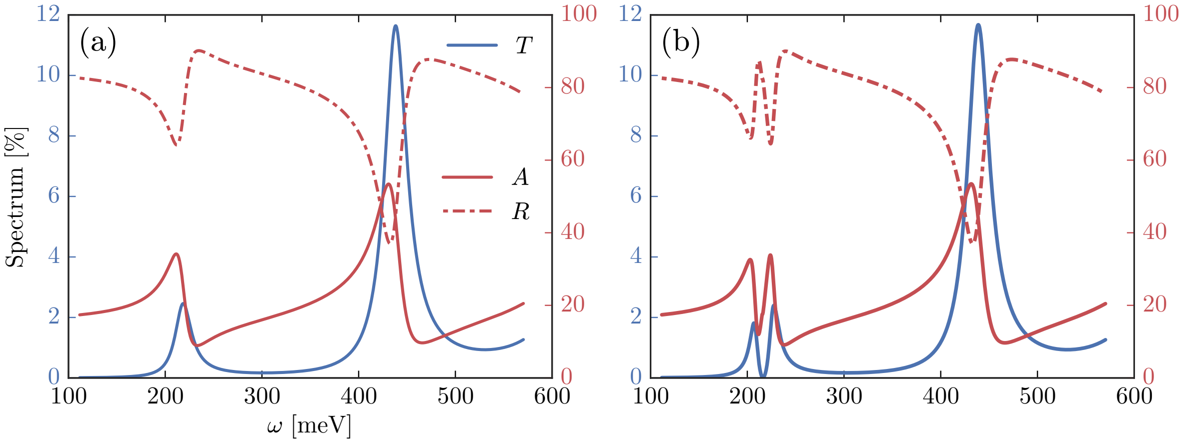

Figure 3.2: Transfer matrix transmission (T), reflectivity (R) and absorption (A) spectra for the (a) bare micro-cavity and (b) the resonator filled with PVAc molecules. Calculations are obtained via the open source library tmm in Python [292].

dielectric function is considered for the gold mirrors (modified to account for very thin reflectors of $\simeq 10$ nm) $\epsilon_{\mathrm{Au}}(\omega) = 1 - \frac{f_0\omega_0^2}{\omega^2 + i\gamma_0\omega} - \sum_{l=1}^{5} \frac{f_l\omega_l^2}{\omega^2 - \omega_l^2 + i\omega\gamma_l}$ with parameters in Table 3.1. In the case of PVAc (layer thickness of 2 μm), we use an explicit parametrisation given by $\epsilon_{\mathrm{PVAc}}(\omega) = \epsilon_B - \frac{f_j}{\omega^2 - k_j^2 + i\omega\Gamma_j}$ with $\epsilon_B = 1.41^2$, $f_j = 7.685 \cdot 10^{-4}\,\mathrm{eV}^2$, $k_j = 0.215$ eV, and $\gamma_j = 1.611$ meV. This parametrisation allows to turn off strong coupling by setting $f_j = 0$, and thus obtain the ‘empty’ cavity properties. As demonstrated in Figure 3.2, the inclusion of the molecular layer implies the splitting of the first cavity mode at $\omega_{\mathrm{IR}} = 215$ meV, into two collective modes, the upper and lower polaritons, with a Rabi splitting of about $\Omega_R = 20.7$ meV.

The transfer-matrix-method is nevertheless unable to address the microscopic details of the energy transfer processes taking place among eigenstates, and in particular, does not permit a distinction between different dissipative or decoherence mechanisms. This is the motivation to explore the microscopic quantum model in the following.

3.2.1. General aspects

Within the RWA, i.e., neglecting processes that create or destroy two excitations, the coherent dynamics of the system is then governed by the Hamiltonian in Equation 2.20b:

$$\hat{H}_{\mathcal{S}} = \omega_{\mathrm{IR}}\hat{a}_c^\dagger\hat{a}_c + \sum_{i=1}^{N}\omega_v^{(i)}\hat{b}^{(i)\dagger}\hat{b}^{(i)} + \sum_{i=1}^{N} g_i(\hat{a}_c\hat{b}^{(i)\dagger} + \hat{a}_c^\dagger\hat{b}^{(i)})\,, \tag{3.1}$$

where $\hat{a}_c$ is the annihilation operator for the cavity mode with frequency ω_{IR}, and $\hat{b}^{(i)}$ is the annihilation operator of the optically active vibrational mode of molecule i, characterised by its frequency $\omega_v^{(i)}$ and its position $\mathbf{r}_i$. The cavity-oscillator interaction is given by g_i, which depends on the cavity electric field strength and the change of the molecular dipole moment under displacement from the equilibrium position (see subsubsection for further details). For simplicity, in this chapter we assume a regular configuration in which all the molecules are identical ($\omega_v^{(i)} = \omega_v$, $g_i = g$), as well as zero detuning ($\omega_{\mathrm{IR}} = \omega_v$). We have explicitly checked that orientational disorder ($g_i \neq g_j$) and inhomogenous broadening ($\omega_v^{(i)} \neq \omega_v^{(j)}$), leading to Gaussian broadening of vibrational spectroscopic signatures, do not significantly affect the results presented below.

Since we will focus on the linear response regime, it is sufficient to include the singly excited vibrational states, as described in subsection 2.1.2[1]. Namely, this is constituted by upper and lower vibro-polaritons $|\pm\rangle$, and the $N-1$ dark states $|d\rangle \in \mathcal{D}$. Regarding loss mechanisms, we can distinguish three types: cavity losses (rate κ), non-radiative internal losses within the molecules (rate γ_{nr}), and dephasing-type interactions. Spontaneous radiative decay in the infrared region is very slow (on the scale of milliseconds) due to the low transition frequencies and can be safely neglected[2].

We now turn to the description of the incoherent dynamics induced by the different loss mechanisms. Whereas cavity losses and nonradiative internal molecular decay can be seen as pure decay channels and included as constant Lindblad terms when analysing the

---

[1] The inclusion of vibrational overtones is straightforward, given the bosonic character of the system Hamiltonian. This leaves most of the derivation presented in the following unchanged but introduces additional prefactors depending on the excitation numbers in the incoherent rates derived below. However, it must be noted that the harmonic approximation gets successively worse the higher excited the molecules become. For simplicity, we thus allow at most one excitation.

[2] Note that there is no Purcell enhancement of the spontaneous emission, as the effect of the cavity mode is already accounted for by including it as a bosonic degree of freedom in the system Hamiltonian, see, e.g., [293, 294]. The remainder of the photonic spectral density in the cavity is flat and actually suppressed below the vacuum value.

system dynamics, dephasing-type interactions must be treated in a more detailed fashion, as we detail below. In the case analysed in this chapter, these interactions are due to elastic scattering of low-frequency rovibrational bath modes with the main vibrational modes involved in strong coupling, described by the interaction Hamiltonian

$$\hat{H}_{\varphi} = \sum_{i=1}^{N} \hat{b}^{(i)\dagger}\hat{b}^{(i)} \sum_{k} \lambda_k^{(i)} (\hat{c}_k^{(i)} + \hat{c}_k^{(i)\dagger}) \,. \tag{3.2}$$

The spatial extension or localisation of the bath modes determines the character of the coupling. In the following, we focus on two limiting scenarios. In the first case, all the vibrational modes are coupled to the same *common* bath (see Figure 3.1a), characterised by delocalised phonons $\hat{c}_k^{(i)} = \hat{c}_k$ with bath Hamiltonian $\hat{H}_b^{\mathrm{com}} = \sum_k \omega_k \hat{c}_k^\dagger \hat{c}_k$. In the second case, each molecular vibrational mode is coupled to an *independent* bath characterised by on-site phonons $\hat{c}_k^{(i)}$, with bath Hamiltonian $\hat{H}_b^{\mathrm{ind}} = \sum_{ik} \omega_k^{(i)} \hat{c}_k^{(i)\dagger} \hat{c}_k^{(i)}$. In both scenarios, we assume that all molecules are identical ($\lambda_k^{(i)} = \lambda_k$ and $\omega_k^{(i)} = \omega_k$).

The frequently used approach of treating dephasing through a frequency-independent Lindblad superoperator acting only on the vibrational modes is not valid in our case as, within the strong coupling regime, the molecule-cavity coupling (frequency Ω_R) is much faster than the correlation time of the phononic environment. Instead, the influence of the background modes has to be taken into account in the *dressed* basis obtained after diagonalising the strong-coupling interaction. The bath is completely characterised by the spectral density $J_\varphi^{(i)}(\omega) = \pi \sum_k \lambda_k^{(i)2} \delta(\omega - \omega_{ik})$ (with $J_\varphi^{(i)}(\omega) = J_\varphi(\omega)$ in our case). The spectral density in organic materials depends strongly on the molecules and the environment where they are placed. In order to obtain general conclusions, we thus use a standard parametrisation of low-frequency vibrational modes, an Ohmic environment with a quadratic cutoff frequency ω_c.

$$J_\varphi(\omega) = \upsilon \omega e^{-(\omega/\omega_c)^2} , \tag{3.3}$$

where υ is a dimensionless constant that determines the system-bath coupling strength[3]. If the system-bath coupling is sufficiently weak, BRW theory [207, 208], detailed in subsection 2.2.1, can be safely applied to derive a master equation for the system dynamics [187, 258]. This approach relies on the first and second *Born approximation*, which calculate the effect of the system-bath coupling up to second-order perturbation theory and assume that the bath state remains unmodified, i.e., the bath density matrix $\hat{\rho}_{\mathcal{E}}$ is

---

[3] The cutoff frequency will be set to model the experiment [140] in section 3.3, in which energy scales for low-frequency modes (e.g. lattice vibrations in the polymer lattice itself, which lie in the range of few meV), are well separated from molecular vibrations (in the order of hundreds of meV).

time-independent (and thermally populated in the following), where $\hat{\rho}_{\mathcal{S}+\mathcal{E}}(t) \simeq \hat{\rho}_{\mathcal{S}}(t) \otimes \hat{\rho}_{\mathcal{E}}$ (In the following the $\mathcal{S}$ index in the reduced density matrix is omitted for notational simplicity.). Additionally, since the decay of the bath correlations $\sim 1/\omega_c$ occurs on a much shorter timescale than the dynamics caused by the interaction with the bath, the *Markov approximation* is used, disregarding all memory effects of the system-bath interaction[4]. In the interaction picture the system density operator $\tilde{\rho}$ will evolve according to Equation 2.25 with $\hat{H}_{\mathcal{I}} = \hat{H}_{\varphi}$. The bath-dependent part of the system-bath coupling is fully encoded in the bath *correlation functions* between the modes on molecular sites i and j, $\phi_{i,j}(\tau)$, as given in Equation 2.28. It is independent of both i and j for a common bath, $\phi_{i,j}^{\text{com}}(\tau) = \phi(\tau)$, while for independent baths, the off-diagonal terms vanish, $\phi_{i,j}^{\text{ind}}(\tau) = \delta_{i,j}\phi(\tau)$, where $\phi(\tau)$ is given by Equation 2.29.

The common approach of using frequency-independent Lindblad terms to describe dephasing is equivalent to neglecting the strong coupling in the incoherent dynamics, i.e., to use only the uncoupled system Hamiltonian $\omega_{\text{IR}}\hat{a}_c^\dagger\hat{a}_c + \omega_v \sum_i \hat{b}^{(i)\dagger}\hat{b}^{(i)}$ in the interaction picture on the right-hand side of Equation 2.25. When the molecule-cavity coupling is comparable to or faster than the decay of bath correlations ($\Omega_R \gtrsim \omega_c$), this is an invalid approximation, and it is crucial to include the full system Hamiltonian when deriving the master equation to satisfy detailed balance [263].

By expressing the system part of $\hat{H}_{\varphi}$ ($\propto \hat{b}^{(i)\dagger}\hat{b}^{(i)}$) in terms of the dressed eigenbasis and neglecting bath-induced energy (Lamb) shifts (see subsection 2.2.1 for more details), we obtain Equation 2.38

$$\partial_t \hat{\tilde{\rho}} = \sum_{i,j=1}^{N} \sum_{p,q,r,s} S_{ij}(\omega_{sr}) u_p^{(i)} u_q^{(i)} u_r^{(j)} u_s^{(j)} \left\{ e^{i(\omega_{pq}-\omega_{sr})t} \left[\hat{\sigma}_{rs}\hat{\tilde{\rho}}(t), \hat{\sigma}_{pq} \right] + \text{H.c.} \right\}, \tag{3.4}$$

where $\hat{\sigma}_{ab} = |a\rangle\langle b|$, $\hat{H}_{\mathcal{S}}|a\rangle = \omega_a |a\rangle$, $\omega_{ab} = \omega_a - \omega_b$, and the sums over p, q, r and s include all system eigenstates. Furthermore, $u_a^{(i)} = \langle a| \hat{b}^{(i)\dagger} |0\rangle$ give the overlaps between system eigenstates and vibrational mode excitations and can be chosen real. The bath noise-power spectrum is given by

$$S(\omega) = \begin{cases} J_\varphi(\omega)[n(\omega)+1] & \omega \geq 0 \\ J_\varphi(-\omega)n(-\omega) & \omega < 0 \end{cases} \tag{3.5}$$

---

[4] The decay of the bath correlation function $\phi(t)$ is generally influenced from the thermal occupation factor in Equation 2.29 at high temperatures, where $\coth(\beta\omega/2) \simeq 2/(\beta\omega)$. However, since J_φ decays to zero exponentially, the extra $1/\omega$ frequency dependence has little effect on the width of the function, and therefore, on the correlation time. In the opposite low-temperature limit, the thermal factor becomes very peaked around $\omega = 0$ with no effect in the width of ϕ in frequency space.

ω_{sr}	$\{pq, rs\}$	Label for γ_{rs}
Ω_R	$\{+-, -+\}$	γ_e
$-\Omega_R$	$\{-+, +-\}$	γ_a
$\dfrac{\Omega_R}{2}$	$\{+d, d'+\}, \{d-, -d'\}$ $\{+d, -d'\}, \{d-, d'+\}$	Γ_e
$-\dfrac{\Omega_R}{2}$	$\{-d, d'-\}, \{d+, +d'\}$ $\{-d, +d'\}, \{d+, d'-\}$	Γ_a
0	$\{++, ++\}, \{--, --\}$ $\{dd', d''d'''\}, \{\pm\pm, \mp\mp\}$ $\{\pm\pm, dd'\}, \{dd', \pm\pm\}$	γ_φ

Table 3.2: Secular terms in the master equation and the labels for the associated 'bare' rates $\gamma_{rs} = 2S(\omega_{sr})$. The dark states are labeled with $d \in 1, 2, ..., N-1$.

For a common bath, $S_{ij}^{\text{com}}(\omega) = S(\omega)$, while for independent baths, $S_{ij}^{\text{ind}}(\omega) = \delta_{i,j} S(\omega)$. Note that $S(0) \equiv \lim_{\omega \to 0^+} S(\omega) = \lim_{\omega \to 0^-} S(\omega)$ is well-defined if $\lim_{\omega \to 0} J_\varphi(\omega)/\omega$ exists[5].

3.2.2. Effective master equation within the secular approximation

In the resulting master equation, the terms in which ω_{pq} differs from ω_{sr} oscillate as a function of time t, which can lead to a violation of the positivity of $\hat{\rho}$ for long times. If the timescale τ_φ of the bath-induced system dynamics is much slower than the coherent dynamics, i.e., $\tau_\varphi \gg \tau_{\text{SC}}$, these terms can be removed by averaging the master equation over a time short compared to τ_φ, but long compared to $\tau_{\text{SC}} \sim 1/\Omega_R$ [295, 296]. We can estimate $\tau_\varphi \sim 1/\gamma_\varphi$, with γ_φ the bare-molecule dephasing rate, for which the total bare-molecule width presents an upper bound, $\gamma_\varphi \leq \gamma = 3.2$ meV [140]. As a consequence, only the *secular* terms $\omega_{pq} = \omega_{sr}$ persist. This secular approximation, outlined in subsection 2.2.1, results in a master equation where populations and coherences are decoupled. We note that the secular approximation aids in the interpretation of the different terms that are obtained, but is not required and indeed only used in some of the results shown in the following.

The secular terms are enumerated in Table 3.2, which lists the states $\{pq, rs\}$ connected by transitions with frequency ω_{sr}, as well as the labels we assign to the "bare"

---

[5] It must be noted that the same approach will hold for electronic dephasing interactions in the weak bath-coupling limit. In particular, we will make use of the same expression Equation 3.4 to recover the weak vibronic limit in the time evolution of organic exciton-polaritons in chapter 7.

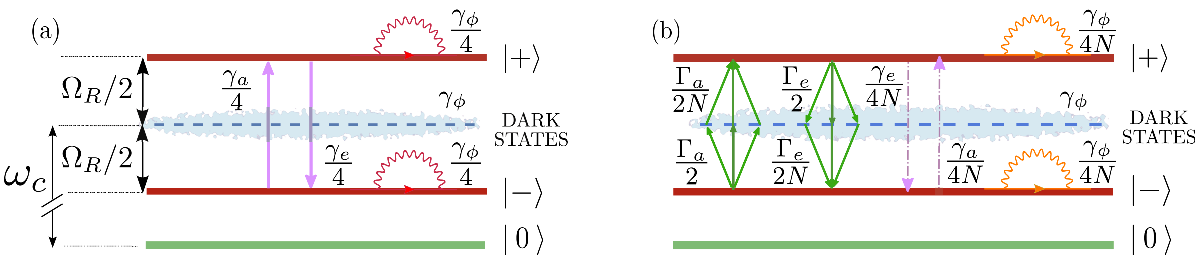

Figure 3.3: Illustration of the different decay and dephasing mechanisms that emerge from our modelling for the two dephasing scenarios: common bath (a) or independent baths (b). The arrows indicate decay processes while wavy lines represent elastic events that produce dephasing. The fuzzy halo around the dark states indicates excitation transfer and dephasing acting within this manifold.

rates $\gamma_{rs} = 2S(\omega_{sr})$, which do not contain the algebraic prefactors. The definition is chosen so that for terms where $pq = sr$, we obtain

$$S(\omega_{sr})\{[\hat{\sigma}_{rs}\tilde{\rho}(t), \hat{\sigma}_{sr}] + \text{H.c.}\} = \gamma_{rs}\mathcal{L}_{\hat{\sigma}_{rs}}[\hat{\rho}]\,, \tag{3.6}$$

where the standard Lindblad superoperator is given in Equation 2.32. Positive frequencies $\omega_{sr} > 0$ correspond to phonon emission where the system transitions from a higher- to a lower-energy state, while negative frequencies $\omega_{sr} < 0$ correspond to phonon absorption. We obtain secular terms connecting the two polaritons ($\gamma_e = 2S(\Omega_R)$, $\gamma_a = 2S(-\Omega_R)$[6]), terms connecting the polaritons with the dark modes ($\Gamma_e = 2S(\Omega_R/2)$, $\Gamma_a = 2S(-\Omega_R/2)$), and terms connecting states with the same energy ($\gamma_\varphi = 2S(0)$, equal to the bare-molecule dephasing rate). The latter give pure dephasing for the polaritons $|+\rangle$, $|-\rangle$, but produce coupling between populations and coherences for all dark states.

The final master equations are obtained by using the properties of the basis transformation matrix $u_a^{(i)}$ to evaluate the algebraic prefactors $\sum_i u_p^{(i)}u_q^{(i)}u_r^{(i)}u_s^{(i)}$ (independent baths) and $\sum_{i,j} u_p^{(i)}u_q^{(i)}u_r^{(j)}u_s^{(j)}$ (common bath) in Equation 2.38. Specifically, we use that *i)* the polariton-vibrational mode overlaps are given by $u_\pm^{(i)} = \pm 1/\sqrt{2N}$, *ii)* dark states are orthogonal to each other ($\sum_i u_d^{(i)}u_{d'}^{(i)} = \delta_{d,d'}$), and *iii)* dark states are orthogonal to the polaritons ($\sum_i u_d^{(i)} = 0$). Note that i and j in the sums are molecule indices (not including the cavity mode), so that $\sum_i u_p^{(i)}u_q^{(i)} = \delta_{p,q}$ is generally not true.

This procedure gives the final secularised master equation for the density operator, given in the Schrödinger picture below. For a common bath with $\phi_{ij}(\tau) = \phi(\tau)$, we find

---

[6] The same γ_a, γ_e are obtained under strong classical driving of a single two-level system [297].

that many terms vanish because of the orthogonality relations, giving

$$\partial_t\hat\rho = -i[\hat H_{\mathcal{S}},\rho] + \frac{\gamma_a}{4}\mathcal{L}_{\hat\sigma_{+-}}[\hat\rho] + \frac{\gamma_e}{4}\mathcal{L}_{\hat\sigma_{-+}}[\hat\rho] + \frac{\gamma_\varphi}{4}\sum_{p=\{+,-\}}\mathcal{L}_{\hat\sigma_{pp}}[\hat\rho] + \gamma_\varphi\mathcal{L}_{\hat{\mathcal{P}}_{\mathcal{D}}}[\hat\rho]\,, \tag{3.7}$$

$$+\frac{\gamma_\varphi}{2}\sum_d(\hat\sigma_{++}\hat\rho\hat\sigma_{dd} + \hat\sigma_{dd}\hat\rho\hat\sigma_{++}) + \frac{\gamma_\varphi}{2}\sum_d(\hat\sigma_{--}\hat\rho\hat\sigma_{dd} + \hat\sigma_{dd}\hat\rho\hat\sigma_{--}) \tag{3.8}$$

$$+\frac{\gamma_\varphi}{4}(\hat\sigma_{++}\hat\rho\hat\sigma_{--} + \hat\sigma_{--}\hat\rho\hat\sigma_{++}), \tag{3.9}$$

where $\hat{\mathcal{P}}_{\mathcal{D}} = \sum_d \hat\sigma_{dd}$ is the projector into the dark-state subspace. The Lindblad terms $\mathcal{L}_{\hat X}[\hat\rho]$ correspond to incoherent excitation transfer between system eigenstates and are depicted schematically in Figure 3.3a. A phonon of frequency Ω_R may be emitted by transferring an excitation from the UP $|+\rangle$ to the LP $|-\rangle$, with rate $\gamma_e/4$. Phonon absorption occurs analogously, with characteristic rate $\gamma_a/4$. Furthermore, the polaritons undergo pure dephasing with rate $\gamma_\varphi/4$. The last term corresponds to bare-molecule dephasing for a common bath, but projected into the degenerate dark-state subspace (using $\hat{\mathcal{P}}_{\mathcal{D}}\sum_i \hat b^{(i)\dagger}\hat b^{(i)}\hat{\mathcal{P}}_{\mathcal{D}} = \hat{\mathcal{P}}_{\mathcal{D}}$). Remarkably, for the case of a common bath, i.e., long-range phonons, the dark states are completely decoupled from the polaritons, and the bright state behaves identically to a *single* oscillator interacting with the EM field.

Turning to the case of independent baths, $\phi_{ij}(\tau) = \delta_{i,j}\phi(\tau)$, we instead find

$$\partial_t\hat\rho = -i[\hat H_{\mathcal{S}},\hat\rho] + \frac{\gamma_a}{4N}\mathcal{L}_{\hat\sigma_{+-}}[\hat\rho] + \frac{\gamma_e}{4N}\mathcal{L}_{\hat\sigma_{-+}}[\hat\rho] \tag{3.10a}$$

$$+\frac{\Gamma_a}{2N}\sum_d(\mathcal{L}_{\hat\sigma_{d-}}[\hat\rho] + \mathcal{L}_{\hat\sigma_{+d}}[\hat\rho]) + \frac{\Gamma_e}{2N}\sum_d(\mathcal{L}_{\hat\sigma_{d+}}[\hat\rho] + \mathcal{L}_{\hat\sigma_{-d}}[\hat\rho]) \tag{3.10b}$$

$$-\frac{\Gamma_a}{4N}\sum_d\left([\hat\sigma_{d-}\hat\rho,\hat\sigma_{d+}] + [\hat\sigma_{+d}\hat\rho,\hat\sigma_{-d}] + \text{H.c.}\right) \tag{3.10c}$$

$$-\frac{\Gamma_e}{4N}\sum_d\left([\hat\sigma_{d+}\hat\rho,\hat\sigma_{d-}] + [\hat\sigma_{-d}\hat\rho,\hat\sigma_{+d}] + \text{H.c.}\right) \tag{3.10d}$$

$$+\frac{\gamma_\varphi}{4N}\sum_{p=+,-}\mathcal{L}_{\hat\sigma_{pp}}[\hat\rho] + \gamma_\varphi\sum_i\mathcal{L}_{\hat{\mathcal{P}}_{\mathcal{D}}\hat b^{(i)\dagger}\hat b^{(i)}\hat{\mathcal{P}}_{\mathcal{D}}}[\hat\rho] \tag{3.10e}$$

$$+\frac{\gamma_\varphi}{2N}\sum_d(\sigma_{++}\hat\rho\hat\sigma_{dd} + \hat\sigma_{dd}\hat\rho\hat\sigma_{++}) + \frac{\gamma_\varphi}{2N}\sum_d(\hat\sigma_{--}\hat\rho\hat\sigma_{dd} + \hat\sigma_{dd}\hat\rho\hat\sigma_{--}) \tag{3.10f}$$

$$+\frac{\gamma_\varphi}{4N}(\hat\sigma_{++}\hat\rho\hat\sigma_{--} + \hat\sigma_{--}\hat\rho\hat\sigma_{++}), \tag{3.10g}$$

which now includes excitation transfer between the polaritons and dark states (Γ_a, Γ_e), driven by phonons of frequency $\Omega_R/2$. While the individual terms are strongly suppressed by the prefactor $1/N$ (with $N \sim 10^{12}$ in the experiments), excitation transfer *into* the dark states still occurs efficiently due to the sum over $N-1$ dark states d. For $N\to\infty$, the *total* population transfer from the polaritons to the dark states thus occurs with rates $\Gamma_a/2$ and $\Gamma_e/2$, as shown in Figure 3.3b. On the other hand, pure dephasing of the polaritons and direct transitions between them through absorption or emission of phonons of frequency Ω_R play a negligible role within this dephasing scenario, as their rates scale as $1/N$. Additional terms couple between different polariton-dark state coherences (Eqs. (3.10c), (3.10d), (3.10e), (3.10f), (3.10g)), without affecting the populations. Finally, the second term in Equation 3.10e again corresponds to a bare-molecule Lindblad dephasing term that has been restricted to act only within the degenerate dark-state subspace. For $N \to \infty$, Equation 3.10 simplifies (for the populations) to

$$\partial_t \hat{\rho} = -i[\hat{H}_{\mathcal{S}}, \hat{\rho}] + \frac{\Gamma_a}{2} \bar{\mathcal{L}}_{\hat{\mathcal{P}}_{\mathcal{D}}-}[\hat{\rho}] + \frac{\Gamma_e}{2} \bar{\mathcal{L}}_{\hat{\mathcal{P}}_{\mathcal{D}}+}[\hat{\rho}] + \gamma_\varphi \sum_i \mathcal{L}_{\hat{\mathcal{P}}_{\mathcal{D}} \hat{b}^{(i)\dagger} \hat{b}^{(i)} \hat{\mathcal{P}}_{\mathcal{D}}}[\hat{\rho}] \,, \tag{3.11}$$

where $\bar{\mathcal{L}}_{\hat{\mathcal{P}}_{\mathcal{D}}\pm}[\hat{\rho}] = \frac{1}{N-1} \sum_d \mathcal{L}_{\hat{\sigma}_{d\pm}}[\hat{\rho}]$ is an averaged Lindblad superoperator inducing equal population transfer from a polariton to all dark states. For large N, the dark states thus act like a sink, and any population transferred to them is trapped and does not further participate in the polariton dynamics. It must be noted that in realistic scenarios dark states will experience, besides a very small radiative decay from their purely vibrational character, a non-radiative decay (rate γ_{nr}), limiting the efficiency of the trapping within the dark state manifold.

As is clear from the expressions for the different decay rates, Ω_R is the parameter that controls the interaction between the *dressed* excitation and the phonon bath. Hence the importance of these decoherence mechanisms is dictated by the spectral density evaluated at Ω_R or $\Omega_R/2$. This is in clear contrast to what we would obtain by treating the interaction $\hat{H}_\varphi$ in the *uncoupled* basis. In that case, the Markov approximation would have resulted in 'standard' Lindblad terms $\gamma_\varphi \mathcal{L}_{\sum_i \hat{b}^{(i)\dagger}\hat{b}^{(i)}}[\hat{\rho}]$ (common bath) or $\gamma_\varphi \sum_i \mathcal{L}_{\hat{b}^{(i)\dagger}\hat{b}^{(i)}}[\hat{\rho}]$ (independent baths). In both cases, the dephasing interaction would be totally controlled by just the zero-frequency limit of the spectral density, resulting in an overestimation of the rates $\gamma_{a,e}$ and $\Gamma_{a,e}$. This fact emphasises the key importance of deriving Lindblad terms in the strongly coupled basis when considering non-flat reservoirs [263][7].

Apart from the decay and dephasing mechanisms induced by the dephasing-type interactions, which conserve the number of excitations, the excited states may decay through non-radiative molecular decay and cavity losses into the ground state $|G\rangle$. These decay processes, which we have neglected in the theory up to now, could be described within the same framework by dissipative coupling with thermal baths (e.g., the photonic modes

---

[7] In this context, the flat $J_\varphi(\omega)$ assumption implies disregarding any trade-off between the rapid system dynamics and the timescales in which incoherent dynamics occur. See derivations in section 2.2 for more details.

outside the cavity). However, as the energy shifts induced by the strong coupling are small compared to the transition frequency ($\Omega_R \ll \omega_v$), we can include them through Lindblad terms for the bare cavity and molecular vibrational modes. After removing nonsecular terms in the eigenstate basis, this gives new Lindblad terms with decay rates of $(\gamma_{nr}/2 + \kappa/2)$ for the two polaritons and γ_{nr} for the dark states.

3.3. Results

In the following, we apply our theoretical framework to the experimental results of Shalabney *et al.* [140]. For the vibrational mode of the *bare* molecules, they report a linewidth of $\gamma = 3.2$ meV, that is a typical value for organic molecules [142], with negligible inhomogeneous broadening (which would translate into a more Gaussian character of the lineshape, see [196, 298]). This linewidth has contributions from nonradiative decay and dephasing, $\gamma = \gamma_{nr} + \gamma_{\varphi}$, which can not be distinguished in the absorption spectrum. Although direct information about the weights of non-radiative and dephasing channels is thus not available, dephasing is in general expected to provide a significant contribution for vibrational transitions [204, 205]. Therefore, in our calculations we will use a factor f [$\gamma_{\varphi} = f\gamma$, $\gamma_{nr} = (1-f)\gamma$] to measure the relative importance of the two channels. In this way, the factor υ in Equation 3.3, which quantifies the strength of the system-bath coupling, is simply given by $\upsilon = f\gamma/(2k_B T_0)$ where $T_0 = 300$ K. The cut-off frequency for the thermal bath of low-frequency rovibrational excitations is chosen as $\omega_c = 6$ meV, corresponding to the range of low-frequency phonon modes in the system [140]. Finally, we use a cavity loss rate of $\kappa = 17$ meV as estimated in [140] through fitting of the transmission spectrum in the strong coupling regime (see also Figure 3.2).

We calculate the absorption spectra by introducing a weak driving term, $\hat{H}_d(t) \sim \hat{a}_c e^{-i\omega t} + \text{H.c.}$, which coherently pumps the cavity mode[8]. The density matrix in the steady-state, $\hat{\rho}_{ss}$, can be calculated in the frame rotating with the driving frequency ω. In this frame, $\hat{H}_d$ is time-independent, but the system frequencies are shifted and the density matrix $\hat{\rho}_{ss}$ depends on ω. The absorption spectrum is then obtained as $A(\omega) \propto \text{Tr}[\hat{\rho}_{ss}(\omega)\hat{a}_c]$. For the numerical implementation, we employ the open-source QuTiP package [275].

Figure 3.4a depicts the theoretical absorption spectra for the parameters reproducing the experimental situation, with Rabi splitting $\Omega_R = 20.7$ meV, for the two possible dephasing scenarios analysed in this work (common or independent baths). Different

---

[8] This corresponds to the vast majority of the experimental scenarios for VSC. Very recently, the case of IR emission driven by thermal pumping has been considered [203].

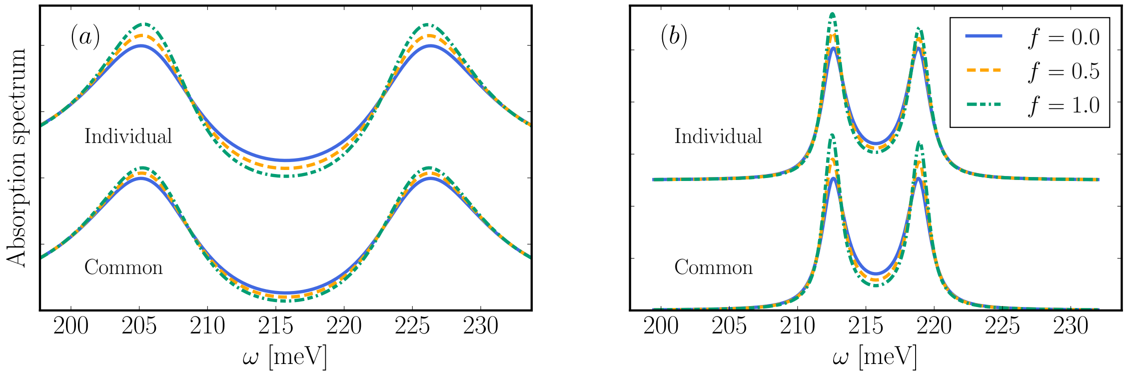

Figure 3.4: Absorption spectra for the two possible dephasing scenarios as a function of f. In both panels the two sets of curves are offset for a better visualization. In panel (a), the parameters used for the calculations are those reported in Ref. [140] (see text), whereas in panel (b), the Rabi splitting and the cavity decay rate are reduced to $\Omega_R = 6.5$ meV and $\kappa = 1$ meV, respectively.

values of f are tested: $f = 0$, $f = 0.5$ and $f = 1$. Both approaches coincide in the limit $f = 0$ (no dephasing), but their behaviour differs for non-zero f, as can be inferred from the different decay rates as rendered in Figure 3.3. The Rabi splitting is much larger than the range of low-frequency vibrations ($\Omega_R \gg \omega_c$) and, hence, all terms connecting levels with different energies ($\gamma_a, \gamma_e, \Gamma_a, \Gamma_e$) are essentially zero. The widths of the polaritons in the absorption spectrum (for $N \to \infty$) are simply given by $\gamma_\pm = \frac{\kappa+\gamma_{nr}}{2} + \frac{\gamma_\varphi}{4} = \frac{\kappa}{2} + (1-\frac{f}{2})\frac{\gamma}{2}$ for a common bath, and $\gamma_\pm = \frac{\kappa+\gamma_{nr}}{2} = \frac{\kappa}{2} + (1-f)\frac{\gamma}{2}$ for independent baths.

This also implies that for both bath scenarios and within the experimental conditions reported in [140, 196], the ensemble of vibrational modes behaves effectively as just a single collective molecular oscillator, the bright state, coupled to the cavity mode. Consequently, the dark modes are effectively decoupled from the system dynamics under external driving. We stress here that the fit used to extract the cavity width κ from the experimental data in [140] is performed under strong coupling. Thus, the change of linewidths predicted by our model would already be present in the observed spectra and is consequently absorbed in the extracted cavity linewidth. This, unfortunately, precludes a direct test of our model based on the experimental absorption data, for which the *bare* cavity linewidth would need to be available.

Furthermore, it is interesting to note that in the case of individual baths, the dephasing contributions to the polariton modes are entirely suppressed, analogous to the well-known suppression of inhomogeneous broadening under strong coupling [299], reported e.g. in inter-subband polaritons [300]. This effect in the polariton linewidths has also been

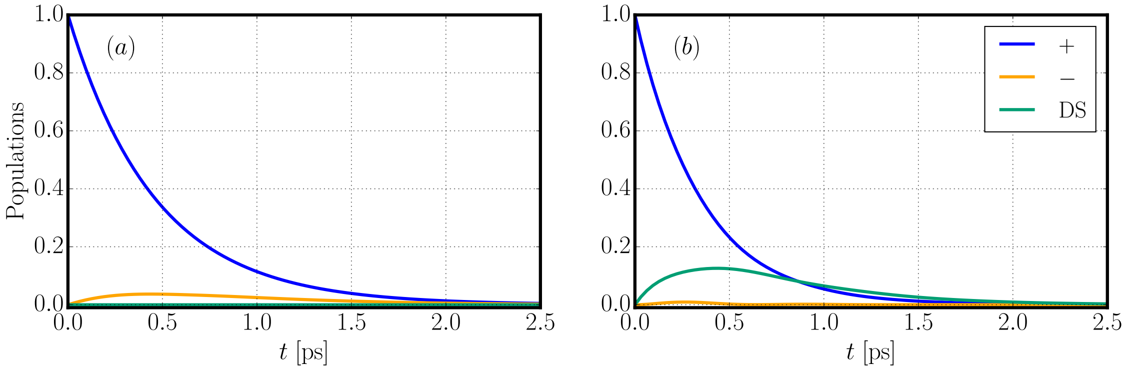

Figure 3.5: Population dynamics starting from the initially excited upper polariton $|+\rangle$ for the two possible dephasing scenarios: (a) Common bath and (b) independent baths. The parameters are the same as in Figure 3.4b, with $f = 0.5$ and $N = 100$. Each panel shows the upper and lower polariton ($\pm$) populations, as well as the total population in all dark states (DS), given by $\mathrm{Tr}(\hat{\mathcal{P}}_{\mathcal{D}}\hat{\rho})$.

dubbed 'motional narrowing' in the semiconductor micro-cavities community and results from the spatial 'averaging' of the delocalised polariton wavefunction over the disorder potential [301]. The link between dephasing and inhomogeneous broadening suppression for polaritons can thus be understood by the fact that they both correspond to related effects, namely temporal fluctuations or a static distribution of the transition energies respectively[9]. In this way, neither dephasing nor inhomogeneous broadening leads to coherent destruction of the Rabi splitting by spoiling the collective superposition of emitters. As we show in chapters 4 and 5, the 'immunity' of vibro-polaritons to dephasing, a large contribution of the homogeneous width of molecular vibrations, has also an impact in Raman-scattering-based devices, enabling e.g. lasers where the operation threshold can be reduced in strong coupling.

The dark modes could play a bigger role in a situation with smaller Rabi splitting, for which, in order to still achieve strong coupling, the cavity losses also need to be reduced as compared to the experiments (e.g., by using thicker mirrors). The resulting absorption spectra are shown in Figure 3.4b, for the same parameters as in Figure 3.4a but now with $\kappa = 1$ meV and $\Omega_R = 6.5$ meV. In both bath scenarios, a slight asymmetry between upper and LP is now noticeable, as the emission of phonons from the UP ($\propto n(\omega)+1$) is more likely than the absorption of phonons in the LP ($\propto n(\omega)$). However, as the involved

---

[9] This is in some sense also analogous to the case of an inhomogeneous cavity field described in [302]: there is no effect on the peak separation of the splitting and, in general, does not lead to an inhomogeneous broadening of the split states

transition frequencies are smaller than the thermal energy, the thermal occupation $n(\omega)$ is significant, and the rates for phonon emission and absorption are comparable. Furthermore, although the phenomenology in the observed absorption spectra is quite similar in both dephasing scenarios, with a reduction of the polariton linewidths for increasing dephasing f, the underlying physics are now quite distinct.

This is demonstrated clearly when inspecting the population dynamics, shown in Figure 3.5 for the case of the UP being initially excited. For the common bath, shown in Figure 3.5a, the dark states are entirely decoupled from the dynamics and population is only transferred between the polaritons. In contrast, in the case of independent baths, shown in Figure 3.5b, the population primarily is transferred from the UP to the dark states, which then decay through nonradiative losses.

In this chapter, the assumption of a weakly coupled bath signifies the environment is unaffected by polariton dynamics. Nevertheless, in chapter 6 we will analyse the breakdown of this limit in ESC, a case where the 'bath' encompasses intra-molecular phonons that become profoundly affected by the strong coupling to optical transitions (excitons). As a result, non-equilibrium vibrational dynamics cannot be disregarded in this limit but instead must be considered in the coherent evolution. Nevertheless, the limit of weak vibronic couplings in exciton-polaritons (e.g. in organic micro-cavities formed by J-aggregates, discussed in chapter 1) can be recreated theoretically in this limit by BRW theory. We analyse this in depth in chapter 7.

3.4. Conclusion

The vibro-polaritons formed in mid-IR micro-cavities are a demonstration of the versatility of organic molecules concerning the formation of polaritons, thanks to the presence of dipole-active transitions at different energy scales. However, the field of VSC differs in its maturity in a significant way from that of ESC. Although the material components in exciton- and vibro-polaritons have a clearly distinctive nature, formal similarities can be expected between both cases. That is precisely a first motivation to have dedicated this chapter to shed light on very fundamental aspects of vibro-polaritons, also aiming to grasp some features of the generally more involved scenario of ESC.

In particular, by using a fully quantum framework, we have studied in detail the phenomenon of collective strong coupling when an ensemble of molecular vibrational modes interacts with a cavity EM mode, as realised experimentally in, for instance, [140, 196]. We have demonstrated that dephasing-type interactions with a thermal bath of background modes in such a system have to be treated beyond the usual Lindblad approximation to represent the effects of the spectral density of bath modes correctly. We have investigated two ‘extreme’ scenarios for the bath, with either a common bath for all molecules or independent baths for each molecule. For the experimentally relevant parameters, we find that the dark modes are almost entirely decoupled from the polaritons in both scenarios, and the bright state behaves almost like a single isolated oscillator. Our findings thus suggest that this type of system is an ideal and simple platform to explore the exciting possibilities of cavity optomechanics at room temperature.

Moreover, we have unveiled common ingredients with the problem of exciton-polariton dynamics. In particular, our results show that the dark states can act as a ‘sink’ for excitations initially residing in the polaritons, where emission cannot occur efficiently, therefore translating into apparently extended lifetimes in the time evolution. This idea is related to the proposed concept of uncoupled ‘exciton-reservoir’ for organic exciton-polaritons [182, 183, 211]. Although this effect is not critical in vibro-polaritons, further studies in chapter 7 will confirm these features are fundamental when addressing the polariton temporal dynamics at optical frequencies.

4 | Vibro-polariton Raman Scattering

4.1. Motivation

In the phenomenon of Raman scattering, a driving laser beam induces an oscillating polarisation in a molecule, which then couples to the polarisation of a vibrational transition of either higher (Stokes) or lower (anti-Stokes) energy, leading to the emission of photons shifted by the vibrational energy. Figure 4.1 illustrates this inelastic scattering process for the first Stokes line of a single molecular vibration, in both the weak- and strong-coupling regimes. In this chapter, we describe the major consequences of the formation of vibro-polariton states in the Raman spectrum of a molecular ensemble. In particular, we investigate the effects of collective VSC in the RS of organic polymers by using a series of increasingly sophisticated models. In this manner, we demonstrate that the primary effect of VSC is a redistribution of the total Raman cross-section, with the Stokes lines for (multiple) vibrational excitation splitting into multiplets corresponding to (multiple) excitation of the lower and upper polaritons. The total cross section (integrated over the emission frequency) is approximately conserved.

This chapter is organised as follows: first, we introduce the essential features of the Raman effect in vibro-polaritons. Starting with a minimal three-level model for molecules in section 4.2, we compare the RS cross section for vibro-polaritons to one of the uncoupled molecules. In this setting, we include further possible effects to infer their influence in vibro-polariton RS, such as permanent dipole moments and orientational effects in the molecules. To verify the previous approach, as well as going beyond it, we introduce additional effects such as vibrational overtones, ultra-strong coupling and incoherent mechanisms in section 4.3. Here, we study the Raman emission spectrum for a single molecule and two molecules, as a minimal model to describe collective effects.

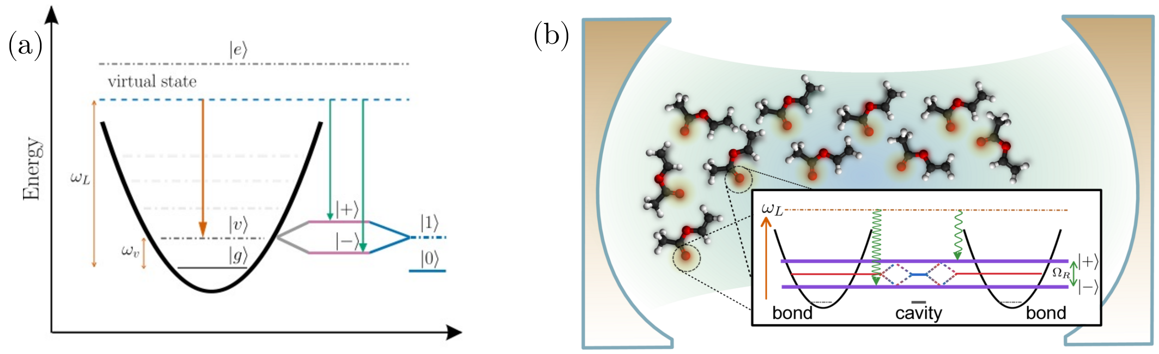

Figure 4.1: (a) Sketch of the RS process for a molecule as a result of excitation with an off-resonant driving field. After coherent excitation, the molecule promotes to a virtual state depicted with a blue dashed line. In the weak coupling regime, the electron decays into the first excited vibrational state, $|v\rangle$ (orange arrow). When this first excited vibrational state is strongly coupled to the cavity mode, $|1\rangle$, the electron can decay to any of the two polaritons, $|+\rangle$ or $|-\rangle$ (blue arrows). (b) Sketch of mid-IR illustrating the Raman effect into delocalised polariton states.

4.2. Macroscopic three-level approach

As a minimal model to reproduce RS, in our first approach we restrict the description of the bare molecules to a three-level (Λ) system consisting of the ground state, $|g\rangle$, with energy ω_g, the first excited vibrational mode, $|v\rangle$, with energy ω_v, and the electronically excited state, $|e\rangle$, with energy ω_e. Additionally, we include a quantised cavity mode, which within the minimal model we restrict to containing at most a single photon, $|1\rangle = \hat{a}_c^\dagger |G\rangle$, with energy ω_{IR}. We use the RWA, which removes off-resonant couplings, under the assumption that the two frequency regions (mid-IR and optical) are well-separated. In all the calculations presented in this work, we will consider the case of zero detuning, i.e., $\omega_{\text{IR}} = \omega_v$. Choosing ω_g as the zero energy, the coherent dynamics of the as system composed of N molecules and a cavity mode is governed by the Hamiltonian

$$\hat{H}^{\text{eff}} = \sum_{i=1}^{N} \omega_e \hat{\sigma}_{ee}^{(i)} + \omega_{\text{IR}} \hat{a}_c^\dagger \hat{a}_c + \sum_{i=1}^{N} [\omega_v \hat{\sigma}_{vv}^{(i)} + g \left(\hat{a}_c^\dagger \hat{\sigma}_{gv}^{(i)} + \text{H.c.} \right)]. \tag{4.1}$$

where VSC is introduced via the last term. Here the superscripts of the transition operators $\hat{\sigma}_{ab} = |a\rangle \langle b|$ specify the molecule that the operator applies to. In addition, the cavity-oscillator interaction is measured by g, which depends on the cavity electric field strength and the change of the molecular dipole moment under displacement from the equilibrium position, but in our calculations will be used as a parameter that fixes the Rabi splitting (see below). For simplicity, we assume a configuration with zero disorder in which all the N molecules are equally coupled to the cavity mode ($g_i = g$). We have checked that this does not affect the conclusions presented here. We note here that in contrast to chapter 3, the Hamiltonian includes an electronically excited state that allows describing the inelastic scattering of optical photons.

We assume that the probe field is far off-resonant and the hierarchy condition $\omega_v \ll \omega_L \ll \omega_e$ is fulfilled. We can then safely work within second-order perturbation theory, standard for Raman processes [303], and neglect losses in the system. In general, the RS cross section associated with a process where the system is excited from the initial state $|i\rangle$ (energy ω_i) to a final state $|f\rangle$ (energy ω_f, with scattered photon energy $\omega_L - \omega_f + \omega_i$) can be written as $\sigma_{R,\omega_f-\omega_i} \propto |\alpha_{fi}|^2$ where $\alpha_{fi} = \langle f|\,\hat{\alpha}\,|i\rangle = \langle f|\,\hat{\mu}\frac{1}{\hat{H}^{\text{eff}}-\omega_L-\omega_i}\hat{\mu}\,|i\rangle$ is the polarisability matrix element between the initial and final states, with $\hat{\mu}$ being the dipole operator and $\hat{H}^{\text{eff}}$ the Hamiltonian. In our case, we only consider dipolar transitions $|g\rangle \rightarrow |e\rangle$, characterised by a dipole moment μ_{ge}, and $|e\rangle \rightarrow |v\rangle$ with dipole moment μ_{ev}, corresponding to an electronic excitation from the ground state and transition from the electronically excited state to the first excited vibrational mode. For vibrational modes that are IR-active (as required for VSC), there are also direct dipole transitions from the ground state to the vibrationally excited state. However, these do not play a role in RS to the vibrationally excited modes, which requires two dipole transitions.

4.2.1. Basic calculation of the Raman cross section

In the weak-coupling regime ($g \rightarrow 0$), the RS process corresponds to an excitation from the global ground state, $|G\rangle = \Pi_{i=1}^{N}\left|g^{(i)}\right\rangle$, followed by decay into a singly excited vibrational state of a molecule, $\left|v^{(i)}\right\rangle$ (shorthand for $\left|v^{(i)}\right\rangle \prod_{j\neq i}\left|g^{(j)}\right\rangle$), with index $i = 1,\ldots,N$ labelling different molecules. In this situation the molecules act independently and the cross section for emission of a photon of energy $\omega_L - \omega_v$ is just the sum of the cross sections associated with each molecule:

$$\sigma_{\mathrm{R},\omega_v} \propto \sum_{i=1}^{N} |\alpha_{v^{(i)}G}|^2 = N\left[\frac{\mu_{ve}\mu_{ge}}{\omega_e - \omega_L}\right]^2. \tag{4.2}$$

In the regime of VSC, vibro-polaritons and dark states, delocalised over the ensemble, are formed. In principle, it could be expected that the formation of collective modes among the molecular bonds leads to an enhancement of the Raman cross section. However, a straightforward calculation shows that the Raman cross sections associated with the dark modes are zero whereas those of the two polaritons (involving photons of energies $\omega_L - \omega_+$ and $\omega_L - \omega_-$) are just half of the Raman cross section evaluated in the weak-coupling limit, Equation 4.2. In other words, when going from the weak to the strong coupling regime, the total Raman cross section is maintained but equally shared between the two polaritons $|\pm\rangle = \frac{1}{\sqrt{2}}|1\rangle \pm \frac{1}{\sqrt{2N}}\sum_{i=1}^{N}|v^{(i)}\rangle$:

$$\sigma_{\mathrm{R},\pm} \propto \frac{N}{2}\left[\frac{\mu_{ve}\mu_{ge}}{\omega_e - \omega_L}\right]^2 . \tag{4.3}$$

The total cross section within the single-vibrational-excitation subspace is thus preserved[1].

4.2.2. Further effects in the macroscopic model

The previous calculation can be readily extended to explore further effects in the Raman cross section. For instance, it is an open question whether permanent dipole moments in the vibrations, arising from different electronegativities in the bond atoms, could influence in the RS after the vibro-polaritons are formed. Such permanent dipole moments enable dipole transitions that do not change the state. In addition, counter-rotating terms responsible for USC effects can lead to orientation of the molecules along the cavity-field polarisation axis (if such axis is well defined). However, it has been shown recently [185] that molecular orientation under ESC depends only on the single-molecule coupling strength without collective enhancement, such that this effect is negligible under realistic experimental conditions.

To account for possible changes, we consider both possibilities by assuming the dipole operator for each molecule to be $\hat{\mu}^{(i)} = \sum_{l,m=\{g,v,e\}}\mu_{lm}\hat{\sigma}^{(i)}_{lm}$ with non-zero diagonal elements and we consider that the dipole moments in the molecular ground states may not be aligned. We therefore write $\hat{\boldsymbol{\mu}}_i = \mathbf{e}_i\hat{\mu}^{(i)}$, where $\mathbf{e}_i = (e_i^{(1)}, e_i^{(2)}, e_i^{(3)})$ is an unitary vector along the alignment direction of the dipole i. The same calculation of the Raman cross section involves a the polarisability tensor, with spatial components $\alpha^{(l,m)} = e_l\bar{\boldsymbol{\alpha}}e_m$, giving

$$\alpha^{(l,m)}_{v^{(i)}G} = \sum_{j,k,n}\langle v^{(i)}|\,\hat{\mu}_j e_j^{(l)}\,|n\rangle \frac{1}{\omega_n - \omega_L}\langle n|\,\hat{\mu}_k e_k^{(m)}\,|G\rangle , \tag{4.5}$$

---

[1] Finally, note that if we instead calculate Rayleigh scattering $\propto |\alpha_{GG}|^2$, we get (for both weak and strong coupling – the calculation is identical) an enhancement of N^2:

$$\sigma_{\mathrm{elas}} \propto \sum_{i=1}^{N}|\alpha_{GG}|^2 = N^2\frac{\mu_{ge}^4}{(\omega_e - \omega_L)^2}. \tag{4.4}$$

where we used $\hat{H}^{\text{eff}} = \sum_n |n\rangle\, \omega_n \,\langle n|$, with n running over all eigenstates. Including the fact that dipole operator can be applied to a molecule in any state

$$\begin{cases} \hat{\mu}_k \,|G\rangle &= \mu_{ge} \left|e^{(k)}\right\rangle + \mu_{gv} \left|v^{(k)}\right\rangle + \mu_{gg} \,|G\rangle \\ \hat{\mu}_j \left|e^{(k)}\right\rangle &= \delta_{jk}(\mu_{ee} \left|e^{(k)}\right\rangle + \mu_{ve} \left|v^{(k)}\right\rangle + \mu_{ge} \,|G\rangle) + (1-\delta_{jk})\mu_{gg} \left|e^{(k)}\right\rangle + \cdots \\ \hat{\mu}_j \left|v^{(k)}\right\rangle &= \delta_{jk}(\mu_{ve} \left|e^{(k)}\right\rangle + \mu_{vv} \left|v^{(k)}\right\rangle + \mu_{gv} \,|G\rangle) + (1-\delta_{jk})\mu_{gg} \left|v^{(k)}\right\rangle + \cdots \end{cases} \tag{4.6}$$

where the dots denote terms with more than one excitation. This gives

$$\sigma^{(l,m)}_{\mathrm{R},\omega_v} \propto \sum_{i=1}^{N} \left[\mathcal{A}^{(l,m)}_i + \mathcal{B}^{(l,m)}_i + \mathcal{C}^{(l,m)}_i\right]^2, \tag{4.7}$$

defining the products of spatial components

$$\mathcal{A}^{(l,m)}_i = \frac{\mu_{ve}\mu_{ge}}{\omega_e - \omega_L} e^{(l)}_i e^{(m)}_i, \tag{4.8}$$

$$\mathcal{B}^{(l,m)}_i = \frac{\mu_{vv}\mu_{gv} e^{(l)}_i e^{(m)}_i + \mu_{gg}\mu_{gv}((\sum_{j=1}^{N} e^{(l)}_j) e^{(m)}_i - e^{(l)}_i e^{(m)}_i)}{\omega_v - \omega_L}, \tag{4.9}$$

$$\mathcal{C}^{(l,m)}_i = \frac{\mu_{gv}\mu_{gg}(\sum_{j=1}^{N} e^{(l)}_j) e^{(m)}_i}{\omega_g - \omega_L}. \tag{4.10}$$

Turning to the VSC case, with the coupling strength $g_i = -\mu_{gv}|\mathbf{E}(\mathbf{r}_i)|(\mathbf{e}_i \cdot \mathbf{e}_E)$ and EM field pointed along $\mathbf{e}_E$. The bright state now follows from $|B\rangle = 2\sum_i g_i \left|v^{(i)}\right\rangle / \Omega_R$ and the cross section realds

$$\sigma^{(l,m)}_{\mathrm{R},\pm} \propto \frac{1}{2\sum_{i=1}^{N} (\mathbf{e}_i \cdot \mathbf{e}_E)^2} \left[\sum_{i=1}^{N} (\mathcal{A}^{(l,m)}_i + \mathcal{B}^{(l,m)}_i + \mathcal{C}^{(l,m)}_i)(\mathbf{e}_i \cdot \mathbf{e}_E)\right]^2. \tag{4.11}$$

Although orientational effects in USC have been discussed to be marginal for the linear spectra of exciton-polaritons [185], to 'intensify' possible effects in the current case we assume perfect orientation is induced in strong coupling. Choosing $\mathbf{e}_E = \mathbf{e}_z$, only the term $\sigma_{\mathrm{R},\pm}$ will remain. In addition, for random orientations in WC, the sums $\sum_{j=1}^{N} e^{(l)}_j$ become negligibly small while a parametrisation in spherical coordinates

$$\mathbf{e}_i(\Omega_i) = (\cos\theta_i \sin\phi_i, \sin\theta_i \sin\phi_i, \cos\phi_i), \tag{4.12}$$

can be exploited to promote sums over index i to integrals over an uniform angular distribution $P(\Omega) = 1/(4\pi)$. The Raman cross section in WC becomes proportional to $\sum_{i=1}^{N} (e^{(l)}_i e^{(m)}_i)^2 \to \int P(\Omega)(\mathbf{e}(\Omega) \otimes \mathbf{e}(\Omega'))^2 \,\mathrm{d}\Omega$: carrying out the integrals, we have shown

$$\frac{\sigma^{(z,z)}_{\mathrm{R},\pm}}{\left\langle \sigma^{(z,z)}_{\mathrm{R},v^{(i)}} \right\rangle} \sim 1, \tag{4.13}$$

and therefore there is no collective enhancement associated to orientational effects.

The previous results point to the existence of a kind of sum rule for the RS cross-section. In order to investigate this in more detail, we analyse the total RS cross section defined as the sum over all possible final states, $|f\rangle$, resulting from inelastic processes when the system is excited from the ground state $|G\rangle$:

$$\Sigma_R \propto \sum\!\!\!\!\!\!\!\int_{f\neq G} |\langle f|\,\hat{\alpha}\,|G\rangle|^2 = \langle G|\,\hat{\alpha}^2\,|G\rangle - \langle G|\,\hat{\alpha}\,|G\rangle^2 \,, \tag{4.14}$$

where we have used the closure relation $\sum\!\!\!\!\!\!\int_f |f\rangle\langle f| = \hat{\mathbf{1}}$, which implies $\sum\!\!\!\!\!\!\int_{f\neq G} = \hat{\mathbf{1}} - |G\rangle\langle G|$. This result is related to general sum rules in linear response theory that have been investigated, e.g., in the context of RS from strongly correlated systems [304–306]. Here, we are interested in the change of the cross-section as the Hamiltonian is changed and VSC is established. By inserting the spectral decomposition of the Hamiltonian in $\hat{\alpha} = \hat{\mu}\frac{1}{\hat{H}^{\text{eff}} - \omega_L - \omega_i}\hat{\mu}$, it can be seen that the total Raman cross section will only be affected by changes in the ground state $|G\rangle$ or intermediate electronically excited states $|n\rangle$ reachable by a single-photon transition, $\langle n|\,\hat{\mu}\,|G\rangle \neq 0$. Vibrational strong coupling primarily affects the *final* states, i.e., the vibrationally excited states that split into polaritons. Furthermore, as the driving frequency, ω_L in standard RS experiments is not close to any eigenstate of the Hamiltonian, any possible changes in the electronically excited states are not expected to have a big effect. This suggests that, within the theoretical framework described above, changes in the total Raman cross-section when going from the weak coupling limit to the strong coupling regime could only come from changes in the ground state of the system. Such changes are induced by the counter-rotating terms in the cavity-emitter coupling, which become important in the USC regime, reached when the Rabi frequency Ω_R is a non-negligible fraction of the transition energy ω_v [75, 77, 79, 155, 307]. The strength of these effects scales (to lowest order) as g^2, such that they are small but non-zero even for small couplings. Furthermore, it has recently been shown that the changes induced in the ground state depend sensitively on the observable that is interrogated [161, 185], with, e.g., bond-length changes only being sensitive to the single-molecule coupling strength, while energy shifts depend on the collective coupling. It is thus necessary to explicitly calculate whether counter-rotating terms could affect the ground state and enhance the RS cross-section, as we do in the following section.

4.3. Microscopic model

In order to check the formalism above, as well as go beyond it, we therefore turn to a microscopic quantum model for the organic molecules interacting with the quantised cavity field. In this formalism, we include counterrotating terms to explore the effects of USC, and additionally incorporate losses and dephasing mechanisms that were not present in the previous approach. The Hamiltonian describing the i^{th} bare molecule is similar to Equation 2.11 but only including a single vibrational mode that is relevant in VSC:

$$\hat{H}^{(i)} = \omega_e \hat{\sigma}_+^{(i)} \hat{\sigma}_-^{(i)} + \omega_v [\hat{b}^{(i)\dagger} \hat{b}^{(i)} + \sqrt{S} \hat{\sigma}_+^{(i)} \hat{\sigma}_-^{(i)} (\hat{b}^{(i)\dagger} + \hat{b}^{(i)})], \tag{4.15}$$

where the electronic transition of the molecule, of energy ω_e, is described by the Pauli ladder operator $\hat{\sigma}^{(i)}$, whereas $\hat{b}^{(i)}$ is the annihilation operator of the optically active vibrational mode of the molecule of energy ω_v. The interaction between electronic and vibrational states is characterised by the Huang-Rhys parameter S ($\Delta = \omega_v S$ is precisely the reorganisation energy of the molecules), which quantifies the phonon displacement between the ground and excited electronic states. The total Hamiltonian also contains the cavity field and the coupling term between the cavity mode and the vibrational states of the molecules:

$$\hat{H}_{\mathcal{S}} = \sum_{i=1}^{N} \hat{H}^{(i)} + \omega_{\text{IR}} \hat{a}_c^\dagger \hat{a}_c + g \sum_{i=1}^{N} (\hat{a}_c + \hat{a}_c^\dagger)(\hat{b}^{(i)} + \hat{b}^{(i)\dagger}), \tag{4.16}$$

where $\hat{a}_c$ is the annihilation operator for the cavity mode with energy ω_{IR}. As in our previous approach above, g describes the cavity-vibrational mode interaction, but the Hamiltonian Equation 4.16 now includes counterrotating terms that do not conserve the number of excitations. Extending the model of chapter 3 slightly, the current Hamiltonian describes both electronic and vibrational degrees of freedom of the molecule, as well as their coupling, in order to allow the description of the RS process. Besides, neither the photonic nor the vibrational degrees of freedom are restricted to the single-excitation subspace. Consequently, this theoretical framework permits to investigate higher Stokes lines, corresponding to vibrational overtones. The photonic and vibrational degrees of freedom form a system of coupled harmonic oscillators, which can be diagonalised analytically, yielding $N+1$ new oscillator modes: the upper and lower polariton modes with frequencies $\omega_\pm = \omega_v \sqrt{1 \pm 2g/\omega_v}$, as well as $N-1$ dark state oscillators at the uncoupled frequencies ω_v. Beyond the limit $2g/\omega_v$ it should be necessary to include self-energy contributions (e.g. the quadratic term in the vector potential $\sim \hat{\mathbf{A}}^2$ in the Coulomb gauge) to avoid a non-physical phase transition [253] translating into a spurious divergence of the RS of the Raman cross section.

To account for both loss and dephasing mechanisms, we rely on the standard Lindblad master equation formalism [187], described in section 2.2. We include decay of the electronic excitations (rate γ_e) and vibrational modes (rate γ_v), as well as the loss of the cavity photons (rate κ). Additionally, we consider elastic scattering with bath modes, which leads to pure electronic (rate γ_e^φ) and vibrational (rate γ_v^φ) dephasing terms. The time evolution of the system density matrix $\hat{\rho}$ is then described by

$$\partial_t \hat{\rho} = -i[\hat{H}_{\mathcal{S}}, \hat{\rho}] + \kappa \mathcal{L}_{\hat{a}_c}[\hat{\rho}] + \sum_{i=1}^{N} (\gamma_e \mathcal{L}_{\hat{\sigma}_-^{(i)}}[\hat{\rho}] + \gamma_v \mathcal{L}_{\hat{b}^{(i)}}[\hat{\rho}] + \gamma_e^\varphi \mathcal{L}_{\hat{\sigma}_+^{(i)}\hat{\sigma}_-^{(i)}}[\hat{\rho}] + \gamma_v^\varphi \mathcal{L}_{\hat{b}^{(i)\dagger}\hat{b}^{(i)}}[\hat{\rho}]), \tag{4.17}$$

where $\mathcal{L}_{\hat{X}}[\hat{\rho}]$ is given by Equation 2.32. We note that in the USC regime, the Hamiltonian does not conserve the number of excitations and the terms $\mathcal{L}_{\hat{a}_c}[\hat{\rho}]$ and $\mathcal{L}_{\hat{b}^{(i)}}[\hat{\rho}]$ actually introduce artificial pumping [308, 309]. We then replace these terms by explicitly calculating the decay introduced by coupling to a zero-temperature bath of background modes with constant spectral density, within BRW theory [207, 208]. As we have shown chapter 3, BRW theory should in principle also be used for the description of vibrational dephasing; however, this does not influence the results presented here significantly, and we thus use Lindblad terms for simplicity.

We additionally introduce a continuous-wave off-resonant laser field at frequency ω_L that collectively drives all emitters, represented by $\hat{H}_d = \Omega_p \sum_i (\hat{\sigma}_-^{(i)} e^{-i\omega_L t} + \hat{\sigma}_+^{(i)} e^{i\omega_L t})$. The emission spectrum is then calculated from the steady-state two-time correlation function of the electronic dipole within a frame rotating at ω_L in which $\hat{H}_d$ is time-independent. This gives the emission spectrum $S(\omega) = \int_{-\infty}^{\infty} e^{i(\omega_L - \omega)\tau} \langle \hat{\sigma}_+(\tau) \hat{\sigma}_-(0) \rangle \, \mathrm{d}\tau$, where $\hat{\sigma}_- = \sum_i \hat{\sigma}_-^{(i)}$, from which we remove the zero-frequency Rayleigh peak (corresponding to elastic scattering) to obtain only the Raman contribution. For the numerical implementation of this microscopic model, we employ the open-source QuTiP package [275].

4.3.1. Single molecule Raman spectrum

We first apply this theoretical framework to study the Raman spectrum when the vibrational mode of a single molecule is coupled to the cavity mode. The results are depicted in Figure 4.2, with parameters chosen to agree with the experiment [212], where the micro-cavity is similar to the case explored in chapter 3. The vibrational frequency is $\omega_v = 215$ meV and the vibrational rates, $\gamma_v = \gamma_v^\varphi = 1.6$ meV, are recovered from the experimental transmission spectrum assuming that half of the total linewidth is due to

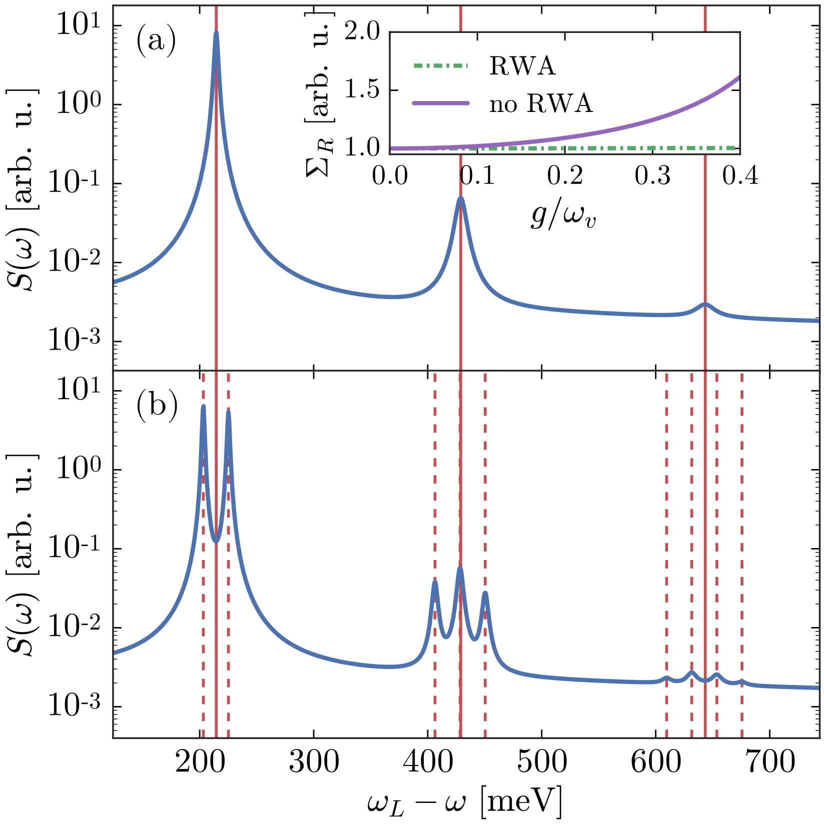

Figure 4.2: Single molecule Raman spectrum in the weak (a) and strong coupling (b) regimes. A weak probe strength $\Omega_p \ll \omega_v$ is used in both cases. The Stokes lines at energies $n\omega_v, n \in \mathbb{N}$ are depicted in orange, while the dashed green lines spectrally located at $\omega^{(n,m)}$ (see main text) show the dressed energies in the strong coupling regime. In this last calculation we allowed for five excitations at most. Inset: total RS probability $\int S(\omega)\mathrm{d}\omega \propto \Sigma_R$ as a function of cavity-oscillator interaction g, within (blue) and without (orange) the rotating wave approximation.

pure dephasing. The cavity losses are accounted for by $\kappa = 1.6$ meV, which is a relatively small value chosen to make the separate peaks clearly visible. Other parameters are chosen in accordance with typical values for polymers: $\omega_e = 5$ eV, $\omega_L \gg \omega_v$, $S = 2$, $\gamma_e = 6.2$ meV and $\gamma_e^{\varphi} = 6.2$ meV. As expected, in the weak-coupling limit, i.e., $g \to 0$ (Figure 4.2a), Stokes lines appear at the vibrational frequencies, $n\omega_v$, with $n \in \mathbb{N}$. When VSC emerges ($\Omega_R = 20$ meV in Figure 4.2b), the nth Stokes line splits into $n+1$ sidebands at $\omega^{(k,l)} = k\omega_- + l\omega_+$ corresponding to the excitation of k lower and l upper polaritons, with $k + l = n$. Importantly, the position of the $n = 1$ Stokes lines coincides with their position in the transmission spectrum, and consequently, the splitting between the two peaks coincides with Ω_R, the Rabi splitting observed in the transmission spectrum. Also, the total Raman signal $\int S(\omega)\, \mathrm{d}\omega \propto \Sigma_R$ stays almost constant when going from the weak to the strong-coupling regime. This result is compatible with the prediction obtained from the pure Hamiltonian approach (Equation 4.14) and confirms the expectation that counter-rotating terms are negligible for the current case of $\Omega_R \ll \omega_v$.

In order to observe changes in the total Raman signal induced by the counter-rotating terms, we render the evolution of the total RS probability as a function of g, shown in the inset of Figure 4.2a) (with all other parameters being the same as those used in the main panels of Figure 4.2). These results demonstrate that under *ultrastrong* coupling, the total Raman cross section could indeed change significantly, as it increases by a factor of more than 1.5 in the limit $g \to \omega_v/2$ (larger values of g are unphysical within this model). However, notice that in the experiments by Shalabney et al. [212], $g/\omega_v \approx 0.05$ and our results show that the ground state is only modified weakly, leading to a total RS probability that is practically unchanged from the weak coupling limit $g \to 0$.

4.3.2. Collective effects in the microscopic model

Our previous results using the microscopic model were obtained for a single molecule and therefore did not include dark vibrational superpositions, which as we addressed previously, show signatures in the linear absorption. As a minimal model to investigate collective effects, we now show the Raman spectrum of two molecules strongly coupled to a cavity mode. For comparison with the single-molecule case, we rescale $g \to g/\sqrt{2}$ to keep the Rabi frequency Ω_R constant. The results (see Figure 4.3) are now also sensitive to the 'collection' operator as different physics arise if we examine either the *coherent* case (obtained from the correlation function of the total dipole operator $\sim \sum_{i=1}^{N} \hat{\sigma}_{-}^{(i)}$) or the *incoherent* sum over different molecules $\sum_i S_i(\omega)$ where $S_i(\omega) \propto \int_{-\infty}^{\infty} e^{i(\omega_L-\omega)\tau} \langle \hat{\sigma}_{+}^{(i)}(\tau)\hat{\sigma}_{-}^{(i)}(0)\rangle$ is the Raman spectrum associated with one molecule. For coherent collection of the emission from both molecules, the same spectral weight redistribution among the two polaritons (split by Ω_R, as in transmission measurements) is exhibited. By comparing with the case of a single molecule (also depicted in the figure), we infer a linear scaling $\propto N$, which is consistent with the Λ-system results (Equation 4.2). This confirms that no collective enhancement of the Raman signal is present. Interestingly, while in coherent collection only the polaritons are observed in the spectrum, for incoherent collection (which could be achieved experimentally using, e.g., a near-field probe), a central peak appears at the bare vibrational energy ω_v, a signature of the vibrational dark state $|d\rangle = \frac{1}{\sqrt{2}}(b^{(1)\dagger} - b^{(2)\dagger})\,|G\rangle$. This demonstrates that the dark state emission is suppressed under coherent collection due to destructive interference (as observed within the Λ-system approach above), even though these states emit on the single-molecule

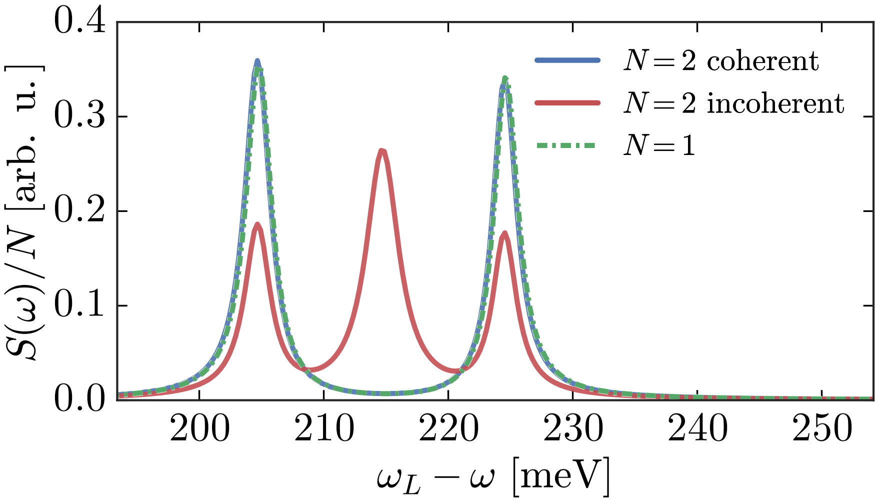

Figure 4.3: First Stokes line of the Raman spectra in the strong coupling regime, for one and two molecules. The chosen parameters are the same as those used for the single-molecule case, with the spectra normalised to the number of molecules N. For the case of two molecules, the spectra for coherent and incoherent collection are depicted. For comparison, the case of a single molecule already shown in Figure 4.2b is also rendered.

level. Nonetheless, the total Raman signal $\int S(\omega)\, \mathrm{d}\omega$ is almost independent of the collection method. Combined with the results above, we can thus conclude that under strong coupling, the total dipole strength ($\propto N$) is redistributed between the modes, but not enhanced significantly.

4.4. Conclusion

Raman scattering is one of the most widespread methods to access information about nuclear vibrations in molecules, providing complementary information to the infrared absorption spectrum, reproduced for vibro-polaritons in chapter 3. In this chapter, we have exploited the fact that the same vibrational mode is also Raman active to address the characteristic fingerprints in the Raman spectrum in the strong coupling regime. In particular, we employed a series of increasingly sophisticated models in order to demonstrate that the primary effect of VSC is a redistribution of the total Raman cross-section, with the Stokes lines for (multiple) vibrational excitation splitting into multiplets corresponding to (multiple) excitation of the lower and upper polaritons. The total cross section (integrated over the emission frequency) is approximately conserved. Using a simple analytical argument, we showed that this is true as long as the USC regime is not reached. Once the Rabi splitting becomes comparable to the transition frequency

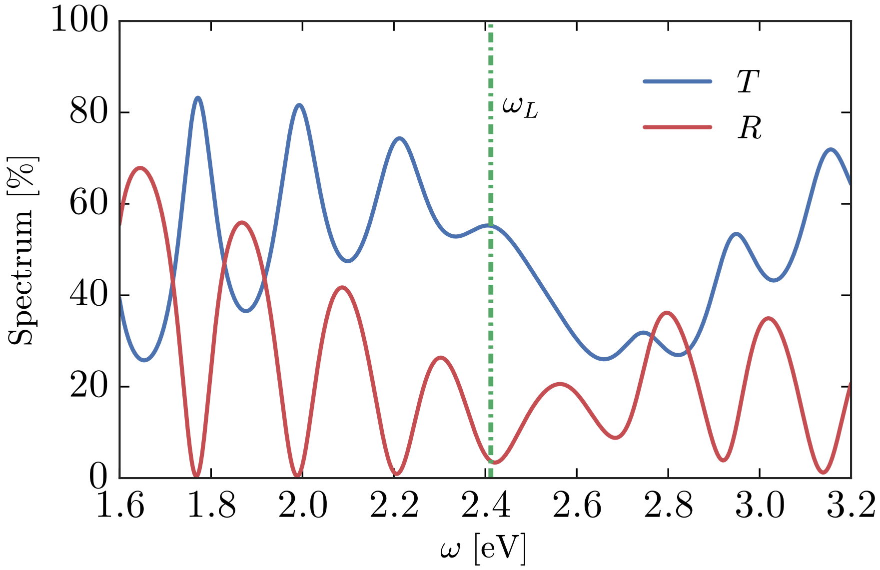

Figure 4.4: Transmission and reflection spectrum for the cavity used in Shalabney et al VSC experiment in the visible region (10 nm− Au mirror −2 μm PVAc -10 nm Au mirror). The dielectric functions employed for the gold mirrors and the molecular layer are introduced in section 3.2.

and ultrastrong coupling is achieved, the induced change in the ground state does lead to an increase of the total integrated Raman cross-section, with an enhancement by less than a factor of two for realistic values. We additionally found that the Stokes lines in the strongly coupled Raman spectrum are located at the same energies (and thus posses the same Rabi splitting) as in the transmission spectrum.

In contrast with the results presented in this chapter, the experiment [212] found a significant enhancement of the Raman signal by two to three orders of magnitude under VSC, as well as an increase in the Rabi splitting between lower and upper polariton by more than a factor of two in the Raman spectrum compared to the transmission spectrum. It must be noted that a straightforward transfer matrix simulation of the experimental micro-cavity shows optical photons (in the experiment $\lambda_L = 514$ nm) are not efficiently confined within the mirrors (see Figure 4.4), therefore excluding stimulated scattering effects. We thus finish by discussing additional effects that could affect RS under VSC and examine whether they can explain the discrepancy between theory and experiment.

First, in our models, we only included a single cavity mode, while a planar cavity supports a continuum of photonic modes. However, the argument based on Equation 4.14 above does not depend on the number of cavity modes or molecules in the system. We have additionally confirmed this by explicitly including multiple cavity modes within the three-level model (not shown). We also neglected the rotational degrees of freedom of the molecules. Additionally, we have checked explicitly that a permanent dipole moment and orientation effects do not lead to an increase of the integrated Raman cross section under strong coupling. One remaining possibility for explaining the increased Raman yield observed in the experiments within linear response is that an (unknown) VSC-induced process could lead to a modification of the bare-molecule dipole transition strengths. This would require an increase by a factor of about $\sqrt[4]{1000} \approx 6$ for each of the dipole moments, μ_{ge} and μ_{ev}. This change is not contained within the state modifications induced by USC that are fully incorporated in our modelling. Nevertheless, the increase in the dipole strengths would not provide an explanation for the increased Rabi splitting observed in Raman vs transmission spectra. Unexpected enhancements of two orders of magnitude in the Raman cross section has also been reported in polaritons formed upon hybridisation of dipole-active phonon resonance of semiconducting (CdS) nanocrystals and THz plasmons [310]. Finally, it is important to remark that later theoretical studies of the same system by Strashko and Keeling [250], have extended our analysis by deriving expressions for the Raman cross section of vibro-polaritons introducing additional effects such as anharmonicities in the PES (leading to polariton-polariton interactions). In agreement with our discussion here, these studies do not unveil the effects responsible for the experimentally observed enhancement.

Finally, we have up to now neglected non-linear effects, and only calculated the linear response of RS. Typically, Raman cross sections are quite small and non-linear effects are thus negligible under weak coupling. However, under strong coupling, the number of populated final states reached by RS is drastically reduced, from (within the first Stokes line) one per molecule to just two extended polaritons. If the effective polariton excitation rate becomes faster than its lifetime, this could lead to an accumulation of polaritons and, subsequently, bosonic enhancement of the RS. Moreover, these non-linear interactions could also induce polariton energy shifts, such that non-linear behaviour could possibly explain both the experimentally observed enhancement as well as energy shift under RS. While a more detailed treatment is outside of the scope of this thesis, it should be noted that order-of-magnitude estimates indicate that in the experiments [212] excitations are created significantly slower than the polariton decay rate. Therefore, non-linear behaviour would only be expected if there is an additional enhancement factor in the system independent of strong coupling (such as, e.g., the presence of local field enhancement at hot spots if the mirror surfaces have rough structure). This highlights the necessity for further theoretical and experimental exploration of non-linear effects in RS processes under VSC.

The investigations presented in this chapter serve to motivate further explorations in the system. As we show in the following chapter 5, while cross sections for RS are typically small even for vibro-polaritons, the process can become highly efficient under strong driving if scattered Stokes photons accumulate sufficiently to lead to stimulated Raman scattering (SRS) [311]. The effective energy conversion from input to output beam can then be exploited to fabricate a highly tunable Raman laser, and VSC paves the way to improve such device and offer new capabilities.

5 | Exploiting Vibro-polaritons to Engineer Novel devices

5.1. Motivation

When a molecular ensemble displaying a Raman active transition is placed inside an optical resonator tuned to the Stokes resonance ω_S, photons at this energy can be accumulated very efficiently leading to stimulated Raman scattering (SRS), which can be exploited to manufacture a very tunable Raman laser. Raman lasers have been realised using a variety of nonlinear media and configurations, such as under pulsed operation in optical fibers [219], non-linear crystals [220], gases [221], or silicon [222], as well as under continuous-wave operation in silicon [223, 224], silica [225] and molecular hydrogen [226]. Since the threshold powers for these systems are typically large, they suffer from detrimental effects such as Kerr non-linearities, four-wave mixing, and heat deposition [220].

In chapter 4 we have proposed a theoretical model for the Raman effect, demonstrating it actually occurs in the vibro-polaritons mediated by their material component. In the first place, this fact results in Stokes lines displaced in the Raman spectrum and, more relevant for the current discussion, it provides a photonic component to the final states of the scattering. Thanks to these novel properties, we theoretically demonstrate in this chapter that the hybrid light-matter nature of vibro-polaritons can be utilised to obtain photon emission from the vibrationally excited final states of a Raman laser. A single-output Raman laser device then becomes analogous to a nondegenerate OPO, which converts an input pump beam into two coherent output beams [227] at different frequencies. In the present case, the 'signal' beam in the visible corresponds to the conventional Raman laser output, while the 'idler' beam is emitted by the vibro-polaritons in the mid-IR. Importantly, the signal and idler beams emitted by OPOs are coherent and have a stable phase relation, as well as providing possibly entangled pairs of photons with nonclassical correlations [228–233]. In addition to the OPO properties, our approach has the advantage over Raman lasers of effectively getting rid of the energy deposited into material vibrations; instead of being dissipated as heat, this energy is emitted in the form of photons. Finally, we show that the coexistence of the upper and LP modes with very similar properties can be exploited to produce an all-optical switch [236, 237]. Here, one (gate) pump beam can be used to switch Raman lasing of a second (signal) pump beam.

This chapter is organised as follows: we discuss first the phenomenon of RS with vibro-polaritons as final states when the system is strongly driven such that it reaches SRS. To this end, we propose a model that extends the minimal three-level approach introduced in section 4.2, by first considering a single pump scenario with frequency matched to optimise the efficiency of SRS into a given polariton and finally by exploiting the coexistence of upper and lower polaritons by adding a second frequency-matched pump. Finally, we characterise the resulting systems in section 5.3 by obtaining semiclassical solutions that characterise the high-excitation solutions and for instance the lasing threshold. In this way, we unveil how vibro-polaritons enable improvements and new features over pre-existing Raman laser devices. Finally, we propose a simple experimental setup to implement such device employing state-of-the-art technology.

5.2. Theoretical model for off-resonant SRS

5.2.1. Single pump setup

The system we consider now (sketched in Figure 5.1a) consists, as in previous chapter of a material with a vibrational transition that is both IR- and Raman-active, placed inside a resonator (e.g. a micro-cavity). The resonator supports now at least two confined modes, a mid-IR mode used to achieve VSC with the vibrational transition, and an optical mode used to accumulate the scattered Stokes photons. For the molecular ensemble, we employ the simplest model in chapter 4, consisting of N non-interacting three-level quantum emitters, formed by the ground state $|g\rangle$ (energy $\omega_g \equiv 0$), the first excited vibrational mode $|v\rangle$ (energy ω_v), and an electronically excited state $|e\rangle$ (energy ω_e). As we described in the previous section, this model captures the principal features of the first Stokes line for RS into vibro-polaritons. While this model can naturally represent organic molecules (as used in current experiments achieving VSC), we note that it can

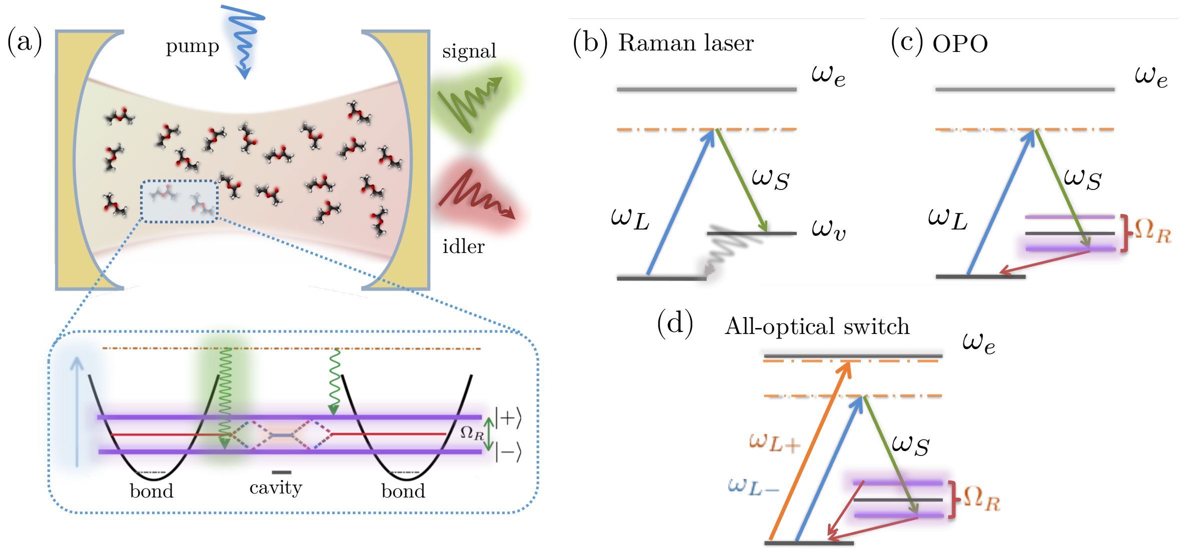

Figure 5.1: (a) Sketch of setup to convert a Raman laser into an OPO through vibrational strong coupling. The lower part of the figure shows the hybridisation between molecular bonds and the infrared cavity mode schematically. (b) In a Raman laser, Raman scattering of the pump (blue arrows) leads to vibrationally excited final states that decay non-radiatively, so that only a signal beam (green) is emitted. (c) Under strong coupling of the vibrational excitations with a resonant cavity mode, the new final states (vibro-polaritons) can decay through photon emission, producing an idler beam as a second output. (d) By adding a second pump both polaritons can be targeted by RS, yielding an all-optical switch with three outputs.

also be used to treat systems such as the nonlinear crystals utilised in existing Raman lasers. Under off-resonant driving as will be considered here, the parameters of $|e\rangle$ can be adjusted such that it represents the full rovibrational manifold of electronically excited states.

The system Hamiltonian is given by $\hat{H}_s = \hat{H}_v + \hat{H}_O$, where $\hat{H}_v$ describes the vibrational excitations and their coupling to the mid-IR cavity mode and it is given by Equation 4.1, and $\hat{H}_O$ describes the excitations and cavity mode at optical energies. We first treat the dynamics of the system under external driving of a single pump mode at frequency ω_L (not resonant with any cavity mode), see Figure 5.1. The optical-frequency Hamiltonian $\hat{H}_O$ then contains the electronic excitations of the molecules, the pump field (which we quantise in order to be able to describe depletion [206]), the cavity mode in the optical (frequency ω_S), and the interactions between the molecular transitions and the optical modes, leading to

$$\hat{H}_O = \omega_S \hat{n}_S + \omega_L \hat{n}_L + \sum_{i=1}^{N} \left[\omega_e \hat{\sigma}_{ee}^{(i)} + \left(g_S \hat{a}_S \hat{\sigma}_{ve}^{(i)\dagger} + g_L \hat{a}_L \hat{\sigma}_{ge}^{(i)\dagger} + \text{H.c.} \right) \right], \tag{5.1}$$

where $\hat{n}_L = \hat{a}_L^\dagger \hat{a}_L$ and $\hat{n}_S = \hat{a}_S^\dagger \hat{a}_S$ are the photon number operators for the pump laser and confined cavity mode, which are coupled (within the RWA) to the ground-excited and excited-vibrational transitions in the molecules, respectively.

When the driving laser is far off-resonant to the electronic transition such that the hierarchy condition $\omega_e \gg \omega_L \gg \omega_v$ is satisfied, as shown below, we can adiabatically eliminate the electronically excited states from the problem [312, 313]. If the laser frequency is moreover chosen such that RS into the 'Stokes' cavity mode S is resonant with one of the polariton modes, i.e., $\omega_L = \omega_S + \omega_p$ (with $p = +$ or $p = -$), scattering to the other polaritonic mode can be neglected, as shown below, under a second RWA.

In the following we illustrate how the aforementioned adiabatic elimination works. As stated above, we assume that the detuning $\Delta = \omega_e - \omega_L$ is large compared with the relevant energy scales for the electronic ground states ($|g^{(i)}\rangle$, $|v^{(i)}\rangle$), and that the interaction terms involving electronic excitations in Equation 5.1 are perturbative. In the following, we denote these terms as $\hat{V} = \hat{V}_+ + \hat{V}_+^\dagger$, where $\hat{V}_+$ contains all the terms *creating* electronic excitations. The occupation of the electronically excited states $|e^{(i)}\rangle$ with free evolution Hamiltonian $\hat{H}_e = \omega_e \sum_{i=1}^N \hat{\sigma}_{ee}^{(i)}$ is hence vanishingly small. In particular, this assumption enables to avoid the coupling of different electronically excited states, simplifying the following treatment. In the adiabatic elimination approach [314], the density matrix equations are solved by assuming a slow evolution of the lowest-lying states $|g^{(i)}\rangle$, $|v^{(i)}\rangle$ and the optical modes $\hat{a}_S$, $\hat{a}_L$, governed by $\hat{H}_g = \hat{H}_v + \omega_S \hat{n}_S + \omega_L \hat{n}_L$. We here ignore contributions originating from the incoherent dynamics within the electronic excited manifold, which could be introduced by means of effective Lindblad terms [313], but are negligible for large detuning. To perform the adiabatic approximation, we *i)* apply the *rotating-frame* transformation $\hat{U} = e^{-i(\omega_S \hat{n}_S + \omega_L \hat{n}_L)t}$ and *ii)* we work in the eigenbasis of $\hat{H}_s$. The resulting Hamiltonian is

$$\hat{H}' = \hat{H}_s - \frac{1}{2} \hat{V}_+'^\dagger(t) \sum_{f,l} \frac{\omega_e}{\omega_e - \omega_f - \omega_l} \hat{H}_e^{-1} \hat{v}_+^{(l,f)} e^{i\omega_f t}. \tag{5.2}$$

Here, $\hat{V}_+'(t)$ has been expanded in terms of its frequency components $f \in (L, S)$, as well as the system eigenstates $l \in (+, -, \{d\})$ that it couples to, giving

$$\hat{V}_+'(t) = \sum_{f,l} \hat{v}_+^{(f,l)} e^{i\omega_f t} = \sum_{i=1}^N \left[g_L \hat{a}_L \hat{\sigma}_{Ge}^{\dagger(i)} e^{i\omega_L t} + g_S \hat{a}_S \left(\sum_{\eta=\{\pm\}} \frac{\hat{\sigma}_{\eta e}^{\dagger(i)}}{\sqrt{2N}} + \sum_d u_{id} \hat{\sigma}_{de}^{\dagger(i)} \right) e^{i\omega_S t} \right]. \tag{5.3}$$

Here, the coefficients appearing between parenthesis follow from the eigenstate expansions $\left|v^{(i)}\right\rangle = (2N)^{-\frac{1}{2}} \sum_{\eta=\{\pm\}} |\eta\rangle + \sum_d u_d^{(i)} |d\rangle$, where $u_d^{(i)}$ is the overlap matrix element between the ith vibrational excitation and dark state d. These coefficients fulfill $\sum_{i=1}^N u_d^{(i)} = 0$ and are further constrained by the orthogonality relation $\sum_{i=1}^N u_d^{(i)} u_{d'}^{(i)} = \delta_{dd'}$. After going back to the nonrotating frame, the resulting effective interaction reads

$$\hat{H}_{\text{int}}^{\text{eff}} = - \sum_{\eta=\{\pm\}} g_{\text{eff}}^{\eta} (\hat{a}_L \hat{a}_S^\dagger \hat{\sigma}_{G\eta}^\dagger + \text{H.c.}), \tag{5.4}$$

with $g_{\text{eff}}^{\eta} = \frac{g_S g_L}{2} \sqrt{\frac{N}{2}} \left[(\omega_e - (\omega_\eta + \omega_S))^{-1} + \Delta^{-1} \right]$. Note here that the contribution of the dark states is identically zero in the effective dynamics. This is due to the fact that we assumed perfect overlap between the involved modes, i.e., we took g, g_S, and g_L to be constant for all involved molecules. Relaxing this condition, the inclusion of the spatial profile of the pump, would give an additional overlap prefactor $g_{\text{eff}}^{\eta} \rightarrow \mathcal{J} g_{\text{eff}}^{\eta}$, with $\mathcal{J} \propto \sum_i u_\eta^{(i)} g_{S,i} g_{L,i}^*$, and also give nonzero coupling to the dark states, but would not otherwise change the results presented in the main text. In addition to the effective interaction, we obtain (nonlinear) energy shifts, given by

$$\hat{H}_{\text{shift}}^{\text{eff}} = -\frac{g_L^2 N}{\Delta} \hat{n}_L \hat{\sigma}_{GG} - \sum_l \frac{g_S^2 \hat{n}_S \hat{\sigma}_{ll}}{\omega_e - (\omega_l + \omega_S)}. \tag{5.5}$$

Under the assumption that the output modes are not significantly populated ($\hat{\sigma}_{GG} \approx 1$, $\hat{n}_S, \hat{\sigma}_{\eta\eta} \ll 1$), the first term just gives a constant energy shift (which we assume to be included into ω_L), while the second term can be neglected. This is a good approximation for typical system parameters even when a large number of output photons is generated, due to the relatively short lifetime of the polaritons. Under this approximation, the vibro-polaritons are well modeled as bosons $[\hat{\sigma}_{G\eta}, \hat{\sigma}_{G\eta'}^\dagger] \simeq \delta_{\eta\eta'}$, and the trilinear interaction Equation 5.6 corresponds to a nondegenerate OPO under the identifications $\hat{a}_S \rightarrow$ signal, $\hat{\sigma}_{Gp} \rightarrow$ idler.

For a laser frequency chosen such that RS to one of the polaritonic modes is resonant with the cavity mode S in the optical, $\omega_L = \omega_S + \omega_p$, with $p \in \{\pm\}$, there are rapidly oscillating terms in Equation 5.4 in the interaction picture with regards to $\hat{H}_g$. Averaging over a time sufficiently big compared to $\tau_{\text{SC}} \sim 1/\Omega_R$, these contributions, which correspond to the coupling of the laser field with the detuned polariton, can be neglected under a *second* rotating wave approximation, yielding

$$\hat{H}_{\text{eff}} \simeq \omega_L \hat{n}_L + \omega_S \hat{n}_S + \omega_p \hat{\sigma}_{pp} - g_{\text{eff}}^p \left(\hat{a}_L \hat{a}_S^\dagger \hat{\sigma}_{Gp}^\dagger + \text{H.c.} \right). \tag{5.6}$$

In Equation 5.6 the effective coupling occurs between laser photons and pairs of Stokes photons and polaritons, while the dark modes are not excited. The coupling strength is given by

$$g_{\text{eff}}^{p} = \sqrt{\frac{N}{2}} \frac{g_S g_L}{\omega_e - (\omega_p + \omega_S)}, \tag{5.7}$$

and is not sensitive to the Rabi splitting of the polaritons. This agrees with the case of linear RS, analysed in chapter 4 where theory predicts a redistribution of the scattering cross-section of the system without further enhancement.

The trilinear interaction in the effective Hamiltonian Equation 5.6 is analogous to a nondegenerate OPO[1], converting an input laser beam into two new modes, the 'signal' (Stokes beam) and 'idler' (vibro-polaritons) [227]. For a standard Raman laser, this analogy is merely formal [311], since most of the excitation in the vibrationally excited states decays non-radiatively and no idler beam is emitted. In the VSC regime, however, the hybrid light-matter nature of the polaritons imbues them with a photonic component, leading to efficient outcoupling in the form of photons. This makes the analogy complete and provides an approach towards converting a Raman laser into an OPO, as sketched in Figure 5.1c. Such a setup could be realised, for example, in cavities made from dielectric distributed Bragg reflectors, which show low losses and have previously been used to achieve strong coupling with both vibrational modes and excitons [127, 200]. We will show in a subsequent subsection 5.3.2 a concrete implementation based on silicon carbide-silicon dioxide mirrors, with PVAc as the active material.

We next discuss the role of losses and dephasing. Within the standard Lindblad master-equation formalism, the density operator $\hat{\rho}$ evolves according to

$$\partial_t \hat{\rho} = -i[\hat{H}_{\text{eff}}, \hat{\rho}] + \kappa_S \mathcal{L}_{\hat{a}_S}[\hat{\rho}] + \kappa_L \mathcal{L}_{\hat{a}_L}[\hat{\rho}] + \tilde{\Gamma}_{\text{vib}}[\hat{\rho}], \tag{5.8}$$

where $\mathcal{L}_X[\hat{\rho}]$ is the Lindblad superoperator given by Equation 2.32. The loss rates of the Stokes and quantised laser modes due to leakage out of the cavity and absorption losses are given by κ_S and κ_L, respectively. The term $\tilde{\Gamma}_{\text{vib}}$ summarises all decoherence mechanisms affecting the vibrationally excited subspace. Under weak coupling, these consist of nonradiative decay of the vibrational excitations to the ground state ($\gamma_v \mathcal{L}_{\hat{\sigma}_{gv}}[\hat{\rho}]$) and pure dephasing induced by elastic collisions with background phonons ($\gamma_\varphi \mathcal{L}_{\hat{\sigma}_{vv}}[\hat{\rho}]$). In the VSC regime, the polaritons additionally decay through the losses associated with

---

[1] Despite the formal analogy with the OPO, the scattering in this system does not occur as a consequence of a $\chi^{(2)}$ non-linearity in the material but instead would result from a $\chi^{(3)}$ process [311]. Moreover, the behaviour described here does not arise in the so-called OPO regime in inorganic micro-cavities [39]. In this case, strong pumping close to the inflection point in the LP branch (the so-called 'magic angle'), yields coherent parametric scattering of the incoming pump field $\{\mathbf{k}_L, \omega_L\}$ into lower energy signal $\{\mathbf{k}_s, \omega_s\}$ and a higher-energy idler polariton mode $\{\mathbf{k}_i, \omega_i\}$.

the mid-IR cavity (κ_c), but the influence of inhomogeneous broadening and dephasing can be suppressed for large enough Rabi splitting(see [299] and chapter 3). The effective decay of the polaritons ($\Gamma_\pm \mathcal{L}_{\hat{\sigma}_{g\pm}}[\hat{\rho}]$) can then have a rate as small as $\Gamma_\pm \approx (\kappa_c + \gamma_v)/2$, significantly below the average of the bare-molecule ($\gamma_v + \gamma_\varphi$) and mid-IR cavity ($\kappa_c$) linewidths. We note here that even under weak coupling, the vibrational excitations can be made to decay mostly through radiation under some circumstances. This regime is reached when the coupling to the cavity is faster than nonradiative decay processes, but not faster than the cavity lifetime, and thus only exists for 'bad cavities', while high-quality cavities as we focus on here directly enter the strong coupling regime as the coupling is increased.

5.2.2. Exploiting the coexistence of the two vibro-polaritons

We next show how the coexistence of two vibro-polariton modes with similar properties allow turning the system into an all-optical switch where emission at one frequency is switched by input at another frequency [236, 237]. This is achieved by including a second pump field, with the two pump frequencies chosen to make the Raman process to the two polariton modes $|+\rangle$ and $|-\rangle$ resonant with the same Stokes frequency,

$$\omega_{L\pm} = \omega_S + \omega_\pm. \tag{5.9}$$

Similarly to the single pump setup above, electronic population will be vanishing under off-resonant conditions and a a similar effective Hamiltonian could be derived. In this case,

$$\hat{H}_d^{(2)} = \sum_{\eta=\{\pm\}} \sqrt{\kappa_{L\eta}} \Phi_{\text{in}}^{\eta} (\hat{a}_{L\eta} e^{-i\omega_{L\eta} t} + \hat{a}_{L\eta}^\dagger e^{i\omega_{L\eta} t}), \tag{5.10}$$

while the pump-system interaction is given by

$$\hat{V}_+ = \sum_{i=1}^{N} \big(g_S \hat{a}_S \hat{\sigma}_{ve}^{(i)\dagger} + \sum_{\eta=\{\pm\}} g_{L\eta} \hat{a}_{L\eta} \hat{\sigma}_{ge}^{(i)\dagger} \big). \tag{5.11}$$

The frequencies $\omega_{L\pm}$ are chosen to satisfy the resonance conditions for both polaritons, $\omega_{L\pm} = \omega_S + \omega_\pm$. The adiabatic elimination of the electronic states proceeds analogously to the single-pump case, giving the effective interaction Hamiltonian

$$\hat{H}_{\text{int}}^{\text{eff}(2)} = - \sum_{\eta,\eta'=\{\pm\}} g_{\text{eff}}^{\eta,\eta'} (\hat{a}_{L\eta'} \hat{a}_S^\dagger \hat{\sigma}_{G\eta}^\dagger + \text{H.c.}), \tag{5.12}$$

where the effective coupling constant of the pump field η with the polariton η' is (using $\Delta_\pm = \omega_e - \omega_{L\pm}$)

$$g_{\text{eff}}^{\eta,\eta'} = \frac{g_S g_{L\eta}}{2}\sqrt{\frac{N}{2}}\left[\frac{1}{\omega_e - (\omega_{\eta'} + \omega_S)} + \frac{1}{\Delta_\eta}\right]. \tag{5.13}$$

The off-diagonal terms $\eta \neq \eta'$ can be neglected under the same *second* RWA we invoked for the OPO case. In addition to the effective interaction, we again obtain extra nonlinear terms, given by

$$\hat{H}_{\text{extra}}^{\text{eff}(2)} = -\sum_{\eta,\eta'} \Lambda_{\text{eff}}^{\eta,\eta'} \hat{\sigma}_{GG}(\hat{a}_{L\eta}^\dagger \hat{a}_{L\eta'} + \text{H.c.}) - \hat{n}_S \sum_l \frac{g_S^2 \hat{\sigma}_{ll}}{\omega_e - (\omega_l + \omega_S)}, \tag{5.14}$$

which in addition to the energy shifts already seen in the single-pump OPO case also contains an extra crossed term coupling the two pump fields. The nonlinear terms Equation 5.14 can again be neglected under the low-occupation assumption and the second RWA. Finally, we thus obtain

$$\hat{H}_{\text{eff}}^{(2)} \simeq \omega_S \hat{n}_S + \sum_{\eta=\{\pm\}} \left[\omega_{L\eta}\hat{n}_{L\eta} + \omega_\eta \hat{\sigma}_{\eta\eta} - g_{\text{eff}}^\eta (\hat{\sigma}_{G\eta}\hat{a}_S \hat{a}_{L\eta}^\dagger + \text{H.c.})\right], \tag{5.15}$$

where we used that $g_{\text{eff}}^{\eta,\eta} = g_{\text{eff}}^\eta$.

Concluded the derivation of the effective model Hamiltonians, our next goal in this chapter is to characterise the performance of the proposed devices. To this end, we carry our a mean-field analysis in the following section.

5.3. Results

5.3.1. Vibro-polariton optical parametric oscillator

In order to characterise the threshold condition and quantum yield of the VSC-based OPO described above, we calculate the steady-state populations under continuous-wave driving of the pump mode, with

$$\hat{H}'_{\text{eff}} = \hat{H}_{\text{eff}} + \Phi_{\text{in}}\sqrt{\kappa_L}(\hat{a}_L e^{-i\omega_L t} + \hat{a}_L^\dagger e^{i\omega_L t}), \tag{5.16}$$

where Φ_{in} parametrises the driving strength. The results derived below are also valid under time-dependent driving as long as the pump amplitude Φ_{in} varies more slowly than the time required to reach the steady-state. We solve the Lindblad master equation Equation 5.8 within the mean-field approximation, in which all fields are assumed to be described by coherent amplitudes [187][2]. This leads to semi-classical Heisenberg-Langevin equations of motion in terms of the slowly-varying amplitudes $\alpha_L = \langle \hat{a}_L \rangle e^{i\omega_L t}$, $\alpha_S = \langle \hat{a}_S \rangle e^{i\omega_S t}$, and $\psi_p = \langle \hat{\sigma}_{Gp} \rangle e^{i\omega_p t}$, given by

$$\partial_t \alpha_L = i g_{\text{eff}}^p \psi_p \alpha_S - \kappa_L \alpha_L + i\sqrt{\kappa_L}\Phi_{\text{in}}, \tag{5.17a}$$

$$\partial_t \alpha_S = i g_{\text{eff}}^p \psi_p^* \alpha_L - \kappa_S \alpha_S, \tag{5.17b}$$

$$\partial_t \psi_p = i g_{\text{eff}}^p \alpha_S^* \alpha_L - \Gamma_p \psi_p. \tag{5.17c}$$

The corresponding steady-state solutions (which agree with the classical treatment of an OPO [315]) can be parametrised in terms of $f = \Phi_{\text{in}}/\Phi_{\text{th}}$, where $\Phi_{\text{th}} = \sqrt{\kappa_L \kappa_S \Gamma_p}/g_{\text{eff}}^p$ is the threshold value for the driving parameter. Below threshold ($f < 1$), neither the polariton nor the Stokes mode are populated ($|\psi_p|^2 = |\alpha_S|^2 = 0$), while the pump mode has population $|\alpha_L|^2 = f^2\Phi_{\text{th}}^2/\kappa_L$. Above threshold ($f \geq 1$), the pump amplitude becomes independent of the driving power (so-called pump clamping), $|\alpha_L|^2 = \Phi_{\text{th}}^2/\kappa_L$, while the Stokes and polariton mode occupations grow linearly with input power, $|\psi_p|^2 = (f-1)\Phi_{\text{th}}^2/\Gamma_p$ and $|\alpha_S|^2 = (f-1)\Phi_{\text{th}}^2/\kappa_S$. This implies that the conversion efficiency approaches 100% if the pumping is sufficiently strong. Explicitly, the quantum yield for conversion of input photons to pairs of Stokes photons and polaritons follows the simple relation

$$\mathcal{Q} = \frac{P_S/\omega_S}{P_{\text{in}}/\omega_L} = 1 - \frac{1}{f}, \tag{5.18}$$

where $P_S/\omega_S = \kappa_S|\alpha_S|^2$ ($= P_p/\omega_p$) is the flux of emitted Stokes photons, and $P_{\text{in}} = \omega_L \Phi_{\text{in}} \Phi_{\text{th}}$ is the input power.

The number of photons emitted at the vibro-polariton frequency (typically in the mid-IR [140]) is equal to the number of generated Stokes photons, multiplied by the radiative emission efficiency of the polaritons, $\beta = \Gamma_p^{\text{rad}}/\Gamma_p$. For zero detuning and a mid-IR cavity without nonradiative losses (such as a dielectric cavity [200]), this is given by $\beta = \frac{\kappa_c}{\kappa_c + \gamma_v}$, which is close to unity for the experimentally relevant regime $\kappa_c \gg \gamma_v$. In a standard Raman laser, the energy deposited into the vibrational modes is converted to heat, limiting the achievable powers [220, 227]. In contrast, the vibro-polariton Raman OPO proposed here converts this energy efficiently into an additional coherent output beam at mid-IR frequencies, and thus simultaneously reduces heating significantly.

Furthermore, the ratio between the thresholds for polariton-based OPO operation under strong coupling and for the bare-molecule Raman laser under weak coupling is

---

[2] Alternative treatments of the OPO problem assume only the pump bosons reduce to complex numbers, keeping the operator nature of signal and idler. This enables to analyse purely quantum behavior in the system and pump-induced renormalisation processes (see [39] for further details)

given by

$$\frac{\Phi_{\text{th}}^{SC}}{\Phi_{\text{th}}^{WC}} = \sqrt{\frac{\Gamma_p}{\gamma_v + \gamma_\varphi}} \approx \sqrt{\frac{\kappa_c}{2\gamma_\varphi}}. \tag{5.19}$$

This demonstrates that for the common case that the inhomogeneous width and dephasing of the vibrational modes are faster than the cavity losses ($\gamma_\varphi > \kappa_c$), the vibro-polariton Raman OPO has a lower threshold power than the equivalent Raman laser. In addition, depending on the relative lifetimes of the vibro-polaritons Γ_p and the Stokes photons κ_S, there can be significant accumulation of population in the vibro-polariton mode, suggesting a roadmap towards achieving vibro-polariton condensation (in analogy to exciton-polariton condensation [43]) based on the high efficiency of SRS[3].

5.3.2. DBR-based implementation

In this section, we illustrate a possible experimental realisation of the setup proposed in subsection 5.2.1. As discussed there, the system needs to possess two confined modes, one in the mid-IR frequency range to achieve vibrational strong coupling, and the other at optical frequencies to accumulate the scattered Stokes photons. The setup proposed here consists of a micro-cavity with mirrors formed by the concatenation of two distributed Bragg reflectors (see Figure 5.2a). As outlined in subsection 1.3.1, DBR micro-cavities based on dielectric materials have been shown to provide sharp (long-lived) cavity modes suitable for achieving strong coupling both at optical [127, 317] and mid-IR frequencies [200]. In the setup proposed here, the inner DBRs provide confinement for the optical mode, while the outer ones confine the mid-IR mode.

Each DBR is a multilayer structure with alternating dielectric layers (refractive indexes n_1, n_2), with layer widths chosen as $\lambda/(4n_1)$ and $\lambda/(4n_2)$, respectively. This leads to efficient reflection in a ‘stop band’ centred at a wavelength λ. The ‘outer’ DBRs are formed by five groups of alternating layers of silicon carbide (SiC) and silica (SiO_2) with widths chosen to provide maximum reflectivity at the frequency of the C=O stretching mode of PVAc, ω_v = 215 meV. The inner mirrors are formed by four groups of layers of SiC and PVAc, with a larger central ‘cavity’ (thickness $\approx$ 204 nm) in the centre that is also filled with PVAc. The inner mirrors then fulfil a double purpose: They provide confinement for the optical mode at the Stokes frequency ω_S and their PVAc-components

---

[3] Saturation effects in the vibro-polaritons, resulting from anharmonicities, could be included after replacing bosons by saturable absorbers and considering a Holstein-Primakoff transformation [316], leading to a population-dependent term $\sim |\psi_p|^2$ in Equation 5.17c.

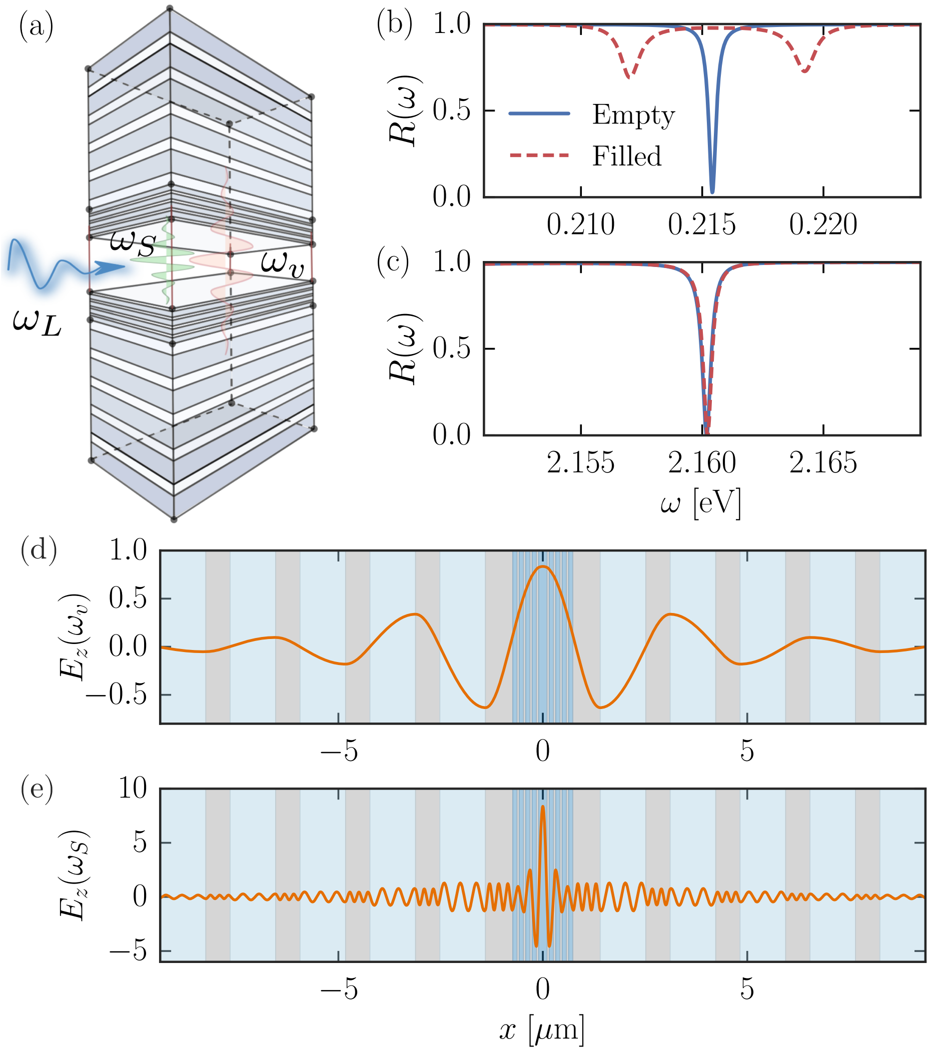

Figure 5.2: (a) Sketch of a double DBR cavity for both mid-IR and optical modes (not to scale). The blue arrow depicts the driving beam, while the green and red fields sketch the confined modes. (b,c) Reflectivity spectra in the mid-IR and visible region. The doublet in (b) is a signature of VSC with the C=O bond stretching mode of PVAc at $\omega_v = 215$ meV. (d,e) Cavity structure and electric field profiles (in arbitrary units) of the mid-IR and optical cavity modes. The DBRs consist of SiC (grey), SiO_2 (light blue), and PVAc (medium blue).

contribute to the vibrational strong coupling between the mid-IR cavity mode of the outer mirrors and the C=O stretch mode of PVAc.

We characterise the system through transfer matrix calculations, using tabulated dielectric functions for SiC and SiO_2 [318], and an explicit parametrisation for PVAc [140], given by $\epsilon_{\mathrm{PVAc}}(\omega) = \epsilon_B - f_j/(\omega^2 - k_j^2 + i\omega\gamma_j)$ with $\epsilon_B = 1.41^2$, $f_j = 7.685 \cdot 10^{-4}$ eV^2, $k_j = 0.215$ eV, and $\gamma_j = 1.611$ meV (introduced also in section 3.2). This parametrisation allows to turn off strong coupling by setting $f_j = 0$, and thus to obtain the 'empty' cavity properties. As demonstrated in Figure 5.2, the proposed double-mirror DBR cavity supports sharp modes both at IR ($\omega_{\mathrm{IR}} \approx 215$ meV, $\kappa_c \approx 0.36$ meV, quality factor $Q_c \approx 600$) and optical frequencies ($\omega_S \approx 2.16$ eV, $\kappa_S \approx 0.30$ meV, $Q_S \approx 7100$). We here tuned the width of the innermost outer-mirror layer to bring the cavity mode into resonance with the C=O bond stretching mode of the PVAc molecules. For the 'filled' cavity ($f_j \neq 0$), we clearly observe a splitting of the mid-IR mode due to vibrational strong coupling, with Rabi splitting $\Omega_R \approx 7.2$ meV (see Figure 5.2b). The mode overlap between the mid-IR polaritons and the Stokes mode is given by $\mathcal{J} \approx 7\%$.

5.3.3. Double driving: vibro-polariton all-optical switch

We finally proceed to the discussion of the two-pump scenario introduced in subsection 5.2.2. Similarly to the single pump setup, we obtain Heisenberg-Langevin equations under driving in the mean-field approximation, out of Equation 5.8 and Equation 5.15,

$$\partial_t \alpha_{L\pm} = i g_{\mathrm{eff}}^{\pm} \psi_{\pm} \alpha_S - \kappa_L \alpha_{L\pm} + i\sqrt{\kappa_{L\pm}} \Phi_{\mathrm{in}}^{\pm}, \tag{5.20a}$$

$$\partial_t \alpha_S = i g_{\mathrm{eff}}^{+} \psi_{+}^{*} \alpha_{L+} + i g_{\mathrm{eff}}^{-} \psi_{-}^{*} \alpha_{L-} - \kappa_S \alpha_S, \tag{5.20b}$$

$$\partial_t \psi_{\pm} = i g_{\mathrm{eff}}^{\pm} \alpha_S^{*} \alpha_{L\pm} - \Gamma_{\pm} \psi_{\pm}. \tag{5.20c}$$

The basic idea for achieving all-optical switching is then to use one of the pump lasers as the input signal ($s = \pm$) and the other pump laser as a gate ($g = \mp$). If the gate beam is turned off, the system is identical to the OPO discussed up to now, and a weak signal beam ($f_s = \Phi_{\mathrm{in}}^s / \Phi_{\mathrm{th}}^s < 1$) will not lead to lasing, such that the corresponding polaritonic mode is not populated. On the other hand, if the gate beam is strong enough to support OPO operation ($f_g > 1$), the RS for even a weak signal beam is stimulated by the macroscopic population of the Stokes mode, $|\alpha_S|^2 \gg 1$. We next demonstrate this idea in more detail by solving for the steady-state.

The relative phases of the different modes are fixed in the steady state, leading to five equations only involving the absolute amplitudes,

$$\kappa_S |\alpha_S| = \sum_{\eta = \{\pm\}} g_{\mathrm{eff}}^{\eta} |\psi_\eta| |\alpha_{L\eta}|, \tag{5.21a}$$

$$\Gamma_{\pm} |\psi_{\pm}| = g_{\mathrm{eff}}^{\pm} |\alpha_{L\pm}| |\alpha_S|, \tag{5.21b}$$

$$\kappa_{L\pm} |\alpha_{L\pm}| = \sqrt{\kappa_{L\pm}} \Phi_{\mathrm{in}}^{\pm} - g_{\mathrm{eff}}^{\pm} |\psi_{\pm}| |\alpha_S|. \tag{5.21c}$$

Before obtaining the stationary solution of Equation 5.21, it is instrumental to first recall the well-known Manley-Rowe relations for beam fluxes and powers [315] in the single-pump case, which follow straightforwardly from the semiclassical equations Eq. (7) in the main text. They connect the fluxes of emitted photons $P_i/\omega_i = \gamma_i|\alpha_i|^2$ in the different modes, with the simple relation

$$\frac{P_S}{\omega_S} = \frac{P_p}{\omega_p} = \frac{P_L^{\mathrm{th}}}{\omega_L}(f-1), \qquad f = \frac{\Phi_{\mathrm{in}}}{\Phi_{\mathrm{th}}}. \tag{5.22}$$

This explicitly shows that RS converts each of the incoming pump photons into a Stokes photon/polariton pair. From Equation 5.22 and the resonance condition $\omega_L = \omega_S + \omega_p$, we obtain the power relation $P_{\mathrm{in}} = P_S + P_p + P_L^{\mathrm{th}}$. This expresses the fact that the input power $P_{\mathrm{in}} = \omega_L \Phi_{\mathrm{in}} \Phi_{\mathrm{th}}$ is shared among the three modes, with a maximum clamped power for the L mode at threshold equal to Φ_{th}^2. From the analogue steady-state relations within the two-pump scenario, a set of generalised Manley-Rowe relations accounting for the exchange of energy between the modes participating in the scattering holds:

$$\frac{P_S}{\omega_S} = \sum_{\eta=\{\pm\}} \frac{P_\eta}{\omega_\eta}, \qquad \frac{P_\pm}{\omega_\pm} = \frac{P_{\mathrm{in}}^{\pm} - P_{L\pm}}{\omega_{L\pm}}, \tag{5.23}$$

where the input power in each of the pump modes $L\pm$ is $P_{\mathrm{in}}^{\pm} = \omega_{L\pm}\sqrt{\kappa_{L\pm}}\Phi_{\mathrm{in}}^{\pm}|\alpha_{L\pm}|$. Employing the resonance conditions for the two pumps, we obtain the global power relation $\sum_{\eta=\{\pm\}} P_{\mathrm{in}}^{\eta} = P_S + \sum_{\eta=\{\pm\}} (P_\eta + P_{L\eta})$, a direct generalisation of Equation 5.22.

We now proceed to solve the steady-state equations under pumping of both modes ($\Phi_{\mathrm{in}}^{\pm} > 0$), Equation 5.21. The following relations between the $L\pm$ amplitudes hold,

$$\frac{\kappa_{L+}|\alpha_{L+}|^2}{\Phi_{\mathrm{th}}^{+2}} + \frac{\kappa_{L-}|\alpha_{L-}|^2}{\Phi_{\mathrm{th}}^{-2}} = 1, \tag{5.24}$$

expressing the fact that the *global* pump amplitude becomes clamped above the threshold due to its connection to a common Stokes mode (with $\Phi_{\mathrm{th}}^{\pm} = \sqrt{\kappa_{L\pm}\kappa_S\Gamma_\pm/g_{\mathrm{eff}}^{\pm}}$). As we will see in the following, this is not the case for each of the pumping amplitudes individually. The relation Equation 5.24 suggests we can define

$$|\alpha_{L+}| = \frac{\Phi_{\mathrm{th}}^{+}}{\sqrt{\kappa_{L+}}}\sin\Theta, \qquad |\alpha_{L-}| = \frac{\Phi_{\mathrm{th}}^{-}}{\sqrt{\kappa_{L-}}}\cos\Theta, \tag{5.25}$$

with mixing angle Θ in the range $\Theta \in (0, \pi/2)$, such that $|\alpha_{L\pm}| > 0$. Inserting this into the steady state-equations leads to a quartic equation for $t = \tan(\Theta/2)$, given by

$$t^4 + 2(\alpha - \beta)t^3 + 2(\alpha + \beta)t - 1 = 0, \tag{5.26}$$

where $\alpha = f_-(\Phi_{\mathrm{th}}^-)^2/(f_+(\Phi_{\mathrm{th}}^+))^2$, and $\beta = [(\Phi_{\mathrm{th}}^+)^2 - (\Phi_{\mathrm{th}}^-)^2]/(f_+(\Phi_{\mathrm{th}}^+)^2)$.

We have checked that this equation has only one physical solution $0 < t < 1$ for arbitrary values of $\alpha > 0)$ and β. The analytical form of the solution of Equation 5.26 is very lengthy and we thus omit it in the following. However, in the degenerate case with equal thresholds ($\Phi^{+}_{\text{th}} = \Phi^{-}_{\text{th}} = \Phi_{\text{th}}$), we get $\beta = 0$ and the equation can be factorised as $(t^2+1)\,(t^2+2\alpha t-1) = 0$, leading to the single physical solution that will be analysed in the following, $t = \sqrt{1+\alpha^2} - \alpha$, with $\alpha = f_-/f_+$.

Stability analysis

The stability of this semiclassical steady-state can inferred by stability analysis. Collecting the solutions amplitudes in the vector $\boldsymbol{v}^{\infty} = (\alpha_S, \psi_+, \alpha_{L+}, \psi_-, \alpha_{L-}, \text{H.c.})$, inserting the linearised solution $\boldsymbol{v}(t) = \boldsymbol{v}^{\infty} + \delta\boldsymbol{v}(t)$ in Eq. (12) and keeping terms $\mathcal{O}(\delta\boldsymbol{v})$, we obtain the time evolution of the fluctuations, $\partial_t \delta\boldsymbol{v}(t) = \boldsymbol{\mathcal{M}}\delta\boldsymbol{v}(t)$. The stability matrix is

$$\boldsymbol{\mathcal{M}} = \left(\begin{array}{c|cc} -\kappa_S \mathbf{1}_{2\times 2} & \boldsymbol{v}_+ & \boldsymbol{v}_- \\ \hline \boldsymbol{u}_+^T & -\boldsymbol{\mathcal{P}}_+ & 0 \\ \boldsymbol{u}_-^T & 0 & -\boldsymbol{\mathcal{P}}_- \end{array}\right), \tag{5.27}$$

where the submatrices are

$$\boldsymbol{v}_{\pm} = i g^{\pm}_{\text{eff}} \begin{pmatrix} 0 & \alpha_{L\pm} & \psi^*_{\pm} & 0 \\ -\alpha^*_{L\pm} & 0 & 0 & -\psi_{\pm} \end{pmatrix}, \tag{5.28a}$$

$$\boldsymbol{u}_{\pm} = i g^{\pm}_{\text{eff}} \begin{pmatrix} \alpha_{L\pm} & 0 & 0 & -\psi^*_{\pm} \\ 0 & -\alpha^*_{L\pm} & \psi_{\pm} & 0 \end{pmatrix}, \tag{5.28b}$$

$$\boldsymbol{\mathcal{P}}_{\pm} = \begin{pmatrix} \Gamma_{\pm} & 0 & -i g^{\pm}_{\text{eff}} \alpha^*_S & 0 \\ 0 & \Gamma_{\pm} & 0 & i g^{\pm}_{\text{eff}} \alpha_S \\ -i g^{\pm}_{\text{eff}} \alpha_S & 0 & \kappa_{L\pm} & 0 \\ 0 & i g^{\pm}_{\text{eff}} \alpha^*_S & 0 & \kappa_{L\pm} \end{pmatrix}. \tag{5.28c}$$

The fluctuations $\delta\boldsymbol{v}(t)$ will grow exponentially in time if the real part of any eigenvalue of $\boldsymbol{\mathcal{M}}$ is positive. This can be tested via the Routh-Huwirtz criterion [319], which provides necessary and sufficient conditions for the roots of the characteristic polynomial $\det\left(\boldsymbol{\mathcal{M}} - \lambda \mathbf{1}_{10\times 10}\right)$ to have negative real part, without explicit knowledge of their values. Applying this criterion proves that the all-optical switch solutions pictured here are stable. From this, the stability of the OPO solutions under single-mode driving follows automatically.

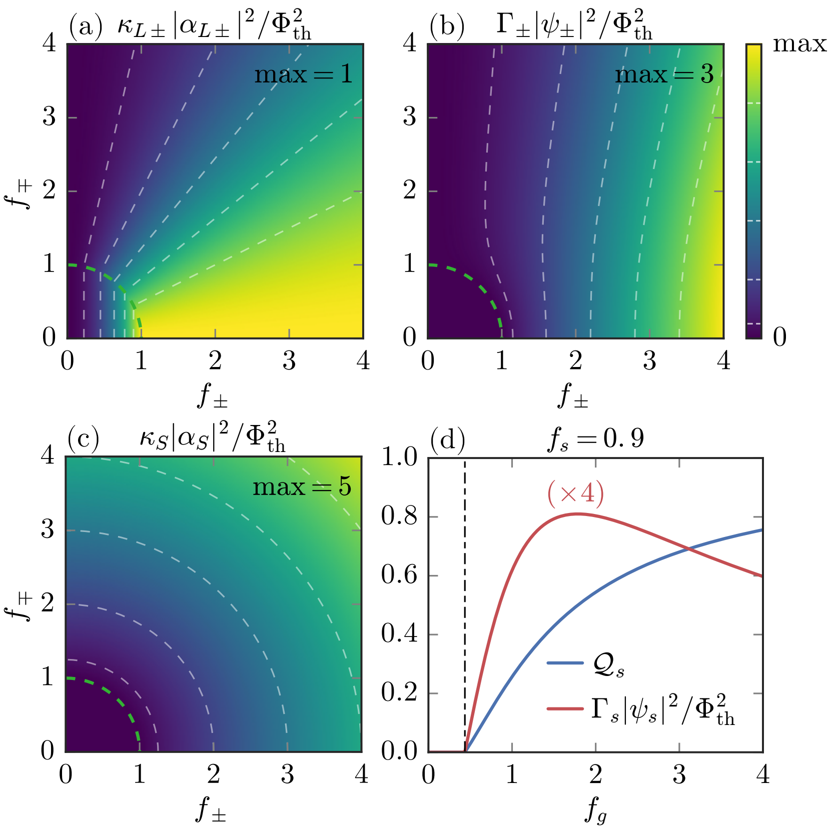

Figure 5.3: Rescaled population densities under two-mode pumping with $\Phi_{\mathrm{th}}^{+} = \Phi_{\mathrm{th}}^{-}$, for (a) the pump mode, (b) the polaritons and (c) the Stokes mode. The green dashed semicircles denote the threshold condition $f_{\mathrm{tot}} \geq 1$. (d) Quantum efficiency $\mathcal{Q}_S$ (blue) and rescaled signal polariton density (red, multiplied by 4 for clarity) at a signal pump strength of $f_s = 0.9$ as a function of the gate pump strength f_g.

Further analysis of mean-field solutions

We now proceed to discuss in further detail the equal threshold solutions. In this case the threshold condition can then be simplified to $f_{\mathrm{tot}} > 1$, where $f_{\mathrm{tot}} = \sqrt{f_+^2 + f_-^2}$. Below threshold ($f_{\mathrm{tot}} < 1$), the mean-field populations are identical to in the single-pump case, with neither the polariton nor the Stokes modes being populated ($|\psi_\pm|^2 = |\alpha_S|^2 = 0$), while the pump mode populations are just determined by the driving of each mode, $|\alpha_{L\pm}|^2 = f_\pm^2 \Phi_{\mathrm{th}}^2/\kappa_L$. Above threshold ($f_{\mathrm{tot}} \geq 1$), the Stokes and polariton mode occupations are given by $|\alpha_S|^2 = (f_{\mathrm{tot}} - 1)\Phi_{\mathrm{th}}^2/\kappa_S$ and $|\psi_\pm|^2 = (f_{\mathrm{tot}} - 1)\Phi_{\mathrm{th}}^2 f_\pm^2/(f_{\mathrm{tot}}^2 \Gamma_\pm)$. In contrast to the single-mode OPO case, the pump mode populations are not clamped to a fixed value above threshold, but are given by $|\alpha_{L\pm}|^2 = \Phi_{\mathrm{th}}^2 f_\pm^2/(f_{\mathrm{tot}}^2 \kappa_{L\pm})$. The input power $P_{\mathrm{in}}^{\pm}$ in each pump mode thus does not depend only on the external driving parameter

$\Phi_{\text{in}}^{\pm}$, but also on the driving of the other mode $\Phi_{\text{in}}^{\mp}$. The mode populations as a function of f_+ and f_- are shown in Figure 5.3. In particular, it should be noted that there is only a single threshold, below which no stimulated emission occurs, and above which all three output modes are populated. Thus, *both* polariton modes show stimulated emission due to the population of the Stokes mode as soon as the total pump power becomes large enough. Consequently, the quantum yield for conversion from each pump mode to the corresponding polariton mode, $\mathcal{Q}_{\pm} = (P_{\pm}/\omega_{\pm})/(P_{\text{in}}^{\pm}/\omega_{L\pm})$, becomes

$$\mathcal{Q}_+ = \mathcal{Q}_- = 1 - \frac{1}{f_{\text{tot}}}. \tag{5.29}$$

In contrast to the 'normal' OPO case in Equation 5.18, the quantum yield of a given polariton does not depend on the corresponding input power ($\propto f_{\pm}^2$), but only on the total one ($\propto f_{\text{tot}}^2$). This demonstrates that the system can indeed be used like a switch, as sketched above: a below-threshold signal beam input $f_s < 1$ does not produce output in the signal polariton if the gate beam is turned off, but is efficiently converted to signal polaritons if the gate is switched on ($f_g^2 > 1 - f_s^2$). The conversion efficiency of the signal can be made high by making the gate beam sufficiently strong, as demonstrated in Figure 5.3d. The switching speed is limited by the lifetime of the longest-lived state in the system, leading to a tradeoff between achieving low thresholds (requiring small losses) and fast switching speeds (requiring large losses).

5.4. Conclusion

To conclude, in this chapter we have demonstrated that by taking advantage of the phenomenon of collective vibrational strong coupling, it is feasible to transform a Raman laser, with a single-output, into an OPO, which converts an input pump beam into two coherent output beams at different frequencies. In the present case, the 'signal' beam in the visible corresponds to the conventional Raman laser output, while the 'idler' beam is emitted by the vibro-polaritons in the mid-IR. On the one hand, this corresponds to a new type of OPO based on RS, a nonlinear process that does not usually allow OPO operation. This could enable novel solid-state micro-cavity devices for applications requiring mutually coherent and/or entangled beams in disparate frequency regions, such as quantum information transmission and storage [234, 235]. On the other hand, even if the second mid-IR output beam is not used, our approach could improve existing Raman lasers by lowering the operating threshold and reducing heat generation. Moreover, such a device could be used as an optically driven mid-IR source in integrated photonic systems.

Finally, thanks to the existence of two similar vibro-polaritons, the proposed device could also operate as an all-optical switch when excited by two adequately designed external beams. Our finding is thus an example of the enormous potential that hybrid light-matter states possess in manipulating light fields and providing novel light sources.

Using other active Raman resonances that are provided with a photonic component, it is possible to think of OPOs based on the same ideas. An example is the phonon-polaritons supported by polar dielectrics such as SiC, employed in our proposed implementation. The Raman cross section in these systems is relatively high, and in particular, it is possible to manufacture nanostructures that allow the confinement or guidance of the scattered signal/idler photons, allowing greater integrability than the cavity proposed here. In this case, the Raman threshold could become lowered by exploiting high non-linearities and the ability to form vibro-polaritons in reduced volumes, rather than using cavities with a high quality factor. As a disadvantage, this type of nanostructures usually has a fixed geometry, preventing the tunability that makes the Raman lasers advantageous in this sense.

In a different line, it would be interesting to address in further detail the effects of dispersion in polaritons and thermalisation towards the 'bottom' of the LP. Compared with organic exciton-polaritons, the effect of dark states, mainly controlled by dephasing-type interactions, as analysed in chapter 3, is substantially smaller, decreasing one of the sources of polariton 'bottleneck' arising from the many dark excitonic states (this issue will be analysed in more detail in chapter 7). Thus, this crucial difference between different kinds of organic polaritons could suppose an advantage in demonstrating in the future polariton accumulation effects for regimes of very large pumpings.

Part II | Electronic Strong Coupling

The next block of this thesis is devoted to the analysis of strong coupling of molecular excitons with optical modes. In section 2.1 we detailed the derivation of the quantum Hamiltonian for an organic micro-cavity in the optical regime. We have assumed that the molecules are close to their equilibrium configuration. This allows the quantisation of the vibrational degrees of freedom in the molecules, yielding a Hamiltonian that does not include non-linear coupling terms. Organic molecules show a multitude of vibrational resonances, and their static and dynamic properties are significantly affected by the intermolecular environment. As we will see in this part, the inclusion of the cavity mode in the collection of molecules induces a photon-mediated 'cross-talk' not only between resonant excitonic states but between vibrational modes sitting on different molecules. This complex interplay gives rise to phenomena of extraordinary richness, with the example of the modification of material and chemical properties in the molecular ensemble and the unusual temporal dynamics of polaritonic states. From the theoretical-modelling point of view, organic exciton-polaritons represent a more challenging scenario compared to vibro-polaritons. In the present case, the more limited analytical insight demands to draw on numerical techniques in order to deal exactly with the non-perturbative timescales of the system, namely, the strong vibronic and photonic coupling in excitons.

We investigate the lower exciton-polariton supported by an organic micro-cavity in chapter 6. The whole phononic spectrum, including nuclear and host environment modes, and the photonic coupling in the molecules are treated in the same footing applying a VMPS. We demonstrate the onset of reduced vibrational reorganisation of the lower polariton for strong light-matter coupling compared to bare electronically excited states, similarly to the recently analysed Holstein–Tavis–Cummings model, which only includes a single vibrational coordinate in the molecules. Moreover, we show the influence of the phononic environment on most electronic and photonic observables can be predicted from just two collective parameters of the vibrational modes, which could be extracted from the linear optical response.

We further explore this system in chapter 7, by calculating the exact many-body time dynamics of the polaritonic states in the micro-cavity. The time evolution problem is handled by employing the TDVMPS algorithm, built upon the approach in previous chapter. We demonstrate signatures of non-Markovian vibronic dynamics and its fingerprints in the far-field photon emission spectrum at arbitrary light-matter interaction scales, ranging from the weak to strong coupling regimes. We analyse both the single and many-molecule cases, showing the crucial role played by the collective motion of molecular nuclei and dark states in determining the polariton dynamics and the subsequent photon emission into the far field.

6 | Exciton-polariton Formation in Organic Microcavities

6.1. Motivation

In this chapter, we present a study of the lowest-energy polaritonic state supported by a small ensemble of organic molecules under strong coupling to an optical microcavity mode, sketched in Figure 6.1a. Under the assumption that molecules are close to their mechanical equilibrium, we include the whole vibrational spectrum of nuclear and environmental modes in our analysis, specified by the spectral density $J_v(\omega)$. The level of modelling of the molecules, therefore, goes beyond the HTC Hamiltonian, but still enables exploration of the full many-body wavefunction employing canonical bosonic operators and thus the toolbox from quantum optics. Due to its mixed threefold photonic-excitonic-phononic character, this eigenstate is dubbed as *lower polaron-polariton* (LPP), adopting the nomenclature in [170]. To treat phononic and photonic processes in the molecules in the same footing, and, also, deal with an arbitrary number of vibrations, we exploit a tensor network representation of the system's wavefunction that extends the widespread matrix product states one-dimensional quantum chains [276]. By this means, the LPP is retrieved by variational minimisation of the TN (leading to the VMPS algorithm in subsection 2.2.2), which filters out the most relevant components mixed in the state capturing their mutual entanglement.

Our results show the robustness of reduced vibrational displacement (RVD) in the LPP wavefunction beyond the single-phonon approximation in the molecules [167, 169], extending its validity to arbitrary structured phononic baths. Moreover, the trend for larger ensembles indicates the suppression of polaron formation in the thermodynamic limit. Intriguingly, we observe that excitonic and photonic components do not depend on specific details of $J_v(\omega)$, provided the net interaction energy of the vibrations be fixed. In particular, they can be reproduced by an effective HTC determined by 2 single-molecule cumulative parameters. These stand for the reorganisation energy Δ [320] introduced in chapter 2, associated with the re-equilibration of the vibrational modes after electronic excitation, and the oscillation frequency Ω_v along the *reaction coordinate*. Conversely, the LPP vibrational properties are strongly molecule-dependent and thus shaped by $J_v(\omega)$.

The following chapter is organised as follows; in section 6.2 we first present the model and outline the TN-based algorithm aimed to target the LPP wavefunction, while section 6.3 is dedicated to discussing its structure in depth, advancing results from the thermodynamic limit. In the first place, we analyse the LPP eigenfrequency and the different regimes that excitonic and photonic states reduced populations show as a function of vibronic coupling. Here, we also analyse the vibration-free polaritonic components that are mixed in the LPP as a result of vibronic coupling. We next focus on the spectrum vibrational displacements as the spectral density is varied. Finally, we show results for a realistic molecule, the Rhodamine 800, where results mentioned above could be experimentally tested.

6.2. Multimode vibrational theory: lower polariton

6.2.1. General theory

Our model includes a collection of N identical molecules, containing a single exciton with frequency ω_e and ladder operators $\hat{\sigma}_{\pm}^{(i)}$ $\left(i = \big(1, \cdots, N\big)\right)$, placed within the volume of a resonant EM mode (frequency $\omega_O = \omega_e$) and annihilation operator $\hat{a}$. The total Hamiltonian contains two different parts, as schematically depicted in Figure 6.1b. First, the system $\mathcal{S}$ that accounts for the excitons within the molecules, the cavity EM mode and its coupling, measured by the collective Rabi frequency Ω_R and treated within the RWA,

$$\hat{H}_{\mathcal{S}} = \omega_O \hat{a}^\dagger \hat{a} + \sum_{i=1}^{N} \omega_e \hat{\sigma}_+^{(i)} \hat{\sigma}_-^{(i)} + \frac{\Omega_R}{2\sqrt{N}} \sum_{i=1}^{N} (\hat{a}^\dagger \hat{\sigma}_-^{(i)} + \hat{\sigma}_+^{(i)} \hat{a}). \tag{6.1}$$

We neglect inter-excitonic interactions, which we assume are screened out by the host environment. In the single-excitation subspace, $\hat{H}_{\mathcal{S}}$ is exactly solvable, as detailed in subsection 2.1.2. Its eigenstates are upper and lower polaritons, which have been raised many times in this thesis, $|\pm\rangle = (\hat{a}^\dagger |G\rangle \pm |B\rangle)/\sqrt{2}$, with frequencies $\omega_\pm = \omega_O \pm$

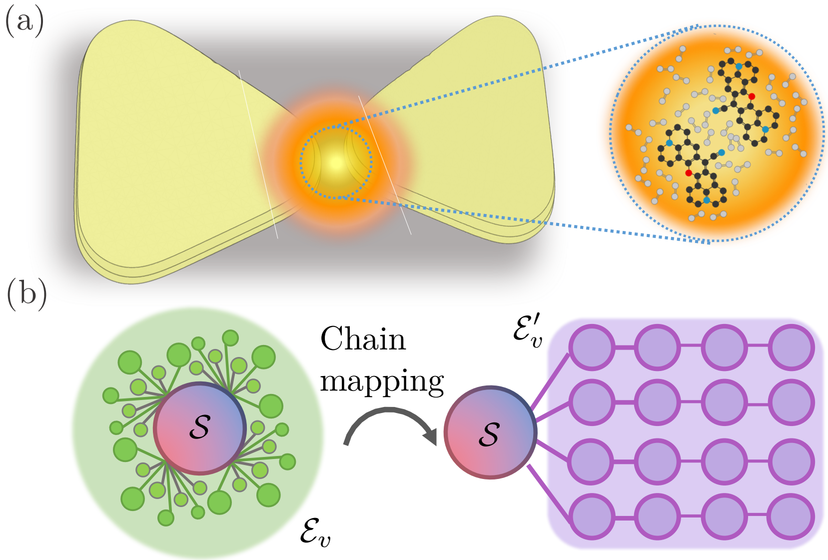

Figure 6.1: (a) Sketch of a molecular ensemble interacting with a confined EM resonance (dashed region) and with the host environment (grey circles). (b) Scheme illustrating the mapping of the vibrational modes yielding the multi-chain Hamiltonian used in the simulations, where the excitons interact with collective reaction coordinates in the molecules.

$\Omega_R/2$, which result from the hybridisation of the collective excitonic *bright* state $|B\rangle = (\sum_{i=1}^{N} \hat{\sigma}_+^{(i)} |G\rangle)/\sqrt{N}$ with the cavity EM mode (here $|G\rangle$ stands for the global vacuum state). In addition, there are $(N-1)$ so-called *dark* states (DS), $|d\rangle \in \mathcal{D}$, which are purely excitonic states of frequency ω_e that are orthogonal to $|B\rangle$.

The second part of the Hamiltonian describes the vibrational subspace $\mathcal{E}_v^{(i)}$ containing a large number M_v of vibrational modes both inside the molecule and in the host environment, and their elastic coupling to the excitons. The k^{th} vibrational mode is approximated by a harmonic oscillator of frequency ω_k (valid close to the equilibrium position) with annihilation operator $\hat{b}_k^{(i)}$ and exciton-phonon coupling strength $\lambda_k^{(i)}$,

$$\hat{H}_v = \sum_{i=1}^{N}\sum_{k=1}^{M_v} \omega_k \hat{b}_k^{\dagger(i)}\hat{b}_k^{(i)} + \sum_{i=1}^{N}\sum_{k=1}^{M_v} \lambda_k^{(i)}(\hat{b}_k^{(i)} + \hat{b}_k^{\dagger(i)})\hat{\sigma}_+^{(i)}\hat{\sigma}_-^{(i)}. \tag{6.2}$$

The properties of these modes, $\{\omega_k^{(i)}, \lambda_k^{(i)}\}$, are encoded in the spectral density $J_v^{(i)}(\omega) = J_v(\omega) = \pi \sum_{k=1}^{M_v} \lambda_k^2 \delta(\omega - \omega_k)$. Here the exciton-phonon coupling does not lead to non-radiative decay [142]. The coupling parameters λ_k describe the relative shifts of electronic potential surfaces between ground and excited states. For the uncoupled molecules ($\Omega_R = 0$), the total Hamiltonian $\hat{H}_{\mathcal{S}} + \hat{H}_v$ becomes a sum of exactly diagonalisable independent-boson-models [251]. Namely, the eigen-excitations or Lang-Firsov polarons can be visualised as localised 'phonon clouds' surrounding the excitons at each molecule:

$|D_i\rangle = e^{-\hat{S}_i} |G\rangle$, $\hat{S}_i = \hat{\sigma}_+^{(i)} \hat{\sigma}_-^{(i)} \sum_k \frac{\lambda_k^{(i)}}{\omega_k^{(i)}} (\hat{b}_k^{(i)} - \hat{b}_k^{(i)\dagger})$.

For typical molecules, when the number of vibrational modes, M_v, becomes large (or even formally infinite when a continuum approximation for $J_v(\omega)$ is used), most standard approaches of quantum optics fail, and even many approximate methods become prohibitively expensive. For instance, direct diagonalisation of the total Hamiltonian is unfeasible, even for $N = 1$. However, a VMPS approach permits to calculate the full wavefunction including all degrees of freedom of either the time-evolved wavefunction after excitation that will be analysed in more detail in chapter 7 or the ground state within the single electronic excitation subspace. This is precisely the 'lower polaron-polariton' [167, 170, 321] analysed in the so-called Holstein-Tavis-Cummings (HTC) model [167, 169, 170, 321], which deals with a single vibrational mode, i.e., $J_{\mathrm{HTC}}(\omega) = \pi \lambda_v^2 \delta(\omega - \omega_v)$. In particular, the Hamiltonian Equation 6.2 extends the HTC to an arbitrary number M_v of vibrational modes.

Here we employ a quasi-exact TN State-based approach for the Hamiltonian $\hat{H}_{\mathcal{S}} + \hat{H}_v$, described in subsection 2.2.2 which permits a non-perturbative exploration of the quantum effects arising in the LPP. It does not rely on any specific form of the spectral density, and in particular, can be used both for discrete and continuous $J_v(\omega)$. To apply this method, we perform an orthogonal mapping of the modes in the N vibrational (green) environments $\mathcal{E}_v^{(i)}$. Relying on the chain-mapping of the vibrational Hamiltonian Equation 6.2, we obtain the *star* coupling structure for $\hat{H}_{\mathcal{S}} + \hat{H}'_v$ introduced in subsection 2.2.2 and sketched in the right part of Figure 6.1b. In this case, operators coupling excitonic and photonic states within subspace $\mathcal{S}$ (red-blue) are represented in the 'root node' at left, from which many branches 'grow' corresponding to transformed environment oscillators that are distributed into chains with length $L = M_v$ [322]. The molecular exciton couples only to a single collective reaction mode [280–283] with frequency Ω_v and coupling strength η following from Equation 2.46. All other chain modes become connected through a nearest-neighbour hopping interaction t_l.

The star Hamiltonian obtained above suggests a quasi-one-dimensional TN representation for efficient numerical implementation of the variational principle. To this end, the LPP wavefunction $|\psi_-\rangle$ is represented by a TN state with maximum bond dimensions D, which directly mimics the coupling structure in the star Hamiltonian (Figure 6.1b). This procedure, coupled with a variational approach to calculate the LPP, leads to a multi-chain variant of the DMRG algorithm for 1D quantum lattices [289], described in subsection 2.2.2. When continuous vibrational spectra are taken into account, the formally infinite phononic chains are truncated at length $L = M_v$, which must be chosen large enough to reach convergence.

We present results for a maximum of $N = 5$ molecules. For large molecule ensembles, a severe memory bottleneck occurs if the system $\mathcal{S}$ is stored in a single root tensor leading to exponential scaling in with N. As shown in [285, 286], it would be possible to restore the efficiency of the numerical method while maintaining precision, by further decomposing the root node into a tree tensor network, determined by entanglement analysis [288], where each final branch represents an exciton or the cavity photon and is coupled to a single chain. This is precisely the approach followed to simulate time dynamics of this system in chapter 7. To further ameliorate memory issues for large phononic (chain) mode occupations, we employ an optimal boson basis for the chain tensors, determined on the fly [278]. A more detailed description of the theoretical approach can be found in [195].

The spectral density in organic materials depends strongly on the molecules and the host matrix. In order to obtain general conclusions, we thus first study the effect of many-mode vibrational dressing on polaritons using a standard parametrisation of low-frequency vibrational modes, the Leggett-type spectral density[1]

$$J_v(\omega) = 2\pi\alpha\omega_c^{1-s}\omega^s\theta(\omega_c - \omega), \qquad s > 0\,, \tag{6.3}$$

where ω_c corresponds to a cutoff energy, α describes the overall strength of the exciton-phonon coupling and the exponent s determines the shape of the spectral density, with $s = 1$ giving a so-called 'Ohmic' spectral density, while $s < 1$ and $s > 1$ correspond to sub- or super-Ohmic densities, respectively. The cutoff ω_c signifies that fast modes $\omega_k > \omega_c$ are reabsorbed in the coupling constants through the adiabatic approximation [260].

It is interesting to note that within the single molecule limit, a regime recently reported in plasmonic nanocavities [40, 135], the Hamiltonian presents direct connections with the well-known Spin-Boson Model (SBM) [260, 323], as we show in subsection 6.2.3.

6.2.2. Single-phononic mode limit

In order to connect our study with the cases available in the literature, we started by briefly discussing the HTC, firstly introduced by [168]. The resulting single-mode Hamiltonian can be solved by various methods, including direct numerical diagonalisation and treatment via variational ansätze [167, 169, 170]. In Figure 6.2 and Figure 6.3 we show the eigenenergies of the system for $N = 1$ and $N = 2$ molecules in the vicinity of

---

[1] Spectral densities of this type have been studied thoroughly in the simplest example of quantum dissipation model, the Spin-Boson Model. See [323] and [260] for further details.

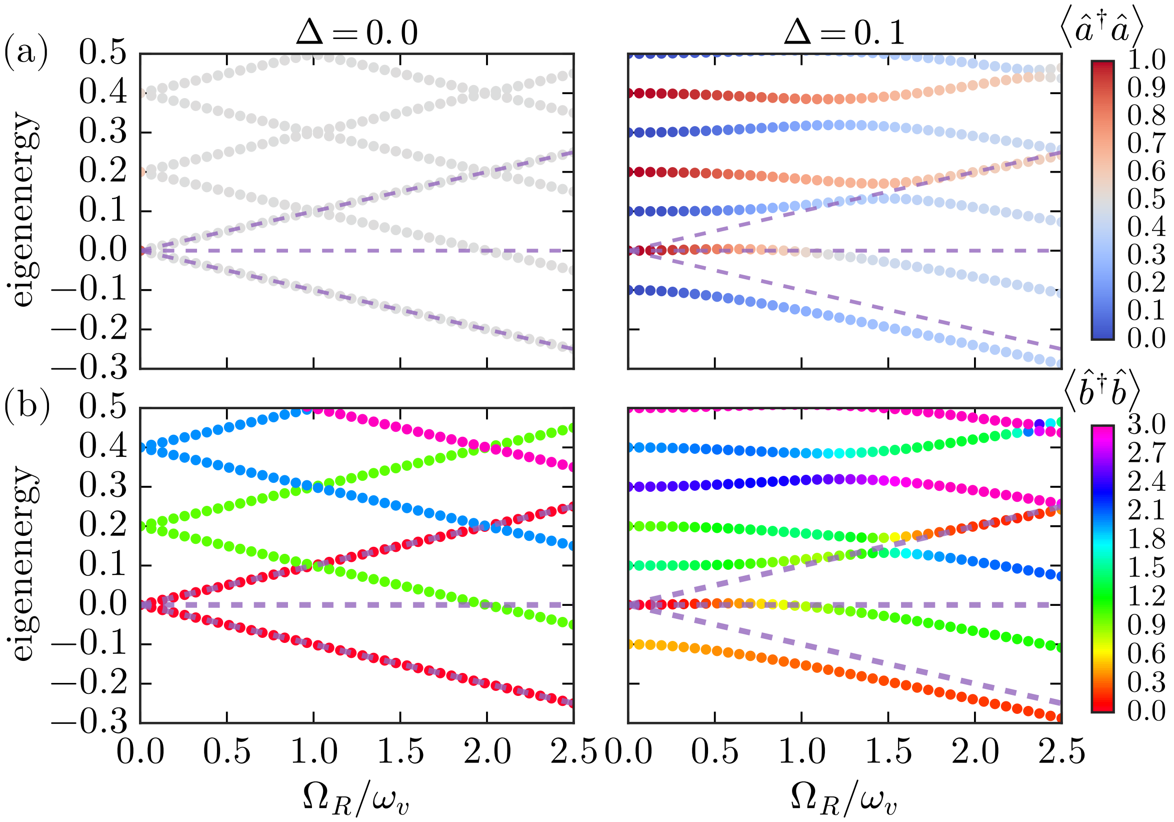

Figure 6.2: (a) Photonic components in the eigenspectrum of the HTC model for a single molecule as a function of the ratio between Rabi frequency Ω_R and vibrational frequency ω_v. (b) Vibrational component. Dashed purple lines indicate the upper and lower vibration-free polariton energies. The energy origin is set at $\omega_e = \omega_O = 0$.

the ground state, with a single electronic/optical excitation in the system at maximum. The coexistence of vibronic and photonic couplings results in an involved eigenspectrum where states are characterised by a triple mixture of vibrational, photonic and excitonic states. In these figures, the color-scale is used for displaying the cavity and vibrational populations, $\langle \hat{a}^\dagger \hat{a} \rangle$ and $\left\langle \hat{b}^\dagger \hat{b} \right\rangle = \sum_i \left\langle \hat{b}_i^\dagger \hat{b} \right\rangle$, respectively.

In the first place, for a single molecule, the 'vibration-free ' eigenstates (left panels for $\Delta = 0$) system are precisely the polaritons described above (eigenstates of $\hat{H}_\mathcal{S}$), together with their vibrational sidebands corresponding to excited molecular phonons. The energies of these states are, therefore $\omega_n^\pm = \omega_\pm + n\omega_v$, $n \in \mathbb{N}$. Conversely, if there is no coupling with the cavity mode (limit $\Delta \gg \Omega_R$), vibronic coupling results in the formation of a polaron with energy $\omega_e - \Delta$. For intermediate energy scales (right panels), the ground state in the single excitation space has a partially polaritonic nature, and so is denoted as lower polar polaron [170]. In Figure 6.2a, higher energy polaritonic sidebands display

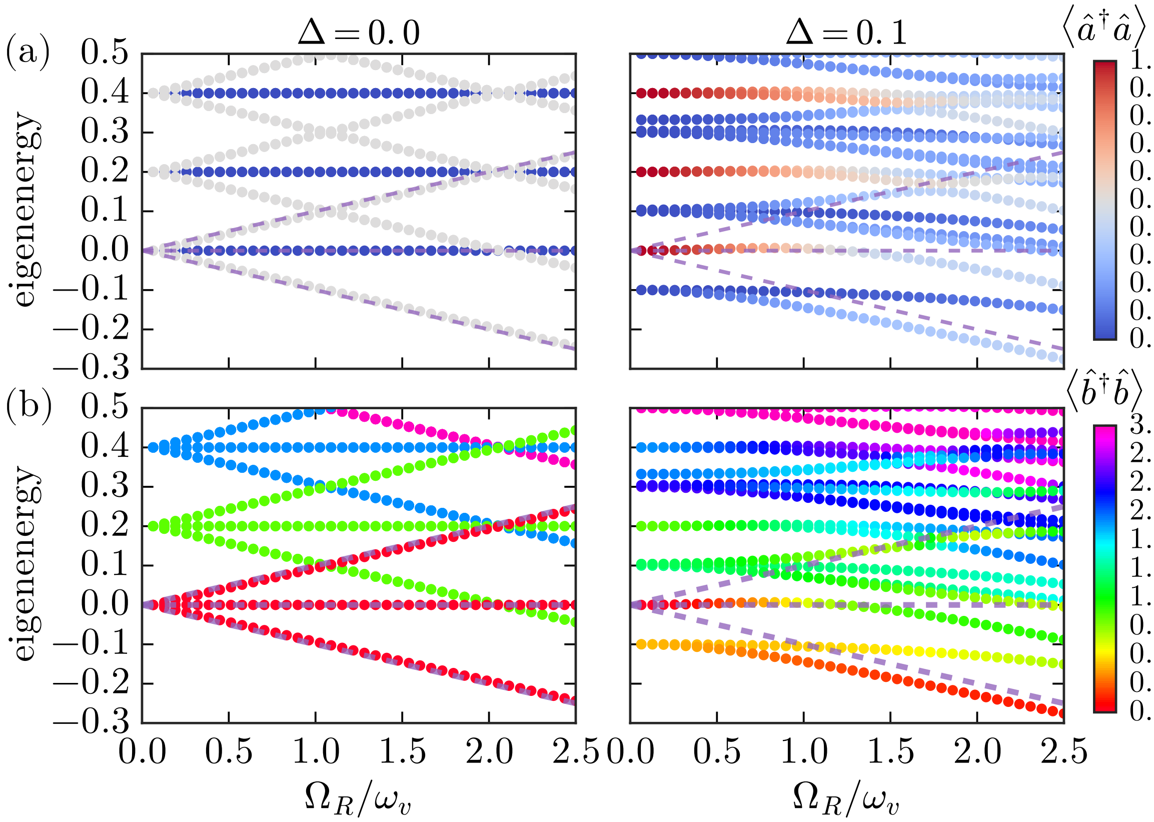

Figure 6.3: (a) Photonic components in the eigenspectrum of the HTC model for two molecules as a function of the ratio between Rabi frequency Ω_R and vibrational frequency ω_v. (b) Total vibrational components, $\left\langle \hat{b}^\dagger \hat{b} \right\rangle = \sum_i \left\langle \hat{b}_i^\dagger \hat{b}_i \right\rangle$. Dashed purple lines indicate the upper and lower vibration-free polariton and excitonic dark state energies. Similarly, $\omega_e = \omega_O = 0$.

anti-crossings caused by vibronic interaction when resonance conditions are met. This is confirmed by the fact that eigenstates do not have a well-defined phonon number in the vicinities of the split regions (see Figure 6.2b). Besides, for large vibronic couplings, the photonic nature of the states is transferred to higher energy excitations, and it is energetically unfavourable to form hybrid light-matter quasiparticles in the system. Similarly, for higher Rabi frequencies the states contain a greater fraction of the 'original' polaritons. As a minimum example of collective behaviour in the eigenstates of the system, we analyse in the following a molecular dimer in the HTC. In this case, the presence of a dark excitonic state $|d\rangle = (\hat{\sigma}_+^{(1)} - \hat{\sigma}_+^{(2)}) |G\rangle / \sqrt{2}$ besides vibrational sidebands (frequencies $\omega_d^n = \omega_e + n\omega_v$, $n \in \mathbb{N}$) is also present for the vibration-free eigenstates represented in the left part of Figure 6.3. Vibronic interaction results in a larger shift of dark states as compared to polaritons because they naturally present greater excitonic components, as inferred from the right panels in Figure 6.3. Eigenenergies present actual crossings in addition to anticrossings, leading to a much richer structure of eigenstates than for $N = 1$ (see [324]). For instance, results show the reduction of the vibrational reorganisation (RVR) in the LPP with the number of molecules, close to the threshold at which reorganisation energy and Rabi frequency become comparable.

In particular, numerical and variational ansätze results for greater N together with a variational ansatz display scaling of this phenomenon as $1/N$. In the thermodynamic limit, therefore, the LPP resembles the bare LP, and the vibrational effects (in particular, the polaron formation) are suppressed. A key observation is that RVR is not observed for the whole ladder of eigenstates, resulting in strong vibronic effects arising in the excited states (for example dynamics triggered by pulsed excitation at high energy). One direct consequence of polaron decoupling is the eventual suppression of the reorganisation energy of excited electrons, which, as first pointed by [167] could be exploited to enhance electron transfer reaction rates.

6.2.3. Single-molecule multimode limit

Within the single electronic/photonic excitation subspace, the single molecule limit can be mapped exactly into SBM. To show this, we consider a shift of the vibrational mode origin in the original Hamiltonian Equation 6.1 before performing the chain transformation. After this shift, described by $\hat{H}_v^{\text{shift}} = e^{\hat{C}} \hat{H}_v e^{-\hat{C}}$ with $\hat{C} = \sum_k \lambda_k (\hat{b}_k - \hat{b}_k^\dagger)/(2\omega_k)$, the light-matter coupling can be expressed through the dynamics of a quasispin $\hat{\Sigma}_- = |e\rangle\langle 1|$ coupled to a bath of bosons, governed by the Hamiltonian $\hat{H}_{\text{SBM}} = \hat{H}_{\mathcal{S}} + \hat{H}_v^{\text{shift}}$

$$\hat{H}_{\text{SBM}} = \frac{\delta}{2}\hat{\Sigma}_z + \frac{g}{2}\hat{\Sigma}_x + \sum_k \left[\omega_k \hat{n}_k + \frac{\lambda_k}{2}\hat{\Sigma}_z(\hat{b}_k + \hat{b}_k^\dagger)\right]. \tag{6.4}$$

Here, we have have introduced $|e\rangle = \hat{\sigma}^+ |G\rangle$ and $|1\rangle = \hat{a}^\dagger |G\rangle$ as shortcuts for the excitonic and photonic states in the single-excitation subspace, respectively.

The SBM constitutes one of the minimal models to study quantum dissipation in solid-state and organic systems, e.g. decoherence of quantum oscillations in qubits [325, 326], impurity moments coupled to bulk magnetic fluctuations [327], and electron transfer in biological molecules [188]. Here, the detuning between the cavity and the zero-phonon line $\delta = \omega_e - \Delta - \omega_O$ plays the role of a bias, where the reorganisation energy follows from

$$\Delta = \frac{1}{\pi}\int_0^\infty \frac{J_v(\omega)}{\omega}\,\mathrm{d}\omega. \tag{6.5}$$

As we have shown in chapter 2, reorganisation energy and Stokes shift (the energy difference between maxima of emission and absorption spectra in organic molecules) are intimately related in the present model, and therefore we can refer to them indistinctly.

The light-matter coupling g favours the mixing of the molecular exciton and the photon, in a similar fashion to the HTC model analysed in previous section, whereas the spin-bath interaction dresses them with vibrational modes, destroying light-matter coherence. In the unbiased case, i.e., when the cavity is resonant with the zero-phonon line, $\omega_O = \omega_e - \Delta$, the Hamiltonian becomes parity symmetric under the exchange $|e\rangle \Leftrightarrow |1\rangle$. This symmetry is known to be spontaneously broken when the vibrational coupling becomes larger than a critical value for sub-Ohmic and Ohmic $J_v(\omega)$, leading to a quantum phase transition in which the ground state is a fully polarised spin state [328]. Translated to the present case, this would signify a novel vibrationally-driven localisation phenomenon in either excitonic or photonic states, precluding the formation of polaritons at the single molecule limit. However, it is questionable whether traces of this transition could be observed in nanocavity systems capable of significant light-matter coupling in the single-molecule case [40, 329], especially considering that we are here neglecting the nonradiative and radiative losses associated with such systems. We thus focus on the following on the many-molecule case ($N > 1$) at zero detuning $\omega_e = \omega_O$, corresponding to the most common experimental setups, while using the analogy to the SBM to make connections to the existing literature.

6.3. Results

6.3.1. Excitonic and photonic features of the LPP

In this section, we study the influence of vibrational dressing on the excitonic and photonic properties of the LPP. We focus on Leggett-type spectral densities, Equation 6.3, with $s = 0.5$, $s = 1$, and $s = 2$ (shown in Figure 6.4a). For ease of reference, we will compare the results with those obtained from the HTC model with parameters $\{\omega_v, \lambda_v\}$. The cut-off frequency ω_c is tuned to maintain constant the reaction coordinate frequency to that of the HTC model $\Omega_v = \omega_c(1+s)/(2+s)$ ($= \omega_v$ in the HTC). We consider an anthracene-like molecule having a vibrational spacing of $\Omega_v = 0.2$ eV, and unless otherwise stated, we assume an ensemble containing $N = 5$ molecules.

In order to investigate the interplay between exciton-photon and exciton-phonon interactions without dealing with the full many-body state, we trace out the vibrational modes to calculate the reduced density matrix, $\hat{\rho}_S = \mathrm{Tr}_{\mathcal{E}_v}\{|\psi_-\rangle \langle\psi_-|\}$. As Figure 6.4b shows, the LPP state becomes more excitonic as the coupling amplitude to the reaction

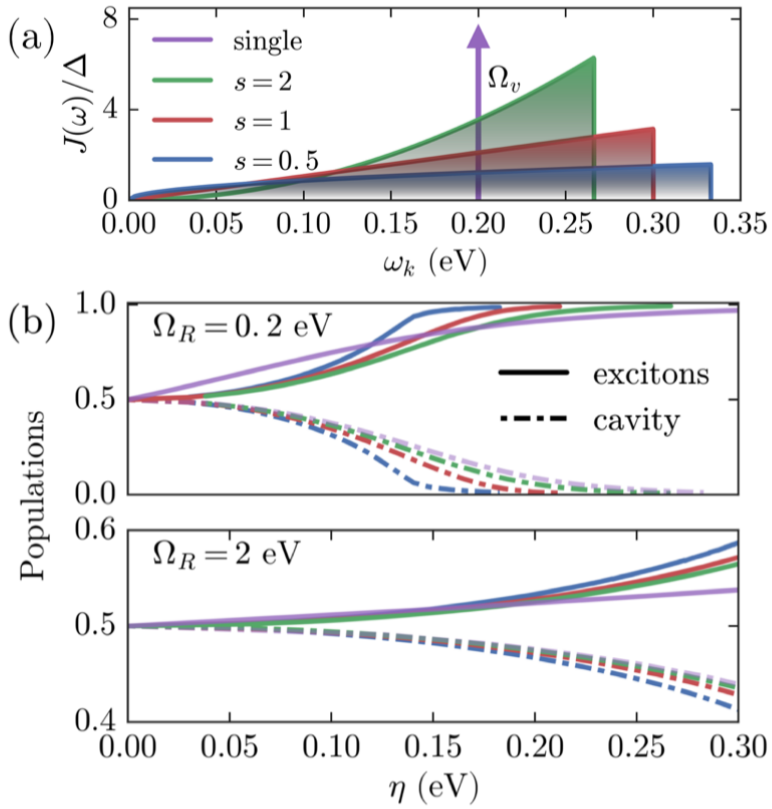

Figure 6.4: (a) Functional forms adopted for the LPP calculation and (b) Reduced populations over subsystem $\mathcal{S}$ in the LPP as a function of the coupling strength to the reaction coordinate η. Here different curves correspond to the different spectral densities in (a), depicting in the upper and lower windows of (b) the cases for Rabi frequency shown.

coordinate η (see chapter 2), given by,

$$\eta = \sqrt{\int_0^{\omega_c} J_v(\omega)\, \mathrm{d}\omega/\pi}, \tag{6.6}$$

is grown, with a more substantial photonic character in a given molecule if the Rabi frequency Ω_R is larger. Such behaviour signals the trade-off between vibrational and photonic coupling scales. Nevertheless, the different curves for different $J_v(\omega)$ clearly indicate that the vibrational influence on the system is not solely determined by the reaction coordinate in the organic molecules. Instead, the remaining ‘dark’ vibrational combinations produce changes that are not captured adequately by η.

These results motivate us to consider the reorganisation energy Δ given in Equation 6.5 as a measure of the global influence of the whole set of phononic modes on the system. This, ($\Delta = \lambda_v^2/\omega_v$ in the HTC model and $\Delta = 2\alpha\omega_c/s$ from Equation 6.3),

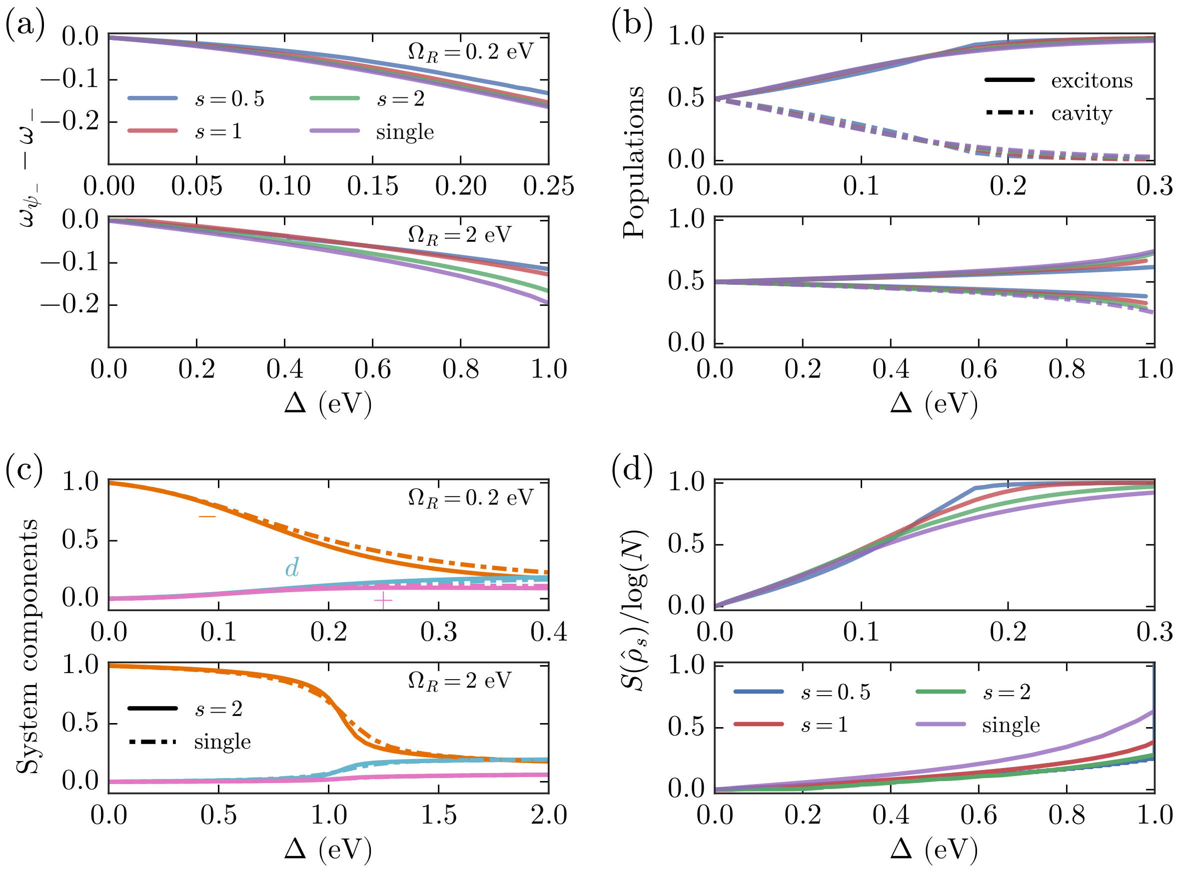

Figure 6.5: (a) Energy shift with respect to the bare lower polaritons ($\Delta = 0$), (b) exciton/photon fractions (c), vibration-free components in the LPP and (d) Von-Neumann entropy of the photonic-excitonic and vibrational states bipartition, as a function of reorganisation energy. In these panels upper panels depict the case $\Omega_R = \Omega_v$ and $\Omega_R = 10\Omega_v = 2$ eV for the lower panels.

relates in our model to the Stokes shift between the bare molecule emission and absorption spectra, namely $\delta\omega = 2\Delta$. We next proceed to include the LPP eigenfrequency ω_{ψ_-} in the discussion. In particular, the values of the shift $\omega_{\psi_-} - \omega_-$ (the bare LP frequency to disregard the linear energy shift by the Rabi frequency in the discussion) as a function of the reorganisation energy can be read from Figure 6.5a. The LPP eigenenergy undergoes a monotonic red-shift as a result of the increased vibrational dressing in electronic and photonic components. Mirroring the results for the HTC model, the slope of the curves differs at either side of the crossover at $\Delta \simeq \Omega_R/2$, being steeper at the large Δ region [169]. Accompanying this trend, the total photonic (excitonic) fractions of the LPP, (diagonal elements in $\hat{\rho}_S$) are decreasing (increasing) very similar functions of the reorganisation energy (Figure 6.5b). Additional insight into the LPP internal structure is gained by considering the weights of the vibration-free eigenstates ($\Delta = 0$) that are mixed into the LPP by the vibronic coupling. As expected, Figure 6.5c reveals that $|\psi_-\rangle$ is constituted by major contributions from the bare LP ($|-\rangle$) and dark states ($|d\rangle \in \mathcal{D}$), with some small fraction of the UP ($|+\rangle$). In particular, in the flatter region where $\Delta \ll \Omega_R/2$ the LPP is well approximated by the bare LP with frequency $\omega_{\psi_-} \simeq \omega_- = \omega_e - \Omega_R/2$.

The results above suggest that in real space the limit at large Rabi frequencies corresponds to a LPP that is a spatially delocalised state over the ensemble and nearly no molecular phonons are excited. In the opposite large Stokes-shift limit, the LPP becomes closer to spatially localised polarons, with a LPP-LP shift of $-\Delta$ (irrespective of $J_v(\omega)$), and no photonic component. The trade-off between the two effects in leads to a relocation of the contribution ρ_{--}, into the dark excitonic states, $\rho_{\mathcal{D},\mathcal{D}}$, with eventual crossover at the large Stokes shift limit, mirroring results for the HTC model in subsection 6.2.2. To further corroborate the existence of the previous extremes we calculate the bipartite entanglement between $\mathcal{S}$ and $\mathcal{E}$, measured by the partial Von Neumann entropy $S(\hat{\rho}_{\mathcal{S}}) = -\mathrm{Tr}(\hat{\rho}_{\mathcal{S}} \log \hat{\rho}_{\mathcal{S}})$. As we observe in Figure 6.5d, correlations in the LPP, absent at $\Delta = 0$, build up for increasing Stokes shift as vibrational states become more mixed with excitons (and indirectly the cavity photon). For large Δ, the formation of polarons entails the saturation of the entanglement entropy at the value $S(\hat{\rho}_{\mathcal{S}}) \simeq \log N$ corresponding to N excitons maximally mixed with the vibrational modes.

In the halfway of the polaritonic and polaronic limits, where neither Ω_R or $J_v(\omega)$ are negligible, the state $|\psi_-\rangle$ possesses a threefold excitonic-photonic-polaronic character. Even in this region, purely $\mathcal{S}$ observables present only quantitative changes depending on the vibrational spectrum of the molecules. A direct consequence is the emergence of an RVD effect when comparing the LPP with uncoupled excitons, arising from an increased Rabi frequency (lower panels in Figure 6.5). In this way, shallower curves in Figure 6.5a,b,c indicate a larger resemblance with the LP in frequency, populations and light-matter coherences respectively, while the entanglement entropy $S(\hat{\rho}_{\mathcal{S}})$ diminishes in Figure 6.5d as Ω_R is augmented due to decoupling from vibrations. In our simulations, we also observed similar effects for a fixed Rabi frequency and growing ensemble size N. The increasing suppression of the vibrational dressing could suggest the onset of polaron decoupling in the limit $N \gg 1$, similar to the one reported for a single mode as observed above [167, 169].

The results above reveal the robustness of the RVD, which does not rely on the fine molecular/host details encoded in $J_v(\omega)$. Instead, the LPP for molecules close to the equilibrium is accurately characterised by the coupling to a reaction coordinate

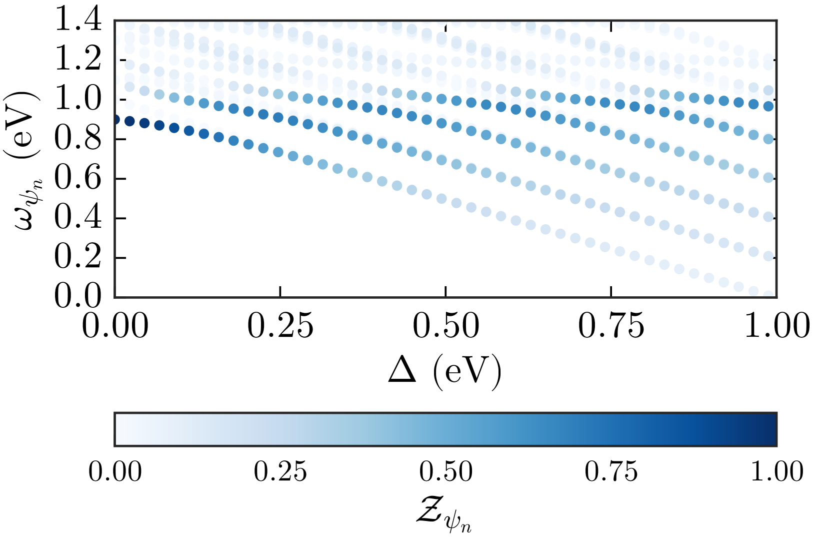

Figure 6.6: Excitation spectrum $|\psi_n\rangle$ of $\hat{H}_{\mathcal{S}} + \hat{H}_v$ for a HTC model with $N = 2$ molecules and $\Omega_R = 0.2$ eV. The color-scale indicates the overlap with the bare lower polariton $\mathcal{Z}_{\psi_n}$ with increasing saturation.

with frequency Ω_v while the global effect of the vibrational modes enters through the full reorganisation energy Δ. To address features analysed above is therefore accurate to consider an effective HTC model, with phonon frequency chosen according to the experimental reaction coordinate frequency and Stokes shift.

The case of polaritons formed upon molecules with large Stokes shift has been recently reported, showing that emission does not occur from the photonic component of polaritons [184]. In this limit, it is more energetically favourable for an exciton to form a polaron rather than hybridise with a photon, as shown by diagonalisation of $\hat{H}_{\mathcal{S}} + \hat{H}_v$. Although TN-based approaches to target excited states have been devised [330], we exploit aforementioned similarities to further visualise the photonic properties of a simpler HTC model with $N = 2$ (see Figure 6.6). In this manner we observe that the quasi-particle weight of the vibration-free polariton $\mathcal{Z}_{\psi_n} = || \langle \psi_- | \psi_n \rangle ||^2$ indeed 'climbs up' to the excited states as Δ is increased, a fingerprint of polaritons at higher energies (see Figure 6.6).

Finally, we noticed quantitative differences as molecular details were varied, which are particularly prominent in the region $\Delta \simeq \Omega_R/2$, where maximum mixing between purely polaritonic and polaronic states is observed, and when vibrational spectrum in the molecules is dominated by slow modes (sub-Ohmic $J_v(\omega)$). While exciton/photon properties have shown to be universal, the impact of light-matter coupling on different

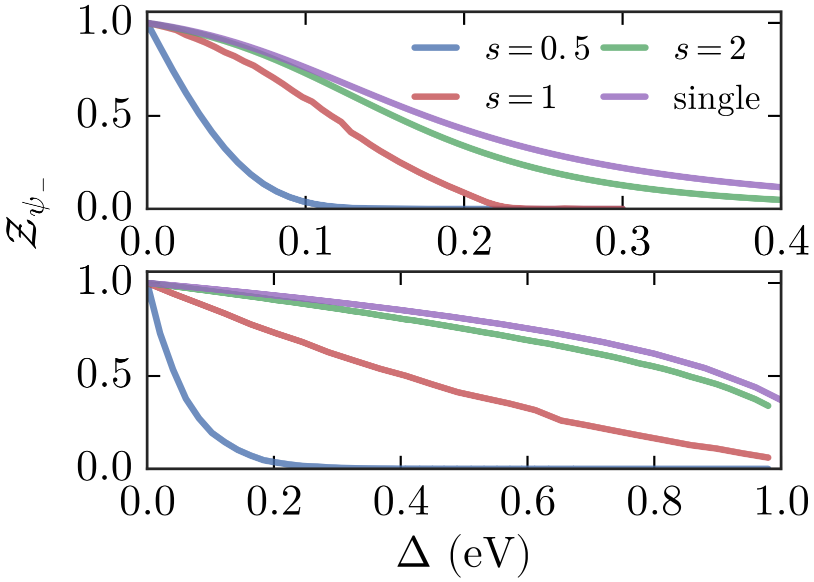

Figure 6.7: Overlap of the LPP wavefunction with the vibration-free polariton $|-\rangle$ for $\Omega_R = 0.2$ eV (upper panel) and $\Omega_R = 2$ eV (lower panel) for the HTC and $J_v(\omega)$ in the form Equation 6.3.

molecular vibrations is averaged out in $\hat{\rho}_S$. These non-trivial features motivate further analysis of the intrinsic vibrational properties in the LPP state, by first calculating a quasiparticle weight $\mathcal{Z}_{\psi_-} = \| \langle \psi_- | - \rangle \|^2$ that indicates how close the LPP is to the vibration-free LP, shown in Figure 6.7. Increased overlaps signal the RVD at large Rabi frequencies and exponents s. It is noteworthy that $\mathcal{Z}_{\psi_-}$, in contrast with the population ρ_{--}, reduced over the whole environment, includes only the overlap with the vibrational vacua $|0\rangle_{\mathcal{E}_v^{(i)}}$. Therefore, when Figure 6.5c and Figure 6.7 are compared, a more polaronic character of the LPP is noticed with larger vibrational dressing for sub-Ohmic $J_v(\omega)$, which agrees with the larger frequency shifts in Figure 6.5a.

In the next section, we further address how individual molecular vibrations in $\mathcal{E}_v^{(i)}$ are affected by polariton formation. To this end, we will analyse several observables resolved in the phononic spectrum frequencies.

6.3.2. Vibrational features of the LPP beyond the HTC model.

Our VMPS approach enables access to the full many-body vibrational component of the LPP wavefunction, which can be exploited to resolve phononic features in frequency space that are disregarded in the HTC model. In this section we show how vibrational observables are shaped by the specific amplitudes in $J_v(\omega)$. To this end, we analyse the frequency-resolved vibrational displacement in the LPP state for the electronically ex-

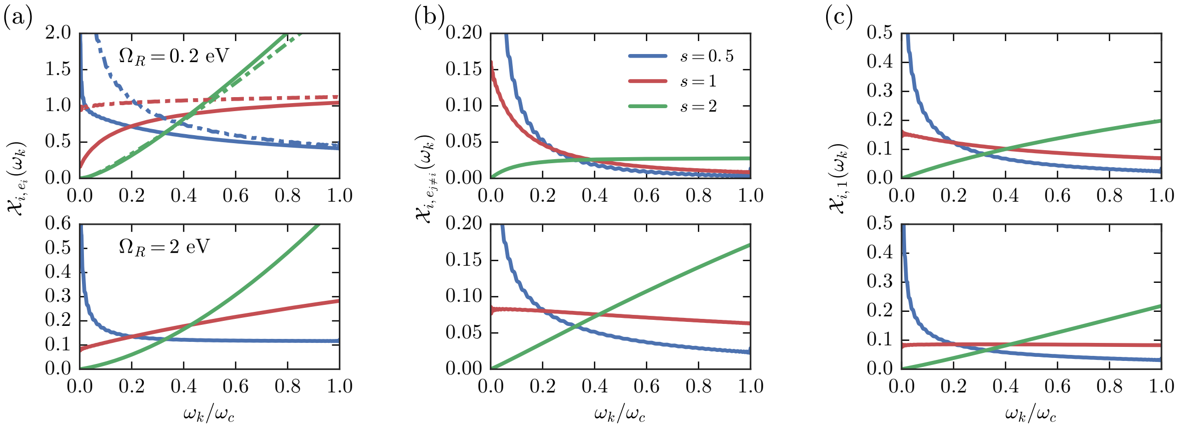

Figure 6.8: Absolute displacement spectrum of the phononic modes for a molecule i, projected on (a) the electronic state of the excited molecule, the electronic state of the unexcited molecule (b) and the cavity photon (c). In these panels we considered $\Omega_v = 0.2$ eV and $N = 5$.

cited molecule i. For further insight we split this observable into *conditional displacement* contributions arising from each system state $|n_\mathcal{S}\rangle \in \mathcal{S}$ mixed into the LPP,

$$\mathcal{X}_{i,n_\mathcal{S}}(\omega_k, \Omega_R, \Delta) = \frac{\left|\left\langle \psi_- | \hat{\mathcal{P}}_{n_\mathcal{S}} (\hat{b}_k^{(i)} + \hat{b}_k^{(i)\dagger}) | \psi_- \right\rangle\right|}{\rho_{n_\mathcal{S},n_\mathcal{S}}}, \tag{6.7}$$

which includes a projector over system states $\hat{\mathcal{P}}_{n_\mathcal{S}}$. Here we normalised by the corresponding system state population, to discern situations where the a state fraction is vanishingly small. In practice, the calculation of Equation 6.7 requires reverting the chain mapping for the $\hat{c}_l^{(i)}$ modes. The displacement spectra in Figure 6.8 shows explicitly the RVD of electronically excited molecules in the LPP , with decreased vibrational displacement $\mathcal{X}_{i,e_i}$ from the bare-molecule value $\mathcal{X}_{i,e_i}(\omega_k, \Omega_R = 0) = \lambda_k^2/\omega_k^2$, when Ω_R is increased (see Figure 6.8a) and a more substantial suppression at low frequencies and smaller s.

The micro-cavity mode induces a 'cross-talk' between otherwise disconnected molecules (in this model we neglected dipole-dipole interactions). This results in a finite contribution of phononic displacement in a given molecule, caused by electronically excited states residing in others, $\mathcal{X}_{i,e_{j\neq i}}$ (see Figure 6.8b), and also a 'molecule-induced' vibrational displacement in the cavity state measured by $\mathcal{X}_{i,1}$. Although these contributions are suppressed for low frequencies at large Ω_R, in a similar way to the 'local' quantity $\mathcal{X}_{i,e_i}$, they slightly augment in a counterintuitive way for larger frequencies. Non-local and cavity mode vibrational dressing present very similar trends, while the second is less sensitive to the Rabi frequency Ω_R (see Figure 6.8b). Moreover, an analysis varying the ensemble size at large Ω_R for $N = 1 - 5$ (not shown) suggests the local vibrational

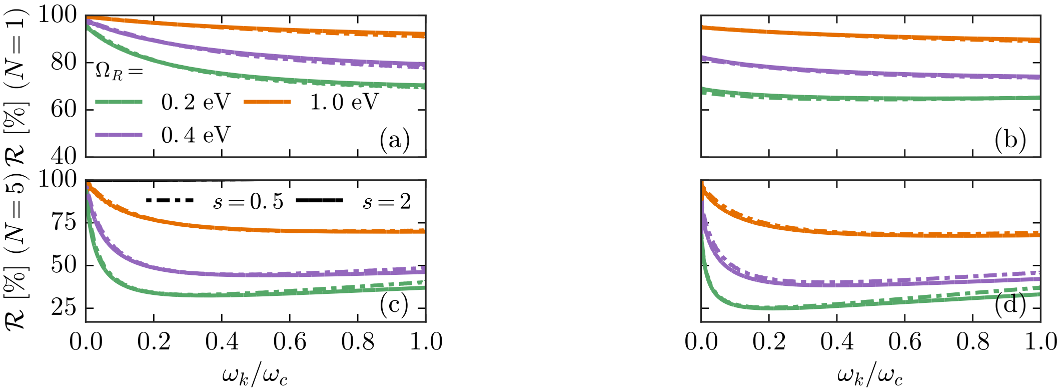

Figure 6.9: Ratio $\mathcal{R}$ between displacement at $\Omega'_R = 2$ eV and lower Rabi frequency displacements, for the SBM at $N = 1$ (a),(b), and $N = 5$ (c),(d). The case $\Delta = 0.01$ eV is shown in left panel ((a),(c)) panel while $\Delta = 0.1$ eV is depicted in the right ((b),(d)). Two distant power laws $s = 0.5$ and $s = 2$ are shown.

displacement $\mathcal{X}_{i,e_i}$ scales for the whole frequency spectrum as $1/N$. These results generalise the scaling predicted by the variational ansatz solution for the HTC [169], which is related with the prefactor $1/\sqrt{N}$ in the coupling between bare electronic states in the LPP. Non-local and cavity-projected vibrational dressing also appear to follow a universal trend of $1/N$ in the cases analysed here. Therefore, despite the indirect connection of molecular vibrations through the cavity in strong coupling, vibrational dressing is collectively suppressed. At moderate Rabi frequency, the situation is different, and the reduction with N depends non-analytically on Ω_R and Δ.

As for the bare molecules, this observable is extremely sensitive to the molecular species supporting the LPP, even when the Stokes shift is kept constant. Therefore, an additional figure of merit that quantifies the strength of the RVD effect for a given molecular ensemble is the ratio

$$\mathcal{R}(\omega_k) = \frac{\mathcal{X}_{i,e_i}(\omega_k, \Omega'_R, \Delta)}{\mathcal{X}_{i,e_i}(\omega_k, \Omega_R, \Delta)}, \tag{6.8}$$

where $\Omega'_R > \Omega_R$ are two Rabi frequencies. Intriguingly, as shown in Figure 6.8, the ratio $\mathcal{R}$ is mostly independent of the power law in $J_v(\omega)$, unveiling another universal characteristic of the model. Therefore, although the LPP is more polaronic for lower s, the suppression at low frequencies is increased in absolute terms in such a way that the *relative suppression* spectrum is molecule-independent.

Exploiting the similarities with the SBM for a single molecule, exposed in the **??**, the intrinsic frequency dependence of $\mathcal{R}$ follows from the variational polaron theory for the SBM ($N = 1$) with 'bias' $\delta = -\Delta$ (provided that $\omega_e = \omega_O$). For large Ω_R and small Δ, bias effects caused by the vibrational reorganisation energy become irrelevant. The slow modes are anti-adiabatic from the perspective of the Rabi oscillations. Hence, they cannot readjust their displacements rapidly enough to track the formation of polaritons arising from light-matter coupling [322], being therefore unable to maximise the vibrational dressing of the electronic states. Vibrational and photonic processes are hence ‘decoupled’ and $\mathcal{R}$ decreases monotonically with the frequency. This picture agrees with the smaller energy shifts for Ohmic and sub-Ohmic spectral densities, corresponding to ‘slow baths’ (see red and blue curves in Figure 6.8a and Figure 6.4a). Conversely, larger exponents s correspond to spectral densities where high-frequency modes are dominant. In particular, these modes are adiabatic from the $\mathcal{S}$ subsystem perspective and lead to larger frequency shifts and phononic displacements. Besides, such effects could induce renormalisation of the coupling parameters, which could be observed for instance in a reduced Rabi splitting in linear response spectrum. The results for $N = 5$ molecules displayed in Figure 6.9 (lower panels) show a more significant suppression of vibrational displacement compared with the SBM. In this case, RVD occurs by the additive contribution of the light-matter coupling, described above, and ensemble effects. Intriguingly, a global minimum in $\mathcal{R}$ is observed for a finite $\omega_k \sim \mathcal{O}(\Omega_R)$, suggesting non-trivial bias effects due to non-negligible reorganisation energy Δ [331].

The results outlined in this section clearly suggest that the HTC model is insufficient to address the non-trivial vibrational features arising for different molecular systems ($J_v(\omega)$) in the LPP, but instead is necessary to have prior knowledge about the vibrational spectroscopy details of the molecule. Nevertheless, we have shown the relative effect of RVD is somewhat irrespective on the frequency details of molecular phonons but is mostly determined by the reaction coordinate frequency and the reorganisation energy. Calculations in previous sections have considered smooth behaviour in the vibrational spectrum. In the following, we show how these ideas can be tested in a molecule with highly structured vibrational features that recreates the conditions found in realistic organic micro-cavities.

6.3.3. Example: the Rhodamine 800 molecule

In typical organic molecules, besides simple power-law spectra at low frequencies, accounted by the power laws in Equation 6.3, more complicated features may arise at high (typically mid-infrared) frequencies, as observed in, e.g., in infrared and Raman spectroscopy where many sharp vibrational resonances are present. In the following, we consider the Rhodamine 800 perchlorate molecular compound (sketched in Figure 6.10b),

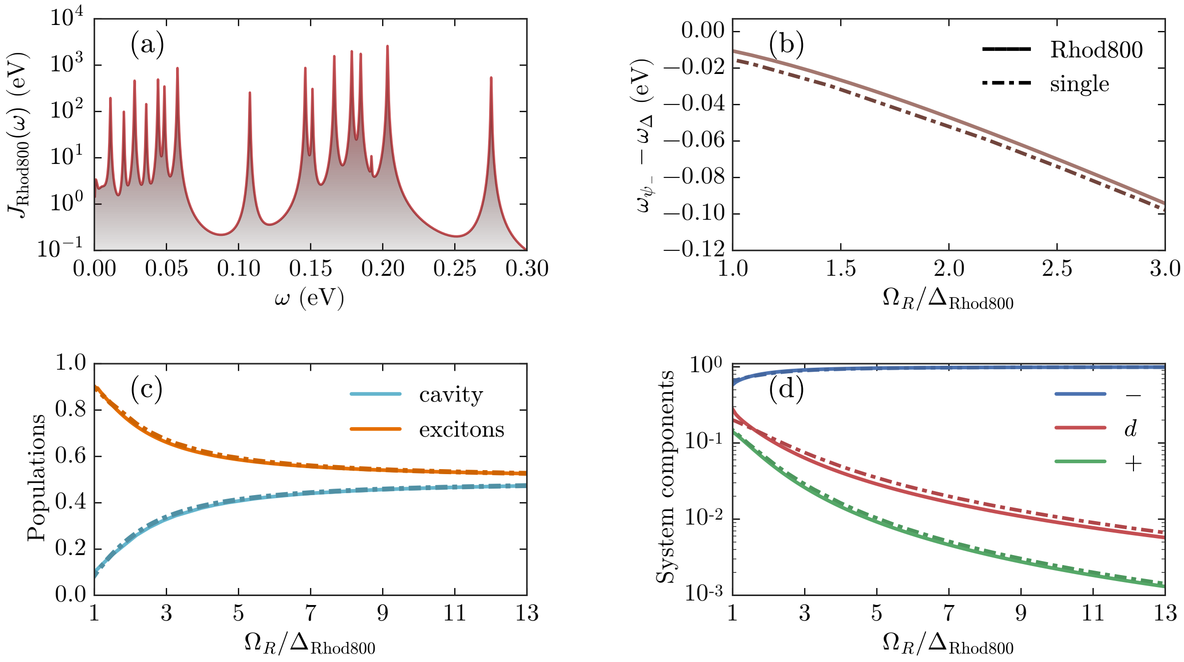

Figure 6.10: Reduced observables for the LPP supported by a dimer of Rhod800 molecules. The total reorganisation energy for the modes that are considered is $\Delta = 112$ meV. The numerical first moment of the spectral density $J_{\mathrm{Rhod800}}(\omega)$, depicted in panel (a) reveals a value of $\Omega_v = 154$ meV.

which constitutes a common choice for a laser gain media and strong coupling experiments [332]. In this case, the phononic information necessary to 'feed' $J_v(\omega)$ is known from vibrational spectroscopy [333]. In particular, the data from three pulse photon echo peak shift (3PEPS) experiments at room temperature (in Fourier space) can be interpolated to give an accurate approximation for the low-frequency part $J_v^{\mathrm{lf}}(\omega)$ [334]. Regarding the high-frequency modes, denoted as Ω_k, we consider that each oscillator is broadened in an amount of $\Gamma \ll \Omega_k$ due to the interaction with a background Ohmic bath of vibrations accounting for vibrational dephasing and decay [280], by taking

$$J_v^{\mathrm{hf}}(\omega, \Omega_k, \gamma_k) = \pi \frac{4\gamma\omega\Omega_k^2\eta^2}{(\Omega_k^2 - \omega^2)^2 + (2\pi\gamma_k\Omega_k\omega)^2}, \tag{6.9}$$

where $\gamma_k = \Gamma/(2\pi\Omega_k)$ is a dimensionless measure of the mode broadening. Firstly, we compared the $\mathcal{S}$ populations of a dimer of Rhod800, with spectral density $J_{\mathrm{Rhod800}}(\omega) = J_v^{\mathrm{lf}}(\omega) + \sum_{k\in\mathrm{hf}} J_v^{\mathrm{hf}}(\omega, \Omega_k, \gamma_k)$, shown in Figure 6.10a, with a HTC model with parameters $\Omega_v^{\mathrm{Rhod800}}, \Delta^{\mathrm{Rhod800}}$ estimated from the experimental spectral density. Strikingly, despite the involved resonant structure of $J_{\mathrm{Rhod800}}(\omega)$, the energy shift in and the reduced density matrix observables present a smooth behaviour as the Rabi frequency Ω_R is varied

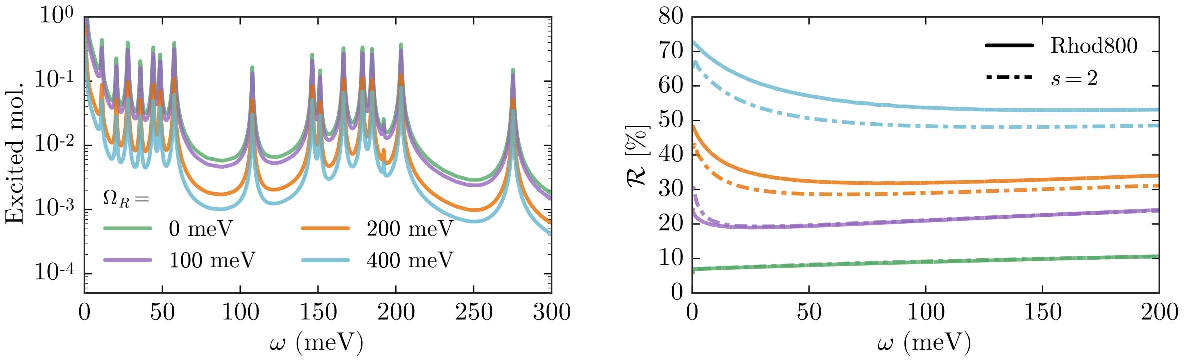

Figure 6.11: (a) Displacement spectrum for the LPP supported by a dimer of Rhod800 molecules, projected on the electronically excited molecule. (b) Ratio between the displacement of the electronically excited molecule at $\Omega'_R = 1.5$ eV and the cases depicted in (a). The remaining parameters are fixed according to Figure 6.10 caption.

(Figure 6.10), which mimics the HTC model. This predicts that the probing of excitonic and photonic characteristics of the LPP supported by an ensemble of arbitrarily complex molecules, close to the mechanical equilibrium, only requires the experimental knowledge of few collective quantities.

However, in agreement with the conclusions drawn for the polynomial spectral densities in Equation 6.3, the vibrational features cannot be described by the HTC model but are profoundly dominated by the vibrational structure of the molecule and the host medium, encoded in $J_v(\omega)$. Phononic displacements of the exciton component of the LPP in Figure 6.11a, mirror the resonant structures in $J_{\mathrm{Rhod800}}(\omega)$. Nevertheless, the relative suppression effect is surprisingly smooth, and it is controlled by just the reaction coordinate frequency Ω_v and the reorganisation energy Δ instead of details in $J_v(\omega)$, as shown by the $\mathcal{R}$ displayed in Figure 6.11b (we choose $s = 2$ for illustration purposes).

6.4. Conclusion

The suppression of vibrational effects in electronically excited states in molecules that form exciton-polaritons is a problem that has recently attracted enormous interest. This is due to the presence of quantised phonons modes in the system, which allows a profound exploration of the properties of the system employing the toolbox of quantum optics. The first calculation that has been taken employs a single phononic mode in the molecules for simplicity, evidencing the catalysis of processes that are dictated by the energy of reorganisation in the excited electronic state (e.g. electron transfer).

In this chapter, we have investigated a microscopic theory that goes beyond current models for the lower polaron polariton in organic micro-cavities, by introducing the whole phononic spectrum. In order to treat the problem numerically, we employed a quasi-exact VMPS algorithm, able to handle the full Hamiltonian including multimode and many molecule effects. We have demonstrated that the RVD of polaritons compared to bare electronic states is more general that could be expected, being indeed a universal feature of strongly-coupled organic micro-cavities in which molecules are close to the equilibrium. Our findings show unambiguosly how, despite the involved phononic spectrum in organic molecules, a large extent of features in the LPP can still be emulated by the HTC model. In this way, different distributions of intra- or extra- molecular vibrational modes lead to similar excitonic and photonic properties of the LPP wavefunction, where only the bath component is appreciably altered. The universal character of the results are not expected to remain in the time evolution of the polaritons supported by this system. As we will show in chapter 7, the reduced density matrix evolution cannot be simply addressed by introducing the reaction coordinate solely.

Alternatively, methods that approach similar problems from the point of view of chemistry have been recently developed [161], without canonical quantisation of molecular vibrations. The results of such models agree with what we have obtained here, and generalise our conclusions to arbitrary electronic PES in the molecules in far-from-equilibrium cases (e.g. chemical reactions) [165]. Using exact diagonalisation, the so-called 'collective protection' (the extension of the RVD regime) has been shown in the thermodynamic limit, by means of suppressed displacements in the polaritonic surfaces. Here, LP and ground state (vacuum) electronic surfaces become identical, with a critical impact on photo-isomerisation reactions. Very recently, experiments have reported fingerprints of chemical changes in strong coupling (in particular, suppression of photo-bleaching in a J-aggregates ensemble) that can be associated with such collective protection [160]. However, there is still a long way to go regarding experiments to obtain conclusive evidence of changes in chemical processes or electronic energy transfer in ESC. The model presented and explored here seeks to generalise the most simple descriptions of the problem, while future prospects along these lines would go towards extended approaches, that are able to introduce multi-dimensional features in the recent field of polaritonic chemistry.

7 | Exciton-polariton Time Evolution in Organic Microcavities

7.1. Motivation

In this chapter, we simulate the temporal dynamics of the polaritons supported by an optical micro-cavity filled with an ensemble of organic molecules, extending the explorations in the previous chapter. For this study, we choose Rhodamine 800 as a prototypical example of an organic molecule (also analysed in subsection 6.3.3). The system under investigation is sketched in Figure 7.1a. This molecule shows prominent features in vibrational spectroscopy, represented in Figure 7.1b (more details in text), which are fully incorporated into our numerical formalism. In our approach, radiative, vibronic and optical processes are treated on an equal footing employing the TDVMPS algorithm outlined in subsubsection 2.2.2, a framework that has been shown to provide quasi-exact solutions when treating the dynamics of open quantum systems [194, 195, 335–337]. Our fundamental study reveals a variety of regimes for the time evolution of the population of polaritons, which experiences vibration-assisted dynamics that translates into distinct far-field emission fingerprints. We observe clear signatures of non-Markovian behaviour in the whole range of light-matter coupling, for both a single molecule and a collection of them, coupled to an EM cavity mode and find that the full vibrational structure of the molecules has to be treated for a complete understanding of the interplay between excitons, phonons, and photons.

This chapter is organised as follows: in section 7.2 we present the model for the time evolution of polaritons supported by an organic micro-cavity, where now it is crucial to include photonic losses in the system, in addition to the tensor-network-based approach

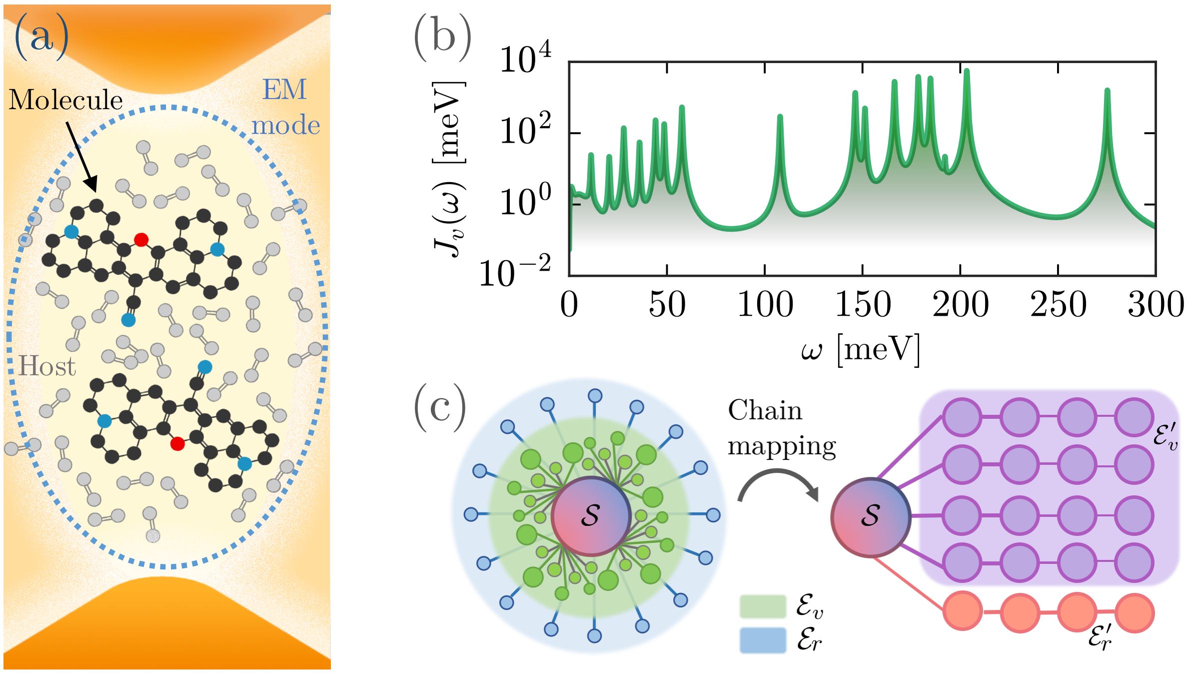

Figure 7.1: (a) Sketch of a molecular ensemble interacting with a confined EM resonance (dashed region) and with the host environment (grey circles). (b) Vibrational spectral density for Rhodamine 800 molecule. (c) Scheme illustrating the mapping of the vibrational modes yielding the multi-chain Hamiltonian used in the simulations.

aimed to calculate the quasi-exact time evolution of polaritons. The results of the numerical simulations are compiled in section 7.3, where our analysis is split into three principal sections. We first provide a thorough study of the dynamics of a single strongly-coupled organic molecule, recently approached in experiments, while we devote the second part to describe the many-molecule limit, where dynamics is strikingly dominated by dark excitonic states. Finally, the last section, where we show the far-field modes and phononic dynamics in real time, provides a connection of the short time polariton dynamics with the experimental time-resolved emission spectrum.

7.2. Multimode vibrational theory. Polariton dynamics

We use a similar model to the Hamiltonian outlined in chapter 6, i.e. it includes a collection of N identical molecules, containing a single exciton with frequency ω_e and ladder operators $\hat{\sigma}_{\pm}^{(i)}$ $(i = (1, \cdots, N))$, placed within the volume of a resonant EM mode (in the present case we set the frequencies $\omega_O = \omega_e = 2.5$ eV), and annihilation operator $\hat{a}$. The bare system $\mathcal{S}$, governed by the Hamiltonian $\hat{H}_{\mathcal{S}}$ in Equation 6.1, therefore accounts for the excitons within the molecules, the cavity EM mode, and their coupling measured by means of the collective Rabi frequency Ω_R and treated within the rotating wave approximation.

In addition, the second part of the Hamiltonian ($\hat{H}_v$ from Equation 6.2) describes the vibrational subspace $\mathcal{E}_v^{(i)}$ containing M_v vibrational modes for each molecule, and their elastic coupling to the excitons. The kth vibrational mode is approximated by a harmonic oscillator of frequency ω_k (valid close to the equilibrium position) with annihilation operator $\hat{b}_k^{(i)}$ and exciton-phonon coupling strength $\lambda_k^{(i)}$. For Rhodamine 800 the vibrational spectral density $J_v(\omega)$ is extracted from the spectroscopic measurements in Ref. [333], as displayed in Figure 7.1b, with vibrational frequencies located in the range $[0, 0.3]$ eV, and reorganisation energy $\Delta = \int_0^\infty \frac{J_v(\omega)}{\pi\omega}\mathrm{d}\omega \approx 112$ meV. We note that while no interactions between different vibrational modes are included in the model, internal vibrational decay is partially represented through the non-zero width of the peaks in $J_v(\omega)$[1].

In typical time-resolved experiments, polariton time evolution is controlled to a large extent by the radiative losses in the cavity. Therefore, it is necessary to include an additional third part, describing the radiative far-field photon modes $\hat{f}_l$ and their coupling to the cavity EM mode,

$$\hat{H}_r = \sum_l \omega_l \hat{f}_l^\dagger \hat{f}_l + \eta_l (\hat{a}^\dagger \hat{f}_l + \hat{f}_l^\dagger \hat{a}). \tag{7.1}$$

In a way similar to vibrational modes, we introduce here the spectral density for the photonic subspace, $\mathcal{E}_r$, as $J_\mathrm{r}(\omega) = \pi \sum_l \eta_l^2 \delta(\omega - \omega_l) = \kappa\omega^3/(2\omega_O^3)$. This term accounts for free-space decay of the bare cavity EM mode with rate $\kappa = 2J_\mathrm{r}(\omega_O)$. Using realistic values for plasmonic/dielectric cavities, we will assume $\kappa = 50$ meV. Note that the coherent coupling to free-space radiative modes induces a small Lamb shift in the effective cavity frequency that depends on the numerical cutoff $\omega_\mathrm{r}^\mathrm{cut}$ ($= 3.5$ eV in the following).

For typical molecules, the large number of vibrational modes, $M_v \sim 10^2$, makes direct diagonalisation of the total Hamiltonian unfeasible, even for $N = 1$. However, the TDVMPS approach permits to calculate the full wave function including all degrees of freedom of either the ‘lower polaron-polariton’ [167, 169, 170, 321] (the ground state within the single electronic excitation subspace), analySed in more detail in chapter 6, or the time-evolved wavefunction after excitation, on which we focus on the following.

---

[1] The effects studied in chapter 3 arising where *vibrational dephasing* timescales are comparable to the Rabi frequency can be disregarded here, since for organic exciton polaritons the Rabi frequency can be as large as $\Omega_R \sim 0.5 - 1$ eV.

In order to apply this method, we perform an orthogonal mapping of the modes in the N vibrational (green) and the free-space photon (blue) environments ($\mathcal{E}_{\mathrm{v}}^{(i)}$ and $\mathcal{E}_{\mathrm{r}}$), leading to the coupling structure sketched in Figure 7.1c. The modes are thus regrouped in chains with length $L = M_v$ [322], with only the first mode coupled to the exciton-photon subspace $\mathcal{S}$ (red-blue). The wave function $|\psi(t)\rangle$ is represented by a tensor network with maximum bond dimensions D with a structure mimicking the transformed Hamiltonian. For large molecule ensembles, a severe memory bottleneck occurs if the system $\mathcal{S}$ is stored in a single root tensor leading to exponential scaling in with N. To restore the efficiency of the numerical method while maintaining precision, we decompose the system into a tree tensor network state, determined by entanglement analysis [285, 286], where each final branch represents an exciton or the cavity photon and is coupled to a single chain. This allows for the treatment of up to $N = 16$ molecules coupled to $16 + 1$ environments with $L > 200$ modes each, i.e., a system with ≈ 3400 coupled degrees of freedom, through a wavefunction described by 10^8 parameters. To further ameliorate memory issues for large chain mode occupations, we employ an optimal boson basis for the chain tensors, determined on the fly [278]. A more detailed description of the theoretical approach can be found in [288] and chapter 2.

7.3. Results

7.3.1. Single molecule reduced dynamics

We explore first the case of single-molecule strong coupling ($N = 1$), recently realised in plasmonic nanocavities [40, 135]. In order to analyse the temporal evolution, we assume that, at $t = 0$, the single excitation resides in the bare (undressed) UP, $|+\rangle$, as would be produced by an incident laser pulse on resonance with the UP and short enough to ensure that nuclear motion can be neglected during its action. Note that for $N = 1$, there are no dark states. Figure 7.2 shows the time evolution of the populations $\{\rho_{GG}, \rho_{\pm\pm}\}$, extracted from the reduced density matrix for subsystem $\mathcal{S}$, $\hat{\rho}_{\mathcal{S}}(t) = \mathrm{Tr}_{\mathcal{E}_v,\mathcal{E}_{\mathrm{r}}}\{|\psi(t)\rangle \langle\psi(t)|\}$. When Ω_R ($= 1$ eV in Figure 7.2a) is much larger than the vibrational frequencies ($\omega_{\mathrm{v}}^{\mathrm{cut}} = 0.3$ eV), the dynamics is characterised by a rapid exponential decay from the bare UP (ρ_{++}) to the ground state (ρ_{GG}) with a negligible population increase of the LP, implying emission of a photon into vacuum. This is exactly what an approach treating $\mathcal{E}_v$ and $\mathcal{E}_{\mathrm{r}}$ as Markovian baths would predict, as there are no available phonon modes that could induce transitions between UP and LP. However, already for the case $\Omega_R = 0.5$ eV, still larger than $\omega_{\mathrm{v}}^{\mathrm{cut}}$, our results show that the coupling to vibrations opens a new de-

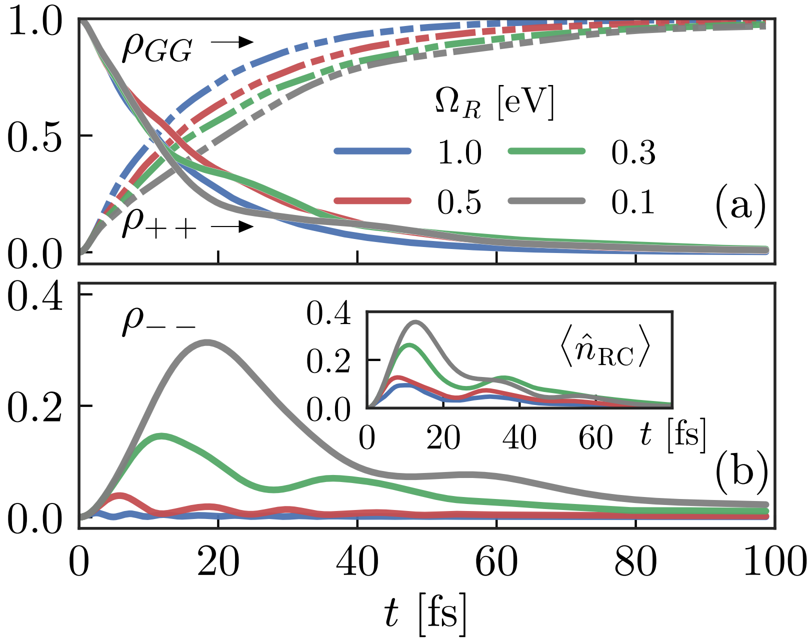

Figure 7.2: Dynamics of reduced density matrix populations for a single molecule as a function of the Rabi frequency Ω_R, including (a) vacuum and upper polariton states and (b) the lower polariton. The inset in (b) shows the occupation of the collective reaction coordinate in the vibrational environment.

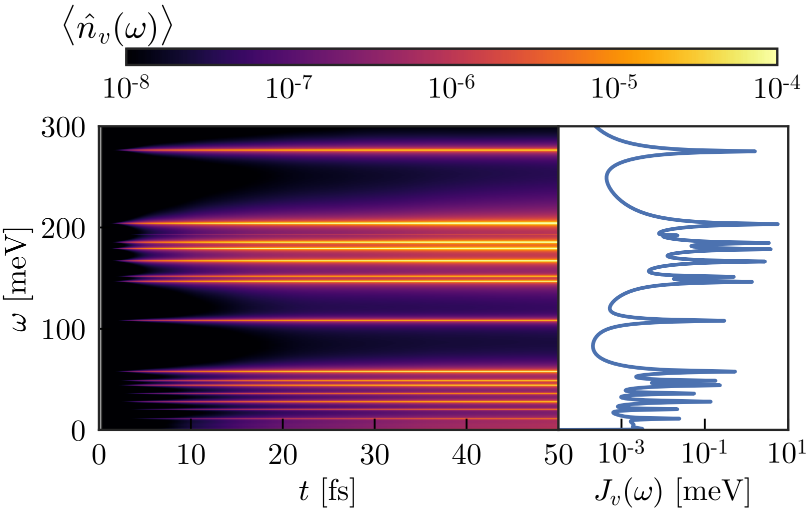

Figure 7.3: (left) Dynamics of the phononic mode populations for a single molecule for a fixed Rabi frequency $\Omega_R = 0.1$ eV and (right) sketch of the spectral density considered.

cay pathway for the UP, which can relax through phonon emission to the LP. A closer look reveals that the emission of photons in the decay $\rho_{++} \rightarrow \rho_{GG}$ is superimposed to a coherent exchange of population between UP and LP (see Figure 7.2b). Moreover, this dynamics is accompanied by a collective excitation of the vibrational spectrum, as displayed by the time evolution of the occupation of the collective reaction coordinate, $\hat{b}_{\text{RC}} = \sum_k \lambda_k \hat{b}_k$ (inset of Figure 7.2b). Neither of these effects could be reproduced by a Markovian approximation, which would lead to single-phonon transitions between polaritons at rates $\Gamma^v_{if} = 2J_v(\omega_{if})$, where $\omega_{if} = \omega_i - \omega_f$ is the transition frequency. As the Rabi splitting is larger than the largest vibrational frequency available, decay into the LP is forbidden within the Markovian limit [187]. The amplitude of these oscillations is enhanced for lower Rabi frequencies, where vibronic and photonic couplings become comparable (see cases $\Omega_R = 0.3$ eV and $\Omega_R = 0.1$ eV in Figure 7.2b). Here the onset of non-exponential behaviour in both ρ_{++} and ρ_{GG} is noticed, resulting in delayed photon emission. In particular, while the UP starts emitting photons immediately, the LP population is maximised after approximately one cycle of coherent oscillation of the reaction coordinate before radiative decay into ρ_{GG} starts to dominate. The collective excitation of the vibrational modes is also visible in the time-dependent vibrational spectrum of (Figure 7.4b), where phonons are emitted at all available phonon frequencies. Moreover, the phonon distribution spreads slightly at large times ($\sim$ 50 fs) forming a tail at low frequencies, as a result of energy transfer between molecular vibrations mediated by the photonic-dressed exciton.

This demonstrates clearly that the large exciton-phonon coupling in a typical organic dye molecule induces strongly non-Markovian coherent dynamics involving excitons, phonons, and photons even under strong light-matter coupling.

7.3.2. Many-molecule reduced dynamics

We next proceed to discuss the many-molecule case, in which dark states have a severe impact on the dynamics [211]. In this section we compare our results with those emerging from a standard quantum optics master equation derived using the Markovian BRW approach [207, 208], as discusses in chapters 2 and 3, which considers solely the value of the spectral density at the transition frequency within the so-called secular approximation and is restricted to single-phonon transitions. We note that while it is possible to derive more advanced Markovian and non-Markovian master equations [261, 262, 338], BRW theory already goes significantly beyond the widely employed Lindblad master equation approach, and allows clear identification of non-Markovian and multi-phonon processes

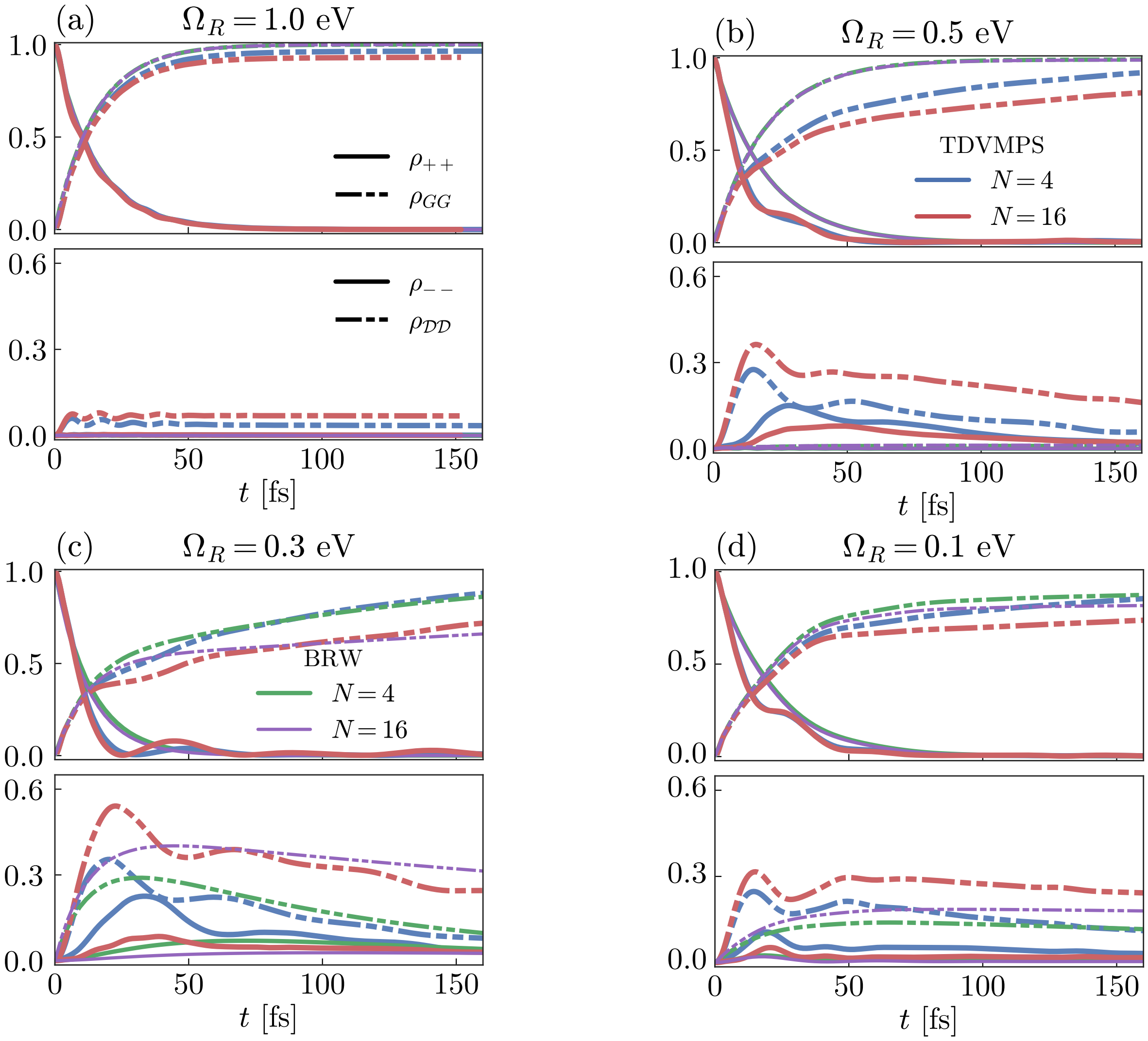

Figure 7.4: Population dynamics for $N > 1$ at different Rabi frequencies (shown in titles). The occupations ρ_{GG}, ρ_{++} are displayed in the upper panels, while ρ_{--}, $\rho_{\mathcal{DD}}$ is shown in the lower ones, with distinctive line styles. Colours blue and red depict cases of $N = 4$ and $N = 16$ while green and purple correspond to the Markovian limit calculated as described in the text.

in the (essentially exact) TDVMPS simulations.

For very large Ω_R (see Figure 7.4a), the UP decays mostly by emission of photons. While vibrational decay to the LP is negligible, some population does reach the DS (given by $\rho_{\mathcal{DD}} = \sum_d \rho_{dd}$), an effect that becomes more effective for larger ensembles. Remarkably, while the photonic decay of the UP population can be accurately determined by the Markovian approach, the prediction for the DS pathway disagrees with the TDVMPS calculation. Markovian BRW theory predicts zero occupation for both DS and LP as there are no phonon modes at the required transition frequencies, while our TD-

VMPS calculation shows that the DS reservoir is indeed populated. This demonstrates that vibration-driven decay from polaritonic states [182, 339, 340] can occur efficiently even when no vibrational modes are resonant with the transition frequency, and that the decoupling from vibrational modes that is found for the LP under collective strong coupling [161, 165, 167, 169, 341] does not prevent decay of the UP.

For smaller values of the Rabi splitting, the UP-DS and DS-LP transition frequencies lie within the range of the vibrational spectrum. Figure 7.4b shows that for $\Omega_R = 0.5$ eV, coherent population transfer to the DS competes with the fast photonic decay of the UP, inducing threefold oscillations $\rho_{++} \leftrightarrow \rho_{\mathcal{DD}} \leftrightarrow \rho_{--}$ that persist over more than 50 fs. As the number of molecules is increased, population is "trapped" more efficiently in the DS, from where it decays to the LP on a timescale of several hundred fs before being emitted. While the intrinsic lifetime of the LP is similar to the UP due to efficient photon leakage out of the cavity, as seen in simulations initialised in the LP (not shown), the refilling from the DS leads to its population persisting over much longer timescales. This observation agrees with the long-time tails exhibited in the dynamics of strongly coupled J-aggregates [82, 149]. As in the case $\Omega_R = 1$ eV, the transitions between UP, DS, and LP are not resonant with any vibrational frequencies in the system. Consequently, within BRW theory the DS and LP remain unpopulated and only fast decay to the ground state through photon emission is observed. In contrast, TDVMPS can represent multi-phonon relaxation and additionally represents the broadening of the UP and LP due to decay, reducing the stringency of vibrational resonance conditions.

Similarly to the single-molecule case, vibrational effects are intensified for smaller Rabi frequencies and coherent oscillations take longer to relax. Interestingly, the numerical agreement between Markovian and non-Markovian approaches is improved in the particular case of $\Omega_R = 0.3$ eV (Figure 7.4c), where the UP-DS transition is quasi-resonant with a vibrational resonance (cf. Figure 7.1c). In this case, while the long-time behaviour is reasonably well approximated by BRW theory, the rapid oscillatory dynamics at short times, including a revival of the UP population and temporary suppression of photonic decay, is averaged out. Additionally, we do not observe a monotonic increase of the LP population for smaller Rabi frequencies, as opposed to the case $N = 1$. In particular, Figure 7.4d displays the case $\Omega_R = 0.1$ eV, where the UP population is only slightly more efficiently transferred to DS and LP than for $\Omega_R = 0.5$ eV (Figure 7.4b). Here the large phonon coupling produces substantial vibrational dressing of DS, and coherence of the polaritons is quickly destroyed.

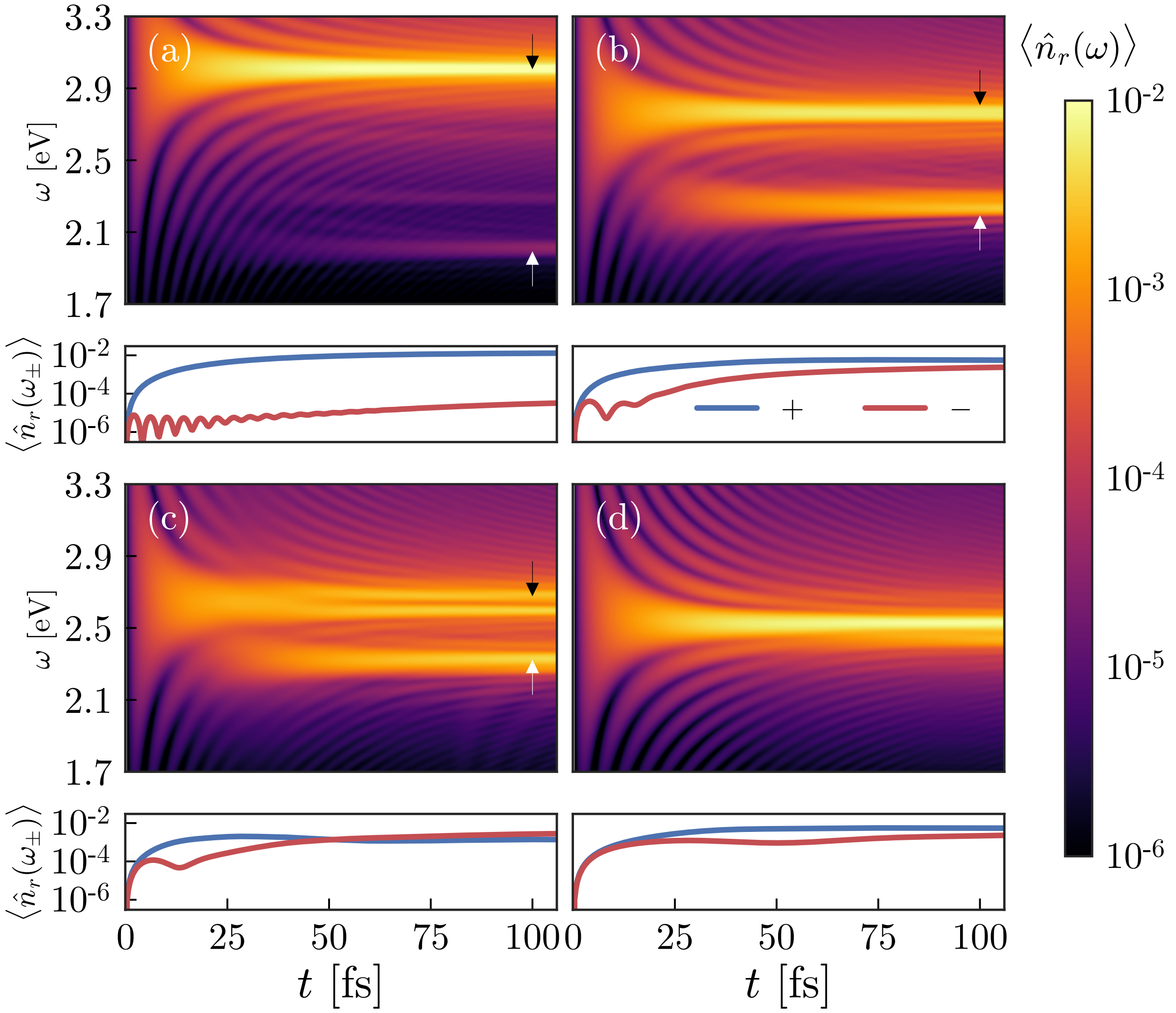

Figure 7.5: Far-field photonic population as a function of frequency and time, for the same Rabi splittings as in Figure 7.4 and $N = 4$. The black and white arrows in panel (a-c) point to the approximate location of the bare UP and LP. Each panel includes in the lower parts cuts at $\omega_\pm$.

7.3.3. Reservoir full coherent dynamics

In typical experiments involving organic polaritons, the collected far-field photons are the main source of available information. The final part of this work is thus devoted to the fingerprints displayed in the time-resolved emission spectrum that originates from the different dynamics regimes that have been analysed above. Thanks to the full access to the reservoir degrees of freedom provided by the TDVMPS approach [195], the emission spectrum can be retrieved from the occupation of the far-field modes $\langle \hat{n}_\mathrm{r}(\omega_l, t)\rangle = \left\langle \psi(t) | \hat{f}_l^\dagger \hat{f}_l | \psi(t) \right\rangle$, and the cumbersome calculation of the time non-local cavity correlation function $\mathcal{C}(t,t') = \left\langle \hat{a}^\dagger(t')\hat{a}(t)\right\rangle$ can be avoided.

For very large Rabi splittings ($\Omega_R = 1$ eV), Figure 7.5a shows dominant photonic emission from the UP, with a series of side lobes converging to the main emission line due to the coherent buildup of population in the free-space mode [342]. At timescales comparable to the reaction coordinate dynamics ($\tau_{\mathrm{RC}} = 2\pi/\omega_{\mathrm{RC}} \simeq 27$ fs), population transfer through the DS reservoir reaches the LP, and its emission is observed as well. This is seen more clearly in cuts at the bare polariton frequencies $\omega_\pm$ (lower panel of Figure 7.5a) that display the building up of photon population in the far-field. The asymptotic growth of the photons emitted by the LP continues after the UP is practically depopulated, due to the continued refilling from the dark states. In addition to the emission from the vibration-free polaritons $|\pm\rangle$, several additional bands at intermediate energies are visible in the emission spectrum. In particular, we observe emission at the bare-molecule emission frequency $\omega_e - 2\Delta \approx 2.276$ eV in all cases, interpreted as due to small cavity admixtures to (vibrationally relaxed) dark states, in line with experimental observations [82, 184].

As the Rabi frequency is diminished, the more efficient coupling from UP to the dark states translates into larger population transfer to the LP and, consequently, into brighter emission at the LP frequency, as well as some sidebands. For the case $\Omega_R = 0.3$ eV depicted in Figure 7.5c, the UP-DS and DS-LP transitions are close to resonant with a vibrational mode of the molecule and a splitting of the emission from the UP is observed. This is consistent with the coherent oscillations observed in Figure 7.4c, and is reminiscent of the splitting between vibrationally dressed and undressed polaritonic states found in the single-mode Holstein-Tavis-Cummings model [186, 324]. Finally, in the last case, $\Omega_R = 0.1$ eV, shown in Figure 7.5d, the closing of the Rabi splitting in emission is observed, suggesting that the system has entered into the weak-coupling regime where light and matter excitations are decoupled.

7.4. Conclusion

Addressing the temporal evolution of polaritons has supposed an obstacle in several areas of organic polaritonics due to the intrinsic complexity of optical processes in molecules. The presence of a strongly coupled EM mode at optical frequencies is an added difficulty, explaining why this has been a historically challenging problem to deal with from a theoretical point of view.

In this chapter, we have unveiled the temporal dynamics of organic polaritons. We have employed a powerful quasi-exact tree tensor network algorithm, which has enabled us to treat a highly structured vibrational reservoir in the molecules and free-space emission of the cavity without additional approximations. The simulations reveal the crucial influence of coherent vibration-driven oscillations between polaritons and dark states and their influence on population transfer to the LP. Our TDVMPS simulations have revealed the importance of multi-phonon and non-Markovian dynamics in the system, as well as the link between the short-time dynamics of excitonic states and the collective vibrational reaction coordinate in the molecules.

The application of these numerical techniques has been strongly inspired by the methods in excitonic transport in biomolecular systems. Similarly, here the coexistence between the sizeable inter-excitonic coupling and the presence of the molecular environment, which is very often out of equilibrium, imply an extremely rich dynamics that ranges from incoherent regimes to coherent transfer of population accompanied by intense excitation of modes vibrational (appointment). These are precisely some of the limits we have found in our study of an organic micro-cavity. In particular, the relationship between the coherence of biological systems and the efficiency of processes such as photosynthesis has given rise to a wide variety of studies that demonstrate a non-trivial role of unexpected quantum effects in conditions of high temperature or environmental noise. One of the following steps in electronic strong coupling (possibly accessible thanks to the tensor-networks machinery described in the last two chapters), would be to study how such excitonic transport mediated by dipole-dipole interactions is in turn influenced by the formation of polaritonic states. This could help to clear fundamental doubts that exist in these systems, providing an additional external parameter to the system, the Rabi splitting determined by the cavity. Further, the role played by the photonic timescale could help to modify the ‘ways’ through which the dynamics of these systems go, opening the door to novel bioinspired materials based on strong coupling.

On the other hand, certain phenomenology found in the temporal dynamics for large ensembles could be understood as harmful if the objective is to achieve a significant population in the lower polariton. An example in which this may be important is the condensation of polaritons, where this variety of ‘polariton bottleneck ’produces a reduction in the efficiency of the macroscopic accumulation of polaritons at the bottom of the LP band. A more in-depth analysis of this situation at larger simulation times, and possibly including finite temperature in the description, could provide answers about how to overcome this experimental challenge in the case of organic polaritons. These are but examples of the extraordinary capabilities of polaritons to modify material properties in the future.

8 | General conclusion and perspective

English

Throughout the research activity summarised in this thesis, we have addressed several topics of interest in the increasingly diffuse boundary that exists between nanophotonics, quantum optics and molecular physics. Namely, chapters 3, 4 and 5 have been dedicated to the very recent field of vibrational strong coupling, which aims to study and make use of polaritons formed out of molecular bonds hybridised with mid-IR photons. Along with this study, we addressed fundamental aspects of the recently reported experiments on linear absorption and Raman scattering, and we proposed possible applications of vibrational strong coupling, including an optical parametric oscillator based on the photonic character of vibro-polaritons. In contrast, chapters 6 and 7 have been devoted to fundamental studies on the exciton-polaritons supported by organic molecules, where molecular and photonic properties in these states communicate and influence each other in a very involved way, which we investigated employing cutting-edge numerical techniques. In this final chapter, the general conclusions of the thesis are presented, together with a synthesis of the current status and future prospects in different lines of research.

Applications of vibro-polaritons

One of the essential points in this thesis has been to unveil possible formal and experimental similarities between different types of organic polaritons. In particular, we have demonstrated how exciton- and vibro-polaritons have intimately related natures. For instance, in chapter 3 we have highlighted the link between vibrational and electronic dephasing interactions, leading to incoherent population transfer between polaritonic and non-emissive molecular excitation superpositions dubbed as dark states. Moreover, in both electronic and vibrational strong coupling, the hybrid character of polaritons translates into photonic properties 'induced' in molecular excitations and vice versa. As a direct consequence, polaritons show phenomena characteristic of molecular systems and photons. An example of the former is the Raman scattering mediated by the material component of vibro-polaritons, addressed in chapter 4, while the latter can be related precisely to the sizable photonic losses in the bad-cavity limit of this system. This is the fundamental idea behind the proposal for an improved coherent light source exploiting stimulated Raman scattering in strong coupling, with respect to conventional Raman lasers, in chapter 5.

At a very fundamental level, is still not completely clear whether vibro-polaritons should exhibit an enhanced Raman signal [212]. Intriguingly, similar signatures could be present in hybrid resonances arising in semiconductor nanocrystals strongly coupled to THz plasmons [310]. Further studies along this line, lying beyond linear theory [343] and the extended versions, which include non-linearities [250], are therefore necessary to fully address the experimental features. Also, a characteristic of current vibrational strong coupling experiments is the required large densities of emitters. This is due in part to the still reduced number of available options for sub-wavelength confinement of mid-IR fields, which would enable a road towards few-emitter vibrational strong coupling. Possible candidates are exploiting phonon-polaritons in Boron Nitride [112] and SiC [109, 110], with large oscillator strengths. In particular, SiC exhibits a large Raman cross section in the mid-IR [344], suggesting the use of phonon-polaritons as the final state of an optical parametric oscillator below the diffraction limit, employing similar ideas to the ones exposed in this thesis.

First demonstrations of vibrational strong coupling have run parallel to experiments testing the potential of organic exciton-polaritons to modify chemical reactions. In particular, these advances refer to the modification of the excited electronic states. Following a similar line, vibro-polaritons have enabled modification of chemical reactions in the electronic ground state [199], suggesting a roadmap towards *bond selectivity* (i.e. ,the ability to control chemical reactions by selecting specific vibrations in molecules leading to specific bond ruptures), which is more typically attained by laser pulses [345]. To address this problem theoretically, as well as predicting novel reaction routes, the methods developed in this thesis would need to be substantially modified to account for potential energy surfaces features away from the equilibrium (e.g. the nature of the vibrational states sitting close to the transition state). To this end, specific details of the molecule might need to be available, requiring a proper interface of the models employed here with ab-initio quantum mechanical modelling [346]. This is possibly one of the most promising applications of vibrational strong coupling, expected to attract interest in the years to come.

On a different issue, the previous similarities suggest a further transfer of ideas, developed for much longer in the prolific field of exciton-polaritons, to vibro-polaritons. In particular, a possible next step that could follow a future experimental demonstration of a laser device in vibrational strong coupling could be to reach vibro-polariton condensation at room temperature, similar to their exciton-polariton counterpart [347]. It is not entirely clear whether Raman scattering could be the optimal choice for reaching polariton accumulation since the Raman effect is intrinsically weak and so requires amplification involving technological complications. The most straightforward alternative, IR absorption, is nevertheless more strict regarding sample preparation, so further studies should address this issue in detail.

In a very different direction, the idea of transferring excitonic energy over long distances exploiting the spatial delocalisation of polaritons could possibly be similarly exploited to tailor the propagation of phononic energy. In particular in polymers, one of the current platforms for vibrational strong coupling, the thermal conductivity is sharply limited by poor phonon and electronic diffusion because of the absence of an ordered crystalline structure [348]. This is one of the reasons behind the widespread use of polymers as thermal and electric isolators. Vibrational strong coupling applied to the propagating phonon modes in this system could, therefore, be an interesting way to enable alternative routes for heat dissipation, (e.g. by converting thermal energy into radiative energy that can scatter out of the system efficiently), or by 'harvesting' heat by properly engineering phononic nanostructures to support field 'hotspots' (see [349]). Prior to this study, it might be interesting to explore in detail the thermal emission mechanisms of polaritons, which have been observed to strongly deviate from the value expected at thermal equilibrium [203].

Finally, one of the great dilemmas in strong coupling, which has mainly been omitted during the exposition, is how to account appropriately for ultrastrong coupling effects in the model. Recent works question the assumption of a single photonic mode in these cases. In this case, tensor-network-based methods may allow to treat numerically this systems and check how these limitations affect the results. This problem is in fact related to the break-down of gauge invariance, emerging from the truncation of material and photonic states.

Organic exciton-polaritons, material and biological science

In the second part of this thesis, we have delved into fundamental aspects of the formation and temporal evolution of organic exciton-polaritons using novel numerical techniques based on tensor networks. In particular, we revisited the calculation of the lower polariton supported by an organic microcavity, a problem of fundamental interest in the novel area of polaritonic chemistry in chapter 6. Our results have shown the robustness in the phenomena of reduction of the role played by the vibrational modes in the lower polariton mode of the system, studied intensely during the last few years. In particular, the fact that strong coupling can be exploited to alter vibronic coupling in the molecules opens exciting possibilities in the line of recently reported and theoretically addressed chemical modifications [160, 166]. Next, we have treated the temporal evolution of the polaritons formed inside an organic microcavity employing similar methods in chapter 7, a problem of great interest in several experiments of fundamental studies and applications of organic polaritons [149, 350]. In particular, the issue of exciton-polariton lifetimes in organic microcavities has received previous interest from the theory side [182, 183], but models relied on very strong approximations such as the Fermi's Golden Rule. We indeed recover some results with an agreement to this approaches for ensembles with small Stokes shift compared to the light-matter coupling energies, as in the case of J-aggregates. However, our results span to the strong vibronic limit, relevant for recent experiments [184]. In this regard, we have demonstrated the 'bottleneck' effect caused by the dark excitonic states in the polariton dynamics. This is indeed a problematic effect if one is interested in attaining macroscopic population in the lower polariton branch and reach condensation/lasing. Further studies could explore the sensitivity of this effect with specific molecular details at larger times, such that a better recipe to circumvent this could be found and energy transfer processes into the lower polariton optimised.

In particular, one of the fields where tensor-network based methods have found a niche to develop intensely is the recent study of non-trivial quantum effects in biological systems [191], such as the considerable efficiency of energy transfer in photosynthetic complexes [172, 173, 189, 190, 290]. In the theoretical description of these different molecular excitons are communicated by dipole-dipole interactions, which are strongly affected by the presence of phonons in the molecular environment, in principle hostile for quantum coherent effects. Numerous studies in the last years are still concerned with these effects [351, 352], and in particular, how the knowledge acquired in this systems can be exploited for 'mimesis' in technological applications [192, 353]. Within this context, an alternative line could be to introduce QED cavity effects to study their influence in biological processes. In this way, the formation of polaritons could serve, first of all, to reveal unknown aspects on the phenomenology of these systems thanks to the further degree of tunability of the cavity mode, and further, to facilitate or emulate non-existent processes in nature by changing energy pathways. From the point of view of strong coupling with EM fields, biomolecules have been received focus in the last years as quantum emitters, both in ex-vivo and in-vivo systems [157, 339, 354, 355].

From the methodological point of view, the tensor network approach employed in this thesis could be readily extended to include temperature effects [284], which, have been shown to play a significant role in biological systems, and, more related to our work, in temperature-assisted emission from a vibronic sideband (anti-Stokes fluorescence) in an organic microcavity [356]. Also, it would be interesting to introduce explicit driving terms to account for more complex observables such that pump-probe spectrum, which enables to infer energy transfer processes and is commonly modelled by Bloch-Redfield methods. This could be done by introducing a time-dependent perturbation Hamiltonian in the semi-classical approximation [240]. In the models that we studied ground and excited electronic state nuclear modes were represented as phonons with the same frequency, but this limitation could be overcome by introducing non-linearities in the excited state Hamiltonian or introducing two different bosonic chains for each molecule. Also, it could be encouraging to model potential energy surfaces features away from the ‘strict’ equilibrium limit such as anharmonicities or even conical intersections, although this would spoil the linear coupling to a boson bath accounting for vibronic interactions. Finally, the update scheme in the tree-TN algorithm employed could be improved for permutation symmetric-systems (such as the zero-disorder scenario studied in this thesis) by devising different sweep procedures avoiding numerical errors accrued by sequential optimisation over each phononic/photonic chain.

Ending remarks

Organic polaritons have proved to be an exciting area of research in the last decades, which nowadays continues to deliver fascinating results right to the present. In this thesis, we addressed several questions that recently have come into focus in the community, both in the already established topic of exciton-polaritons and in the extremely young of vibro-polaritons. In particular, our investigations are not more but a test of how the knowledge that arises in the boundaries between research areas can enable not only new capabilities but also raise fundamental questions about already established theories, to be answered by forthcoming research. As an example, a detailed model for strong coupling involves revisiting the underlying assumptions of simplified quantum optics theory when dealing with the matter. On the opposite side, strong coupling as a subtopic of material science introduces the possibility of reversibly modifying capacities to initiate chemical reactions, transport energy or improve the efficiency of laser devices. Organic molecules are also a platform in which exotic phases of matter, such as Bose-Einstein condensates, can occur under much less restrictive conditions, such as room temperature, increased interaction strengths and ease of sample fabrication. With these observations new and exciting avenues of study have been opened up with possible applications in ultrafast optical switches, energy harvesting systems, low-threshold lasers, optical amplifiers and systems for polariton logic.

Today, it is still uncertain whether organic polaritons could have a technological impact, but the answer to that question is indeed getting closer. With a growing interest in the area, further applications imported from the numerous neighbouring areas are around the corner, promoting an expansion of the field and paving the way to take organic polaritons into the realm of practical applications. In this sense, it is therefore not unusual to imagine a future in which the combination of what nature gives us can be combined with the precise control of light at the quantum level, leading us to new directions, where the canonical distinction between physics, chemistry, biology and computer science fades completely.

Castellano

A lo largo de la actividad investigadora compilada en esta tesis, hemos tratado diversos temas de interés en la cada vez más difusa frontera que existe entre la nanofotónica, la óptica cuántica y la física molecular. A saber, los capítulos 3, 4 y 5 han estado dedicados al muy reciente campo de acoplamiento fuerte vibracional, el cual tiene como objetivo estudiar y hacer uso de los polaritones formados a partir de vibraciones moleculares hibridizadas con fotones en el infrarrojo medio. A lo largo de este estudio, hemos tratado aspectos fundamentales relativos a los experimentos recientemente publicados del espectro absorción y dispersión Raman, y hemos propuesto posibles aplicaciones del acoplo fuerte vibracional, incluyendo un oscilador paramétrico óptico basado en el carácter fotónico de los vibro-polaritones. En contraste, los capítulos 6 y 7 han sido dedicados a estudios fundamentales en los excitones-polaritones soportados por microcavidades ópticas, donde estados moleculares y fotónicos del sistema se comunican e influencian mutuamente de manera compleja, la cual hemos investigado empleando técnicas numéricas recientes. En este ultimo capítulo, se presentan las conclusiones generales de la tesis, junto a una síntesis del estatus actual del campo así como las perspectivas de futuro en diferentes líneas de investigación.

Aplicaciones de los vibro-polaritones

Uno de los puntos esenciales en esta tesis ha sido revelar posibles similitudes formales y experimentales entre diferentes tipos de polaritones orgánicos. En particular, hemos demostrado cómo excitones- y vibro-polaritones poseen naturalezas íntimamente conectadas. Por ejemplo, en el capítulo 3 hemos resaltado el vínculo entre las interacciones resultantes de la decoherencia vibracional y electrónica, lo cual lleva a una transferencia de población incoherente entre estados polaritónicos y superposiciones de excitationes moleculares no emisivas denominadas estados oscuros. Además, tanto en el acoplamiento fuerte electrónico como vibracional, el carácter híbrido de los polaritones se traduce en propiedades fotónicas 'inducidas' en excitaciones moleculares y viceversa. Como consecuencia directa, los polaritones muestran a la vez fenómenos característicos de los sistemas moleculares y los fotones. Un ejemplo de lo primero es la dispersión Raman mediada por la componente material de vibropolaritones, tratada en el capítulo 4, mientras que ejemplos del último son las considerables pérdidas fotónicas el límite de 'mala' cavidad en este sistema. Ésta es la idea fundamental detrás de la propuesta de una fuente de luz coherente con capacidades aumentadas que explota la dispersión estimulada de Raman en el régimen de acoplamiento fuerte en el capítulo 5, con respecto a los láseres Raman.

A nivel fundamental, aún no está completamente claro si los vibro-polaritones deberían exhibir una señal Raman aumentada [212]. Curiosamente, 'huellas' de efectos similares estarían presentes en resonancias híbridas surgidas en nano-cristales semiconductores fuertemente acoplados a plasmones en el THz [310]. Más estudios a lo largo de esta línea, fuera de los límites de la teoría lineal [343] así como de sus versiones extendidas, las cuales incluyen ciertas no-linealidades [250], son por lo tanto necesarias para abordar completamente la reproducción de las medidas experimentales. Además, una característica de los experimentos de acoplo fuerte vibracional en la actualidad es la gran densidad de emisores requerida. Esto se debe en parte al número aún reducido de opciones disponibles para el confinamiento, por debajo del límite de difracción, de los campos electromagnéticos en el infrarrojo medio, lo que permitiría un camino hacia un el régimen de acoplamiento fuerte vibrational con tan sólo un número reducido de emisores. Entre los posibles candidatos están los fonones-polaritones en nitruro de boro [112] y el carburo de silicio [109, 110], que exhiben resonancias muy absorptivas. En particular, SiC exhibe además una gran sección eficaz Raman en el infrarrojo medio [344], sugiriendo el uso de fonones-polaritones como el estado final de una oscilador paramétrico óptico en escalas por debajo de la longitud de onda de operación y empleando ideas similares a las expuestas en esta tesis.

Las primeras demostraciones del régimen de acoplamiento fuerte vibracional han ocurrido en paralelo a los experimentos que prueban el potencial de los excitones-polaritones orgánicos para modificar las reacciones químicas. En particular, estos avances se refieren a la modificación de los estados electrónicos excitados. Siguiendo una línea similar, los vibro-polaritones abren un camino hacia cómo lograr modificación de reacciones químicas en el estado electrónico fundamental [199], sugiriendo una posible vía hacia la llamada *selectividad de enlace* (esto es, la capacidad de controlar reacciones químicas seleccionando vibraciones moleculares concretas, con el fin de conducir a rupturas de enlace específicas), que es más típicamente conseguida empleando pulsos láser [345]. Con el objeto de abordar este problema teóricamente, así como predecir nuevas rutas en reacciones químicas, los métodos desarrollados en esta tesis requerirían ser sustanciamente modificados para explicar las características de las superficies de potencial electrónico fuera del equilibrio (por ejemplo, la naturaleza de los estados vibracionales en las cercanías del estado de transición). Para tal fin, es posiblemente necesario disponer de detalles específicos de la molécula, lo cual requiere una interfaz adecuada de los modelos empleados a lo largo de esta tesis con simulaciones cuánticas ab-initio [346]. Ésta es posiblemente una de las aplicaciones más prometedoras del acoplo fuerte vibracional, y que posiblemente atraiga más interés en los próximos años.

En otro respecto, las similitudes previas sugieren una nueva transferencia de ideas, desarrollada durante mucho más tiempo en el prolífico campo de excitones-polaritones, a vibro-polaritones. En particular, un posible siguiente paso, que podría seguir a una futura demostración experimental de un dispositivo láser en el régimen de acoplo fuerte vibracional, podría ser lograr la condensación de vibro-polaritones a temperatura ambiente, de modo similar a su contrapartida en excitones-polaritones [347]. No está del todo claro si la dispersión Raman podría ser la elección óptima para alcanzar la acumulación de polaritones, ya que dicho efecto es intrínsecamente débil y, por lo tanto, requiere una amplificación y a su vez complicaciones tecnológicas. La alternativa más directa, la absorción infrarroja, es no obstante más estricta con respecto a la preparación de la muestra, y por tanto, estudios futuros deberían tratar estos aspectos en detalle.

En una dirección muy diferente, la idea de transferir energía excitónica a largas distancias explotando la deslocalización espacial de polaritones podría posiblemente ser empleado de manera similar para controlar la propagación de energía fonónica. En particular en polímeros, una de las plataformas actuales para el acoplo fuerte vibracional, la conductividad térmica está fuertemente limitada por la pobre difusión de electrones y fonones debido a la ausencia de una estructura cristalina ordenada [348]. Ésta es por ejemplo una de las razones tras el uso generalizado de polímeros como aislantes térmicos y eléctricos. El acoplamiento fuerte vibracional aplicado a los modos de fonones de propagación en este sistema podría ser, por lo tanto, una forma interesante de habilitar rutas alternativas para la disipación de calor (por ejemplo, transformando la energía térmica en energía radiativa que pueda ser eficientemente emitida) o 'recolectando' el calor mediante la ingeniería adecuada de nanoestructuras fonónicas para soportar 'hotspots' de campo (ver [349]). Previamente a este estudio, podría ser interesante explorar en detalle los mecanismos de emisión térmica de polaritones [203], la cual, como se ha observado, se desvía fuertemente del valor esperado en el equilibrio térmico.

Finalmente, uno de los grandes dilemas en el régimen de acoplamiento fuerte, que se ha omitido principalmente durante la exposición, es cómo explicar adecuadamente los efectos de acoplamiento ultrafuerte a modos fotónicos en el modelo. Trabajos recientes cuestionan la suposición de un único modo fotónico en estas situaciones. En este caso, los métodos numéricos basados en las redes tensoriales podrían permitir tratar numéricamente estos sistemas y verificar cómo estas limitaciones afectan a los resultados. De hecho, este problema está relacionado con la ruptura de invariancia gauge, que surge del truncamiento de los estados materiales y fotónicos.

Excitones-polaritones orgánicos, ciencias de materiales y biológicas

En la segunda parte de esta tesis, hemos profundizado en aspectos fundamentales de la formación y evolución temporal de excitones-polaritones orgánicos empleando para ello técnicas numéricas recientes basadas en redes tensoriales. En particular, revisitamos el cálculo del polaritón inferior soportado por una microcavidad orgánica, un problema de interés fundamental en el reciente campo de la química polaritónica en el capítulo 6. Nuestros resultados han demostrado la solidez de los fenómenos de reducción del papel desempeñado por los modos de vibración en el polaritón inferior del sistema, estudiados intensamente durante los últimos años. En particular, el hecho de que se pueda explotar el acoplamiento fuerte para alterar el acoplamiento vibrónico en las moléculas abre posibilidades interesantes en la línea experimental de modificaciones químicas, abordadas teóricamente en tiempos recientes [160, 166]. A continuación, hemos tratado la evolución temporal en los polaritones en una microcavidad orgánica empleando métodos similares a los anteriores en el capítulo 7, un problema de gran interés de cara a varios experimentos de carácter tanto fundamental como enfocados en las aplicaciones de polaritones orgánicos [149, 350]. En particular, la cuestión de las vidas medias de los excitones-polaritones en microcavidades orgánicas ya ha recibido interés desde el punto de vista teórico [182, 183], aunque no obstante los modelos han estado basados en aproximaciones muy fuertes como la denominada Regla de Oro de Fermi. De hecho, nuestros resultados presentan acuerdo de estos métodos en el caso de colectivos moleculares con desplazamiento energético de Stokes reducido en comparación con las energías de acoplamiento a modos fotónicos, como es el caso de los J-aggregates. Sin embargo, nuestros resultados abarcan además el límite de acoplamiento vibrónico fuerte, de relevancia en experimentos recientes [184]. En este sentido, hemos demostrado el efecto de ‘cuello de botella’ causado por los estados excitónicos oscuros en la dinámica de los polaritones. Este es de hecho un efecto problemático si se está interesado en obtener población macroscópica en la en el polaritón inferior y lograr condensación/laseo. Otros estudios podrían explorar la sensibilidad de este efecto incluyendo detalles moleculares específicos a escalas temporales más largas, de modo que se pueda encontrar una mejor receta para eludir estos problemas y se optimicen los procesos de transferencia de energía hacia el polaritón inferior.

En particular, uno de los campos donde los métodos basados en redes tensoriales han encontrado un nicho en el que desarrollarse profundamente es el reciente estudio de efectos cuánticos no triviales en sistemas biológicos [191], responsables por ejemplo de la enorme eficiencia en la transferencia de energía en complejos fotosintéticos [172, 173, 189, 190, 290]. En la descripción teórica de estos sistemas diferentes excitones moleculares se comunican mediante interacciones dipolo-dipolo, que se ven fuertemente afectadas por la presencia de fonones en el entorno molecular, que cabrían esperar fueran hostiles para los efectos de coherencia cuántica. Ésta es un área de intenso interés durante los últimos años, en la cual conclusiones previas están siendo constantemente puestas a prueba [351, 352], y en particular, donde se busca entender cómo el conocimiento adquirido puede ser explotado para 'mímesis' en aplicaciones tecnológicas [192, 353]. En este contexto, una línea alternativa podría ser introducir efectos de la electrodinámica cuántica de cavidades con el fin de estudiar su influencia en los procesos biológicos. De esta forma, la formación de polaritones podría servir, en primer lugar, para revelar aspectos desconocidos sobre la fenomenología de estos sistemas gracias a la mayor facilidad en el control del modo de cavidad, y además, para facilitar o emular procesos inexistentes en la naturaleza cambiando las vías de circulación de la energía. Desde el punto de vista del acoplamiento fuerte con campos electromagnéticos, las biomoléculas han recibido foco en los últimos años como emisores cuánticos, tanto en sistemas in vivo como ex vivo [157, 339, 354, 355].

Desde el punto de vista metodológico, el algoritmo basado en redes tensoriales empleado en esta tesis podría extenderse directamente para incluir los efectos de temperatura [284], los cuales han demostrado jugar un papel significativo en los sistemas biológicos y, más relacionados con nuestro trabajo, en emisión asistida por temperatura desde estados vibrónicos excitados (fluorescencia anti-Stokes) en una microcavidad orgánica [356]. Además, sería interesante introducir términos de bombeo explícito para dar cuenta de observables más complejos tales como el espectros 'bidimensionales', los cuales permiten inferir procesos de transferencia de energía y que son comúnmente modelados mediante métodos de Bloch-Redfield. Esto podría hacerse, por ejemplo, introduciendo un Hamiltoniano de perturbación dependiente del tiempo en la aproximación semiclásica [240]. Por otra parte, en los modelos que estudiamos los modos nucleares en estado fundamental electrónicos y excitados han sido representados como fonones con la misma frecuencia, pero esta limitación podría superarse introduciendo no linealidades en el Hamiltoniano para el estado excitado o introduciendo dos cadenas bosónicas diferentes para cada molécula. Además, podría ser alentador modelar las características de las superficies energéticas potenciales más allá del equilibrio, tales como anarmonicidades explícitas o incluso intersecciones cónicas, aunque esto destruiría el acoplamiento lineal a un baño de bosones que da cuenta de las interacciones vibrónicas. Finalmente, el esquema de actualización en el algoritmo tree-TN empleado podría mejorarse para los sistemas con simetría de permutación (como corresponde al escenario de cero desorden estudiado en esta tesis) a través del diseño de diferentes procedimientos de 'barrido' en el algoritmo que eviten errores numéricos acumulados por la optimización secuencial sobre cada cadena fonónica/fotónica.

Observaciones finales

Los polaritones orgánicos han demostrado ser un área interesante de investigación en las últimas décadas, que continúa ofreciendo resultados fascinantes hasta el presente. En esta tesis, hemos abordado diversas preguntas que recientemente han atraído el foco de la comunidad, tanto en el ya establecido campo de excitones-polaritones como en el extremadamente joven de los vibro-polaritones. En particular, nuestras investigaciones no son sino una prueba de cómo el conocimiento que surge en los límites entre las áreas de investigación puede ser origen no solo nuevas capacidades sino también plantear preguntas fundamentales sobre teorías ya establecidas, a ser respondidas en muchos casos mediante investigaciones próximas. Como ejemplo, modelizar detalladamente el régimen de acoplamiento fuerte en moléculas implica en ciertos casos revisar las suposiciones subyacentes en típicas teorías de óptica cuántica simplificadas. En el lado opuesto, el acoplamiento fuerte como un subtema de la ciencia de los materiales introduce la posibilidad de modificar reversiblemente las capacidades para iniciar reacciones químicas, transportar energía o mejorar la eficiencia de los dispositivos láser. Las moléculas orgánicas también son una plataforma de interés para estudiar fases exóticas en la materia, tales como los condensados de Bose-Einstein, los cuales pueden formarse bajo condiciones mucho menos restrictivas, como temperatura ambiente, mayor intensidad en las interacciones y facilidad de fabricación de las muestras. En base a estas observaciones, se han abierto nuevas y emocionantes vías de estudio con posibles aplicaciones en interruptores ópticos ultrarrápidos, sistemas de recolección de energía, láseres de baja potencial umbral, amplificadores ópticos y sistemas lógicos basados en polaritones.

Hoy en día, aún no está claro si los polaritones orgánicos podrían tener un impacto tecnológico, pero la respuesta a esa pregunta está cada vez más cerca. Con un creciente interés en el campo, otras aplicaciones importadas desde las numerosas áreas vecinas están a la vuelta de la esquina, promoviendo su expansión y allanando el camino para llevar a los polaritones orgánicos al ámbito de las aplicaciones prácticas. En este sentido, no es inusual imaginar un futuro en el que la combinación de lo que nos da la naturaleza se pueda mezclar con el control preciso de la luz a nivel cuántico, llevándonos a nuevas direcciones, donde la distinción canónica entre física, química, la biología y la ciencia computacional se desvanezcan por completo.

Bibliography

[1] D. Gabor. A new microscopic principle (1948). (cited on p. 1)

[2] E. N. Leith and J. Upatnieks. Reconstructed Wavefronts and Communication Theory*. Journal of the Optical Society of America **52**, 1123 (1962). (cited on p. 1)

[3] R. S. Ohl. Light-Sensitive Electric Device Including Silicon (1948). (cited on p. 1)

[4] P. G. Chapin DM, Fuller CS. A new p–n junction photocell for converting solar radiation into electrical power. J Appl Phys **25**, 676 (1954). (cited on p. 1)

[5] W. Shockley and H. J. Queisser. Detailed balance limit of efficiency of p-n junction solar cells. Journal of Applied Physics **32**, 510 (1961). (cited on p. 1)

[6] A. Einstein. Zur Quantentheorie der Strahlung. Mitteilungen der Physikalischen Gesellschaft Zürich **18**, 47 (1916). (cited on p. 1)

[7] N. Basov and A. Prokhorov. Application of molecular beams for the radiospectroscopic study of rotational molecular spectra. Zh. Eksp. Teor. Fiz **27**, 431 (1954). (cited on p. 1)

[8] J. P. Gordon, H. J. Zeiger, and C. H. Townes. Molecular microwave oscillator and new hyperfine structure in the microwave spectrum of nh_3. Phys. Rev. **95**, 282 (1954). (cited on p. 1)

[9] A. L. Schawlow and C. H. Townes. Infrared and optical masers. Physical Review **112**, 1940 (1958). (cited on p. 1)

[10] T. H. Maiman. Stimulated optical radiation in Ruby. Nature **187**, 493 (1960). (cited on p. 1)

[11] K. Kao and G. Hockham. Dielectric-fibre surface waveguides for optical frequencies. Proceedings of the Institution of Electrical Engineers **113**, 1151 (1966). (cited on p. 1)

[12] F. P. Kapron, D. B. Keck, and R. D. Maurer. Radiation losses in glass optical waveguides. Applied Physics Letters **17**, 423 (1970). (cited on p. 1)

[13] W. S. Boyle and G. E. Smith. Charge coupled semiconductor devices. Bell Syst Tech J **49**, 587 (1970). (cited on p. 1)

[14] G. F. Amelio, M. F. Tompsett, and G. E. Smith. Experimental Verification of the Charge Coupled Device Concept. Bell System Technical Journal **49**, 593 (1970). (cited on p. 1)

[15] Nature milestones: Photons. Nature Materials **9**, S1 (2010). (cited on p. 1)

[16] A. Einstein. On the electrodynamics of moving bodies (Zur Elektrodynamik bewegter Körper). Annalen der Physik **17**, 891 (1905). (cited on p. 1)

[17] P. A. M. Dirac. The Quantum Theory of the Emission and Absorption of Radiation. Proceedings of the Royal Society A: Mathematical, Physical and Engineering Sciences **114**, 243 (1927). (cited on pages 1 and 3)

[18] R. J. Glauber. Photon Correlations. Proc. Roy. Soc. (London) A238 Chap. II Phil. Trans. Roy. Soc. London A250 **9**, 289 (1962). (cited on pages 1 and 3)

[19] S. Wiesner. Conjugate coding. ACM SIGACT News **15**, 78 (1983). (cited on p. 1)

[20] C. H. Bennett, G. Brassard, R. Jozsa, A. Peres, and W. K. Wootters. Teleporting an Unkown Quantum State via Dual Classical and EPR Channels. Physical Review Letters **70**, 1895 (1993). (cited on p. 1)

[21] M. A. Nielsen and I. L. Chuang. *Quantum Computation and Quantum Information* (2010). (cited on p. 1)

[22] K. J. Schafer, B. Yang, L. F. Dimauro, and K. C. Kulander. Above threshold ionization beyond the high harmonic cutoff. Physical Review Letters **70**, 1599 (1993). (cited on p. 1)

[23] P. B. Corkum. Plasma perspective on strong field multiphoton ionization. Physical Review Letters **71**, 1994 (1993). (cited on p. 1)

[24] P. B. Corkum and F. Krausz. Attosecond science. Nature Physics **3**, 381 (2007). (cited on p. 1)

[25] S. Gigan, H. R. Böhm, M. Paternostro, F. Blaser, G. Langer, J. B. Hertzberg, K. C.

Schwab, D. Bäuerle, M. Aspelmeyer, and A. Zeilinger. Self-cooling of a micromirror by radiation pressure. Nature **444**, 67 (2006). (cited on pages 1 and 23)

[26] O. Arcizet, P. F. Cohadon, T. Briant, M. Pinard, and A. Heidmann. Radiation-pressure cooling and optomechanical instability of a micromirror. Nature **444**, 71 (2006). (cited on pages 1, 23, and 28)

[27] A. Schliesser, P. Del'Haye, N. Nooshi, K. J. Vahala, and T. J. Kippenberg. Radiation pressure cooling of a micromechanical oscillator using dynamical backaction. Physical Review Letters **97**, 243905 (2006). (cited on pages 1 and 23)

[28] M. Aspelmeyer, T. J. Kippenberg, and F. Marquardt. Cavity optomechanics. Reviews of Modern Physics **86**, 1391 (2014). (cited on pages 1 and 23)

[29] E. Yablonovitch. Inhibited spontaneous emission in solid-state physics and electronics. Physical Review Letters **58**, 2059 (1987). (cited on pages 1 and 10)

[30] S. John. Strong localization of photons in certain disordered dielectric superlattices. Physical Review Letters **58**, 2486 (1987). (cited on p. 1)

[31] M. Lončar, A. Scherer, and Y. Qiu. *Photonic crystal laser sources for chemical detection*, volume 82 (2003). (cited on p. 1)

[32] G. Mie. Beiträge zur optik trüber medien, speziell kolloidaler metallösungen. Annalen der physik **330**, 377 (1908). (cited on p. 1)

[33] R. H. Ritchie. Plasma Losses by Fast Electrons in Thin Films. Physical Review **106**, 874 (1957). (cited on p. 1)

[34] T. W. Ebbesen, H. J. Lezec, H. F. Ghaemi, T. Thio, and P. A. Wolff. Extraordinary optical transmission through sub-wavelenght hole arrays. Nature **391**, 667 (1998). (cited on p. 1)

[35] D. K. Gramotnev and S. I. Bozhevolnyi. Plasmonics beyond the diffraction limit (2010). (cited on p. 1)

[36] Y. Kaluzny, P. Goy, M. Gross, J. M. Raimond, and S. Haroche. Observation of self-induced Rabi oscillations in two-level atoms excited inside a resonant cavity: The ringing regime of superradiance. Physical Review Letters **51**, 1175 (1983). (cited on pages 2 and 5)

[37] I. Pockrand, A. Brillante, and D. Möbius. Exciton–surface plasmon coupling: An

experimental investigation. The Journal of Chemical Physics (1982).
(cited on pages 2 and 5)

[38] P. Törmä and W. L. Barnes. Strong coupling between surface plasmon polaritons and emitters: A review. Reports on Progress in Physics **78**, 13901 (2015).
(cited on pages 2 and 22)

[39] A. Kavokin, J. Baumberg, G. Malpuech, and F. Laussy. *Microcavities* (2008).
(cited on pages 2, 8, 9, 94, and 97)

[40] R. Chikkaraddy, B. De Nijs, F. Benz, S. J. Barrow, O. A. Scherman, E. Rosta, A. Demetriadou, P. Fox, O. Hess, and J. J. Baumberg. Single-molecule strong coupling at room temperature in plasmonic nanocavities. Nature **535**, 127 (2016).
(cited on pages 2, 11, 12, 18, 115, 119, and 134)

[41] B. Rousseaux, D. G. Baranov, M. Käll, T. Shegai, and G. Johansson. Comparative study of plasmonic antennas for strong coupling and quantum nonlinearities with single emitters. arXiv preprint arXiv:1803.04941 (2018). (cited on p. 2)

[42] D. Porras, C. Ciuti, J. J. Baumberg, and C. Tejedor. Polariton dynamics and Bose-Einstein condensation in semiconductor microcavities. Physical Review B - Condensed Matter and Materials Physics **66**, 853041 (2002). (cited on p. 2)

[43] J. Kasprzak, M. Richard, S. Kundermann, A. Baas, P. Jeambrun, J. M. Keeling, F. M. Marchetti, M. H. Szymánska, R. André, J. L. Staehli, V. Savona, P. B. Littlewood, B. Deveaud, and L. S. Dang. Bose-Einstein condensation of exciton polaritons. Nature **443**, 409 (2006). (cited on pages 2 and 98)

[44] A. Amo, J. Lefrère, S. Pigeon, C. Adrados, C. Ciuti, I. Carusotto, R. Houdré, E. Giacobino, and A. Bramati. Superfluidity of polaritons in semiconductor microcavities. Nature Physics **5**, 805 (2009). (cited on p. 2)

[45] D. Sanvitto and S. Kéna-Cohen. The road towards polaritonic devices. Nature Materials **15**, 1061 (2016). (cited on pages 2, 6, 7, and 21)

[46] T. W. Ebbesen. Hybrid light–matter states in a molecular and material science perspective. Accounts of chemical research **49**, 2403 (2016). (cited on pages 2 and 7)

[47] P. Michetti, L. Mazza, G. C. L. Rocca, G. La Rocca, and G. C. L. Rocca. *Organic Nanophotonics*. Nano-Optics and Nanophotonics (Springer Berlin Heidelberg, Berlin, Heidelberg, 2015). (cited on p. 2)

[48] R. J. Glauber. The quantum theory of optical coherence. Physical Review **130**, 2529 (1963). (cited on p. 3)

[49] V. Weisskopf and E. Wigner. Berechnung der natürlichen Linienbreite auf Grund der Diracschen Lichttheorie. Zeitschrift für Physik **63**, 54 (1930). (cited on pages 3 and 4)

[50] W. E. Lamb and R. C. Retherford. Fine structure of the hydrogen atom by a microwave method. Physical Review **72**, 241 (1947). (cited on p. 3)

[51] H. Casimir. On the attraction between two perfectly conducting plates. Proc. K. Ned. Akad. **360**, 793 (1948). (cited on p. 3)

[52] S. Haroche and J. M. Raimond. *Exploring the Quantum: Atoms, Cavities, and Photons* (2010). (cited on p. 3)

[53] G. Rempe, H. Walther, and N. Klein. Observation of quantum collapse and revival in a one-atom maser. Physical Review Letters **58**, 353 (1987). (cited on pages 3 and 11)

[54] M. Brune, S. Haroche, J. M. Raimond, L. Davidovich, and N. Zagury. Manipulation of photons in a cavity by dispersive atom-field coupling: Quantum-nondemolition measurements and generation of Schrödinger cat states. Physical Review A **45**, 5193 (1992). (cited on p. 3)

[55] M. Brune, E. Hagley, J. Dreyer, X. Maître, A. Maali, C. Wunderlich, J. M. Raimond, and S. Haroche. Observing the progressive decoherence of the "meter" in a quantum measurement. Physical Review Letters **77**, 4887 (1996). (cited on p. 3)

[56] E. T. Jaynes and F. W. Cummings. Comparison of Quantum and Semiclassical Radiation Theories with Application to the Beam Maser. Proceedings of the IEEE **51**, 89 (1963). (cited on p. 3)

[57] R. J. Thompson, G. Rempe, and H. J. Kimble. Observation of normal-mode splitting for an atom in an optical cavity. Physical Review Letters **68**, 1132 (1992). (cited on pages 3, 5, and 11)

[58] S. Scheel and S. Y. Buhmann. Macroscopic Quantum Electrodynamics—Concepts and Applications. Acta Physica Slovaca **58**, 675 (2008). (cited on pages 4 and 29)

[59] L. Novotny and B. Hecht. *Principles of nano-optics*, volume 9781107005464 (2009). (cited on p. 4)

[60] E. M. Purcell. Spontaneous Emission Probabliities at Radio Frquencies. Physical

Review **69**, 674 (1946). (cited on p. 4)

[61] J. D. Jackson. Classical Electrodynamics (1999). (cited on p. 4)

[62] W. H. Louisell and W. H. Louisell. *Quantum statistical properties of radiation*, volume 7 (Wiley New York, 1973). (cited on p. 4)

[63] K. H. Madsen, S. Ates, T. Lund-Hansen, A. Löffler, S. Reitzenstein, A. Forchel, and P. Lodahl. Observation of non-markovian dynamics of a single quantum dot in a micropillar cavity. Physical Review Letters **106** (2011). (cited on p. 5)

[64] C. Cohen-Tannoudji, B. Diu, and F. Laloe. Quantum Mechanics - Vol 1 - Cohen-Tannoudji.pdf (2006). (cited on p. 5)

[65] D. L. Mills and E. Burstein. Polaritons: The electromagnetic modes of media (1974). (cited on p. 5)

[66] D. L. Mills and V. M. Agranovich. *Surface Polaritons: Electromagnetic Waves at Surfaces and Interfaces* (North-Holland publ., 1982). (cited on p. 5)

[67] D. N. Basov, M. M. Fogler, and F. J. García De Abajo. Polaritons in van der Waals materials (2016). (cited on p. 6)

[68] C. Weisbuch, M. Nishioka, A. Ishikawa, and Y. Arakawa. Observation of the coupled exciton-photon mode splitting in a semiconductor quantum microcavity. Physical Review Letters **69**, 3314 (1992). (cited on p. 6)

[69] D. G. Lidzey, D. D. C. Bradley, M. S. Skolnick, T. Virgili, S. Walker, and D. M. Whittaker. Strong exciton-photon coupling in an organic semiconductor microcavity. Nature **395**, 53 (1998). (cited on pages 6 and 18)

[70] G. H. Wannier. The structure of electronic excitation levels in insulating crystals. Physical Review **52**, 191 (1937). (cited on p. 6)

[71] J. Frenkel. On the transformation of light into heat in solids. i. Physical Review **37**, 17 (1931). (cited on p. 6)

[72] A. Auer and G. Burkard. Entangled photons from the polariton vacuum in a switchable optical cavity. Physical Review B - Condensed Matter and Materials Physics **85** (2012). (cited on p. 6)

[73] C. Ciuti and I. Carusotto. Input-output theory of cavities in the ultrastrong coupling

regime: The case of time-independent cavity parameters. Physical Review A - Atomic, Molecular, and Optical Physics **74** (2006). (cited on p. 6)

[74] D. Dini, R. Köhler, A. Tredicucci, G. Biasiol, and L. Sorba. Microcavity polariton splitting of intersubband transitions. Physical review letters **90**, 116401 (2003). (cited on p. 6)

[75] C. Ciuti, G. Bastard, and I. Carusotto. Quantum vacuum properties of the intersubband cavity polariton field. Physical Review B - Condensed Matter and Materials Physics **72**, 1 (2005). (cited on pages 6 and 80)

[76] A. A. Anappara, S. De Liberato, A. Tredicucci, C. Ciuti, G. Biasiol, L. Sorba, and F. Beltram. Signatures of the ultrastrong light-matter coupling regime. Physical Review B - Condensed Matter and Materials Physics **79** (2009). (cited on p. 6)

[77] J. Casanova, G. Romero, I. Lizuain, J. J. García-Ripoll, and E. Solano. Deep strong coupling regime of the Jaynes-Cummings model. Physical Review Letters **105** (2010). (cited on pages 6 and 80)

[78] S. De Liberato. Light-matter decoupling in the deep strong coupling regime: The breakdown of the purcell effect. Physical Review Letters **112** (2014). (cited on p. 6)

[79] T. Niemczyk, F. Deppe, H. Huebl, E. P. Menzel, F. Hocke, M. J. Schwarz, J. J. Garcia-Ripoll, D. Zueco, T. Hümmer, E. Solano, A. Marx, and R. Gross. Circuit quantum electrodynamics in the ultrastrong-coupling regime. Nature Physics **6**, 772 (2010). (cited on pages 7 and 80)

[80] G. Scalari, C. Maissen, D. Turčinková, D. Hagenmüller, S. De Liberato, C. Ciuti, C. Reichl, D. Schuh, W. Wegscheider, M. Beck, and J. Faist. Ultrastrong coupling of the cyclotron transition of a 2D electron gas to a THz metamaterial. Science **335**, 1323 (2012). (cited on p. 7)

[81] C. Maissen, G. Scalari, F. Valmorra, S. Cibella, R. Leoni, C. Reichl, C. Charpentier, W. Wegscheider, M. Beck, and J. Faist. Ultrastrong Coupling in the Near-field of Complementary Split Ring Resonators **1**. (cited on p. 7)

[82] J. George, T. Chervy, A. Shalabney, E. Devaux, H. Hiura, C. Genet, and T. W. Ebbesen. Multiple Rabi Splittings under Ultrastrong Vibrational Coupling (2016). (cited on pages 7, 21, 22, 23, 28, 35, 138, and 140)

[83] F. Barachati, J. Simon, Y. A. Getmanenko, S. Barlow, S. R. Marder, and

S. Kéna-Cohen. Tunable Third-Harmonic Generation from Polaritons in the Ultrastrong Coupling Regime. ACS Photonics (2018). (cited on p. 7)

[84] J. George, T. Chervy, A. Shalabney, E. Devaux, H. Hiura, C. Genet, and T. W. Ebbesen. Multiple Rabi Splittings under Ultrastrong Vibrational Coupling. Physical Review Letters **117** (2016). (cited on p. 7)

[85] C. Cohen-Tannoudji, J. Dupont-Roc, and G. Grynberg. *Photons and Atoms* (1997). (cited on pages 8, 28, and 35)

[86] K. J. Vahala. Optical microcavities (2003). (cited on p. 8)

[87] J. M. Gérard, B. Sermage, B. Gayral, B. Legrand, E. Costard, and V. Thierry-Mieg. Enhanced spontaneous emission by quantum boxes in a monolithic optical microcavity. Physical Review Letters **81**, 1110 (1998). (cited on p. 9)

[88] A. C. Atre, A. García-Etxarri, H. Alaeian, and J. A. Dionne. Mid-IR near-perfect absorption with a SiC photonic crystal with angle-controlled polarization selectivity. Advanced Optical Materials **1**, 327 (2013). (cited on p. 9)

[89] I. Carusotto and C. Ciuti. Quantum fluids of light. Reviews of Modern Physics **85**, 299 (2013). (cited on p. 9)

[90] V. Lefèvre-Seguin and S. Haroche. Towards cavity-QED experiments with silica microspheres. Materials Science and Engineering: B **48**, 53 (1997). (cited on p. 10)

[91] D. W. Vernooy, V. S. Ilchenko, H. Mabuchi, E. W. Streed, and H. J. Kimble. High-Q measurements of fused-silica microspheres in the near infrared. Optics Letters **23**, 247 (1998). (cited on p. 10)

[92] F. Vollmer and S. Arnold. Whispering-gallery-mode biosensing: label-free detection down to single molecules. Nature Methods **5**, 591 (2008). (cited on p. 10)

[93] R. Shankar, I. Bulu, and M. Lončar. Integrated high-quality factor silicon-on-sapphire ring resonators for the mid-infrared. Applied Physics Letters **102**, 051108 (2013). (cited on p. 10)

[94] J. Faist, F. Capasso, D. L. Sivco, C. Sirtori, A. L. Hutchinson, and A. Y. Cho. Quantum cascade laser. Science **264**, 553 (1994). (cited on p. 10)

[95] M. Henriksson. *Mid-infrared optical parametric oscillators* (2013). (cited on p. 10)

[96] T. Yoshle, A. Scherer, J. Hendrickson, G. Khitrova, H. M. Gibbs, G. Rupper, C. Ell, O. B. Shchekin, and D. G. Deppe. Vacuum Rabi splitting with a single quantum dot in a photonic crystal nanocavity. Nature **432**, 200 (2004). (cited on p. 10)

[97] Y. Akahane, T. Asano, B.-S. Song, and S. Noda. High-Q photonic nanocavity in a two-dimensional photonic crystal. Nature **425**, 944 (2003). (cited on p. 10)

[98] R. Shankar and M. Lončar. Silicon photonic devices for mid-infrared Applications (2014). (cited on p. 10)

[99] T.-H. Xiao, Z. Zhao, W. Zhou, M. Takenaka, H. K. Tsang, Z. Cheng, and K. Goda. Mid-infrared germanium photonic crystal cavity. Optics Letters **42**, 2882 (2017). (cited on p. 10)

[100] J. Bellessa, C. Bonnand, J. C. Plenet, and J. Mugnier. Strong coupling between surface plasmons and excitons in an organic semiconductor. Physical Review Letters **93**, 036404 (2004). (cited on pages 10, 28, and 30)

[101] H. Memmi, O. Benson, S. Sadofev, and S. Kalusniak. Strong Coupling between Surface Plasmon Polaritons and Molecular Vibrations. Physical Review Letters **118**, 1 (2017). (cited on pages 10, 23, and 30)

[102] F. G. De Abajo. Colloquium: Light scattering by particle and hole arrays. Reviews of Modern Physics **79**, 1267 (2007). (cited on p. 10)

[103] B. Auguié and W. L. Barnes. Collective resonances in gold nanoparticle arrays. Physical review letters **101**, 143902 (2008). (cited on p. 10)

[104] S. R. Rodriguez, M. C. Schaafsma, A. Berrier, and J. Gmez Rivas. Collective resonances in plasmonic crystals: Size matters. In *Physica B: Condensed Matter*, volume 407, 4081 (2012). (cited on p. 10)

[105] A. I. Väkeväinen, R. J. Moerland, H. T. Rekola, A. P. Eskelinen, J. P. Martikainen, D. H. Kim, and P. Törmä. Plasmonic surface lattice resonances at the strong coupling regime. Nano Letters **14**, 1721 (2014). (cited on pages 10 and 18)

[106] G. Zengin, M. Wersäll, S. Nilsson, T. J. Antosiewicz, M. Käll, and T. Shegai. Realizing strong light-matter interactions between single-nanoparticle plasmons and molecular excitons at ambient conditions. Physical Review Letters **114** (2015). (cited on pages 11 and 18)

[107] M. K. Kim, H. Sim, S. J. Yoon, S. H. Gong, C. W. Ahn, Y. H. Cho, and Y. H. Lee.

Squeezing Photons into a Point-Like Space. Nano Letters **15**, 4102 (2015). (cited on p. 11)

[108] F. Benz, M. K. Schmidt, A. Dreismann, R. Chikkaraddy, Y. Zhang, A. Demetriadou, C. Carnegie, H. Ohadi, B. De Nijs, R. Esteban, J. Aizpurua, and J. J. Baumberg. Single-molecule optomechanics in "picocavities". Science **354**, 726 (2016). (cited on p. 11)

[109] C. R. Gubbin, F. Martini, A. Politi, S. A. Maier, and S. De Liberato. Strong and Coherent Coupling between Localized and Propagating Phonon Polaritons. Physical Review Letters **116** (2016). (cited on pages 11, 144, and 150)

[110] C. R. Gubbin, S. A. Maier, and S. De Liberato. Theoretical investigation of phonon polaritons in SiC micropillar resonators. Physical Review B **95**, 1 (2017). (cited on pages 11, 144, and 150)

[111] F. J. Alfaro-Mozaz, P. Alonso-González, S. Vélez, I. Dolado, M. Autore, S. Mastel, F. Casanova, L. E. Hueso, P. Li, A. Y. Nikitin, and R. Hillenbrand. Nanoimaging of resonating hyperbolic polaritons in linear boron nitride antennas. Nature Communications **8** (2017). (cited on p. 11)

[112] M. Autore, P. Li, I. Dolado, F. J. Alfaro-Mozaz, R. Esteban, A. Atxabal, F. Casanova, L. E. Hueso, P. Alonso-González, J. Aizpurua, A. Y. Nikitin, S. Vélez, and R. Hillenbrand. Boron nitride nanoresonators for Phonon-Enhanced molecular vibrational spectroscopy at the strong coupling limit. Light: Science and Applications **7** (2018). (cited on pages 11, 23, 144, and 150)

[113] C. A. Kocher and E. D. Commins. Polarization correlation of photons emitted in an atomic cascade. Physical Review Letters **18**, 575 (1967). (cited on p. 11)

[114] P. N. Prasad. *Nanophotonics* (John Wiley & Sons, 2004). (cited on p. 11)

[115] A. Gruber, A. Dräbenstedt, C. Tietz, L. Fleury, J. Wrachtrup, and C. Von Borczyskowski. Scanning confocal optical microscopy and magnetic resonance on single defect centers. Science **276**, 2012 (1997). (cited on p. 11)

[116] D. Wasserman, T. Ribaudo, S. A. Lyon, S. K. Lyo, and E. A. Shaner. Room temperature midinfrared electroluminescence from InAs quantum dots. Applied Physics Letters **94** (2009). (cited on p. 11)

[117] D. Pile. Mid-infrared: Intraband quantum dots. Nature Photonics **9**, 7 (2014).

(cited on p. 11)

[118] C.-C. Hou, H.-M. Chen, J.-C. Zhang, N. Zhuo, Y.-Q. Huang, R. A. Hogg, D. T. Childs, J.-Q. Ning, Z.-G. Wang, F.-Q. Liu, *et al.* Near-infrared and mid-infrared semiconductor broadband light emitters. Light: Science & Applications **7**, 17170 (2018). (cited on p. 11)

[119] J. L. O'Brien, G. J. Pryde, A. G. White, T. C. Ralph, and D. Branning. Demonstration of an all-optical quantum controlled-NOT gate. Nature **426**, 264 (2003). (cited on p. 11)

[120] B. P. Lanyon, M. Barbieri, M. P. Almeida, T. Jennewein, T. C. Ralph, K. J. Resch, G. J. Pryde, J. L. O'Brien, A. Gilchrist, and A. G. White. Quantum computing using shortcuts through higher dimensions. 0804.0272 (2008). (cited on p. 11)

[121] J. I. Cirac and H. J. Kimble. Quantum optics, what next? Nature Photonics **11**, 18 (2017). (cited on p. 11)

[122] T. K. Hakala, J. J. Toppari, A. Kuzyk, M. Pettersson, H. Tikkanen, H. Kunttu, and P. Törmä. Vacuum rabi splitting and strong-coupling dynamics for surface-plasmon polaritons and rhodamine 6G molecules. Physical Review Letters **103**, 1 (2009). (cited on pages 12 and 18)

[123] A. Mishra, R. K. Behera, P. K. Behera, B. K. Mishra, and G. B. Behera. Cyanines during the 1990s: a review. Chemical Reviews **100**, 1973 (2000). (cited on pages 12 and 15)

[124] F. Würthner, T. E. Kaiser, and C. R. Saha-Möller. J-aggregates: From serendipitous discovery to supramolecular engineering of functional dye materials (2011). (cited on p. 12)

[125] C. Iodoform. Ternary compounds, organic semiconductors (2000). (cited on p. 12)

[126] S. Kéna-Cohen, M. Davanço, and S. Forrest. Strong exciton-photon coupling in an organic single crystal microcavity. Physical review letters **101**, 116401 (2008). (cited on pages 12 and 18)

[127] S. Kéna-Cohen and S. R. Forrest. Room-temperature polariton lasing in an organic single-crystal microcavity. Nature Photonics **4**, 371 (2010). (cited on pages 12, 21, 94, and 98)

[128] E. E. JELLEY. Spectral Absorption and Fluorescence of Dyes in the Molecular State. Nature **138**, 1009 (1936). (cited on p. 12)

[129] J. Franck and E. Teller. Migration and photochemical action of excitation energy in crystals. The Journal of Chemical Physics **6**, 861 (1938). (cited on p. 12)

[130] G. D. Scholes. Designing light-harvesting antenna systems based on superradiant molecular aggregates. Chemical Physics **275**, 373 (2002). (cited on p. 12)

[131] S. K. Saikin, A. Eisfeld, S. Valleau, and A. Aspuru-Guzik. Photonics meets excitonics: Natural and artificial molecular aggregates. Nanophotonics **2**, 21 (2013). (cited on p. 12)

[132] M. Mohseni, Y. Omar, G. S. Engel, and M. B. Plenio. *Quantum effects in biology* (2014). (cited on p. 12)

[133] D. G. Lidzey, D. D. C. Bradley, A. Armitage, S. Walker, and M. S. Skolnick. Photon-mediated hybridization of Frenkel excitons in organic semiconductor microcavities. Science **288**, 1620 (2000). (cited on p. 12)

[134] J. Dintinger, S. Klein, F. Bustos, W. L. Barnes, and T. W. Ebbesen. Strong coupling between surface plasmon-polaritons and organic molecules in subwavelength hole arrays. Physical Review B - Condensed Matter and Materials Physics **71**, 35424 (2005). (cited on pages 12, 18, and 28)

[135] G. Zengin, G. Johansson, P. Johansson, T. J. Antosiewicz, M. Käll, and T. Shegai. Approaching the strong coupling limit in single plasmonic nanorods interacting with J-aggregates. Scientific Reports **3** (2013). (cited on pages 12, 18, 115, and 134)

[136] P. Vasa, W. Wang, R. Pomraenke, M. Lammers, M. Maiuri, C. Manzoni, G. Cerullo, and C. Lienau. Real-time observation of ultrafast Rabi oscillations between excitons and plasmons in metal nanostructures with J-aggregates. Nature Photonics **7**, 128 (2013). (cited on p. 12)

[137] D. Melnikau, D. Savateeva, A. Susha, A. L. Rogach, and Y. P. Rakovich. Strong plasmon-exciton coupling in a hybrid system of gold nanostars and J-aggregates. Nanoscale Research Letters **8**, 2 (2013). (cited on p. 12)

[138] V. May and O. Kühn. *Intramolecular Electronic Transitions* (2011). (cited on pages 12, 30, and 32)

[139] B. Stuart. *Infrared spectroscopy* (Wiley Online Library, 2005). (cited on p. 12)

[140] A. Shalabney, J. George, J. Hutchison, G. Pupillo, C. Genet, and T. W. Ebbesen. Coherent coupling of molecular resonators with a microcavity mode. Nature

Communications **6**, 5981 (2015).
(cited on pages 13, 22, 29, 57, 59, 60, 63, 65, 69, 70, 72, 97, 99, and 188)

[141] H. H. Jaffe and A. L. Miller. The fates of electronic excitation energy. Journal of Chemical Education **43**, 469 (1966). (cited on p. 13)

[142] A. Nitzan. Chemical Dynamics in Condensed Phases: Relaxation, Transfer, and Reactions in Condensed Molecular Systems (Oxford Graduate Texts). ChemPhysChem **8**, 1250 (2006). (cited on pages 13, 69, and 113)

[143] A. Nitzan, J. Jortner, and P. Rentzepis. Internal conversion in large molecules. Molecular Physics **22** (1971). (cited on p. 14)

[144] C. M. Marian. Spin-orbit coupling and intersystem crossing in molecules. Wiley Interdisciplinary Reviews: Computational Molecular Science **2**, 187 (2012).
(cited on p. 15)

[145] D. G. Lidzey and D. M. Coles. Strong Coupling in Organic and Hybrid-Semiconductor Microcavity Structures. In *Organic and Hybrid Photonic Crystals*, 243 (Springer, 2015).
(cited on p. 15)

[146] J. H. Song, Y. He, A. V. Nurmikko, J. Tischler, and V. Bulovic. Exciton-polariton dynamics in a transparent organic semiconductor microcavity. Physical Review B - Condensed Matter and Materials Physics **69** (2004). (cited on p. 16)

[147] P. G. Savvidis, L. G. Connolly, M. S. Skolnick, D. G. Lidzey, and J. J. Baumberg. Ultrafast polariton dynamics in strongly coupled zinc porphyrin microcavities at room temperature. Physical Review B - Condensed Matter and Materials Physics **74** (2006).
(cited on p. 16)

[148] T. Virgili, D. Coles, a. Adawi, C. Clark, P. Michetti, S. Rajendran, D. Brida, D. Polli, G. Cerullo, and D. Lidzey. Ultrafast polariton relaxation dynamics in an organic semiconductor microcavity. Physical Review B **83**, 2 (2011). (cited on p. 16)

[149] T. Schwartz, J. A. Hutchison, J. Léonard, C. Genet, S. Haacke, and T. W. Ebbesen. Polariton dynamics under strong light-molecule coupling. ChemPhysChem **14**, 125 (2013). (cited on pages 16, 21, 138, 146, and 152)

[150] R. Berera, R. van Grondelle, and J. T. M. Kennis. Ultrafast transient absorption spectroscopy: principles and application to photosynthetic systems. Photosynthesis Research (2009). (cited on p. 16)

[151] E. Romero, V. I. Novoderezhkin, and R. Van Grondelle. Quantum design of photosynthesis for bio-inspired solar-energy conversion (2017). (cited on p. 16)

[152] D. C. Harris and M. D. Bertolucci. *Symmetry and spectroscopy: an introduction to vibrational and electronic spectroscopy* (Courier Corporation, 1978). (cited on p. 16)

[153] C. N.B., D. L.H., and W. S.E. *Introduction to infrared and Raman spectroscopy* (Elsevier Science, 1990). (cited on p. 16)

[154] P. Vasa, R. Pomraenke, G. Cirmi, E. De Re, W. Wang, S. Schwieger, D. Leipold, E. Runge, G. Cerullo, and C. Lienau. Ultrafast manipulation of strong coupling in metal-molecular aggregate hybrid nanostructures. ACS Nano **4**, 7559 (2010). (cited on p. 18)

[155] T. Schwartz, J. A. Hutchison, C. Genet, and T. W. Ebbesen. Reversible switching of ultrastrong light-molecule coupling. 2011 Conference on Lasers and Electro-Optics Europe and 12th European Quantum Electronics Conference, CLEO EUROPE/EQEC 2011 **106**, 196405 (2011). (cited on pages 18 and 80)

[156] D. M. Coles, Y. Yang, Y. Wang, R. T. Grant, R. A. Taylor, S. K. Saikin, A. Aspuru-Guzik, D. G. Lidzey, J. K. H. Tang, and J. M. Smith. Strong coupling between chlorosomes of photosynthetic bacteria and a confined optical cavity mode. Nature Communications **5**, 5561 (2014). (cited on p. 18)

[157] D. M. Coles, L. C. Flatten, T. Sydney, E. Hounslow, S. K. Saikin, A. Aspuru-Guzik, V. Vedral, J. K.-H. Tang, R. A. Taylor, J. M. Smith, *et al.* Polaritons in Living Systems: Modifying Energy Landscapes in Photosynthetic Organisms Using a Photonic Structure. arXiv preprint arXiv:1702.01705 (2017). (cited on pages 18, 147, and 153)

[158] R. Chikkaraddy, V. A. Turek, N. Kongsuwan, F. Benz, C. Carnegie, T. Van De Goor, B. De Nijs, A. Demetriadou, O. Hess, U. F. Keyser, and J. J. Baumberg. Mapping Nanoscale Hotspots with Single-Molecule Emitters Assembled into Plasmonic Nanocavities Using DNA Origami. Nano Letters **18**, 405 (2018). (cited on p. 18)

[159] J. A. Hutchison, T. Schwartz, C. Genet, E. Devaux, and T. W. Ebbesen. Modifying chemical landscapes by coupling to vacuum fields. Angewandte Chemie - International Edition **51**, 1592 (2012). (cited on p. 18)

[160] B. Munkhbat, M. Wersäll, D. G. Baranov, T. J. Antosiewicz, and T. Shegai. Suppression of photo-oxidation of organic chromophores by strong coupling to plasmonic nanoantennas . (cited on pages 18, 130, 146, and 152)

[161] J. Galego, F. J. Garcia-Vidal, and J. Feist. Cavity-induced modifications of molecular structure in the strong-coupling regime. Physical Review X **5**, 41022 (2015). (cited on pages 18, 34, 80, 130, and 138)

[162] K. Bennett, M. Kowalewski, and S. Mukamel. Novel photochemistry of molecular polaritons in optical cavities. Faraday Discuss. **194**, 259 (2016). (cited on p. 18)

[163] M. Kowalewski, K. Bennett, and S. Mukamel. Non-adiabatic dynamics of molecules in optical cavities. Journal of Chemical Physics **144**, 1 (2016). (cited on p. 18)

[164] J. Flick, M. Ruggenthaler, H. Appel, and A. Rubio. Atoms and molecules in cavities, from weak to strong coupling in quantum-electrodynamics (QED) chemistry. Proceedings of the National Academy of Sciences **114**, 3026 (2017). (cited on p. 18)

[165] J. Galego, F. J. Garcia-Vidal, and J. Feist. Suppressing photochemical reactions with quantized light fields. Nature Communications **7**, 1 (2016). (cited on pages 19, 130, and 138)

[166] J. Galego, F. J. Garcia-Vidal, and J. Feist. Many-Molecule Reaction Triggered by a Single Photon in Polaritonic Chemistry. Physical Review Letters **119** (2017). (cited on pages 19, 146, and 152)

[167] F. Herrera and F. C. Spano. Cavity-Controlled Chemistry in Molecular Ensembles. Physical Review Letters **116**, 238301 (2016). (cited on pages 19, 111, 114, 115, 118, 122, 133, and 138)

[168] J. A. Ćwik, S. Reja, P. B. Littlewood, and J. Keeling. Polariton condensation with saturable molecules dressed by vibrational modes. Epl **105**, 47009 (2014). (cited on pages 19 and 115)

[169] M. A. Zeb, P. G. Kirton, and J. Keeling. Exact States and Spectra of Vibrationally Dressed Polaritons. ACS Photonics **5**, 249 (2018). (cited on pages 19, 111, 114, 115, 121, 122, 126, 133, and 138)

[170] N. Wu, J. Feist, and F. J. Garcia-Vidal. When polarons meet polaritons: Exciton-vibration interactions in organic molecules strongly coupled to confined light fields. Physical Review B **94**, 195409 (2016). (cited on pages 19, 111, 114, 115, 116, and 133)

[171] U. Schollwock. The density-matrix renormalization group: a short introduction. Philosophical Transactions of the Royal Society A: Mathematical, Physical and

Engineering Sciences **369**, 2643 (2011). (cited on pages 20, 43, 46, 49, and 50)

[172] J. Prior, A. W. Chin, S. F. Huelga, and M. B. Plenio. Efficient simulation of strong system-environment interactions. Physical Review Letters **105**, 1 (2010). (cited on pages 20, 21, 46, 146, and 152)

[173] A. W. Chin, S. F. Huelga, and M. B. Plenio. Chain Representations of Open Quantum Systems and Their Numerical Simulation with Time-Adaptive Density Matrix Renormalisation Group Methods. Semiconductors and Semimetals **85**, 115 (2011). (cited on pages 20, 21, 45, 46, 146, and 152)

[174] J. A. Hutchison, A. Liscio, T. Schwartz, A. Canaguier-Durand, C. Genet, V. Palermo, P. Samor??, T. W. Ebbesen, P. Samorì, and T. W. Ebbesen. Tuning the work-function via strong coupling. Advanced Materials **25**, 2481 (2013). (cited on p. 20)

[175] E. Orgiu, J. George, J. A. Hutchison, E. Devaux, J. F. Dayen, B. Doudin, F. Stellacci, C. Genet, J. Schachenmayer, C. Genes, G. Pupillo, P. Samorì, and T. W. Ebbesen. Conductivity in organic semiconductors hybridized with the vacuum field. Nature Materials **14**, 1123 (2015). (cited on p. 20)

[176] X. Zhong, T. Chervy, L. Zhang, A. Thomas, J. George, C. Genet, J. A. Hutchison, and T. W. Ebbesen. Energy Transfer between Spatially Separated Entangled Molecules. Angewandte Chemie - International Edition **56**, 9034 (2017). (cited on p. 20)

[177] J. Schachenmayer, C. Genes, E. Tignone, and G. Pupillo. Cavity enhanced transport of excitons. Physical Review Letters **114**, 1 (2014). (cited on p. 20)

[178] J. Feist and F. J. Garcia-Vidal. Extraordinary exciton conductance induced by strong coupling. Physical Review Letters **114**, 1 (2015). (cited on p. 20)

[179] J. D. Plumhof, T. Stöferle, L. Mai, U. Scherf, and R. F. Mahrt. Room-temperature Bose-Einstein condensation of cavity exciton-polaritons in a polymer. Nature Materials **13**, 247 (2014). (cited on p. 21)

[180] S. R. K. Rodriguez, J. Feist, M. A. Verschuuren, F. J. Garcia Vidal, and J. Gómez Rivas. Thermalization and cooling of plasmon-exciton polaritons: Towards quantum condensation. Physical Review Letters **111** (2013). (cited on p. 21)

[181] M. Ramezani, A. Halpin, A. I. Fernández-Domínguez, J. Feist, S. R.-K. Rodriguez, F. J. Garcia-Vidal, and J. Gómez Rivas. Plasmon-exciton-polariton lasing. Optica **4**, 31 (2017). (cited on p. 21)

[182] M. Litinskaya, P. Reineker, and V. M. Agranovich. Fast polariton relaxation in strongly coupled organic microcavities. In *Journal of Luminescence*, volume 110, 364 (2004). (cited on pages 21, 24, 73, 138, 146, and 152)

[183] P. Michetti and G. C. La Rocca. Exciton-phonon scattering and photoexcitation dynamics in J-aggregate microcavities. Physical Review B - Condensed Matter and Materials Physics **79** (2009). (cited on pages 21, 24, 73, 146, and 152)

[184] S. Baieva, O. Hakamaa, G. Groenhof, T. T. Heikkila, and J. J. Toppari. Dynamics of strongly coupled modes between surface plasmon polaritons and photoactive molecules: The effect of the stokes shift. ACS Photonics **4**, 28 (2017). (cited on pages 21, 123, 140, 146, and 152)

[185] J. A. Ćwik, P. Kirton, S. De Liberato, and J. Keeling. Excitonic spectral features in strongly coupled organic polaritons. Physical Review A **93**, 33840 (2016). (cited on pages 21, 78, 79, and 80)

[186] F. Herrera and F. C. Spano. Theory of Nanoscale Organic Cavities: The Essential Role of Vibration-Photon Dressed States. ACS Photonics **5**, 65 (2018). (cited on pages 21 and 140)

[187] H.-P. Breuer and F. Petruccione. *The Theory of Open Quantum Systems* (Oxford University Press, 2007). (cited on pages 21, 37, 38, 63, 82, 97, and 136)

[188] M. B. Plenio and S. F. Huelga. Dephasing-assisted transport: Quantum networks and biomolecules. New Journal of Physics **10** (2008). (cited on pages 21 and 118)

[189] A. W. Chin, J. Prior, R. Rosenbach, F. Caycedo-Soler, S. F. Huelga, and M. B. Plenio. The role of non-equilibrium vibrational structures in electronic coherence and recoherence in pigment-protein complexes. Nature Physics **9**, 113 (2013). (cited on pages 21, 146, and 152)

[190] M. B. Plenio, J. Almeida, and S. F. Huelga. Origin of long-lived oscillations in 2D-spectra of a quantum vibronic model: Electronic versus vibrational coherence. Journal of Chemical Physics **139** (2013). (cited on pages 21, 146, 152, and 153)

[191] E. Collini, C. Y. Wong, K. E. Wilk, P. M. Curmi, P. Brumer, and G. D. Scholes. Coherently wired light-harvesting in photosynthetic marine algae at ambient temperature. Nature **463**, 644 (2010). (cited on pages 21, 146, and 152)

[192] E. Romero, R. Augulis, V. I. Novoderezhkin, M. Ferretti, J. Thieme, D. Zigmantas, and

R. Van Grondelle. Quantum coherence in photosynthesis for efficient solar-energy conversion. Nature Physics **10**, 676 (2014). (cited on pages 21, 146, and 153)

[193] F. D. Fuller, J. Pan, A. Gelzinis, V. Butkus, S. S. Senlik, D. E. Wilcox, C. F. Yocum, L. Valkunas, D. Abramavicius, and J. P. Ogilvie. Vibronic coherence in oxygenic photosynthesis. Nature Chemistry **6**, 706 (2014). (cited on p. 21)

[194] J. Haegeman, J. I. Cirac, T. J. Osborne, I. Pižorn, H. Verschelde, and F. Verstraete. Time-dependent variational principle for quantum lattices. Physical Review Letters **107**, 70601 (2011). (cited on pages 21, 51, 131, and 188)

[195] F. A. Schröder and A. W. Chin. Simulating open quantum dynamics with time-dependent variational matrix product states: Towards microscopic correlation of environment dynamics and reduced system evolution. Physical Review B **93**, 1 (2016). (cited on pages 21, 45, 51, 52, 115, 131, 139, and 188)

[196] J. P. Long and B. S. Simpkins. Coherent coupling between a molecular vibration and fabry-perot optical cavity to give hybridized states in the strong coupling limit. ACS Photonics **2**, 130 (2015). (cited on pages 22, 59, 69, 70, and 72)

[197] B. S. Simpkins, K. P. Fears, W. J. Dressick, B. T. Spann, A. D. Dunkelberger, and J. C. Owrutsky. Spanning Strong to Weak Normal Mode Coupling between Vibrational and Fabry-Pérot Cavity Modes through Tuning of Vibrational Absorption Strength. ACS Photonics **2**, 1460 (2015). (cited on p. 22)

[198] W. Ahn, I. Vurgaftman, A. D. Dunkelberger, J. C. Owrutsky, and B. S. Simpkins. Vibrational Strong Coupling Controlled by Spatial Distribution of Molecules within the Optical Cavity. ACS Photonics acsphotonics.7b00583 (2017). (cited on p. 22)

[199] A. Thomas, J. George, A. Shalabney, M. Dryzhakov, S. J. Varma, J. Moran, T. Chervy, X. Zhong, E. Devaux, C. Genet, J. A. Hutchison, and T. W. Ebbesen. Ground-State Chemical Reactivity under Vibrational Coupling to the Vacuum Electromagnetic Field. Angewandte Chemie - International Edition **55**, 11462 (2016). (cited on pages 22, 144, and 150)

[200] M. Muallem, A. Palatnik, G. D. Nessim, and Y. R. Tischler. Strong Light-Matter Coupling and Hybridization of Molecular Vibrations in a Low-Loss Infrared Microcavity. Journal of Physical Chemistry Letters **7**, 2002 (2016). (cited on pages 22, 94, 97, and 98)

[201] S. R. Casey and J. R. Sparks. Vibrational strong coupling of organometallic complexes.

Journal of Physical Chemistry C **120**, 28138 (2016). (cited on pages 22 and 28)

[202] R. M. Vergauwe, J. George, T. Chervy, J. A. Hutchison, A. Shalabney, V. Y. Torbeev, and T. W. Ebbesen. Quantum Strong Coupling with Protein Vibrational Modes. Journal of Physical Chemistry Letters **7**, 4159 (2016). (cited on p. 22)

[203] T. Chervy, A. Thomas, E. Akiki, R. M. A. Vergauwe, A. Shalabney, J. George, E. Devaux, J. A. Hutchison, C. Genet, and T. W. Ebbesen. Vibro-Polaritonic IR Emission in the Strong Coupling Regime. ACS Photonics acsphotonics.7b00677 (2017). (cited on pages 23, 69, 145, and 151)

[204] D. W. Oxtoby. Dephasing of Molecular Vibrations in Liquids. Advances in Chemical Physics **40**, 1 (1979). (cited on pages 23 and 69)

[205] Y. Tanimura and S. Mukamel. Two-dimensional femtosecond vibrational spectroscopy of liquids. The Journal of Chemical Physics **99**, 9496 (1993). (cited on pages 23 and 69)

[206] H. J. Carmichael. *Statistical Methods in Quantum Optics 2*. Theoretical and Mathematical Physics (Springer Berlin Heidelberg, Berlin, Heidelberg, 2008). (cited on pages 24 and 91)

[207] A. G. Redfield. Nuclear magnetic resonance saturation and rotary saturation in solids. Physical Review **98**, 1787 (1955). (cited on pages 24, 41, 59, 63, 82, and 136)

[208] R. K. Wangsness and F. Bloch. The dynamical theory of nuclear induction. Physical Review **89**, 728 (1953). (cited on pages 24, 41, 59, 63, 82, and 136)

[209] A. Kolli, E. J. O'Reilly, G. D. Scholes, and A. Olaya-Castro. The fundamental role of quantized vibrations in coherent light harvesting by cryptophyte algae. Journal of Chemical Physics **137**, 174109 (2012). (cited on p. 24)

[210] E. J. O'Reilly and A. Olaya-Castro. Non-classicality of the molecular vibrations assisting exciton energy transfer at room temperature. Nature Communications **5**, 3012 (2014). (cited on p. 24)

[211] M. Litinskaya and P. Reineker. Loss of coherence of exciton polaritons in inhomogeneous organic microcavities. Physical Review B - Condensed Matter and Materials Physics **74**, 165320 (2006). (cited on pages 24, 73, and 136)

[212] A. Shalabney, J. George, H. Hiura, J. A. Hutchison, C. Genet, P. Hellwig, and T. W. Ebbesen. Enhanced Raman Scattering from Vibro-Polariton Hybrid States. Angewandte Chemie - International Edition **54**, 7971 (2015).

(cited on pages 24, 57, 82, 84, 86, 87, 144, and 150)

[213] S. Nie and S. R. Emory. Probing single molecules and single nanoparticles by surface-enhanced Raman scattering. Science **275**, 1102 (1997). (cited on p. 24)

[214] A. Campion and P. Kambhampati. Surface-enhanced Raman scattering. Chemical Society Reviews **27**, 241 (1998). (cited on p. 24)

[215] J. Kneipp, H. Kneipp, and K. Kneipp. SERS—a single-molecule and nanoscale tool for bioanalytics. Chemical Society Reviews **37**, 1052 (2008). (cited on p. 24)

[216] P. Roelli, C. Galland, N. Piro, and T. J. Kippenberg. Molecular cavity optomechanics as a theory of plasmon-enhanced Raman scattering. Nature Nanotechnology **11**, 164 (2016). (cited on p. 24)

[217] P. Saurabh and S. Mukamel. Two-dimensional infrared spectroscopy of vibrational polaritons of molecules in an optical cavity. The Journal of chemical physics **144**, 124115 (2016). (cited on p. 24)

[218] B. Xiang, R. F. Ribeiro, A. D. Dunkelberger, J. Wang, Y. Li, B. S. Simpkins, J. C. Owrutsky, J. Yuen-Zhou, and W. Xiong. Two-dimensional infrared spectroscopy of vibrational polaritons. Proceedings of the National Academy of Sciences 201722063 (2018). (cited on p. 24)

[219] R. H. Stolen, E. P. Ippen, and A. R. Tynes. Raman oscillation in glass optical waveguide. Applied Physics Letters **20**, 62 (1972). (cited on pages 25 and 89)

[220] H. M. Pask. The design and operation of solid-state Raman lasers. Progress in Quantum Electronics **27**, 3 (2003). (cited on pages 25, 89, and 97)

[221] F. Benabid, J. C. Knight, G. Antonopoulos, and P. S. J. Russell. Stimulated Raman scattering in hydrogen-filled hollow-core photonic crystal fiber. Science **298**, 399 (2002). (cited on pages 25 and 89)

[222] O. Boyraz and B. Jalali. Demonstration of a silicon Raman laser. Optics Express **12**, 5269 (2004). (cited on pages 25 and 89)

[223] H. Rong, R. Jones, A. Liu, O. Cohen, D. Hak, A. Fang, and M. Paniccia. A continuous-wave Raman silicon laser. Nature **433**, 725 (2005). (cited on pages 25 and 89)

[224] H. Rong, S. Xu, Y. H. Kuo, V. Sih, O. Cohen, O. Raday, and M. Paniccia.

Low-threshold continuous-wave Raman silicon laser. Nature Photonics **1**, 232 (2007). (cited on pages 25 and 89)

[225] T. J. Kippenberg, S. M. Spillane, D. K. Armani, and K. J. Vahala. Ultralow-threshold microcavity Raman laser on a microelectronic chip. Optics Letters **29**, 1224 (2004). (cited on pages 25 and 89)

[226] J. K. Brasseur, K. S. Repasky, and J. L. Carlsten. Continuous-wave Raman laser in H_2. Optics Letters **23**, 367 (1998). (cited on pages 25 and 89)

[227] R. W. Boyd. *The Nonlinear Optical Susceptibility* (Elsevier, 2008), third edition. (cited on pages 25, 89, 94, and 97)

[228] D. F. Walls. Squeezed states of light. Nature **306**, 141 (1983). (cited on pages 25 and 90)

[229] M. D. Reid and P. D. Drummond. Quantum correlations of phase in nondegenerate parametric oscillation. Physical Review Letters **60**, 2731 (1988). (cited on pages 25 and 90)

[230] M. Xiao, L. A. Wu, and H. J. Kimble. Precision measurement beyond the shot-noise limit. Physical Review Letters **59**, 278 (1987). (cited on pages 25 and 90)

[231] A. Heidmann, R. J. Horowicz, S. Reynaud, E. Giacobino, C. Fabre, and G. Camy. Observation of quantum noise reduction on twin laser beams. Physical Review Letters **59**, 2555 (1987). (cited on pages 25 and 90)

[232] S. Ramelow, L. Ratschbacher, A. Fedrizzi, N. K. Langford, and A. Zeilinger. Discrete tunable color entanglement. Physical Review Letters **103**, 2 (2009). (cited on pages 25 and 90)

[233] A. S. Coelho, F. A. S. Barbosa, K. N. Cassemiro, A. S. Villar, M. Martinelli, and P. Nussenzveig. Three-Color Entanglement. Science **326**, 823 (2009). (cited on pages 25 and 90)

[234] E. Saglamyurek, N. Sinclair, J. Jin, J. A. Slater, D. Oblak, W. Tittel, F. Bussières, M. George, R. Ricken, and W. Sohler. Broadband waveguide quantum memory for entangled photons (Invited Paper). 2011 IEEE Photonics Society Summer Topical Meeting Series **469**, 4 (2011). (cited on pages 25 and 104)

[235] A. Lenhard, M. Bock, C. Becher, S. Kucera, J. Brito, P. Eich, P. Müller, and J. Eschner. Telecom-heralded single-photon absorption by a single atom. Physical Review A -

Atomic, Molecular, and Optical Physics **92**, 63827 (2015). (cited on pages 25 and 104)

[236] J. Midwinter. *Optical Bistability, Controling Light with Light*, volume 133 of *Quantum Electronics Series* (Academic Press, 1986). (cited on pages 25, 90, and 95)

[237] A. M. Dawes, L. Illing, S. M. Clark, and D. J. Gauthier. Applied physics: All-optical switching in rubidium vapor. Science **308**, 672 (2005). (cited on pages 25, 90, and 95)

[238] R. P. *The Quantum Theory of Radiation*, volume 138 (Courier Corporation, 1936). (cited on p. 28)

[239] D. P. Craig and T. Thirunamachandran. Molecular quantum electrodynamics : an introduction to radiation-molecule interactions. Theoretical chemistry xi, 324 p. (1984). (cited on p. 28)

[240] D. A. Steck. Quantum and Atom Optics Author contact information :. Book **47** (2007). (cited on pages 28, 36, 147, and 153)

[241] M. Pope and C. E. Swenberg. *Electronic Processes in Organic Crystals and Polymers* (1999). (cited on p. 28)

[242] T. Neuman, R. Esteban, D. Casanova, F. J. García-Vidal, and J. Aizpurua. Coupling of Molecular Emitters and Plasmonic Cavities beyond the Point-Dipole Approximation. Nano Letters **18**, 2358 (2018). (cited on p. 29)

[243] A. Cuartero-González and A. I. Fernández-Domínguez. Light-Forbidden Transitions in Plasmon-Emitter Coupling. arXiv preprint arXiv:1803.04737 (2018). (cited on p. 29)

[244] N. Rivera, I. Kaminer, B. Zhen, J. D. Joannopoulos, and M. Soljačić. Shrinking light to allow forbidden transitions on the atomic scale. Science **353**, 263 (2016). (cited on p. 29)

[245] H. Zoubi and G. C. La Rocca. Microscopic theory of nonlinear polariton interactions in strongly coupled hybrid organic-inorganic microcavities. Physical Review B - Condensed Matter and Materials Physics **76** (2007). (cited on p. 29)

[246] N. W. Ashcroft and N. D. Mermin. Solid State Physics (1976). (cited on p. 29)

[247] M. Born and R. Oppenheimer. Zur Quantentheorie der Molekeln. Annalen der Physik **389**, 457 (1927). (cited on p. 30)

[248] J. C. Tully. Perspective on "Zur Quantentheorie der Molekeln". Theoretical Chemistry

Accounts: Theory, Computation, and Modeling (Theoretica Chimica Acta) **103**, 173 (2000). (cited on p. 30)

[249] P. W. Atkins and R. Friedman. *Molecular Quantum Mechanics*, volume 134 (2011). (cited on p. 31)

[250] A. Strashko and J. Keeling. Raman scattering with strongly coupled vibron-polaritons. Physical Review A **94** (2016). (cited on pages 32, 87, 144, and 150)

[251] G. D. Mahan. *Many-Particle Physics* (Springer Science & Business Media, Boston, MA, 2000). (cited on pages 33, 40, and 113)

[252] J. George, A. Shalabney, J. A. Hutchison, C. Genet, and T. W. Ebbesen. Liquid-phase vibrational strong coupling. Journal of Physical Chemistry Letters **6**, 1027 (2015). (cited on p. 35)

[253] K. Rzaewski, K. Wódkiewicz, and W. Zakowicz. Phase transitions, two-level atoms, and the A^2 term. Physical Review Letters **35**, 432 (1975). (cited on pages 35 and 82)

[254] J. Keeling. Coulomb interactions, gauge invariance, and phase transitions of the Dicke model. Journal of Physics Condensed Matter **19** (2007). (cited on p. 36)

[255] M. Tavis and F. W. Cummings. Exact solution for an N-molecule-radiation-field Hamiltonian. Physical Review **170**, 379 (1968). (cited on p. 36)

[256] M. Tavis and F. W. Cummings. Approximate solutions for an N-molecule-radiation-field Hamiltonian. Physical Review **188**, 692 (1969). (cited on p. 36)

[257] G. Compagno, R. Passante, and F. Persico. *Atom-field interactions and dressed atoms*, volume 17 (Cambridge University Press, 2005). (cited on p. 36)

[258] C. W. Gardiner and P. Zoller. *Quantum noise : a handbook of Markovian and non-Markovian quantum stochastic methods with applications to quantum optics* (Springer Berlin Heidelberg, 2004). (cited on pages 37 and 63)

[259] Á. Rivas and S. F. Huelga. *Open Quantum Systems. An Introduction* (Springer, 2011). (cited on pages 37 and 40)

[260] U. Weiss. *Quantum Dissipative Systems*, volume 10 (World Scientific, 2012). (cited on pages 37 and 115)

[261] I. Wilson-Rae and A. Imamoğlu. Quantum dot cavity-QED in the presence of strong

electron-phonon interactions. Physical Review B - Condensed Matter and Materials Physics **65**, 1 (2002). (cited on pages 37 and 136)

[262] C. Roy and S. Hughes. Phonon-dressed mollow triplet in the regime of cavity quantum electrodynamics: Excitation-induced dephasing and nonperturbative cavity feeding effects. Physical Review Letters **106**, 247403 (2011). (cited on pages 37 and 136)

[263] H. J. Carmichael and D. F. Walls. Master equation for strongly interacting systems. Journal of Physics A: Mathematical, Nuclear and General **6**, 1552 (1973). (cited on pages 38, 64, and 68)

[264] J. Cerrillo and J. Cao. Non-Markovian dynamical maps: Numerical processing of open quantum trajectories. Physical Review Letters **112** (2014). (cited on p. 39)

[265] R. P. Feynman and F. L. Vernon. The theory of a general quantum system interacting with a linear dissipative system. Annals of Physics **281**, 547 (2000). (cited on p. 39)

[266] N. Makri. Improved Feynman propagators on a grid and non-adiabatic corrections within the path integral framework. Chemical Physics Letters **193**, 435 (1992). (cited on p. 39)

[267] Y. Tanimura and R. Kubo. Time Evolution of a Quantum System in Contact with a Nearly Gaussian-Markoffian Noise Bath. Journal of the Physical Society of Japan **58**, 101 (1989). (cited on p. 39)

[268] J. Jeske and J. H. Cole. Derivation of Markovian master equations for spatially correlated decoherence. Physical Review A - Atomic, Molecular, and Optical Physics **87** (2013). (cited on p. 40)

[269] H. Bahouri, J.-Y. Chemin, and R. Danchin. *Fourier Analysis and Nonlinear Partial Differential Equations*, volume 343 (Springer Science & Business Media, 2011). (cited on p. 40)

[270] G. Lindblad. On the generators of quantum dynamical semigroups. Communications in Mathematical Physics **48**, 119 (1976). (cited on p. 40)

[271] M. Thorwart, E. Paladino, and M. Grifoni. Dynamics of the spin-boson model with a structured environment. Chemical Physics **296**, 26 (2003). (cited on p. 41)

[272] P. M. Visser and G. Nienhuis. Solution of quantum master equations in terms of a non-Hermitian Hamiltonian. Physical Review A **52**, 4727 (1995). (cited on p. 41)

[273] R. Sáez-Blázquez, J. Feist, A. Fernández-Domínguez, and F. García-Vidal. Enhancing photon correlations through plasmonic strong coupling. Optica **4**, 1363 (2017). (cited on p. 41)

[274] J. Jeske, D. J. Ing, M. B. Plenio, S. F. Huelga, and J. H. Cole. Bloch-Redfield equations for modeling light-harvesting complexes. Journal of Chemical Physics **142**, 064104 (2015). (cited on p. 41)

[275] J. R. Johansson, P. D. Nation, and F. Nori. QuTiP 2: A Python framework for the dynamics of open quantum systems. Computer Physics Communications **184**, 1234 (2013). (cited on pages 41, 69, and 82)

[276] R. Orús. A practical introduction to tensor networks: Matrix product states and projected entangled pair states (2014). (cited on pages 43, 45, and 111)

[277] M. Srednicki. Entropy and area. Phys. Rev. Lett. **71**, 666 (1993). (cited on p. 44)

[278] C. Guo, A. Weichselbaum, J. Von Delft, and M. Vojta. Critical and strong-coupling phases in one- and two-bath spin-boson models. Physical Review Letters **108**, 1 (2012). (cited on pages 45, 115, and 134)

[279] J. Biamonte and V. Bergholm. Tensor Networks in a Nutshell. arXiv preprint arXiv:1708.00006 (2017). (cited on p. 45)

[280] A. Garg, J. N. Onuchic, and V. Ambegaokar. Effect of friction on electron transfer in biomolecules. The Journal of Chemical Physics **83**, 4491 (1985). (cited on pages 46, 114, and 128)

[281] T. Renger and R. A. Marcus. On the relation of protein dynamics and exciton relaxation in pigment-protein complexes: An estimation of the spectral density and a theory for the calculation of optical spectra. Journal of Chemical Physics **116**, 9997 (2002). (cited on pages 46 and 114)

[282] J. Iles-Smith, N. Lambert, and A. Nazir. Environmental dynamics, correlations, and the emergence of noncanonical equilibrium states in open quantum systems. Physical Review A - Atomic, Molecular, and Optical Physics **90**, 1 (2014). (cited on pages 46 and 114)

[283] M. Thoss, H. Wang, and W. H. Miller. Self-consistent hybrid approach for complex systems: Application to the spin-boson model with Debye spectral density. Journal of Chemical Physics **115**, 2991 (2001). (cited on pages 46 and 114)

[284] I. de Vega and M.-C. Bañuls. Thermofield-based chain-mapping approach for open quantum systems. Physical Review A **92**, 052116 (2015).
(cited on pages 46, 147, and 153)

[285] S. Szalay, M. Pfeffer, V. Murg, G. Barcza, F. Verstraete, R. Schneider, and Ö. Legeza. Tensor product methods and entanglement optimization for ab initio quantum chemistry. International Journal of Quantum Chemistry **115**, 1342 (2015).
(cited on pages 48, 115, and 134)

[286] Y. Y. Shi, L. M. Duan, and G. Vidal. Classical simulation of quantum many-body systems with a tree tensor network. Physical Review A - Atomic, Molecular, and Optical Physics **74**, 1 (2006). (cited on pages 48, 115, and 134)

[287] G. Vidal. Entanglement Renormalization. Phys. Rev. Lett. **99**, 220405 (2007).
(cited on p. 49)

[288] F. A. Y. N. Schröder, D. H. P. Turban, A. J. Musser, N. D. M. Hine, and A. W. Chin. Multi-dimensional Tensor Network Simulation of Open Quantum Dynamics in Singlet Fission . (cited on pages 49, 52, 115, and 134)

[289] S. R. White. Density matrix formulation for quantum renormalization groups. Physical Review Letters **69**, 2863 (1992). (cited on pages 49 and 114)

[290] A. W. Chin, Á. Rivas, S. F. Huelga, and M. B. Plenio. Exact mapping between system-reservoir quantum models and semi-infinite discrete chains using orthogonal polynomials. Journal of Mathematical Physics **51** (2010).
(cited on pages 50, 146, and 153)

[291] J. Haegeman, C. Lubich, I. Oseledets, B. Vandereycken, and F. Verstraete. Unifying time evolution and optimization with matrix product states. Physical Review B **94**, 165116 (2016). (cited on p. 51)

[292] S. J. Byrnes. Multilayer optical calculations. arXiv preprint arXiv:1603.02720 (2016).
(cited on pages 61 and 188)

[293] A. González-Tudela, P. A. Huidobro, L. Martín-Moreno, C. Tejedor, and F. J. García-Vidal. Reversible dynamics of single quantum emitters near metal-dielectric interfaces. Physical Review B - Condensed Matter and Materials Physics **89** (2014).
(cited on p. 62)

[294] A. Delga, J. Feist, J. Bravo-Abad, and F. J. Garcia-Vidal. Quantum emitters near a

metal nanoparticle: Strong coupling and quenching. Physical Review Letters **112** (2014). (cited on p. 62)

[295] R. Dümcke and H. Spohn. The proper form of the generator in the weak coupling limit. Zeitschrift für Physik B Condensed Matter and Quanta **34**, 419 (1979). (cited on p. 65)

[296] H. Spohn. Kinetic equations from Hamiltonian dynamics: Markovian limits. Reviews of Modern Physics **52**, 569 (1980). (cited on p. 65)

[297] P. R. Eastham, A. O. Spracklen, and J. Keeling. Lindblad theory of dynamical decoherence of quantum-dot excitons. Physical Review B - Condensed Matter and Materials Physics **87**, 195306 (2013). (cited on p. 66)

[298] G. K. Wertheim, M. A. Butler, K. W. West, and D. N. E. Buchanan. Determination of the Gaussian and Lorentzian content of experimental line shapes. Review of Scientific Instruments **45**, 1369 (1974). (cited on p. 69)

[299] R. Houdré, R. P. Stanley, and M. Ilegems. Vacuum-field Rabi splitting in the presence of inhomogeneous broadening: Resolution of a homogeneous linewidth in an inhomogeneously broadened system. Physical Review A - Atomic, Molecular, and Optical Physics **53**, 2711 (1996). (cited on pages 70 and 95)

[300] J. M. Manceau, G. Biasiol, N. L. Tran, I. Carusotto, and R. Colombelli. Immunity of intersubband polaritons to inhomogeneous broadening. Physical Review B **96** (2017). (cited on p. 70)

[301] D. M. Whittaker, P. Kinsler, T. A. Fisher, M. S. Skolnick, A. Armitage, A. M. Afshar, J. S. Roberts, G. Hill, and M. A. Pate. Motional narrowing in semiconductor microcavities. Superlattices and Microstructures **22**, 91 (1997). (cited on p. 71)

[302] S. Haroche. Fundamental systems in quantum optics. Les Houches Summar School Session **53** (1992). (cited on p. 71)

[303] S. Mukamel. *Principles of Nonlinear Optical Spectroscopy.* 6 (Oxford University Press on Demand, 1999). (cited on p. 77)

[304] J. Kosztin and A. Zawadowski. Violation of the F-Sum Rule for Raman-Scattering in Metals. Solid State Communications **78**, 1029 (1991). (cited on p. 80)

[305] J. K. Freericks, T. P. Devereaux, M. Moraghebi, and S. L. Cooper. Optical sum rules that relate to the potential energy of strongly correlated systems. Physical Review Letters **94**, 216401 (2005). (cited on p. 80)

[306] L. de' Medici, A. Georges, and G. Kotliar. Sum-rules for Raman scattering off strongly correlated electron systems. Physical Review B **77**, 245128 (2008). (cited on p. 80)

[307] Y. Todorov, A. M. Andrews, R. Colombelli, S. De Liberato, C. Ciuti, P. Klang, G. Strasser, and C. Sirtori. Ultrastrong light-matter coupling regime with polariton dots. Physical Review Letters **105**, 1 (2010). (cited on p. 80)

[308] S. De Liberato, D. Gerace, I. Carusotto, and C. Ciuti. Extracavity quantum vacuum radiation from a single qubit. Physical Review A - Atomic, Molecular, and Optical Physics **80**, 1 (2009). (cited on p. 82)

[309] F. Beaudoin, J. M. Gambetta, and A. Blais. Dissipation and ultrastrong coupling in circuit QED. Physical Review A **84**, 043832 (2011). (cited on p. 82)

[310] X. Jin, A. Cerea, G. C. Messina, A. Rovere, R. Piccoli, F. De Donato, F. Palazon, A. Perucchi, P. Di Pietro, R. Morandotti, S. Lupi, F. De Angelis, M. Prato, A. Toma, and L. Razzari. Reshaping the phonon energy landscape of nanocrystals inside a terahertz plasmonic nanocavity. Nature Communications **9**, 763 (2018). (cited on pages 87, 144, and 150)

[311] A. Penzkofer, A. Laubereau, and W. Kaiser. High intensity Raman interactions. Progress in Quantum Electronics **6**, 55 (1979). (cited on pages 88 and 94)

[312] E. Brion, L. H. Pedersen, and K. Mølmer. Adiabatic elimination in a lambda system. Journal of Physics A: Mathematical and Theoretical **40**, 1033 (2007). (cited on p. 92)

[313] F. Reiter and A. S. Sørensen. Effective operator formalism for open quantum systems. Physical Review A - Atomic, Molecular, and Optical Physics **85**, 032111 (2012). (cited on p. 92)

[314] H. Feshbach. Unified theory of nuclear reactions. Annals of Physics **5**, 357 (1958). (cited on p. 92)

[315] A. Yariv and W. H. Louisell. Theory of the Optical Parametric Oscillator. IEEE Journal of Quantum Electronics **2**, 118 (1966). (cited on pages 97 and 100)

[316] T. Holstein and H. Primakoff. Field dependence of the intrinsic domain magnetization of a ferromagnet. Physical Review **58**, 1098 (1940). (cited on p. 98)

[317] K. S. Daskalakis, S. A. Maier, R. Murray, and S. Kéna-Cohen. Nonlinear interactions in an organic polariton condensate. Nature Materials **13**, 271 (2014). (cited on p. 98)

[318] E. D. Palik. *Handbook of optical constants*, volume 2 (Academic Press, 1998). (cited on p. 99)

[319] I. S. Gradshteyn, I. M. Ryzhik, A. Jeffrey, Y. V. Geronimus, M. Y. Tseytlin, and Y. C. Fung. *17 Fourier, Laplace, and Mellin Transforms*, volume 103 (Elsevier, 1981), eigth edition. (cited on p. 102)

[320] R. A. Marcus. On the theory of oxidation-reduction reactions involving electron transfer. I. The Journal of Chemical Physics **24**, 966 (1956). (cited on p. 112)

[321] F. C. Spano. Optical microcavities enhance the exciton coherence length and eliminate vibronic coupling in J-aggregates. Journal of Chemical Physics **142** (2015). (cited on pages 114 and 133)

[322] A. W. Chin, J. Prior, S. F. Huelga, and M. B. Plenio. Generalized polaron ansatz for the ground state of the sub-Ohmic spin-boson model: An analytic theory of the localization transition. Physical Review Letters **107**, 1 (2011). (cited on pages 114, 127, and 134)

[323] A. J. Leggett, S. Chakravarty, A. T. Dorsey, M. P. Fisher, A. Garg, and W. Zwerger. Dynamics of the dissipative two-state system. Reviews of Modern Physics **59**, 1 (1987). (cited on p. 115)

[324] F. Herrera and F. C. Spano. Dark Vibronic Polaritons and the Spectroscopy of Organic Microcavities. Physical Review Letters **118** (2017). (cited on pages 118 and 140)

[325] T. A. Costi and R. H. McKenzie. Entanglement between a qubit and the environment in the spin-boson model. Physical Review A - Atomic, Molecular, and Optical Physics **68**, 4 (2003). (cited on p. 118)

[326] D. V. Khveshchenko. Quantum impurity models of noisy qubits. Physical Review B - Condensed Matter and Materials Physics **69** (2004). (cited on p. 118)

[327] S. Sachdev, C. Buragohain, and M. Vojta. Quantum impurity in a nearly critical two-dimensional antiferromagnet. Science **286**, 2479 (1999). (cited on p. 118)

[328] S. Sachdev. Quantum Phase Transitions. In *Handbook of Magnetism and Advanced Magnetic Materials*, 1, 1 (2007). (cited on p. 119)

[329] R. Liu, Z.-K. Zhou, Y.-C. Yu, T. Zhang, H. Wang, G. Liu, Y. Wei, H. Chen, and X.-H. Wang. Strong light-matter interactions in single open plasmonic nanocavities at the quantum optics limit. Physical review letters **118**, 237401 (2017). (cited on p. 119)

[330] P. E. Dargel, A. Wöllert, A. Honecker, I. P. McCulloch, U. Schollwöck, and T. Pruschke. Lanczos algorithm with matrix product states for dynamical correlation functions. Physical Review B - Condensed Matter and Materials Physics **85**, 205119 (2012). (cited on p. 123)

[331] S. Bera, A. Nazir, A. W. Chin, H. U. Baranger, and S. Florens. Generalized multipolaron expansion for the spin-boson model: Environmental entanglement and the biased two-state system. Physical Review B - Condensed Matter and Materials Physics **90**, 1 (2014). (cited on p. 127)

[332] F. Valmorra, M. Bröll, S. Schwaiger, N. Welzel, D. Heitmann, and S. Mendach. Strong coupling between surface plasmon polariton and laser dye rhodamine 800. Applied Physics Letters **99** (2011). (cited on p. 128)

[333] N. Christensson, B. Dietzek, A. Yartsev, and T. Pullerits. Electronic photon echo spectroscopy and vibrations. Vibrational Spectroscopy **53**, 2 (2010). (cited on pages 128 and 133)

[334] S. A. Passino, Y. Nagasawa, and G. R. Fleming. Three pulse stimulated photon echo experiments as a probe of polar solvation dynamics: Utility of harmonic bath models. Journal of Chemical Physics **107**, 6094 (1997). (cited on p. 128)

[335] J. Prior, A. W. Chin, S. F. Huelga, and M. B. Plenio. Efficient simulation of strong system-environment interactions. Physical Review Letters **105**, 50404 (2010). (cited on p. 131)

[336] A. W. Chin, J. Prior, R. Rosenbach, F. Caycedo-Soler, S. F. Huelga, and M. B. Plenio. The role of non-equilibrium vibrational structures in electronic coherence and recoherence in pigment-protein complexes. Nature Physics **9**, 113 (2013). (cited on p. 131)

[337] M. L. Wall, A. Safavi-Naini, and A. M. Rey. Simulating generic spin-boson models with matrix product states. Physical Review A **94**, 53637 (2016). (cited on p. 131)

[338] D. P. S. McCutcheon and A. Nazir. Quantum dot Rabi rotations beyond the weak exciton-phonon coupling regime. New Journal of Physics **12**, 113042 (2010). (cited on p. 136)

[339] D. M. Coles, N. Somaschi, P. Michetti, C. Clark, P. G. Lagoudakis, P. G. Savvidis, and D. G. Lidzey. Polariton-mediated energy transfer between organic dyes in a strongly coupled optical microcavity. Nature Materials **13**, 712 (2014).

(cited on pages 138, 147, and 153)

[340] J. D. Pino, J. Feist, and F. J. Garcia-Vidal. Quantum theory of collective strong coupling of molecular vibrations with a microcavity mode. New Journal of Physics **17**, 53040 (2015). (cited on p. 138)

[341] J. del Pino, F. A. Y. N. Schröder, A. W. Chin, J. Feist, and F. J. Garcia-Vidal. Tensor Network simulation of polaritonic chemistry with organic molecules. (in preparation) . (cited on p. 138)

[342] L. Argenti, R. Pazourek, J. Feist, S. Nagele, M. Liertzer, E. Persson, J. Burgdörfer, and E. Lindroth. Photoionization of helium by attosecond pulses: Extraction of spectra from correlated wave functions. Physical Review A - Atomic, Molecular, and Optical Physics **87**, 53405 (2013). (cited on p. 140)

[343] J. Del Pino, J. Feist, and F. J. Garcia-Vidal. Signatures of Vibrational Strong Coupling in Raman Scattering. Journal of Physical Chemistry C **119**, 29132 (2015). (cited on pages 144 and 150)

[344] L. D. Merkle, J. Zhang, G. Allen, J. W. Dawson, and M. Dubinskii. Raman gain of SiC as a potential medium for Raman lasers. In *Optical Components and Materials XII*, volume 9359, 935904 (International Society for Optics and Photonics, 2015). (cited on pages 144 and 150)

[345] H. Frei, L. Fredin, and G. C. Pimentel. Vibrational excitation of ozone and molecular fluorine reactions in cryogenic matrices. The Journal of Chemical Physics **74**, 397 (1981). (cited on pages 144 and 150)

[346] I. N. Levine, D. H. Busch, and H. Shull. *Quantum chemistry*, volume 5 (Prentice Hall Upper Saddle River, NJ, 2000). (cited on pages 145 and 150)

[347] C. P. Dietrich, A. Steude, L. Tropf, M. Schubert, N. M. Kronenberg, K. Ostermann, S. Höfling, and M. C. Gather. An exciton-polariton laser based on biologically produced fluorescent protein. Science Advances (2016). (cited on pages 145 and 151)

[348] J. E. Mark *et al. Physical properties of polymers handbook*, volume 1076 (Springer, 2007). (cited on pages 145 and 151)

[349] C. Gonzalez-Ballestero, J. Feist, E. Moreno, and F. J. Garcia-Vidal. Harvesting excitons through plasmonic strong coupling. Physical Review B - Condensed Matter and Materials Physics (2015). (cited on pages 145 and 151)

[350] E. Eizner, K. Akulov, T. Schwartz, and T. Ellenbogen. Temporal Dynamics of Localized Exciton-Polaritons in Composite Organic-Plasmonic Metasurfaces. Nano Letters **17**, 7675 (2017). (cited on pages 146 and 152)

[351] H.-G. Duan, V. I. Prokhorenko, R. J. Cogdell, K. Ashraf, A. L. Stevens, M. Thorwart, and R. J. D. Miller. Nature does not rely on long-lived electronic quantum coherence for photosynthetic energy transfer. Proceedings of the National Academy of Sciences (2017). (cited on pages 146 and 153)

[352] F. Ma, E. Romero, M. R. Jones, V. I. Novoderezhkin, and R. van Grondelle. Vibronic Coherence in the Charge Separation Process of the Rhodobacter sphaeroides Reaction Center. The Journal of Physical Chemistry Letters (2018). (cited on pages 146 and 153)

[353] G. D. Scholes, G. R. Fleming, A. Olaya-Castro, and R. Van Grondelle. Lessons from nature about solar light harvesting (2011). (cited on pages 146 and 153)

[354] A. Tsargorodska, M. L. Cartron, C. Vasilev, G. Kodali, O. A. Mass, J. J. Baumberg, P. L. Dutton, C. N. Hunter, P. Törmä, and G. J. Leggett. Strong Coupling of Localized Surface Plasmons to Excitons in Light-Harvesting Complexes. Nano Letters (2016). (cited on pages 147 and 153)

[355] R. T. Grant, R. Jayaprakash, D. M. Coles, A. Musser, S. De Liberato, I. D. W. Samuel, G. A. Turnbull, J. Clark, and D. G. Lidzey. Strong coupling in a microcavity containing β-carotene. Optics Express (2018). (cited on pages 147 and 153)

[356] K. Georgiou, R. Jayaprakash, A. Askitopoulos, D. M. Coles, P. G. Lagoudakis, and D. G. Lidzey. Generation of Anti-Stokes Fluorescence in a Strongly Coupled Organic Semiconductor Microcavity. Arxiv (2018). (cited on pages 147 and 153)

List of Figures

List of Tables

Publications related to the content of this thesis

5. *Tensor network simulation of non-Markovian dynamics in organic polaritons.*
   Javier Del Pino, Florian Schröder, Alex Chin, Francisco. J. García-Vidal and Johannes Feist.(2018)
   Submitted to Physical Review Letters.

4. *Tensor Network simulation of polaritonic chemistry with organic molecules.*
   Javier Del Pino, Florian Schröder, Alex Chin, Francisco. J. García-Vidal and Johannes Feist. (2018)
   In preparation for submission to Physical Review B.

3. *Exploiting Vibrational Strong Coupling to make an Optical Parametric Oscillator out of a Raman Laser.*
   Javier Del Pino, Francisco. J. García-Vidal and Johannes Feist. (2016).
   Physical Review Letters, 117 (27), 277401.

2. *Signatures of Vibrational Strong Coupling in Raman Scattering.*
   Javier Del Pino, Johannes Feist and Francisco. J. García-Vidal. (2015).
   J. Phys. Chem. C, **2015**, 119 (52).

1. *Quantum theory of collective strong coupling of molecular vibrations with a microcavity mode.*
   Javier Del Pino, Johannes Feist and Francisco. J. García-Vidal. (2015).
   New Journal of Physics **17** 053040.
   (Highlighted in *Ensemble strong coupling* - W. L. Barnes (2015) New Journal of Physics **17** 081001)

Vibrational and electronic strong light-matter coupling with molecular excitations

This thesis is devoted to the investigation of polaritons supported by organic microcavities. Two distinct types of such states are present in these systems, namely, exciton-polaritons and vibro-polaritons, formed upon the hybridisation of molecular excitations with optical and mid-infrared photons respectively. We provide fundamental investigations in both scenarios, by employing models of increased complexity that are tractable in the framework of quantum optics and quasi-exact methods in condensed matter physics. Our results demonstrate the crucial role of the molecular environment and phonons in determining the steady-state linear spectra, the internal structure and the short-time dynamics of organic polaritons.

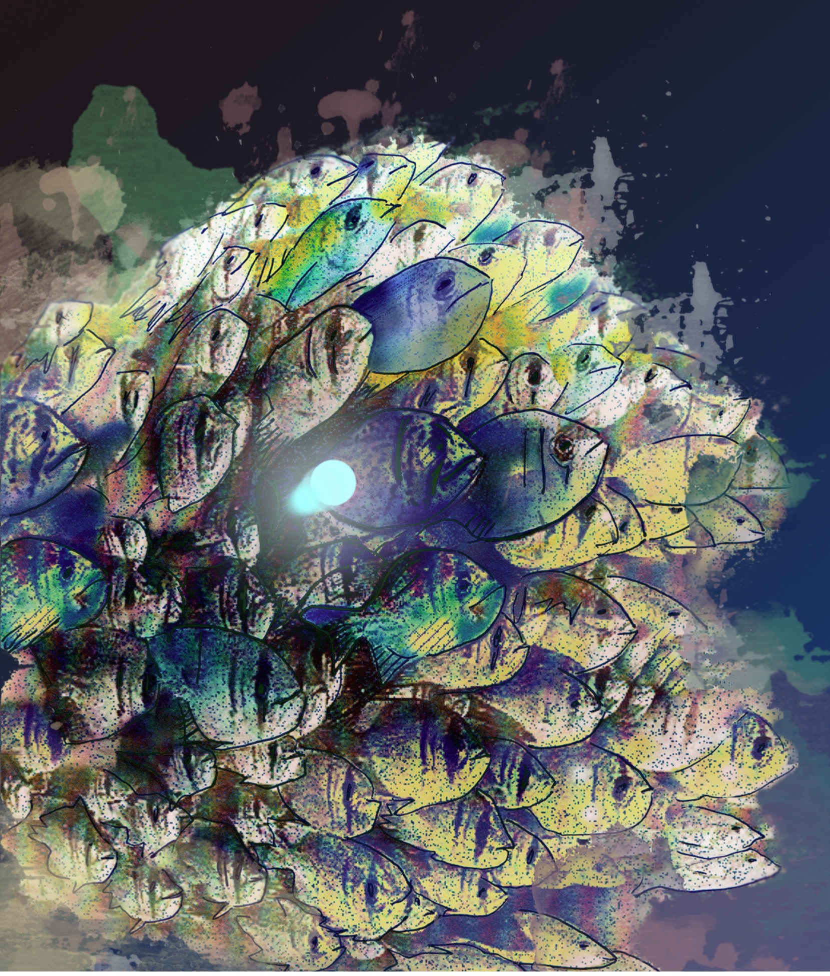

1968-
2018